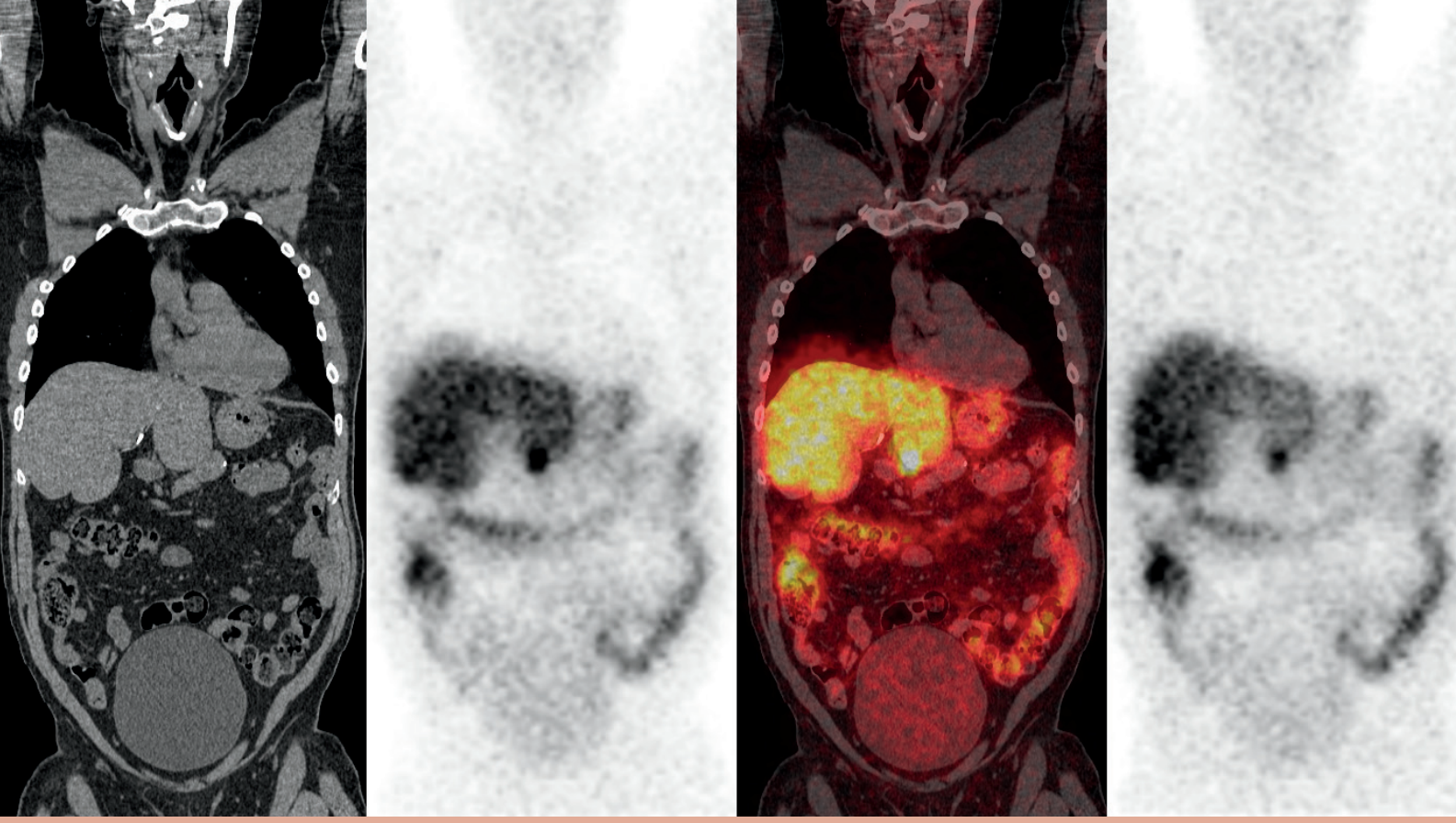

IAEA HUMAN HEALTH SERIES

No. 36

SPECT/CT Atlas of Quality Control and Image Artefacts

IAEA
International Atomic Energy Agency

IAEA HUMAN HEALTH SERIES PUBLICATIONS

The mandate of the IAEA human health programme originates from Article II of its Statute, which states that the "Agency shall seek to accelerate and enlarge the contribution of atomic energy to peace, health and prosperity throughout the world". The main objective of the human health programme is to enhance the capabilities of IAEA Member States in addressing issues related to the prevention, diagnosis and treatment of health problems through the development and application of nuclear techniques, within a framework of quality assurance.

Publications in the IAEA Human Health Series provide information in the areas of: radiation medicine, including diagnostic radiology, diagnostic and therapeutic nuclear medicine, and radiation therapy; dosimetry and medical radiation physics; and stable isotope techniques and other nuclear applications in nutrition. The publications have a broad readership and are aimed at medical practitioners, researchers and other professionals. International experts assist the IAEA Secretariat in drafting and reviewing these publications. Some of the publications in this series may also be endorsed or co-sponsored by international organizations and professional societies active in the relevant fields.

There are two categories of publications in this series:

IAEA HUMAN HEALTH SERIES

Publications in this category present analyses or provide information of an advisory nature, for example guidelines, codes and standards of practice, and quality assurance manuals. Monographs and high level educational material, such as graduate texts, are also published in this series.

IAEA HUMAN HEALTH REPORTS

Human Health Reports complement information published in the IAEA Human Health Series in areas of radiation medicine, dosimetry and medical radiation physics, and nutrition. These publications include reports of technical meetings, the results of IAEA coordinated research projects, interim reports on IAEA projects, and educational material compiled for IAEA training courses dealing with human health related subjects. In some cases, these reports may provide supporting material relating to publications issued in the IAEA Human Health Series.

All of these publications can be downloaded cost free from the IAEA web site:

http://www.iaea.org/Publications/index.html

Further information is available from:

Marketing and Sales Unit
International Atomic Energy Agency
Vienna International Centre
PO Box 100
1400 Vienna, Austria

Readers are invited to provide their impressions on these publications. Information may be provided via the IAEA web site, by mail at the address given above, or by email to:

Official.Mail@iaea.org.

SPECT/CT ATLAS OF QUALITY CONTROL AND IMAGE ARTEFACTS

The following States are Members of the International Atomic Energy Agency:

AFGHANISTAN
ALBANIA
ALGERIA
ANGOLA
ANTIGUA AND BARBUDA
ARGENTINA
ARMENIA
AUSTRALIA
AUSTRIA
AZERBAIJAN
BAHAMAS
BAHRAIN
BANGLADESH
BARBADOS
BELARUS
BELGIUM
BELIZE
BENIN
BOLIVIA, PLURINATIONAL STATE OF
BOSNIA AND HERZEGOVINA
BOTSWANA
BRAZIL
BRUNEI DARUSSALAM
BULGARIA
BURKINA FASO
BURUNDI
CAMBODIA
CAMEROON
CANADA
CENTRAL AFRICAN REPUBLIC
CHAD
CHILE
CHINA
COLOMBIA
CONGO
COSTA RICA
CÔTE D'IVOIRE
CROATIA
CUBA
CYPRUS
CZECH REPUBLIC
DEMOCRATIC REPUBLIC OF THE CONGO
DENMARK
DJIBOUTI
DOMINICA
DOMINICAN REPUBLIC
ECUADOR
EGYPT
EL SALVADOR
ERITREA
ESTONIA
ESWATINI
ETHIOPIA
FIJI
FINLAND
FRANCE
GABON
GEORGIA
GERMANY
GHANA
GREECE
GRENADA
GUATEMALA
GUYANA
HAITI
HOLY SEE
HONDURAS
HUNGARY
ICELAND
INDIA
INDONESIA
IRAN, ISLAMIC REPUBLIC OF
IRAQ
IRELAND
ISRAEL
ITALY
JAMAICA
JAPAN
JORDAN
KAZAKHSTAN
KENYA
KOREA, REPUBLIC OF
KUWAIT
KYRGYZSTAN
LAO PEOPLE'S DEMOCRATIC REPUBLIC
LATVIA
LEBANON
LESOTHO
LIBERIA
LIBYA
LIECHTENSTEIN
LITHUANIA
LUXEMBOURG
MADAGASCAR
MALAWI
MALAYSIA
MALI
MALTA
MARSHALL ISLANDS
MAURITANIA
MAURITIUS
MEXICO
MONACO
MONGOLIA
MONTENEGRO
MOROCCO
MOZAMBIQUE
MYANMAR
NAMIBIA
NEPAL
NETHERLANDS
NEW ZEALAND
NICARAGUA
NIGER
NIGERIA
NORTH MACEDONIA
NORWAY
OMAN
PAKISTAN
PALAU
PANAMA
PAPUA NEW GUINEA
PARAGUAY
PERU
PHILIPPINES
POLAND
PORTUGAL
QATAR
REPUBLIC OF MOLDOVA
ROMANIA
RUSSIAN FEDERATION
RWANDA
SAINT LUCIA
SAINT VINCENT AND THE GRENADINES
SAN MARINO
SAUDI ARABIA
SENEGAL
SERBIA
SEYCHELLES
SIERRA LEONE
SINGAPORE
SLOVAKIA
SLOVENIA
SOUTH AFRICA
SPAIN
SRI LANKA
SUDAN
SWEDEN
SWITZERLAND
SYRIAN ARAB REPUBLIC
TAJIKISTAN
THAILAND
TOGO
TRINIDAD AND TOBAGO
TUNISIA
TURKEY
TURKMENISTAN
UGANDA
UKRAINE
UNITED ARAB EMIRATES
UNITED KINGDOM OF GREAT BRITAIN AND NORTHERN IRELAND
UNITED REPUBLIC OF TANZANIA
UNITED STATES OF AMERICA
URUGUAY
UZBEKISTAN
VANUATU
VENEZUELA, BOLIVARIAN REPUBLIC OF
VIET NAM
YEMEN
ZAMBIA
ZIMBABWE

The Agency's Statute was approved on 23 October 1956 by the Conference on the Statute of the IAEA held at United Nations Headquarters, New York; it entered into force on 29 July 1957. The Headquarters of the Agency are situated in Vienna. Its principal objective is "to accelerate and enlarge the contribution of atomic energy to peace, health and prosperity throughout the world''.

IAEA HUMAN HEALTH SERIES No. 36

SPECT/CT ATLAS OF QUALITY CONTROL AND IMAGE ARTEFACTS

INTERNATIONAL ATOMIC ENERGY AGENCY
VIENNA, 2019

COPYRIGHT NOTICE

Marketing and Sales Unit, Publishing Section
International Atomic Energy Agency
Vienna International Centre
PO Box 100
1400 Vienna, Austria
fax: +43 1 26007 22529
tel.: +43 1 2600 22417
email: sales.publications@iaea.org
www.iaea.org/publications

Printed by the IAEA in Austria
December 2019
STI/PUB/1860

IAEA Library Cataloguing in Publication Data

Names: International Atomic Energy Agency.
Title: SPECT/CT atlas of quality control and image artefacts / International Atomic Energy Agency.
Description: Vienna : International Atomic Energy Agency, 2019. | Series: IAEA human health series, ISSN 2075–3772 ; no. 36 | Includes bibliographical references.
Identifiers: IAEAL 19-01276 | ISBN 978–92–0–103919–4 (paperback : alk. paper) | ISBN 978–92–0–159219–4 (pdf)
Subjects: LCSH: Single-photon emission computed tomography. | Tomography — Atlases. | Diagnostic imaging. | Quality control.
Classification: UDC 616–073(084) | STI/PUB/1860

FOREWORD

In recent years, hybrid single photon emission computed tomography (SPECT)/computed tomography (CT) imaging has become increasingly prevalent in nuclear medicine and diagnostic radiology. To accurately interpret SPECT/CT images, it is important to understand the principles of image formation and the biological distribution of the radiopharmaceutical, and also to understand the types of image artefact that can arise from these imaging systems. This publication presents an overview of quality control procedures in SPECT and SPECT/CT and describes the pitfalls and artefacts that can occur in these imaging modalities.

A series of case studies of image artefacts are presented that can occur, with descriptions of their causes and the steps that can be taken to avoid their recurrence. Of the 67 case studies in this publication, some are actual clinical cases, while others use phantoms in order to yield valuable data. The atlas is intended to be used as a guide on how to take appropriate quality control measures and to assist with problem analyses and prevention. It is hoped that this publication will be especially useful for medical physicists, physicians, nuclear medicine and diagnostic radiology professionals, and service engineers.

The IAEA wishes to express its appreciation to all those who contributed to the drafting and review of this publication, particularly J.C. Dickson (United Kingdom), S. Holm (Denmark), O. Mawlawi (United States of America) and C.C. Robilotta (Brazil). The IAEA officer for this publication was G.L. Poli of the Division of Human Health.

EDITORIAL NOTE

Although great care has been taken to maintain the accuracy of information contained in this publication, neither the IAEA nor its Member States assume any responsibility for consequences which may arise from its use.

This publication does not address questions of responsibility, legal or otherwise, for acts or omissions on the part of any person.

Guidance provided here, describing good practices, represents expert opinion but does not constitute recommendations made on the basis of a consensus of Member States.

The use of particular designations of countries or territories does not imply any judgement by the publisher, the IAEA, as to the legal status of such countries or territories, of their authorities and institutions or of the delimitation of their boundaries.

The mention of names of specific companies or products (whether or not indicated as registered) does not imply any intention to infringe proprietary rights, nor should it be construed as an endorsement or recommendation on the part of the IAEA.

The IAEA has no responsibility for the persistence or accuracy of URLs for external or third party Internet web sites referred to in this book and does not guarantee that any content on such web sites is, or will remain, accurate or appropriate.

CONTENTS

1. INTRODUCTION

1.1. BACKGROUND

Single photon emission computed tomography (SPECT) is a modality whose roots were established in the early 1960s following the work of Kuhl and Edwards [1]. However, it was not until the advent of systems using the Anger gamma camera in the 1970s that SPECT was established as a technology that would be recognizable today [2–4]. Little changed from these original gamma camera tomographic systems until the work of Hasegawa [5] in the 1990s, which combined a SPECT and a computed tomography (CT) system in what is known as a hybrid SPECT/CT scanner. This was nearly ten years before the inception of the first positron emission tomography/computed tomography (PET/CT) scanner. The adoption of SPECT/CT systems into routine clinical use initially proved to be slow. However, all major manufacturers have now released SPECT/CT systems with various specifications and capabilities.

1.2. OBJECTIVE

The complexity of a combined SPECT/CT system requires rigorous quality control procedures. Similarly, the wealth of information provided by combined SPECT/CT examinations needs to be complemented with a thorough understanding of potential pitfalls and artefacts arising from the combined imaging procedure. SPECT/CT, as with any other imaging modality, is acceptable for routine clinical and research applications only if technical pitfalls can be avoided prospectively; if artefacts from incorrect or suboptimal acquisition procedures can be recognized and, whenever possible, corrected retrospectively; and if the resulting image information can be interpreted correctly, which entails an appreciation of variants of the represented image information.

1.3. SCOPE

This publication presents an overview of quality control procedures in SPECT and SPECT/CT and describes the pitfalls and image artefacts that can occur. Clearly, it is impossible for any book to cover all potentially encountered image artefacts at every site that uses a SPECT or SPECT/CT system. However, an understanding of the source of these artefacts will help to support improved SPECT/CT operations along with the high quality standards required for an increased acceptance of this modality. Guidance provided here, describing good practices, represents expert opinion but does not constitute recommendations made on the basis of a consensus of Member States.

1.4. STRUCTURE

This publication builds on the IAEA Quality Control Atlas for Scintillation Camera Systems [6], published in 2003, and compliments the PET/CT Atlas on Quality Control and Image Artefacts [7], published in 2014. Section 2 provides a brief overview of the basic principles of emission tomography, CT and the use of CT images for attenuation correction (AC) of SPECT images, and concludes with a survey of SPECT and SPECT/CT systems currently available. Section 3 describes the required quality control procedures for the operation of SPECT and SPECT/CT systems in routine clinical practice, and additional literature is provided in the references. Section 4 presents the case studies of artefacts from different sources, ranging from hardware malfunctions to patient induced artefacts. Each case study includes some background, a description and some guidance on how to interpret and understand the nature of the artefacts and ways to avoid them.

2. SPECT AND SPECT/CT SYSTEMS

2.1. EMISSION TOMOGRAPHY

2.1.1. Basic design

SPECT is a modality whose roots were established in the early 1960s following the work of Kuhl and Edwards [1]. However, it was not until the advent of systems using the Anger gamma camera [2–4] that SPECT was recognized as a novel imaging technology (see Fig. 1(a)). Typically, SPECT systems use a gamma camera detector capable of rotating around the object of interest, and projection images are acquired at multiple angles to provide the information necessary to reconstruct a three dimensional distribution of activity. Until recently, little had changed from these original gamma camera tomographic systems (see Fig. 1(b)), although configurations of two, three and even four detector heads were developed to speed up the process of SPECT data acquisition (see Fig. 1(c)). Based on some of these designs, SPECT systems specific to different areas of nuclear medicine have been developed — namely, nuclear cardiology and the brain (see Fig. 1(d)).

More recently, equipment manufacturers have focused on novel SPECT systems that differ from the standard gamma camera SPECT design. There has been a move towards hybrid SPECT/CT systems, and replacing the scintillation detector based gamma camera systems with detectors based on semiconductor technology. The introduction of SPECT/CT systems has been driven, at least initially, for the attenuation correction of myocardial perfusion studies and basic anatomical mapping, with more recent developments focusing on better anatomical mapping and quantitative evaluation of SPECT studies. Furthermore, imaging devices are now available that

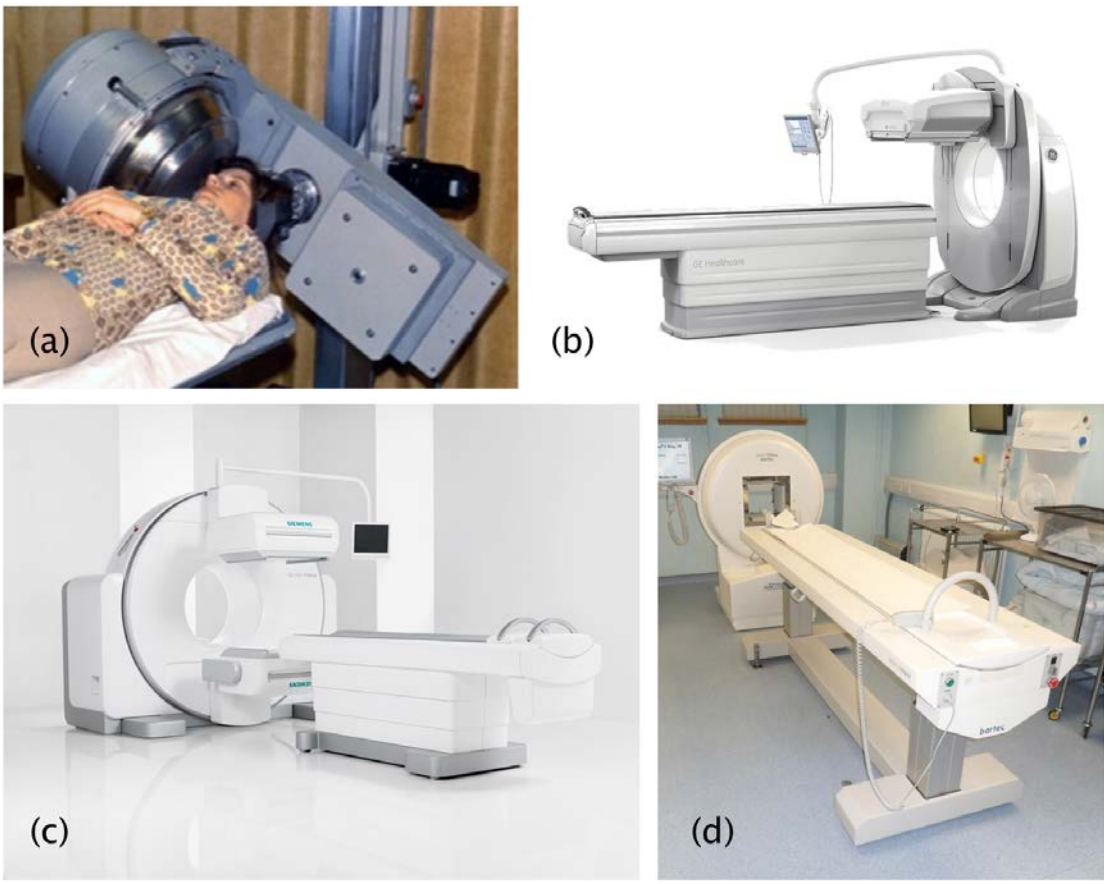

FIG. 1. (a) An original gamma camera design (courtesy of R. Jaszczak and reproduced with permission courtesy of IOP Publishing) and (b) a modern equivalent (courtesy of GE Healthcare). (c) Multidetector designs (courtesy of Siemens Healthineers) have led to (d) application specific devices (courtesy of Mediso Medical Imaging Systems).

either replace the photomultiplier tube of a scintillation detector with pin or silicon drift diodes, or that replace the complete detector with designs based on semiconductor materials such as cadmium zinc telluride (CZT). The use of semiconductor designs has several advantages. Compared to a typical scintillation detector, solid state systems offer much more compact imaging devices, which can lead to improved patient comfort and a reduced scanner footprint. There are also additional benefits in performance that come with these systems [8, 9]. For example, improvements in energy resolution offer clear benefits in dual radionuclide scanning, while high count rate performance provides advantages in first-pass and dynamic imaging. Other improvements, such as discontinuing the use of photomultiplier tubes, also offer the possibility of combining SPECT with magnetic resonance (MR) in hybrid SPECT/MR scanners (see Fig. 2 for examples of current solid state based SPECT imaging systems).

2.1.2. Acquisition

A number of parameters are required to define the SPECT acquisition. As with standard gamma camera imaging, the number of acquired counts determines the noise properties of the image. Since there is a limit to the activity that can be administered to a patient, count and noise levels are controlled by imaging time. SPECT requires images acquired at multiple angles, so the noise level at each of these angles needs to be considered. If the time per projection is overextended, the acquisition could become prohibitively long, and the radiopharmaceutical distribution might change. Conversely, very short projection times can result in low counts and high image noise level, which might destabilize certain reconstructions [10]. Another factor that determines the level of image noise is the pixel size used. Typically, SPECT acquisitions use either 64 × 64 or 128 × 128 matrices with some zoom factor, resulting in pixel sizes between approximately 2 mm and 8 mm. With spatial resolution of modern systems

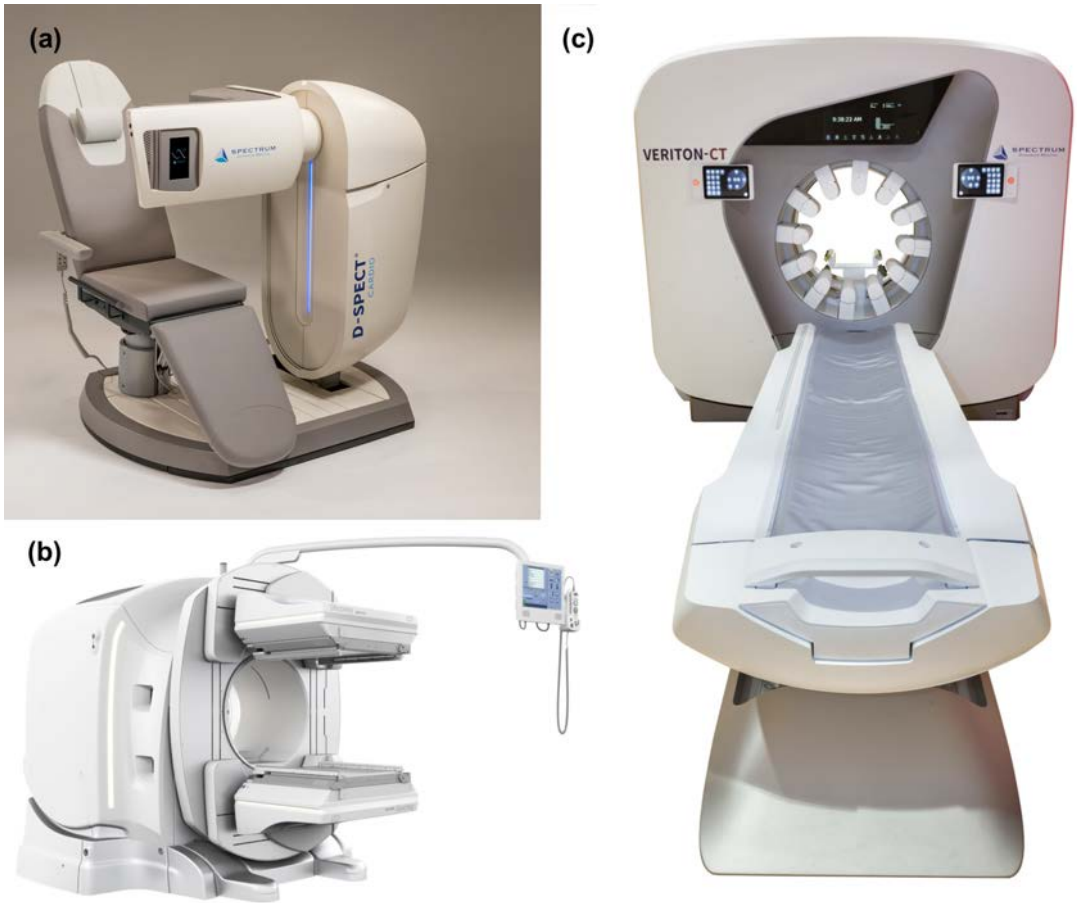

FIG. 2. SPECT systems with semiconductor technology: (a) D-SPECT cardio dedicated cardiac system (courtesy of Spectrum Dynamics Medical SA); (b) Discovery 670 CZT all purpose SPECT/CT system (courtesy of GE Healthcare); and (c) Veriton wholebody system (courtesy of Spectrum Dynamics Medical SA).

in the range of 8–10 mm, there is no benefit to acquire with smaller pixel sizes, while larger pixel sizes are avoided because of sampling and partial volume issues.

To obtain SPECT data, images from multiple angles are acquired by rotating the detector(s) around the object of interest. Traditionally, SPECT requires images obtained from 360 degrees of arc, which for multiple head systems can be split between each detector, for example 180 degrees of arc per detector for dual headed systems (see Fig. 3(a)). However, a split acquisition approach requires well matched detector sensitivities to avoid bias artefacts. In nuclear cardiology, because of the left anterior sided position of the heart, images using 180 degrees of arc are commonly acquired between right anterior oblique (RAO) to left posterior oblique (LPO) positions. This provides optimal resolution and limits attenuation losses over the heart area compared to a full 360 degree arc acquisition, but it does lead to distortion in the right posterior part of the reconstructed data due to the distance dependent resolution of the collimator not being balanced out by an opposed view (see Fig. 3(c)). Fortunately, this area is not diagnostically helpful in typical cardiac studies. To make this type of acquisition more efficient on dual detector systems, the two detectors are positioned into a 90 degree or L-mode configuration to form a right angle (see Fig. 3(b)). One additional rotational option available in many SPECT systems is the choice of 'step-and-shoot', or continuous acquisition mode. In the step-and-shoot mode, the detectors are stationary during the acquisition of projection data, with a short quick movement used to move between different projection angles. In continuous mode, data are being acquired while the detector moves at a constant speed, with the data binned into angular projections as the detectors rotate. Continuous mode therefore slightly reduces the acquisition time, at the cost of some blurring of the projection data.

As with planar imaging, collimation plays a key role in the performance and acquisition of SPECT systems. Spatial resolution in SPECT is often inferior to that of planar imaging. This is due to the increased distance between

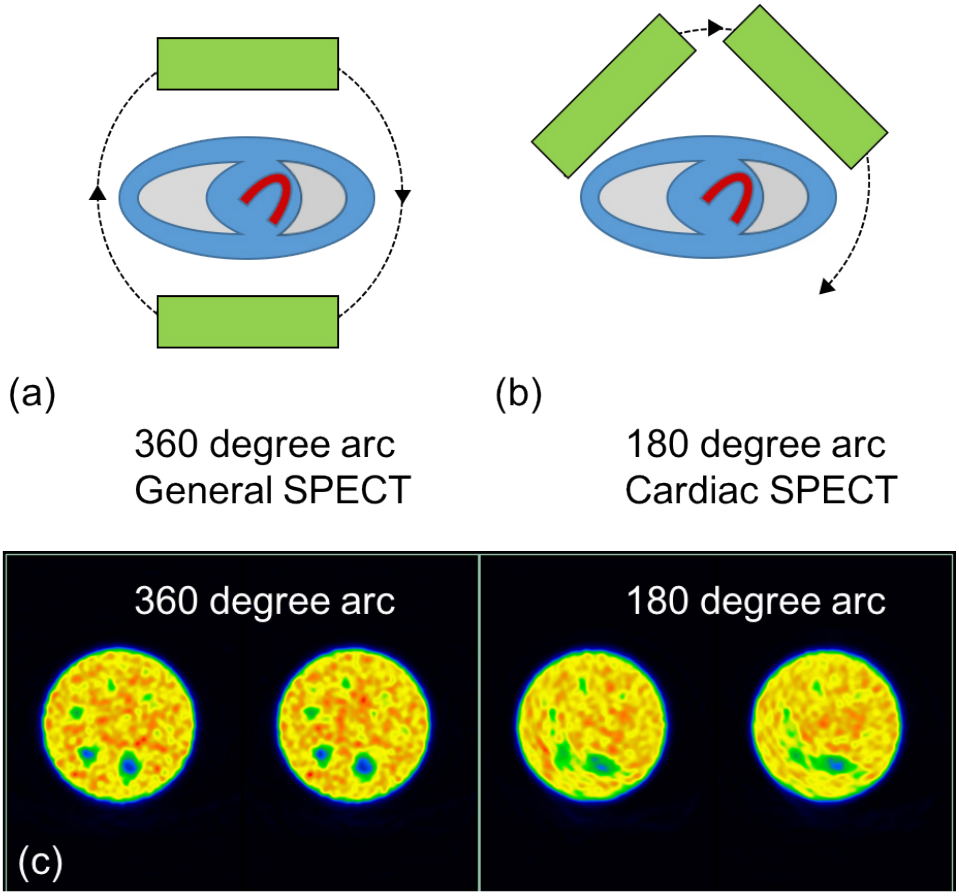

FIG. 3. (a) The standard position for SPECT on a dual detector system is for each detector opposed to each other with each detector travelling through 180 degrees to acquire over 360 degrees of arc. (b) In nuclear cardiology, a right angle (L-mode) approach is commonly used to acquire data over 180 degrees of arc. (c) Acquiring over 180 degrees of arc can lead to distortion in areas distant to the acquired projections.

the individual detectors and the source in SPECT, and the additional resolution losses from the tomographic reconstruction process. To limit this problem, non-circular orbits are frequently used, with the patient–collimator distance minimized for each projection angle. This works well, although it is frequently avoided in head imaging, where collisions between the patient and the detector could cause significant harm. In this application, circular orbits are used instead, with the patient couch elevated so that the patient–collimator distance is minimized and relatively consistent around the head. Furthermore, higher resolution collimators are preferred where available, with increased injected activities used to compensate for the loss in system sensitivity. There has also been a move to more novel collimator designs created for specific applications. In brain imaging, for example, fan beam collimators have been used to improve the spatial resolution of SPECT imaging without reducing the sensitivity. More recently, developments in slit-slat and multiple pinhole collimators [11–13] have led to the introduction of clinical and pre-clinical systems for SPECT.

Similarly in the field of nuclear cardiology, the use of novel collimator designs has also been explored. Fan beam collimators have again been popular, with designs adopting an off-centre plane [14] or using variable focal planes [15]. More recently, the use of ultra high sensitivity collimators has been introduced in an effort to drastically improve patient throughput [16, 17]. Typically, such systems have shown that diagnostic quality images can be produced at a quarter of the time or administered activity compared to standard SPECT systems [18]. The typical trade-off of using high sensitivity collimators is a corresponding loss of spatial resolution. However, developments in tomographic reconstruction algorithms have led to new approaches that model these losses, allowing for the recovery of spatial resolution (see Section 2.1.4). This combination of high sensitivity collimators and resolution model reconstruction algorithms allows for the use of imaging protocols with shortened acquisition times (or reduced administered activities) while still maintaining spatial resolution.

A consequence of the use of shortened acquisition times is that it offers greater potential for the implementation of dynamic SPECT. Acquiring dynamic SPECT data allows the user to look at the changes in the distribution of the radiopharmaceutical over time. Until recently, with standard SPECT acquisitions typically taking 20–30 minutes, the available temporal resolution was only useful for applications looking at relatively slow tracer kinetics or displacement studies [19, 20]. However, with the introduction of high sensitivity SPECT systems the potential to achieve the temporal resolution required to track first-pass kinetics and to perform kinetic modelling can be realized [21].

2.1.3. Image reconstruction

To form a three dimensional image, the individually acquired images obtained from different angles undergo a mathematical reconstruction process. The two different reconstruction processes typically available in clinical systems are filtered back projection (FBP) and iterative reconstruction [22, 23].

The process of FBP is shown in Fig. 4. Taking an object with two point sources of activity, Fig. 4 shows that the image or projection acquired at each angle will be different. In an anterior view, the two point sources are

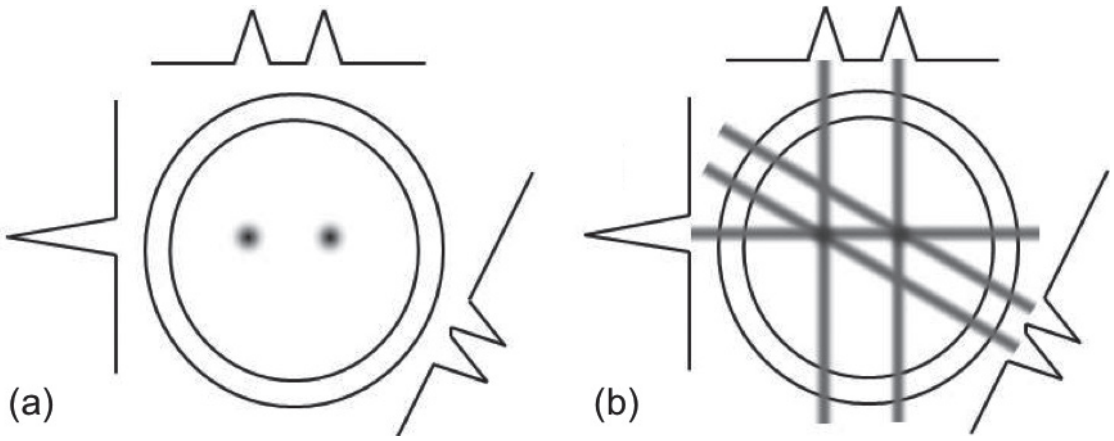

FIG. 4. (a) The acquisition of projection data from a source distribution and (b) its subsequent back projection to form the original image.

represented as two individual objects, while in an oblique view, two objects will be seen, albeit with a different distance between the sources. In the lateral view, however, the image will show only one object, with a signal equal to the sum of the two source activities. Prior to reconstruction, only projection data are available, and the distribution of source activity is unknown. By back projecting the projection data onto a blank image matrix and summing contributions from each back projection, the image of two point sources starts to become resolved. In Fig. 4, only one transaxial slice is represented to demonstrate the reconstruction process. In clinical SPECT, however, because a two dimensional planar image is acquired at each projection angle, it is possible to reconstruct a stack of consecutive multiple slides to form a three dimensional object.

One of the consequences of the back projection process is that the resultant image is a blurred version of the original object. To address this, a ramp filter is applied before the back projection process. For ideal mathematical projection data, FBP yields an exact solution. However, because SPECT is noisy, a modification of the ramp filter is required, usually by applying a low pass filter such as Butterworth or Hann filters. The type and form of low pass filter depend on the spatial resolution requirements and noise characteristics of the data.

Iterative reconstruction takes a different approach to the reconstruction process (see Fig. 5). In this method, an algorithm predicts what the image might be, for example suggesting that 100 counts are in each voxel. An estimate is then made of the projections that would result from this predicted image. In its simplest form, this would be a basic forward projection step of image into projection images, but it can also consider factors such as attenuation of photons or resolution losses (see Section 2.1.4). A comparison is then made between the acquired projection images and the estimated forward projections. If the two image sets are identical or similar enough to within a pre-set acceptable difference, the reconstruction algorithm can stop, and the estimated image can be assumed to be a good representation of the true image. If there are significant differences between estimated and acquired projection data, then an updated estimate is generated based on the ratio of the acquired and estimated data. This process can then go through multiple iterations until a good representation of the object has been achieved. One such process is maximum likelihood expectation maximization (MLEM) [24, 25].

One of the issues with MLEM is that during the iterative process the estimated image can become increasingly noisy (see Fig. 6). Smoothing can be used to control this noise, albeit with the consequential loss in spatial resolution. Alternatively (and more commonly performed), this effect can be accomplished by stopping the iterative reconstruction process earlier. As can be seen in Fig. 6, at 20 iterations the image looks suitable for diagnosis. However, a consequence of stopping the iterative reconstruction early is that the true value of uptake of the radiopharmaceutical is not reached. Furthermore, the level of convergence to the true value can vary in different parts of the image, which means the relative accuracy will change across the image. A possible solution is to use maximum a posteriori reconstruction, which uses prior information from, for example, CT or magnetic resonance imaging to regulate and control the iterative process more effectively [26, 27]. Such reconstruction algorithms are being implemented in PET/CT systems, and are being introduced into SPECT/CT systems [28]. An alternative is to

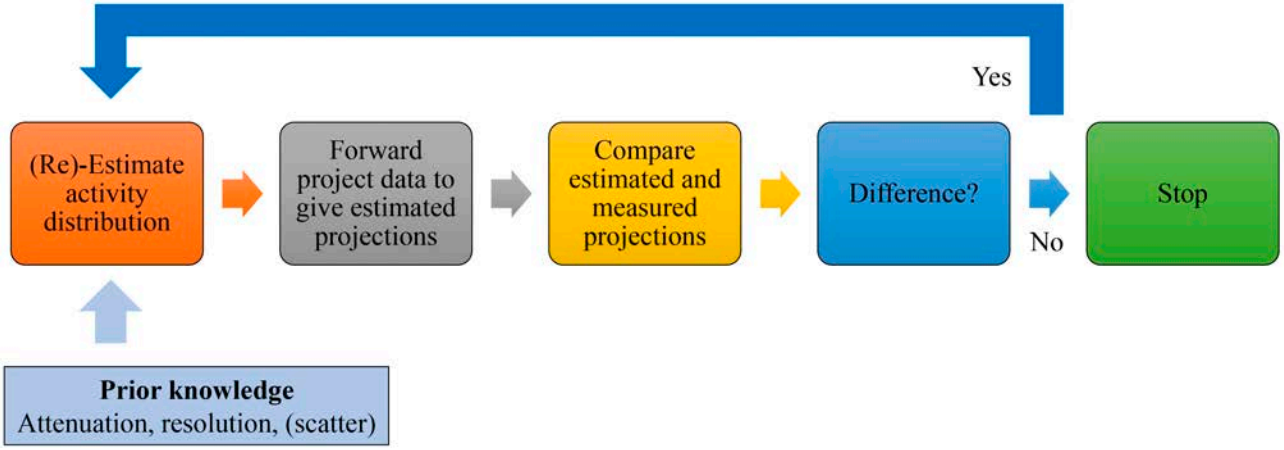

FIG. 5. Diagrammatic description of iterative reconstruction.

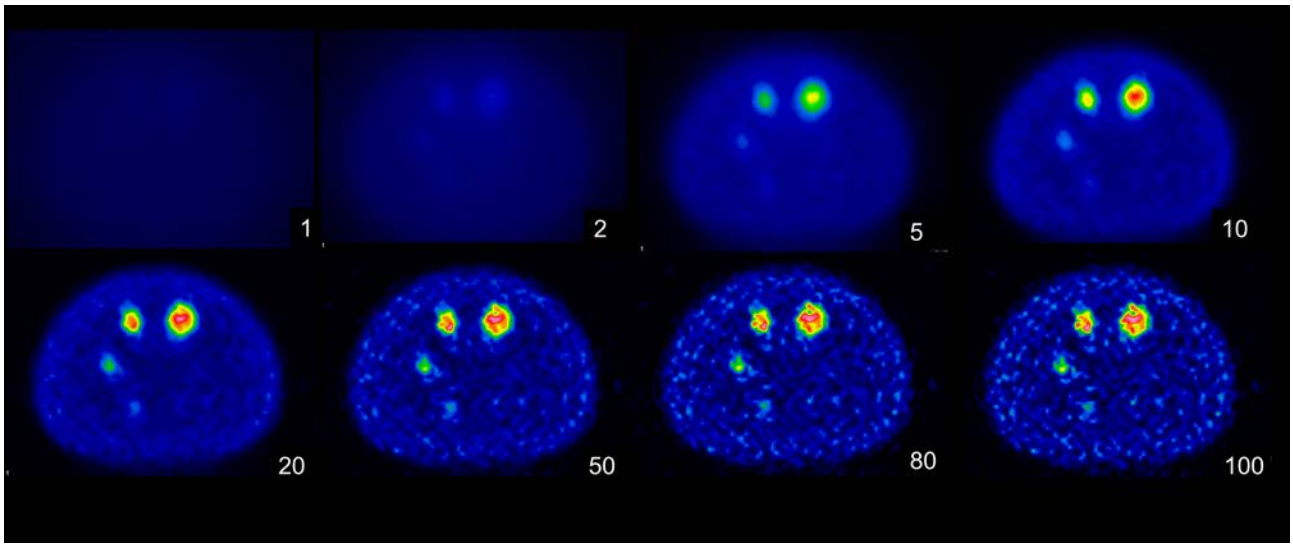

FIG. 6. Formation of image with increasing numbers of iterations.

use FBP algorithms for imaging techniques where accurate quantification is required, although this technique has artefacts of its own, and it is difficult to implement correction algorithms into the reconstruction.

Another issue with MLEM is the speed of the reconstruction process. It is mathematically demanding to perform MLEM reconstruction, particularly at 120 or 128 projections, with each containing 128 × 128 pixels. This becomes even more challenging when reconstructing electrocardiogram (ECG) gated acquisitions, with up to 16 bins for each projection. Ordered subset expectation maximization (OSEM) is commonly used to speed up the reconstruction process, typically by a factor of ten [29]. In this technique, instead of using the complete set of projections, only a subset of estimated and acquired projections is compared at a time in a series of subiterations. Hence with a typical OSEM reconstruction of 2 iterations and 20 subsets using a 120 projection acquisition, 20 subiterations of 6 angle comparisons will be made for each full iteration. The resultant image is found to be equivalent to 40 (= 2 × 20) full iterations of MLEM. As with FBP, following MLEM or OSEM reconstruction, post-reconstruction filtering is often applied to produce images with acceptable noise characteristics.

2.1.4. Corrections

On gamma camera based SPECT systems, there can be significant mechanical stress on the detector-to-gantry mounts as the system rotates during the SPECT acquisition. As a result, the mechanical centre of the field of view (FOV) from the perspective of the detector can be different to the reconstructed centre of the image originally assumed by the reconstruction software. For example, on a dual detector system, with the detectors in an anterior and posterior position, the centre of the FOV is likely to be in concordance with the assumed centre of the reconstructed image (see Fig. 7(a)). However, when both detectors are in a lateral position, the force of gravity may position the mechanical centre slightly lower than the software assumed centre (see Fig. 7(b)), while detectors in a 90 degree configuration (see Fig. 7(c)) demonstrate a mixed picture with one detector in concordance, and the second detector in discordance with the assumed centre of rotation (COR). As the detectors rotate to different positions during a SPECT acquisition, the gravitational effect on the detectors and the resulting shift away from the assumed COR will change. This effect can be accounted for by a COR correction (see Section 3.2.4), which characterizes the difference in the mechanical and image centres of rotation, and is applied prior to image reconstruction. Several COR corrections are often required depending on the number of collimator and detector configurations available, with each providing slightly different mechanical challenges to the gantry.

Other corrections can be applied during the reconstruction process. Correction for the attenuation of photons within the body is commonly applied in SPECT. For applications in which the attenuating material can be assumed to be constant in its density, calculated attenuation based on defined boundaries and a linear attenuation coefficient can be used [30]. Application of this technique is most frequently seen in neurological SPECT studies. An alternative method for areas with non-uniform attenuation is to use transmission imaging for AC. Such systems can

use radionuclide transmission sources, or now more commonly CT, to provide tomographic maps of attenuation. Figure 8(a) shows how, for a point source, the projections from the estimated image can be derived using 'forward projection' in the iterative reconstruction. By adding the information from an attenuation map (see Fig. 8(b)), it can

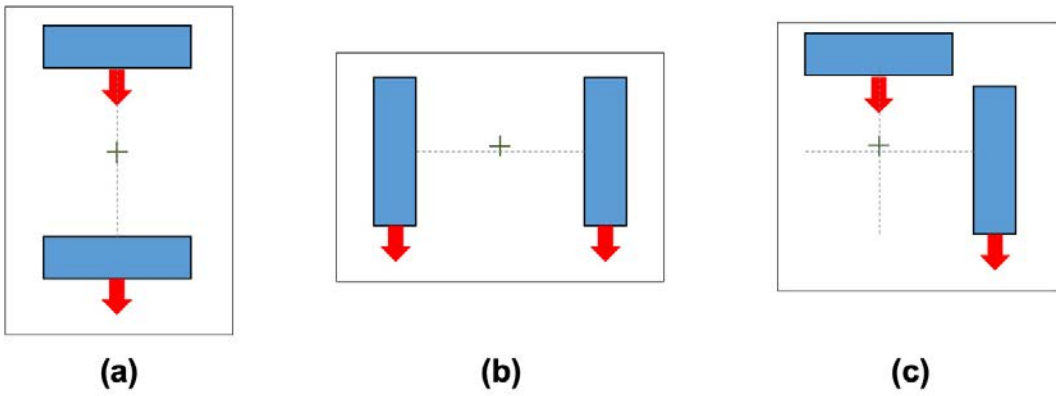

FIG. 7. Mechanical stress on a dual detector system. (a) When the detectors are in the anterior/posterior position, the projection of the mechanical COR corresponds with the software COR. (b) With detectors in the lateral position, this might not be the case. (c) In a 90 degree configuration, the differences in mechanical stresses can require a different COR correction.

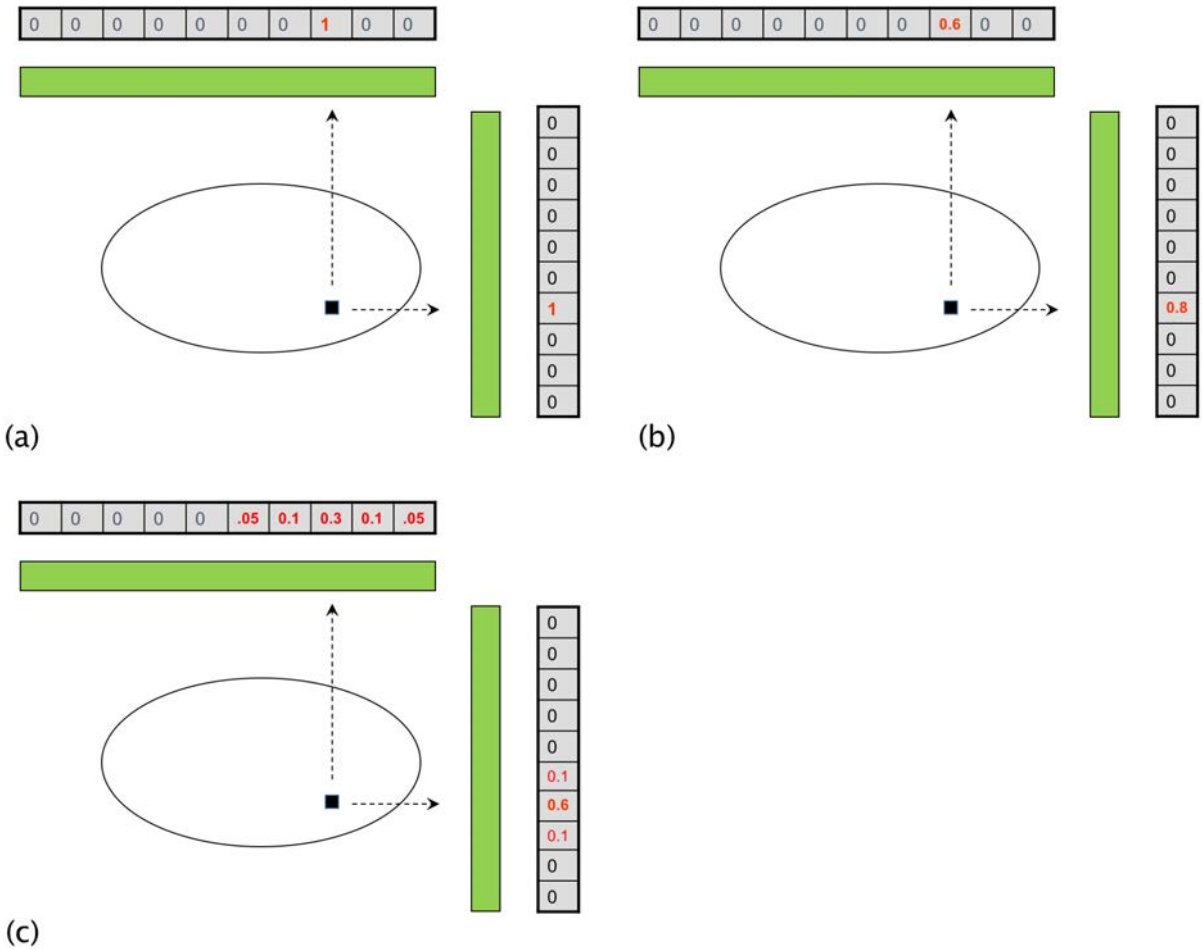

FIG. 8. Estimates of projections in iterative reconstruction (a) without attenuation, (b) including the effect of attenuation and (c) including the effects of both attenuation and resolution losses.

be seen how the estimated projections might change depending on the position of the source. This is how AC can be incorporated into the iterative reconstruction. A similar technique can be used to model resolution losses into the reconstruction. Figure 8(c) shows how, instead of a single point representation of the source, the probability of where the count could occur can be spread depending on the source-to-collimator distance — a distance affecting the spatial resolution of the image. Corrections for other physical effects, such as scatter, can be incorporated into the reconstruction process [31], although simpler multiple energy window methodologies are currently more commonly performed before the reconstruction process [32, 33].

2.2. COMPUTED TOMOGRAPHY

2.2.1. Acquisition

CT is similar to SPECT in terms of the reconstruction process. Using a rotating X ray tube detector system, projections are acquired at multiple angles and reconstructed to form three dimensional images. The main difference between the techniques is that the projections in CT use the measurement of the attenuation of an external X ray radiation source to form the image, whereas in emission tomography an external detector measures the distribution of in vivo radioactivity. Thus, the radiation fluence in CT is much more intense and much shorter in duration than in SPECT because the radiation source can be switched on and off at will, and the intensity of the beam can also be selected and collimated to the volume slices of interest. Nor does it dwell before and after imaging, which is the case in emission imaging.

The hardware involved in CT is quite different to that in SPECT. Opposite to the X ray source is an array of X ray detectors, typically 16–64 channels covering 2–4 cm in axial width and a few degrees in arc in the axial direction (see Fig. 9(a)). The array is arranged to capture multiple slices of information simultaneously (see Fig. 9(b)), albeit with a much reduced axial extent compared to SPECT detectors. Slice configurations can use some or all channels to produce a multitude of slice options. The intense radiation used in CT allows for the rapid continuous rotation of the source and detector, which typically sit on a slip ring to allow multiple uninterrupted revolutions. Following each revolution, the patient couch can be moved to increase the amount of the patient scanned, using what is known as axial mode. Alternatively, the imaging couch can move continuously during the gantry rotation to acquire tomographic data in helical mode.

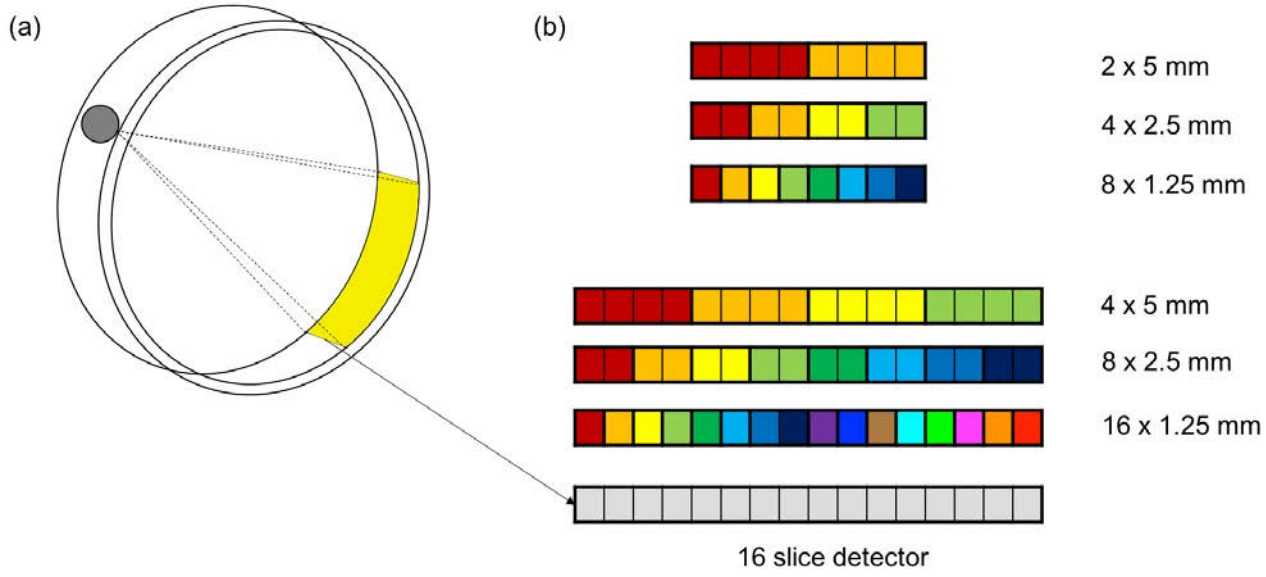

FIG. 9. (a) Schematic diagram of a typical CT system, showing an X ray source detector array pair with arc. (b) The detector array is organized over a few degrees of arc in the axial direction and can acquire multiple slices of data simultaneously. A subgroup of eight channels in this example can be chosen to limit the axial extent, if required.

On account of the continuous motion and high photon flux (typically five orders of magnitude greater than seen in nuclear medicine), CT scans involve many more projections in the reconstruction. Furthermore, unlike in SPECT, the reconstructed matrix size in CT is typically fixed to an array of 512 × 512 pixels within a reconstructed slice. If smaller pixels are required, or if there is a lot of empty space in the image, a smaller fan beam (collimated field size) is used. In the axial plane, the array of detectors can be configured to produce more or fewer slices per rotation (see Fig. 9(b)), depending on the slice thickness required and level of noise. CT acquisitions have a number of parameters which define the type and quality of the image (see Fig. 10). The following subsections describe the reasons and consequences of parameter choices.

2.2.1.1. Tube voltage

The potential difference across the CT tube determines the maximum energy of X ray photons produced. Typically in a range of discrete values between 80 kV and 140 kV, higher potential differences are chosen when more penetrating radiation is required (i.e. for large patients), with smaller voltages used with smaller and paediatric patients. The contrast in the image depends on the tube voltage chosen (see Section 2.3.1), with lower voltages creating larger differences in attenuation and therefore better contrast. A consequence of using higher tube voltages is that, for a given tube current, the radiation output and dose rate from the tube increases (almost by the square of voltage), thus increasing patient radiation doses (for a fixed rotation time). On some modern systems, tube voltage can be automatically chosen by the CT system, based on the preview scan.

2.2.1.2. Tube current

The current across the tube determines (for a given kV) the number of X ray photons produced. As mA increases, the number of photons produced increases linearly, which results in more photons being detected and

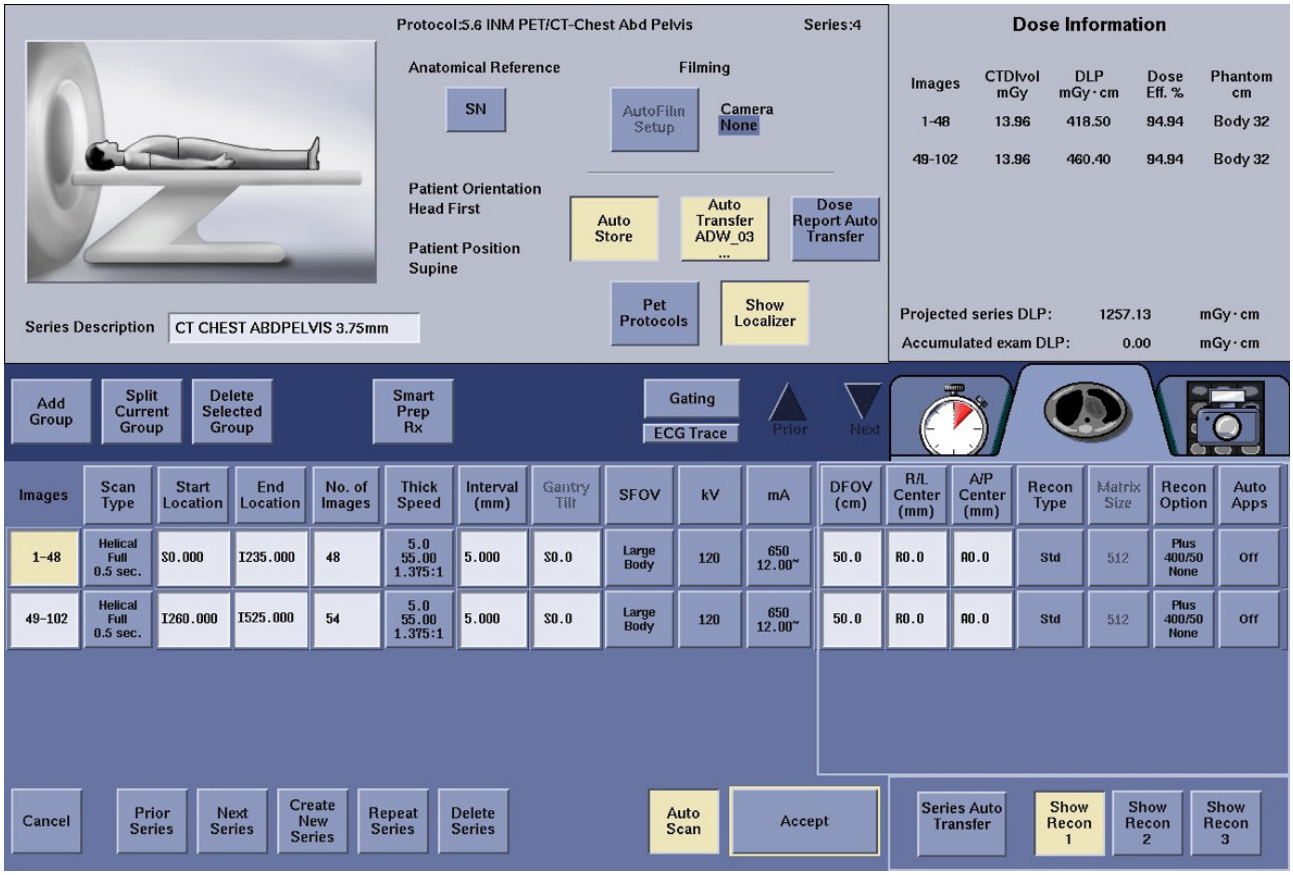

FIG. 10. An example of a CT acquisition configuration screen, showing the different parameters.

therefore an improved image quality resulting from higher signal to noise ratios, but also a higher patient radiation dose. On many CT systems, the mA can be modulated to decrease automatically the radiation output in areas or projections with low attenuation. For example, when scanning the chest, the values of attenuation are less than when scanning the pelvis, so it is possible to reduce the photon flux (i.e. mA) when scanning the lung region compared to the pelvic region. Similarly, for most patients, the thickness in the anterior–posterior direction is less than that when acquiring lateral projection data. It is possible therefore to vary the mA used at different angles depending on patient thickness. Tube current varies between 10 mA and 700 mA, with currents above 500 mA only (and seldomly) used for special applications.

2.2.1.3. Rotation time

In addition to the tube current, the total number of X ray photons detected for a given projection is determined by the dwell time at that angle, which is given as the rotation time. A complete 360 degree gantry rotation typically takes between 0.3 s and 2 s. The rotation time used often depends on the application: in nuclear cardiology, where there is a need to 'freeze' cardiac motion, the shortest rotations times are used with 180 degree reconstructions. For most other applications, rotation times of around 0.5–1.0 s are used. The total number of photons reaching the detector is proportional to the product of tube current and exposure time (referred to as milliampere-seconds, mAs), with the values of the two components being determined by the temporal resolution required.

2.2.1.4. Scanning mode

Scanning mode is normally used to describe whether the scanner table moves following each rotation of the gantry (axial mode), or if it moves continuously during the rotation motion to scan the patient in helical mode. If helical mode is selected, a further parameter needs to be defined. The pitch determines how fast the table moves during a rotation. Higher pitches (wider spirals) offer shorter scanning durations and lower radiation doses at the cost of poorer axial spatial resolution and higher noise. A third scanning mode is the cine or dynamic mode, which produces multiple images at a given body position and is typically used for tracking CT contrast over time or for dealing with motion, such as respiration.

2.2.2. Image reconstruction

Reconstruction of CT data offers similar options to those used in SPECT. Up until 2008, almost all CT scanners only utilized FBP for image reconstruction. The technique in CT is similar to that used in SPECT, with projections from the rotating X ray tube detector pair undergoing filtering and back projection to produce a three dimensional stack of two dimensional images. There are, however, some subtle differences. One difference is that CT requires a series of blank scans or air calibrations to reconstruct the attenuation map. An air calibration or blank scan is simply a scan that is performed without an object in the CT FOV. Typically performed at the beginning of the day for a series of kV, mA and detector configurations [34, 35], air calibrations are pulled into the reconstruction process so that the attenuation from the patient can be calculated as a ratio to the signal measured with nothing in the FOV.

The geometry involved in CT is also different from that used in SPECT. In CT, a fan beam geometry is used in which a point source of X rays irradiates an arc of detectors to yield non-parallel projection data for a given image angle (see Fig. 11(a)). Furthermore, with the axial extent of the detector array now reaching up to 16 cm in specialist volumetric scanners, data are also no longer parallel in the axial direction either (see Fig. 11(b)). For ease of reconstruction, it is normal to group parallel projections before the reconstruction starts (see Fig. 11(c)). An additional challenge in reconstruction is when data are acquired helically. In this instance, interpolation of projection data is used to allow the reconstruction of a stack of transaxial slices (see Fig. 11(d)).

The second option for reconstruction, as in SPECT, is iterative reconstruction. This technique was the original form of reconstruction available for CT. However, because of computational and image quality issues, the technique was quickly replaced by FBP. More recently, an improvement in computational power and algorithm developments has led to the re-emergence of the technique. Iterative reconstruction in CT is basically similar to that used in emission tomography. Following a first estimate from FBP, a series of iterations, typically involving forward and back projection, are used to calculate the best match between an image estimate and the measured projection

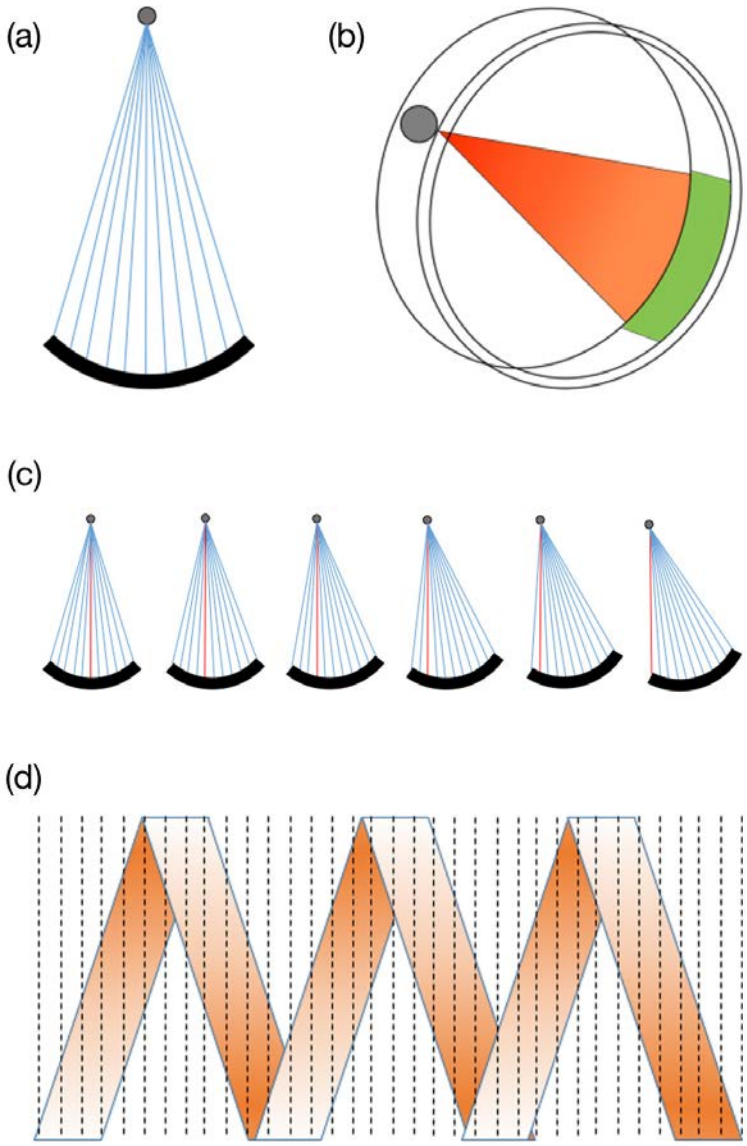

FIG. 11. Geometry involved in CT. (a) Most CT scanners work with a fan beam geometry. (b) With extended axial extent. (c) For reconstruction parallel projections, data are rebinned prior to reconstruction. (d) Helical scans require interpolation to derive slice information from the acquired data.

data. The advantages over standard FBP is that by including a model of the noise process and the imaging system (e.g. X ray source and detector array), image artefacts and noise can be potentially reduced, thereby improving overall image quality. The success in reducing image noise allows lower dose CT protocols to be adopted. Each manufacturer has its unique 'black box' solution to iterative reconstruction, taking subtly different approaches. A good general description of iterative reconstruction in CT and the approaches followed by the manufacturers is given by Willemink [34]. A fuller, more mathematical description is given in the review by Beister et al. [36].

2.3. CT BASED ATTENUATION CORRECTION FOR SPECT

2.3.1. Attenuation correction

In order to obtain reliable quantitative images in SPECT, it is necessary to determine how attenuation by the overlying tissues and organs influence acquired data. Even without a need for quantification, the relationship

between observed activities in tissues of different density and at different depths in the body is strongly influenced by attenuation and the inherent inconsistency of non-corrected projections. Historically in SPECT (as well as in PET), AC was based on transmission sources (either lines or points). In PET, the correction can be performed in the projection space before using FBP because the correction factor for a given projection element depends only on the properties of the attenuating object and not on the source localization. In SPECT, however, the correction also depends on the actual source depth. Therefore, the implementation in SPECT requires that the correction be included in an iterative reconstruction loop. Single photon emitters which have been used for attenuation measurements are ^{153}Gd and ^{133}Ba. However, due to the limited photon flux available from such sources, the acquisition time is considerable; and even when simultaneous acquisition could be used, the necessary corrections for the 'cross-contamination' between emission and transmission counts would significantly contribute to the noise. In this regard, AC in SPECT using transmission sources has not been widely adopted in clinical use.

With the introduction of CT to SPECT systems, the adoption of AC has become more widespread. The information provided in a CT measurement is basically that of tissue specific attenuation and, compared to the results from transmission sources, this 'μ map' is essentially noiseless. The reconstructed CT image contrast owes its anatomical information to the fact that different tissues have slightly different composition and density, and therefore different (linear) attenuation coefficients. The standard Hounsfield unit (HU) of CT numbers is calculated from a linear scaling of the reconstructed attenuation coefficients, assigning the values −1000 to air and 0 to water [37]. However, photon attenuation is strongly dependent on the photon energy, and therefore a 'translation' or 'downscaling' of the μ map is needed between the effective CT energy and the relevant photon energy used for emission imaging. For PET, one such translation for each CT energy suffices, since all nuclides used in PET have the same annihilation photon energy of 511 keV. For SPECT, the need for downscaling to individual single photon energies adds to the complexity.

The energy dependency of (mass) attenuation coefficients for all elements is different but well known [38, 39], and the mass attenuation of a compound material or mixture is determined by its elemental composition alone, each element having its own dependency on energy. Overall, the mass attenuation cross-section at the energies relevant to CT and SPECT is dominated by the sum of Compton scattering σ_c and photoelectric absorption τ, while pair production κ cannot occur (see Fig. 12).

Compton scattering is almost independent of the atomic number (Z) and has a low dependency of the photon energy (E), while photoelectric absorption depends strongly on both Z (power of 3–4) and E (power of −3). At effective CT energies of 50–80 keV, and for the soft tissue components, Compton scatter alone is of significance, while for bone the photo absorption is important too (see Fig. 13).

2.3.2. Models for attenuation correction calculation from CT data

Each pixel of a CT image represents a mixture of elements, and the same composite value (in HU) can in principle result from different underlying mixtures of unknown elemental composition and densities. Therefore, the problem of energy translation does not have a strictly unique mathematical solution free of assumptions. Empirical approaches have been shown to solve the problem adequately in most situations. However, exceptions can lead to artefacts, which are covered in subsequent sections.

It is evident from Fig. 13 that a simple scaling with one common HU-to-μ value factor cannot account for the difference in materials, even among homogeneous pixels. A segmentation of the CT volume into the two major components of bone and non-bone (soft tissue), assigning a single SPECT μ value to each of the two domains, on the other hand cannot itself reflect the fact that both types of tissue can still have very different densities (e.g. in the lung volume the density is only ~0.3 g/cm^3).

The common way to resolve this is to use a pixel wise scaling via a bilinear function (see Fig. 14). It represents the μ value as a continuous and unique function of HU and, therefore, does not require image segmentation. The method generally assumes the presence only of air (−1000 HU), water or soft tissue (~0 HU) and bone (~1000 HU). The lower part of the curve (line) intercepts at zero attenuation and therefore represents a simple scaling corresponding to the density of a mixture of air and soft tissue. The upper curve (line) represents a mixture of soft tissue and bone. The separation point corresponds to pure soft tissue (of density ~1 g/cm^3) and the slope accounts for an increasing amount of compact bone (~1.9 g/cm^3) in the mixture. Originally proposed only for use with the highest available CT energy (voltage 140 kV) to minimize the scaling factors and the effects of their potential uncertainties, it has later been generalized to variable CT energy as well as to variable SPECT photon energy [40].

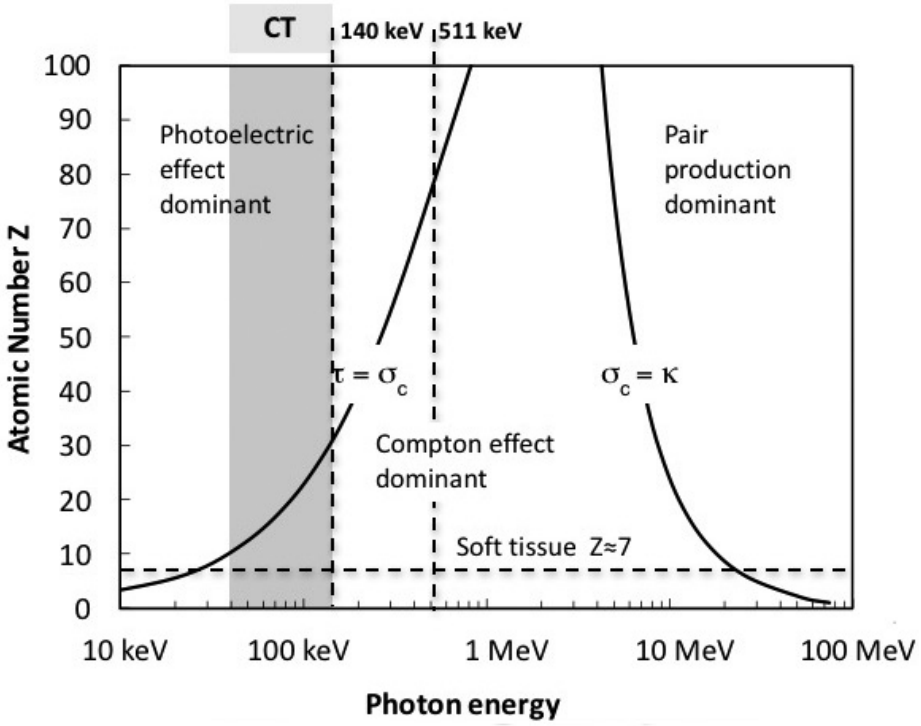

FIG. 12. Diagram with (E,Z) dependency of mass attenuation coefficients. The two 'curtain edges' are formed by curves representing the points in an (E,Z) diagram where two of the interaction cross-sections τ, σ and κ are equal. The horizontal dashed line (Z ≈ 7) shows that, for soft tissue, Compton scattering is dominating between 20 keV and 25 MeV. The vertical line at 140 keV shows that, for ^{99m}Tc, Compton scattering is the more important effect up to Z = 30. The line at 511 keV (PET) is shown for comparison.

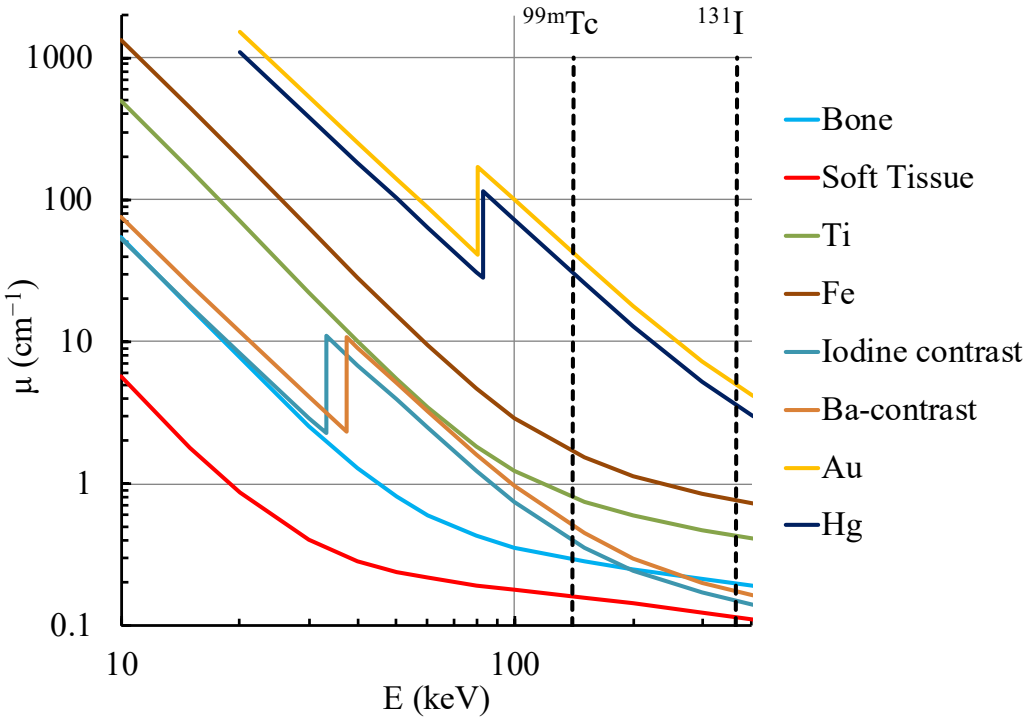

FIG. 13. Linear attenuation coefficients (cm^{-1}) for some materials of interest in SPECT/CT. At low energy (mainly photo absorption), compact bone and soft tissue differ by an order of magnitude owing to differences in Z; at higher energies (Compton scattering), they differ only by the density factor (<2). Two contrast media (iodine and barium), two typical metals for prostheses (titanium and iron) and elements for dental work (mercury and gold) are shown (see also Table 1, Section 2.3.2). In CT contrast materials (iodine and barium) and in metallic implants or dental work, photo absorption is dominant for CT as well as for 140 keV photons.

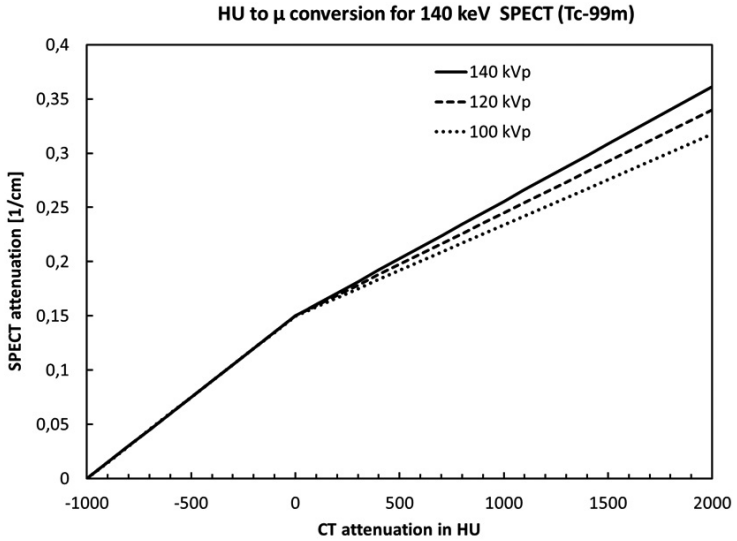

FIG. 14. Translation of HU to linear attenuation coefficients at 140 keV for SPECT (based on Ref. [40]). Example of an implementation of the bilinear method for three CT energies (given as kV) and conversion to SPECT (140 keV).

Once the μ map is known, it can be included as part of the system matrix in the loop of an iterative reconstruction (e.g. attenuation weighted OSEM). Violation of the assumptions by the presence of other materials (e.g. contrast agents and metal) can result in image artefacts, which are shown and discussed in later sections. Various proprietary extensions of the conversion methods have been introduced to reduce these effects. Table 1 shows linear attenuation values at a CT effective energy of 80 keV, at 140 keV (^{99m}Tc) and 364 keV (^{131}I), as well as the CT to SPECT ratios, the 'downscaling factor', for some tissues and materials of interest.

TABLE 1. LINEAR ATTENUATION COEFFICIENTS FOR CT AND SPECT

Material	Density (g/cm^3)	μ (cm^{-1})			Ratio (downscaling factor)	
		80 keV	140 keV	364 keV	80/140	80/364
Soft tissue	1.06	0.193	0.162	0.116	1.20	1.67
Compact bone	1.92	0.428	0.295	0.198	1.45	2.17
Ti (Z = 22)	4.5	1.83	0.794	0.427	2.30	4.27
Fe (Z = 26)	7.8	4.64	1.67	0.770	2.77	6.03
Iodine contrast	1.3	1.23	0.401	0.151	3.07	8.15
$BaSO_4$ contrast	1.5	1.61	0.502	0.174	3.22	9.27
Au (Z = 79)	19.3	107	42.7	4.98	2.50	21.4
Hg (Z = 80)	13.6	71.5	30.8	3.58	2.32	20.0

Note: Mass attenuation values are calculated using XCOM [38] and multiplied by density to provide linear attenuation values. The composition and density of soft tissue and bone are from Ref. [41]. Values for the four elements shown (iron, gold, mercury and titanium) are for pure elemental material. The μ values at 80 keV for gold and mercury are calculated as a mean of the values above and below the K edge. The values for the contrast agents are for the material before administration and dilution in the patient: the iodine contrast is an aqueous solution of a commercial product containing 300 mg/mL of iodine; and the barium contrast is a suspension in water containing 600 mg/mL of $BaSO_4$.

2.4. BENEFITS OF SPECT/CT

2.4.1. Functional mapping

A key benefit of SPECT/CT is the ability to map function derived from nuclear medicine imaging onto the anatomical information from CT. With the exception of neurological applications, where the poor soft tissue contrast of CT is limiting, the advantages of SPECT/CT are very clear.

In oncology, many radiopharmaceuticals are specific for tumour physiology, which can be extremely beneficial, particularly for agents that are also used for radionuclide therapy. An obvious consequence of this is that these tracers also provide limited anatomical information, which makes the localization of metastatic or nodal disease difficult. An example of the benefits of functional mapping is shown in Fig. 15. In this ^{123}I-metaiodobenzylguanidine (mIBG) study, the SPECT images suggest that the uptake is in the liver, but it is not completely clear which areas of the liver actually show this uptake. Once the CT images are provided, not only is it possible to determine the regions of the affected liver tissue, but this can be done with great anatomical accuracy on the CT image.

In cardiology, the use of myocardial perfusion SPECT to assess coronary artery disease is an extremely powerful examination that helps cardiologists to distinguish between reversible and irreversible ischemia. Although helpful, the data do not offer information on the vessels that might be causing the ischemia. A diagnosis of irreversible ischemia typically results in the patient being referred to the interventional suite for an invasive fluoroscopic angiography to confirm the location of the occlusion and to explore whether an interventional technique can be performed to clear the blockage. With SPECT/CT, there is a non-invasive alternative. Information on vessel occlusion can be explored using CT coronary angiography, which together with myocardial SPECT can potentially provide information about functional and anatomical deficits in one patient visit. Unfortunately, CT coronary angiography requires a high specification CT scanner, which is only available in a small number of clinical SPECT/CT systems. An example of a combined cardiac perfusion emission scan with a CT coronary angiography investigation performed in the same visit is shown in Fig. 16.

A functional mapping application of SPECT/CT that has seen significant success is in the assessment of orthopaedic injury. Bone SPECT, with agents such as ^{99m}Tc-methylene diphosphonate (MDP) or hydroxyethylene diphosphonate (HDP) is very good at highlighting areas of high bone turnover that are caused by fractures or mechanical stresses. It also provides some anatomical information to localize these injuries. However, the superior anatomical detail offered by CT provides better localization than SPECT alone, with the exquisite spatial resolution also providing additional information on the type of bone injury. Combining bone SPECT and CT has therefore proved incredibly helpful in the assessment of bone fractures and mechanical stresses (see Fig. 17).

2.4.2. Quantitative SPECT

An advantage of accurate AC provided from CT is the possibility of performing quantitative SPECT. One of the earliest applications of quantitative SPECT/CT was in the field of nuclear cardiology to assess reversible and irreversible ischemia, with visual interpretation typically involved in the assessment of relative perfusion deficits. This generally works well. However, in larger patients the attenuation from breast tissue in females or from the diaphragm in males can lead to apparent reductions in uptake which are not real and purely the consequence of photon attenuation. This creates subsequent problems when the data are used to derive bullseye plots and compared to normal databases. Calculated AC such as those described by Chang [30] are ineffective for this application because the assumption of uniform attenuation throughout the body is clearly not valid in the thoracic region, where soft tissue, lung and bone attenuation is present. Applying AC with CT on a multimodality SPECT/CT system can clearly be helpful, as can be seen in Fig. 18. In this example, the inferior wall of the myocardium highlighted in the slice data shows relatively homogenous uptake in the AC data (upper slice of each pair), while when no attenuation correction (NAC) is applied, there appears to be reduced perfusion in the lower slice of each pair. This is also observed in the bullseye or polar representation on the right of Fig. 18, where comparisons to normal databases are typically made. On the right bullseye plot (no correction), there appears to be reduced perfusion which is less significant in the left bullseye plot (with correction).

In neurology, the benefit of CT based attenuation correction (CTAC) for quantitative analysis is less clear. Although quantification in clinical, neurological SPECT is performed, particularly in dopamine transporter and

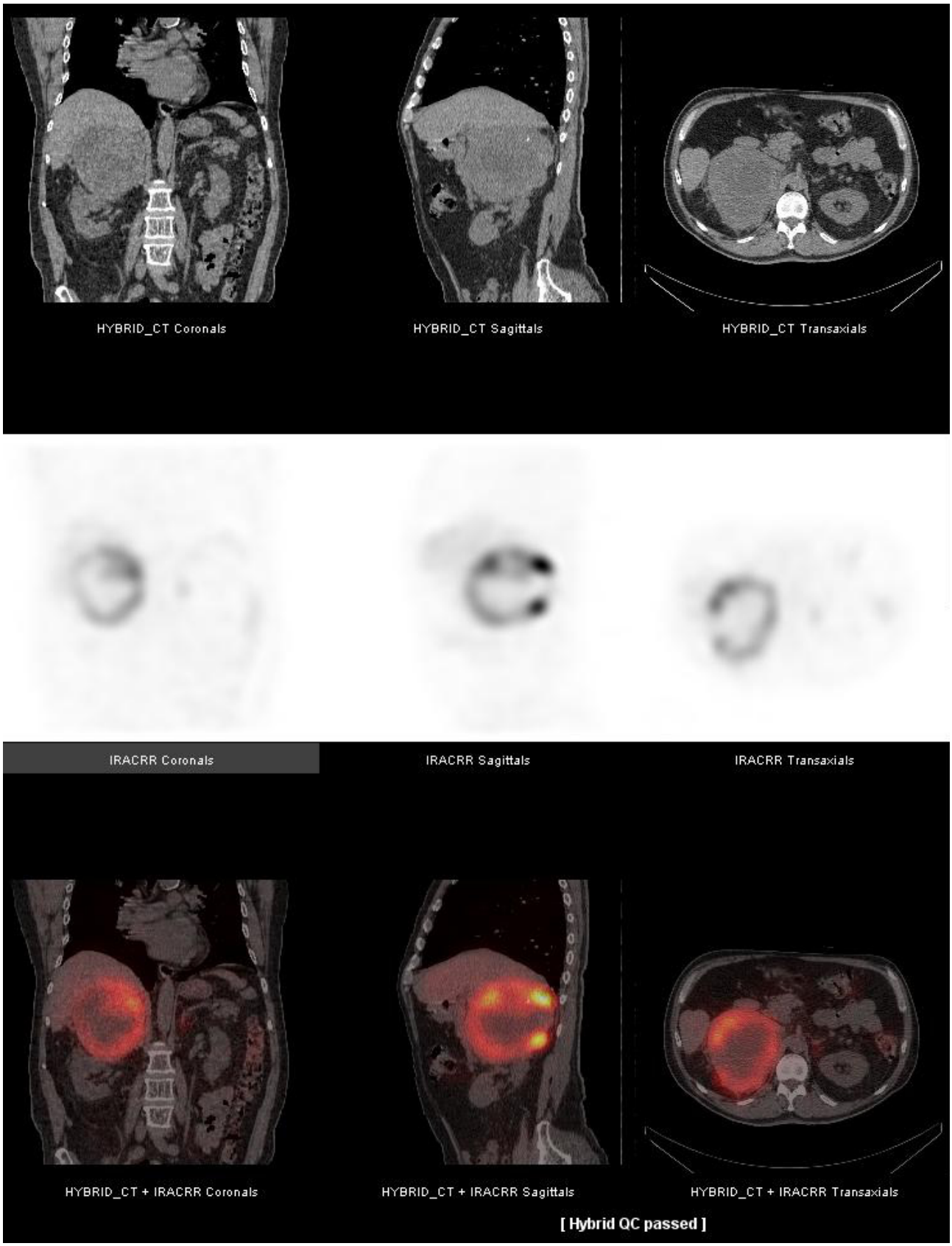

FIG. 15. ^{123}I mIBG SPECT/CT study of the lower thorax/upper abdomen. The SPECT only study highlights uptake of the radiopharmaceutical in the liver. With the addition of CT, the affected area of the liver becomes clearer and the SPECT uptake is also shown to correspond with features on the CT.

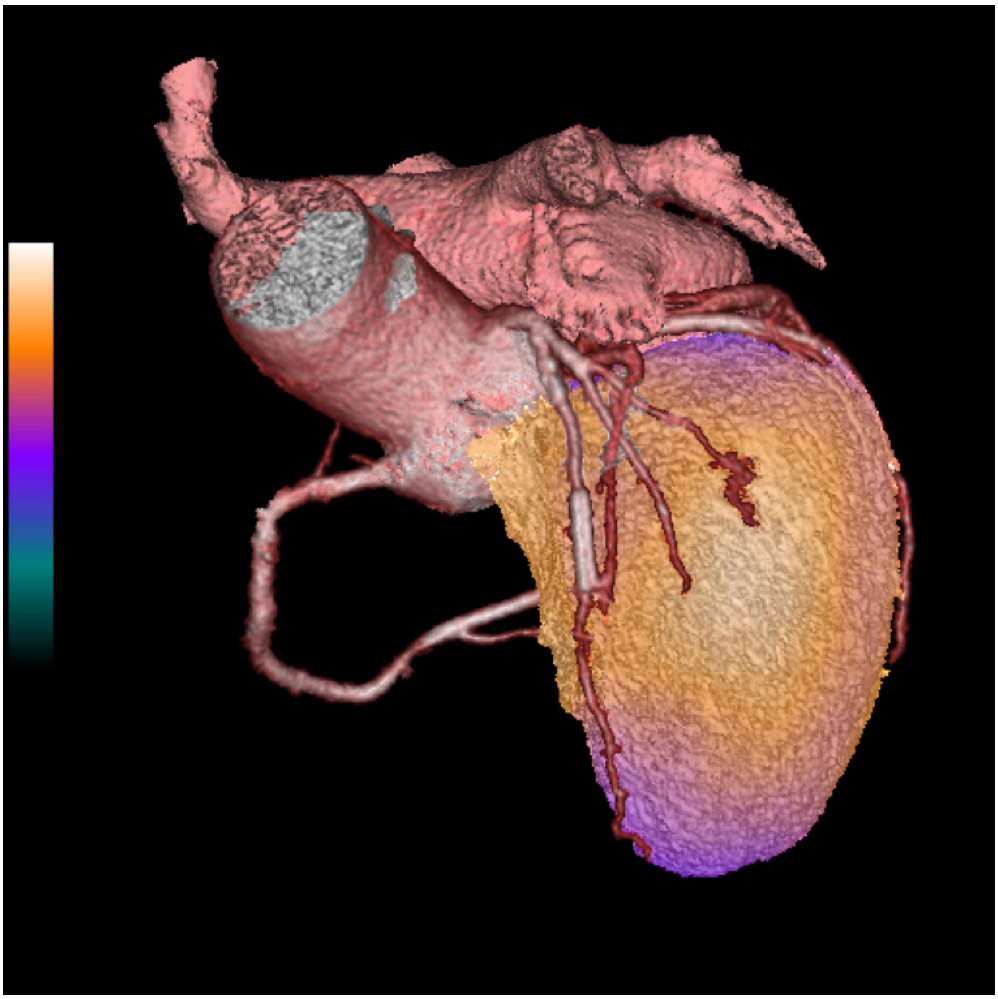

FIG. 16. Combined emission perfusion scan and CT coronary angiography performed in the same imaging session.

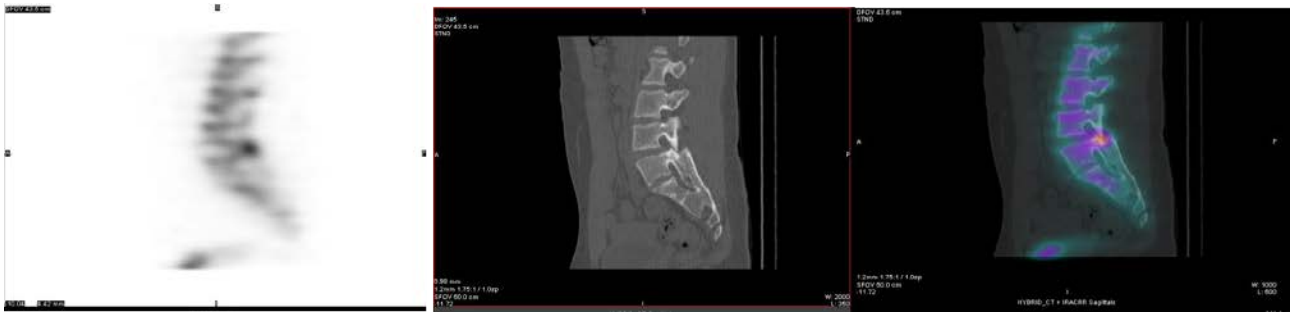

FIG. 17. SPECT, CT and fused SPECT/CT of an orthopaedic bone injury.

regional cerebral blood flow imaging, a calculated Chang approach is typically used for AC. This method can work well; however, difficulties with highly attenuating head supports, and defining brain outlines, can lead to inaccuracies and variability, which can be overcome using a low dose CT for AC.

A more recent application of quantitative SPECT is being implemented in oncology imaging. With the expansion of radionuclide therapies, there is growing interest in using quantitative SPECT to determine activity in tumours or organs so that dosimetric estimates can be performed. After some form of calibration, it is possible to use CTAC together with other corrections (e.g. scatter) to determine the activity concentration in these areas [42].

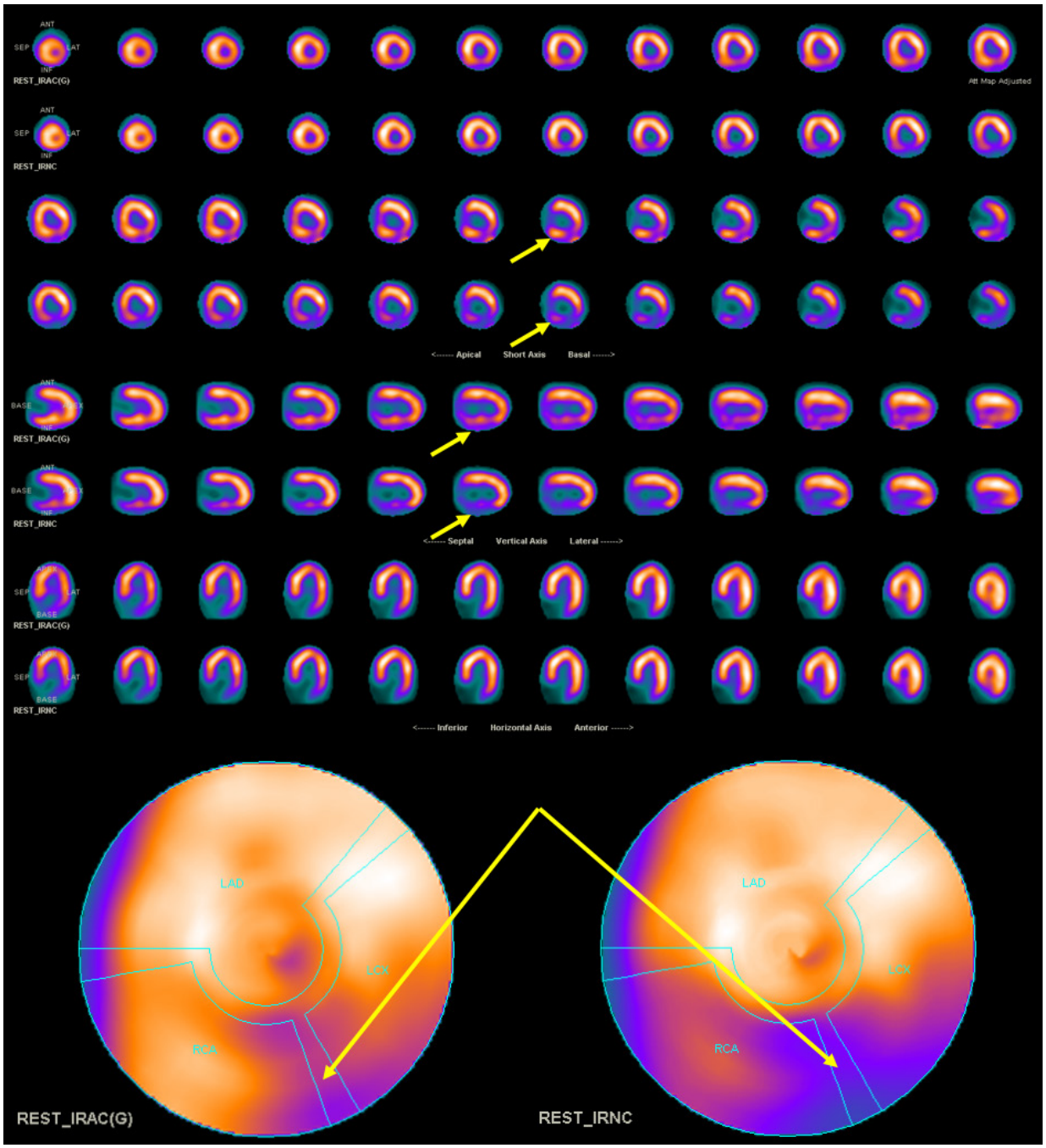

FIG. 18. Cardiac SPECT/CT study with upper slice of each pair of slices showing CTAC data, while the lower slice of each pair represents data with no AC applied. At the bottom, AC (left) and NAC data (right) are shown as bullseye plots. The yellow arrows indicate AC recovering attenuated counts (left) and diminished in the NAC data (right).

By applying the techniques over a series of images taken at different time intervals, it is then possible to determine the accumulated activity and therefore the organ or tumour dose. Until recently, this technique had been performed with users applying their own corrections and calibrations. However, manufacturers are now integrating information and corrections into their own algorithms to provide direct activity concentration values in SPECT images with greater ease.

2.5. COMMERCIALLY AVAILABLE SPECT/CT SYSTEMS

Since its inception by Hasegawa in the early 1990s (see also Ref. [43]), all the major manufacturers have released SPECT/CT systems with various specifications and capabilities. A description and comparison of some of these systems can be found in Seret et al. [44].

2.5.1. General Electric

In 1999, General Electric was the first of the major manufacturers to release a clinical SPECT/CT system with its Millennium VG Hawkeye product. The system used a low mA (2.5 mA) dental X ray tube and fan beam detector system placed on the same slip gantry as the gamma camera detectors. Rotating at a slow speed of 16 s per rotation, this 140 kV system provided axially acquired data with a 1 cm slice thickness using a photon flux (mAs) adequate for AC of SPECT data and localization of SPECT features. In the following years, updates were released providing 2 × 5 mm and the 4 × 5 mm slice thicknesses with a choice of kV (120 kV or 140 kV) and the possibility of performing high pitch helical scans in order to reduce scan time and dose.

General Electric has since released the Optima 640 and a range of systems in the Discovery 670 series with varying degrees of functionality. The Optima 640 is a SPECT system with a four slice CT scanner, offering slice thicknesses of 2.5 mm and 5 mm, a tube current range of 10–30 mA, two tube voltages (120 kV and 140 kV) and the possibility of axial and helical scanning. The Discovery 670 series uses 8 and 16 slice CT subsystems with a wider range of tube voltages, rotation times, tube current and slice thicknesses, and includes options such as CT iterative reconstruction and semiconductor (CZT) detector technology. This series is designed for a wide multitude of SPECT/CT applications with the exception of cardiac CT. For combined cardiac SPECT and CT applications, General Electric has produced the Discovery 570c, which incorporates a CZT multipinhole cardiac SPECT system with a 64 slice CT subsystem capable of acquiring CT coronary angiography studies.

2.5.2. Mediso

The SPECT/CT product from Mediso is the AnyScan system, which offers the possibility of SPECT, CT and PET in the same gantry. In terms of the SPECT/CT system, the AnyScan provides a 16 slice CT system with a wide range of tube voltages, currents, pitches and slice thicknesses.

2.5.3. Philips

The first SPECT/CT product from Philips was the Precedence SPECT/CT. Based on the Skylight SPECT, the two models Precedence 6 and Precedence 16 are based on traditional 6 and 16 slice CT systems, respectively. Following the Precedence, Philips released the Brightview XCT. This system used the standard conventional Brightview platform and added a flat panel cone beam CT subsystem with a 14 cm axial FOV and fast (12 s) and slow (60 s) rotation speeds. Using a tube voltage of 120 kV and current range of 5–20 mA, this low dose approach is in some ways similar to the initial strategy taken by General Electric with the Hawkeye systems, although with smaller slice thicknesses (0.33 mm) and the capability of acquiring a 40 cm SPECT FOV in three gantry rotations by using 180 degree reconstructions.

2.5.4. Siemens

The three SPECT/CT products from Siemens are the Symbia T2, T6 and T16 with 2, 6 and 16 slice CT subsystems, respectively. The two slice system has more limited functionality compared to the T6 and T16; and because of this, it is more limited in the clinical applications for which it can be used. The T6 and T16 are effectively identical albeit with a different number of slices that can be acquired per rotation, and can be used for a wide range of clinical uses with the exception of advanced cardiac applications. Siemens have updated the product series to include the Symbia Intevo and Intevo Excel xSPECT systems, which automatically draw in corrections and quantitative reconstruction methods to provide quantitative values of uptake in the image in terms of kBq/cm^3 or standardized uptake value (SUV). These systems also allow the possibility to use iterative reconstruction of CT data.

3. QUALITY CONTROL OF SPECT AND SPECT/CT

A quality control programme for SPECT and SPECT/CT systems is necessary to ensure optimal clinical image quality. Elements of such a programme should include system calibrations and corrections as well as testing of system performance characteristics at an interval consistent with that of a potential change in, or failure of, that particular characteristic. These tests should be inclusive of both SPECT and CT (if applicable) components of the system.

Several organizations, such as the IAEA, the American Association of Physicists in Medicine (AAPM), the European Association of Nuclear Medicine (EANM) and the National Electrical Manufacturers Association (NEMA), have independently developed recommendations for gamma camera/SPECT and SPECT/CT quality control and testing. Although these recommendations have many similarities in what should be tested, they also have differences in the testing method and frequency. Overall, there is consensus that testing should be performed for both the planar as well as the tomographic imaging modes of a system and that the planar tests should be conducted under both intrinsic as well as extrinsic (i.e. with collimators in place) conditions. A list of tests specific to planar/SPECT and CT components of a hybrid system and their frequency as recommended by the different organizations is presented in Table 2, Section 3.1. In addition, a brief description of only the SPECT tests in the recommendations is provided in the following sections. (No such descriptions are provided for planar tests, since this publication is specific to SPECT imaging.) More detailed description of these tests can be found in the references given.

Prior to any testing, updated system calibrations and corrections should be performed by a medical physicist or a service engineer to ensure optimal system condition. Depending on the gamma camera make and model, these calibrations and corrections should include at a minimum:

— Detector energy correction and spatial distortion (non-linearity) maps;
— Intrinsic detector (including radionuclide specific) and system (also known as extrinsic, with collimator) uniformity maps;
— Peaking (radionuclide photopeak energy window centring);
— Detector high voltage/photomultiplier tube gain adjustments (tuning);
— SPECT COR/multiple head registration (MHR); and SPECT/CT FOV registration.

3.1. ROUTINE PERIODIC PLANAR, SPECT AND SPECT/CT QUALITY CONTROL TESTS

There are a number of gamma camera quality control tests that are performed at various frequencies to ensure the proper operation of the scanner. These tests are divided between planar, SPECT, SPECT/CT and CT related tests. A list of these tests and their frequencies as determined by various organizations is provided in Table 2. A description of each of the SPECT and SPECT/CT tests is in Sections 3.2–3.4.

3.2. SPECT AND SPECT/CT TESTING

Of the group of tests specific to planar mode operation, some quality control tests are also essential for optimal SPECT and SPECT/CT imaging. These tests include planar uniformity, peaking and pixel size.

3.2.1. Planar uniformity

Uniformity is a measure of a gamma camera's response to a uniform source of irradiation. It is quantified intrinsically as the degree of uniformity exhibited by the detector itself or extrinsically as the uniformity exhibited by the combination of the detector and collimator together. Depending on the particular gamma camera make and model, it may be more convenient to acquire either intrinsic or extrinsic floods on a daily basis. If intrinsic floods are acquired daily, then periodic (e.g. weekly or monthly) acquisition of extrinsic floods for the various collimators should be specified to monitor for collimator damage. If extrinsic floods are acquired daily, then

TABLE 2. QUALITY CONTROL TESTS AND THEIR FREQUENCIES

	IAEA [45]	AAPM TG177 [46]	NEMA NU 1-2018 [47]	EANM [48, 49]
System checks				
Physical inspection	A	A + Y		A
Safety interlocks		A + Y		D
Collimator and detector head mountings and collimator damage	D			D
Detector head shielding leakage	A	A + Y	A	A
Basic computer timing	½Y			
Computer timing in dynamic acquisition	½Y			
ECG gated acquisition	½Y			
Multiple window spatial registration	A + ½Y	A + Y*	A	A + ½Y/Y
Computer monitors		A + Y		
Good practice checks				
Energy calibration of pulse height analyser	D			D
Background count rate	D			D
Flood field uniformity and sensitivity	D	D		D
Film processing (if available)	D			
Planar tests				
Peaking	W			
Intrinsic uniformity for ^{99m}Tc	A + W	A + M	A	A + W/M
Intrinsic uniformity other isotopes	½Y			Q
Intrinsic resolution and linearity	A + ½Y	A + Y	A	A + ½Y
Intrinsic hydration	½Y	A + Y		*
Intrinsic count rate	A + ½Y	A + Y	A	*
Energy resolution		A + Y	A	A
System uniformity	A + ½Y			
System resolution	A + W	A + W	A	A
System planar sensitivity	A + ½Y	A + Y	A	
System count rate with scatter			A	

TABLE 2. QUALITY CONTROL TESTS AND THEIR FREQUENCIES (cont.)

	IAEA [45]	AAPM TG177 [46]	NEMA NU 1-2018 [47]	EANM [48, 49]
Whole body system resolution		A + Y*	A	A + Y
Whole body scanning constancy		*		
Collimator penetration and scatter			A	
Collimator hole alignment	A			*
SPECT				
Centre of rotation	A + W/M	M*	A	W/M
Pixel size	A + ½Y			A + ½Y
SPECT uniformity	A + ½Y	A + Y		
SPECT resolution in air	A + ½Y	A + Y	A	A + ½Y
SPECT resolution with scatter	A + ½Y	A + Y	A	*
SPECT image contrast	A + ½Y	A + Q		½Y
Slice thickness	A + ½Y			
System volume sensitivity			A	
Detector to detector sensitivity			A	A
Sensitivity/uniformity with rotation	A			
Head to head registration			A	
SPECT/CT				
SPECT/CT image quality		A + Q	A	
SPECT/CT spatial registration		A + Y	A	M
CT				
CT number accuracy/linearity		D		A + M
CT dose assessment		A + Y		
CT image quality assessment		D		D

Note: A — acceptance; D — daily; W — weekly; M — monthly; Q — quarterly; ½Y — half yearly; Y — yearly; * — optional.

periodic (e.g. weekly or monthly) acquisition of an intrinsic flood should be specified, as collimator responses may mask subtle intrinsic detector non-uniformities.

Intrinsic uniformity is usually measured using a point source (~37 MBq of ^{99m}Tc) placed at a distance equivalent to 5 FOV from the detector surface, to expose the entire detector to a uniform photon flux (within 1%);

while extrinsic uniformity is usually measured using a ^{57}Co sheet source placed directly onto the detector head. In both cases, data can be acquired for a total of 5–10 million counts using a matrix size of 256 × 256 pixels. On some systems, floods (intrinsic or extrinsic) of both scanner heads can be acquired at the same time. It is important to remember that, depending upon the initial activity, a new ^{57}Co sheet source may have sufficient ^{56}Co and ^{58}Co impurities to cause high dead time, and thus suboptimal floods, owing to their high energy gamma emissions that easily penetrate through the septa of most collimators used clinically. Fortunately, the half-lives of ^{56}Co (77 d) and ^{58}Co (71 d) are much shorter than ^{57}Co (272 d), so their effect will dissipate over time.

Intrinsic and extrinsic uniformities are evaluated using visual assessment, which involves comparing the flood images to earlier ones or to expert observer judgement as to whether or not the image quality is acceptable. Alternatively, NEMA uniformity quantitative results may be calculated and compared to manufacturer's specifications or to established limits based on initial or past results. These calculations include integral and differential uniformity (IU, DU) for the useful and central fields of view (UFOV, CFOV), where IU and DU are calculated as:

$$\mathrm{IU} = \frac{\max - \min}{\max + \min} \times 100(\%) \qquad \mathrm{DU} = \frac{\mathrm{high} - \mathrm{low}}{\mathrm{high} + \mathrm{low}} \times 100(\%)$$

where min and max are the minimum and maximum counts in pixels lying within the UFOV or CFOV, and high and low are the maximum and minimum count difference in any five contiguous pixels in the X and Y directions within the UFOV or CFOV. The CFOV is the area defined by 75% of the UFOV linear dimensions (see Fig. 19).

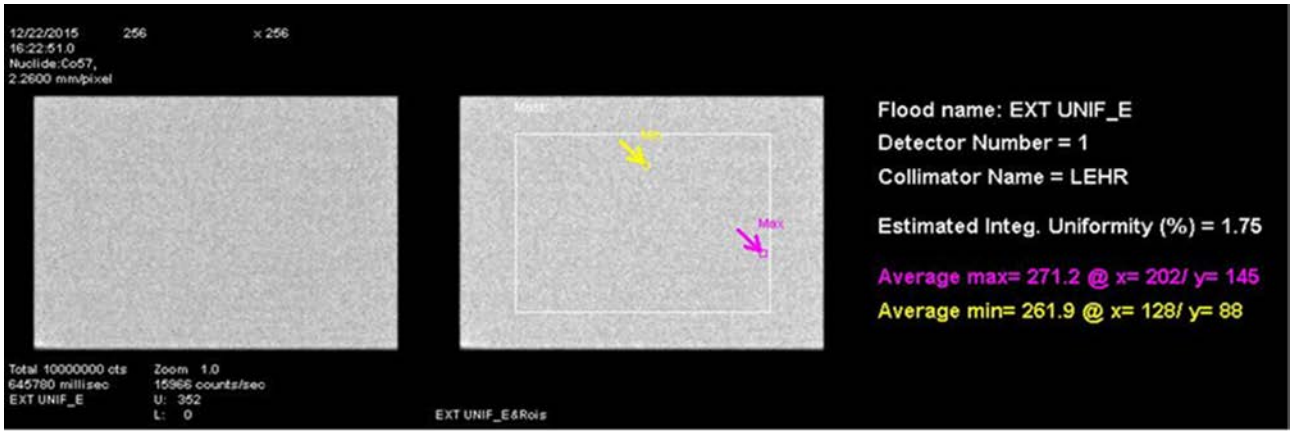

FIG. 19. Extrinsic uniformity results from a General Electric Millennium gamma camera.

3.2.2. Peaking

Peaking is the ability to centre an energy window over a radionuclide's gamma or X ray emission photopeak that is used for imaging. Peaking should be performed intrinsically using a point source of about 37 MBq at a distance equivalent to at least 5 FOVs from the detector to expose the entire detector to a uniform photon flux. Peaking should be performed for all radionuclides used clinically. Peak shifts should be ≤ ±3% of the photopeak energy for ^{99m}Tc and ^{57}Co and ≤ ±5% for other radionuclides. Peaking is automated on some systems, while other systems require manual positioning of energy windows. On most systems, the energy spectrum is displayed as a histogram of counts versus energy with energy window limits shown as vertical lines. It can be useful to look at this spectrum prior to imaging patients. A narrower energy window provides better scatter rejection but also reduces the number of unscattered counts recorded in the image. Flood images acquired off-peak are characterized by visible tubes (see Fig. 20), while an on-peak image shows no such tubing effect (see Fig. 21).

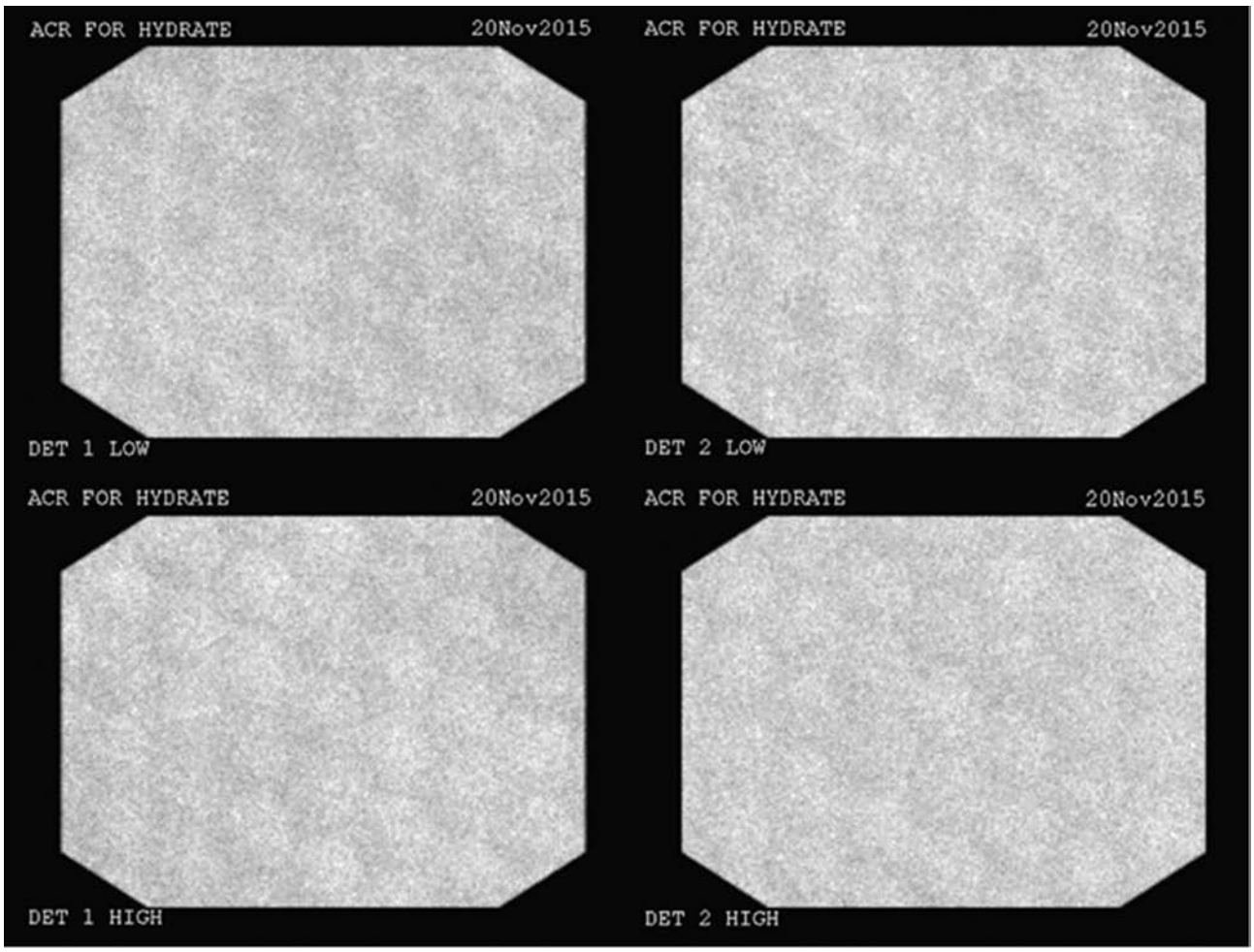

FIG. 20. Flood images of ^{99m}Tc (140 keV photopeak; energy window of 20%) acquired off-peak, using a photopeak centred at 126 keV (top row) and 154 keV (bottom row) for both heads.

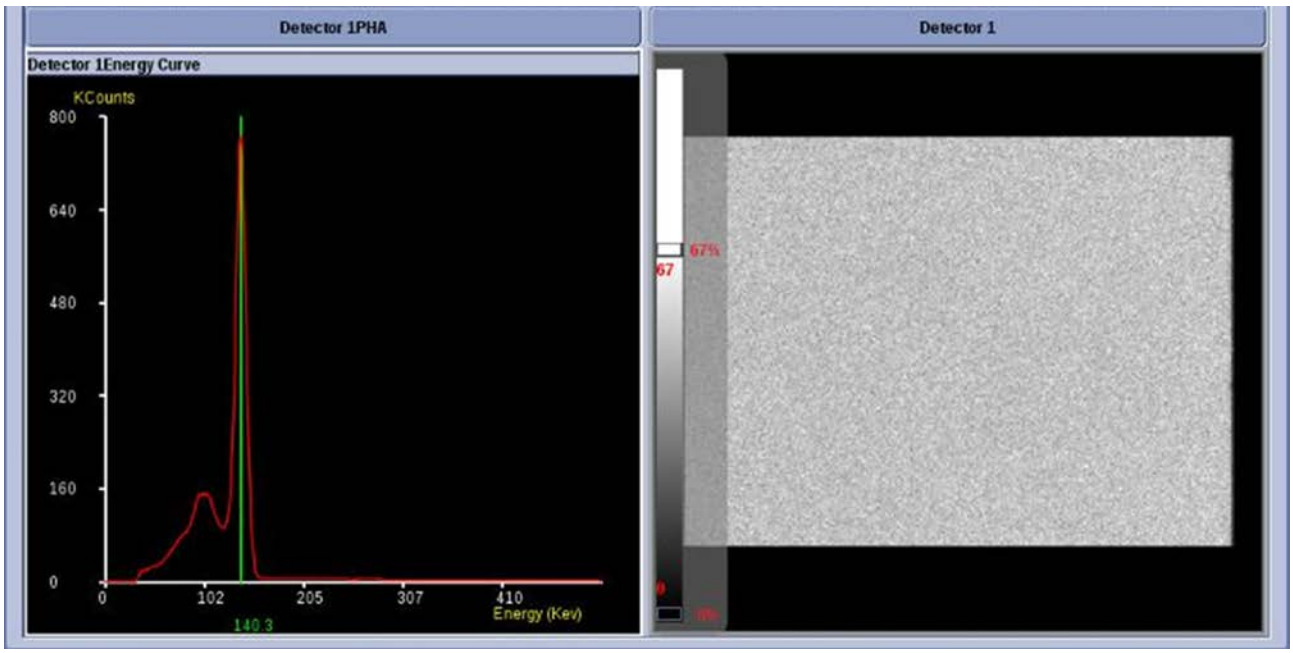

FIG. 21. Energy spectrum and flood image of ^{99m}Tc (140 keV photopeak) acquired on-peak showing a uniform count density across the image.

3.2.3. Pixel size

This test is used to verify the accuracy of the pixel size. In SPECT, this value has implications for quantitative evaluation applicable for AC as well as determining organ sizes from resultant tomographic images. Pixel size is determined using point sources or line sources (according to NEMA) placed at known locations along the X and Y directions and imaged in planar mode. The centroid of these sources is then determined and the distance between them calculated. This distance is then divided by the number of pixels that separate the point sources to determine the pixel size in the X and Y direction. It is essential that the distance between the point sources (typically ≥10 cm) be accurate to within 1 mm.

3.2.4. Centre of rotation and multiple head registration

The COR measurement verifies the alignment between the projection of the SPECT system axis of rotation (AOR) and the centre pixel column(s) in the acquired projection image matrices. The MHR test, on the other hand, is used to ensure that each detector head in a multiple detector SPECT system samples the same volume — which means that the image of a point source on one detector is exactly at the same location on a mirror image of a second detector placed at 180 degrees apart from the first detector. It is necessary, however, that the detector heads always be parallel to the AOR (without head tilt).

Both of these tests are conducted as a verification of system calibrations for COR and MHR. The calibration of both COR and MHR is usually combined in one test to be performed for each scanner model according to the manufacturer's procedure manual. The correction is collimator dependent, and on some SPECT systems, separate calibrations are required for all detector configurations (e.g. 180 and 90 degrees). The 90 degree configuration is typically used only for cardiac SPECT imaging.

The verification tests are described in Refs [45, 47] and use point sources placed at pre-set locations within the FOV of the scanner. A SPECT scan of the sources is then acquired, and the offset locations (mean, maximum and standard deviation) of the point sources from the COR is determined for each angle. This process is repeated for each detector head (see Fig. 22). Manufacturers have pre-set tolerance values for these offsets, and if the value is exceeded, the test results in a failed outcome. In such cases, a service call should be placed to rectify the issue before the scanner can be placed for clinical use.

3.2.5. SPECT uniformity

The purpose of this test is to evaluate the tomographic image uniformity. It is conducted using a SPECT performance phantom (e.g. Jaszczak phantom). The inclusion of the cold spheres and rods sections in the phantom is optional for this test; however, it is good practice, since they can potentially be used for the resolution and contrast (image quality) tests described later. The phantom is filled with about 370 MBq of ^{99m}Tc and mixed well before positioning at isocentre. Tomographic phantom imaging is then performed with 120–128 views, using a 128 × 128 matrix and the smallest possible radius of rotation. The number of counts per view varies between different standards but is typically in the range of 240 000–500 000. Upon completion, image reconstruction is performed with all manufacturer corrections, including AC using FBP with sharp filter [45] or a Hann/Butterworth filter using an order and cut-off frequency that would be used for clinical studies [46].

The analysis of tomographic uniformity (see Fig. 23) also varies between the different standards and ranges from visual inspection [46] to the calculation of contrast of an image artefact as a measure of non-uniformity (see Ref. [45], which also includes a visual assessment of the images).

3.2.6. SPECT resolution

The purpose of this test is to evaluate the tomographic image resolution. The different methods performed depend on the standard used and range from: the visual inspection of the rods section of a SPECT performance phantom to determine the minimum size rods [46]; to an evaluation of the radial, tangential and axial full width at half maximum (FWHM) of the point sources in air used for the COR test described in Section 3.2.4 [45, 47]; or determining the FWHM of three line sources in a water phantom [47]. Reference [45] also includes a visual assessment of the resolution (see Fig. 24). In any one of these tests, it should be noted that resolution is highly

dependent on the radius of rotation used and that the obtained results in air are considerably different from those measured in water due to scattering effects.

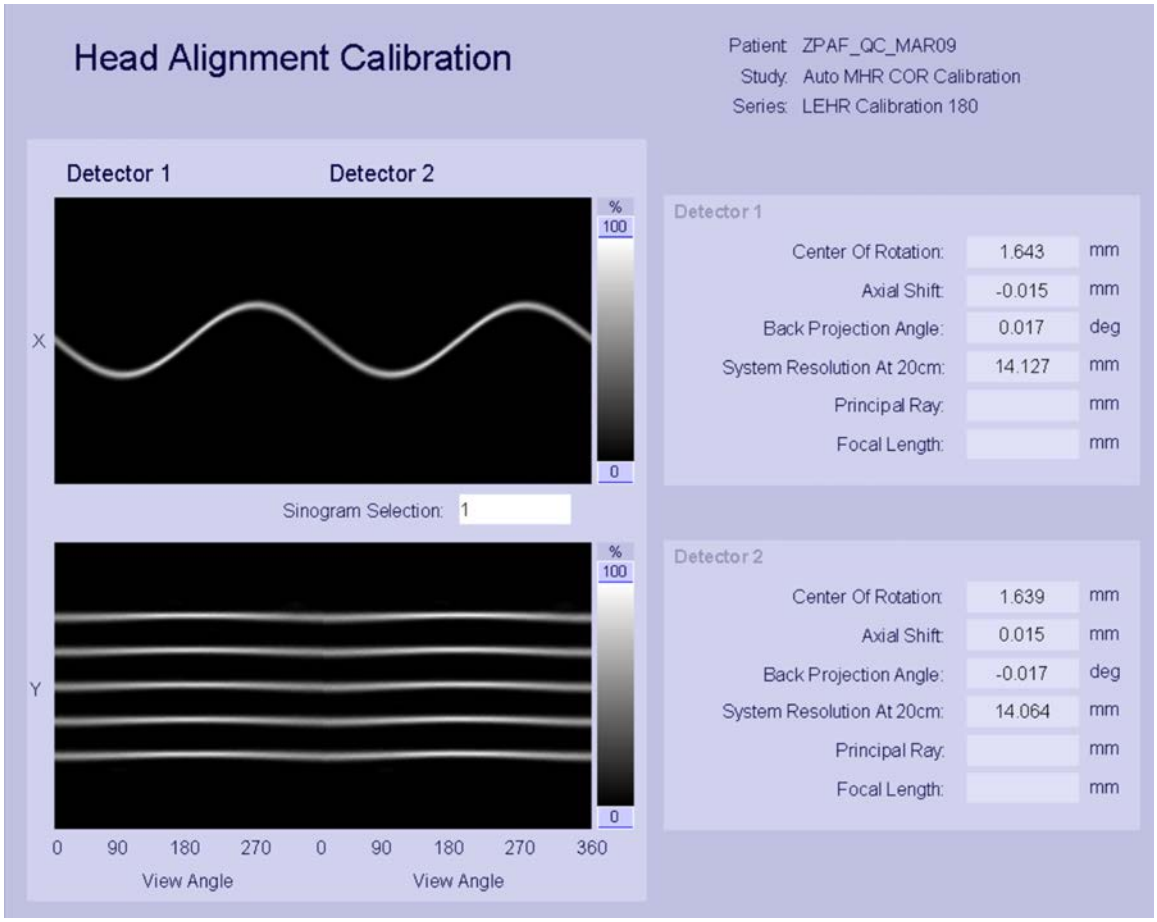

FIG. 22. COR calibration results using five point sources.

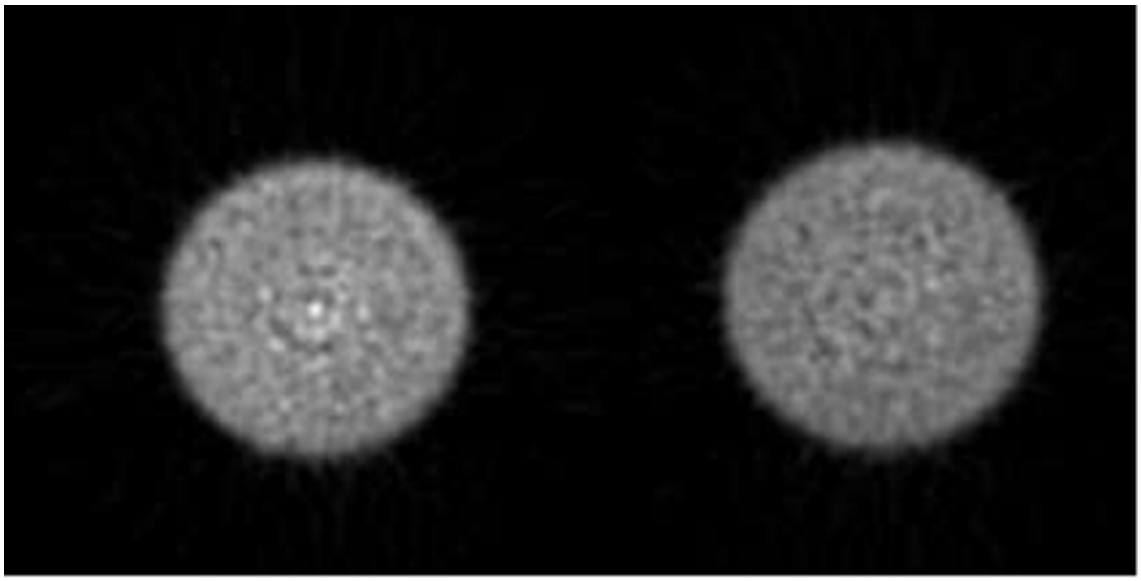

FIG. 23. Images of the uniform section of a SPECT performance phantom showing ring artefacts (left) and good image uniformity (right).

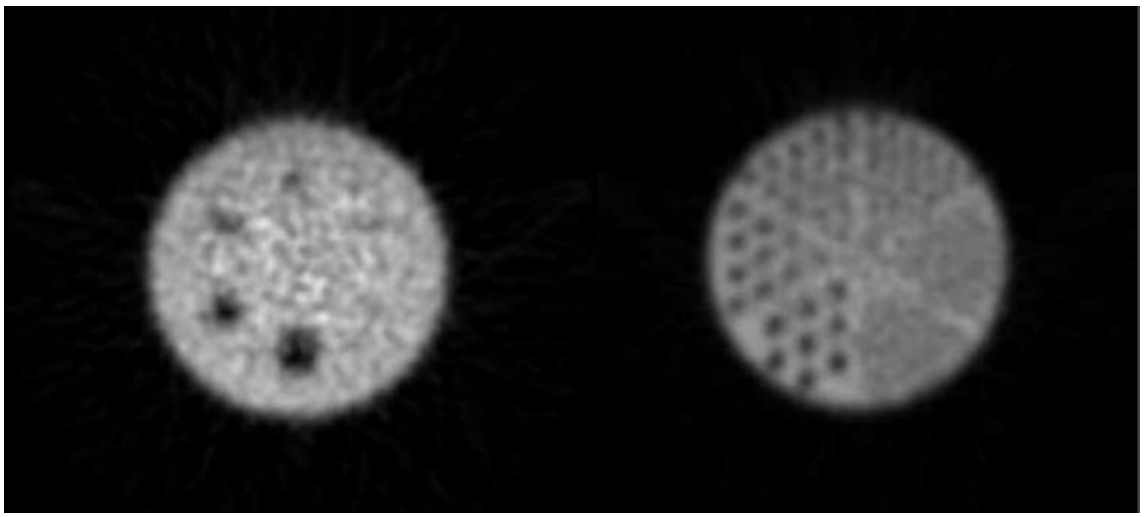

FIG. 24. Solid spheres (left) and rods sections (right) of a SPECT performance phantom showing the different size spheres and rods. In the left image, the fourth sphere (15.9 mm) is visible. The image on the right shows that the third (9.5 mm) or fourth (7.9 mm) rods section is visible.

3.2.7. SPECT image contrast

The purpose of this test is to evaluate the tomographic image contrast. A SPECT performance phantom is also used here with the solid spheres in place (see Fig. 24). Phantom data acquisition and image reconstruction are performed as described in the previous sections. Image contrast is reported using visual assessment as the smallest visible sphere.

3.2.8. Slice thickness

This test is unique to Ref. [45] and is used to test the thickness of a tomographic slice at the centre of the FOV. The test uses a point source in air as described in Section 3.2.4. Analysis is performed by drawing a line profile through the point source along the axial direction and the FWHM of the profile determined. The results of this test are highly dependent on the radius of rotation, which should be set to 15 cm or, if this is not possible, then the smallest radius possible. A circular orbit of rotation should be used.

3.2.9. System volume sensitivity

This test is unique to the NEMA standard [47]. The system volume sensitivity is the total system sensitivity to a uniform concentration of activity in a specific cylindrical phantom. This measurement is dependent on detector configuration, collimator type, radionuclide type, energy window setting and source configuration, among other factors. The test is conducted using a uniform cylindrical phantom 20 cm in diameter. The phantom is injected with a known amount of activity and positioned at isocentre. SPECT acquisition with at least 120 views, but no more than 128, should be acquired, with each view acquired for 10 s. Field uniformity corrections or any other mechanisms that alter the number of counts in these projection images are to be disabled (with the exception of decay correction). The total count rate can then be determined by summing the total number of counts in all projections and dividing it by the total acquisition time. The system volume sensitivity can then be determined by dividing the count rate by the activity concentration.

3.2.10. Sensitivity and uniformity with rotation

This test is unique to Ref. [45] and is used to determine variations in system sensitivity as a function of angular position of the detector. The test requires imaging a flood source of about 185 MBq that can be safely attached to the collimator face. A tomographic scan is then acquired with different rotation speeds while keeping the

same number of views. Analysis is then performed by calculating the mean and standard deviation of the number of counts per view for the different speeds. Any variation in sensitivity exceeding 1% as a function of angle (view) for each speed can be attributed to a lack of magnetic shielding or mechanical drive problems.

3.3. CT TESTING

In addition to SPECT quality control testing, a hybrid SPECT/CT system requires that the CT component of the system undergo a similar set of quality control tests. If the CT component is to be used for diagnostic CT scans, then a complete evaluation of the CT scanner should be performed by a medical physicist, and the results reported [35].

3.3.1. Tube warm up and air calibrations

CT quality control consists of several tests, the first of which is an X ray tube warm up procedure. This is necessary to bring the X ray tube to its optimal operating temperature to stabilize temperatures of both the cathode and anode and aid in extending the lifetime of the X ray tube. This procedure takes about one minute to finish.

Tube warm up is followed by an air calibration (or fast calibration) procedure, which comprises a series of calibrations and system tests, such as checking the operation of the data acquisition system converter board, collimator calibration, gantry balancing, mylar window cleanliness, focal spot position, and finally an array of detector gain calibrations performed at different X ray tube voltages based on user predefined settings. The overall procedure takes about 20–30 minutes depending on scanner manufacturer and model as well as the user predefined voltage settings.

3.3.2. Uniformity, noise, linearity, resolution and artefacts

Following tube warm up and air calibration, a CT number uniformity, linearity, image resolution and low contrast detectability test is then performed using a water filled phantom which includes inserts. The phantom, which is supplied with the scanner, allows for all these tests to be performed in a single scan and is placed on a holder and then positioned centrally in the FOV (see Fig. 25). A scan of the phantom is acquired with pre-set parameters, but typically at 120 kV, the most common clinically used tube voltage. Regions of interest (ROIs) are then drawn on the resultant images at different locations and slices to evaluate CT number uniformity (see Fig. 26), linearity (accuracy), resolution (see Fig. 27) and slice thickness. The CT images are also evaluated for the presence of artefacts (see Fig. 28). For uniformity, it is expected that the CT number in the ROIs does not change significantly across the FOV. The standard deviation of CT numbers within the ROIs of the uniformity test are also used to assess

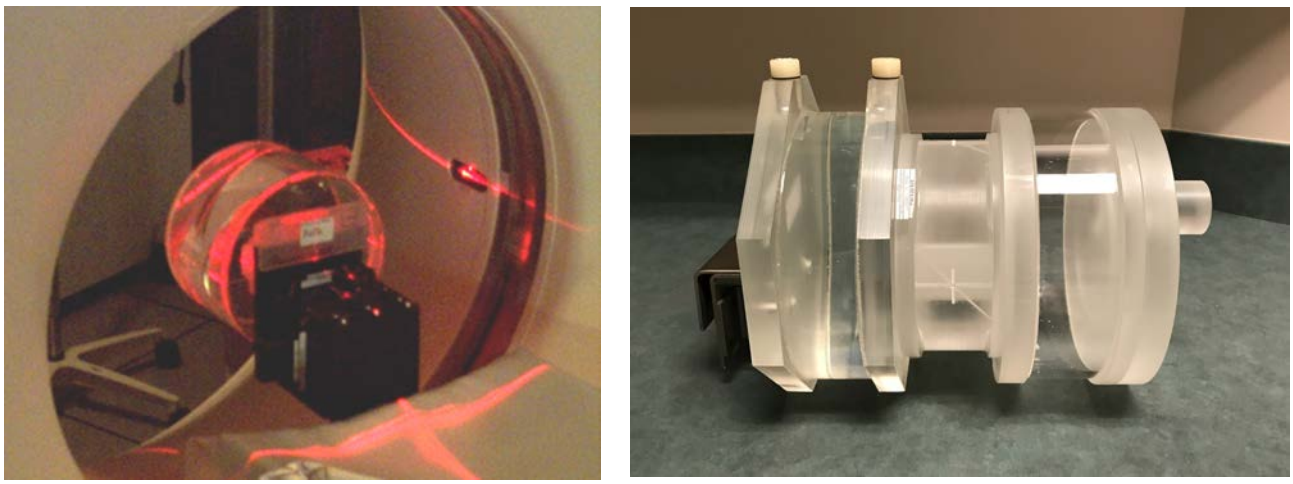

FIG. 25. Examples of CT phantoms.

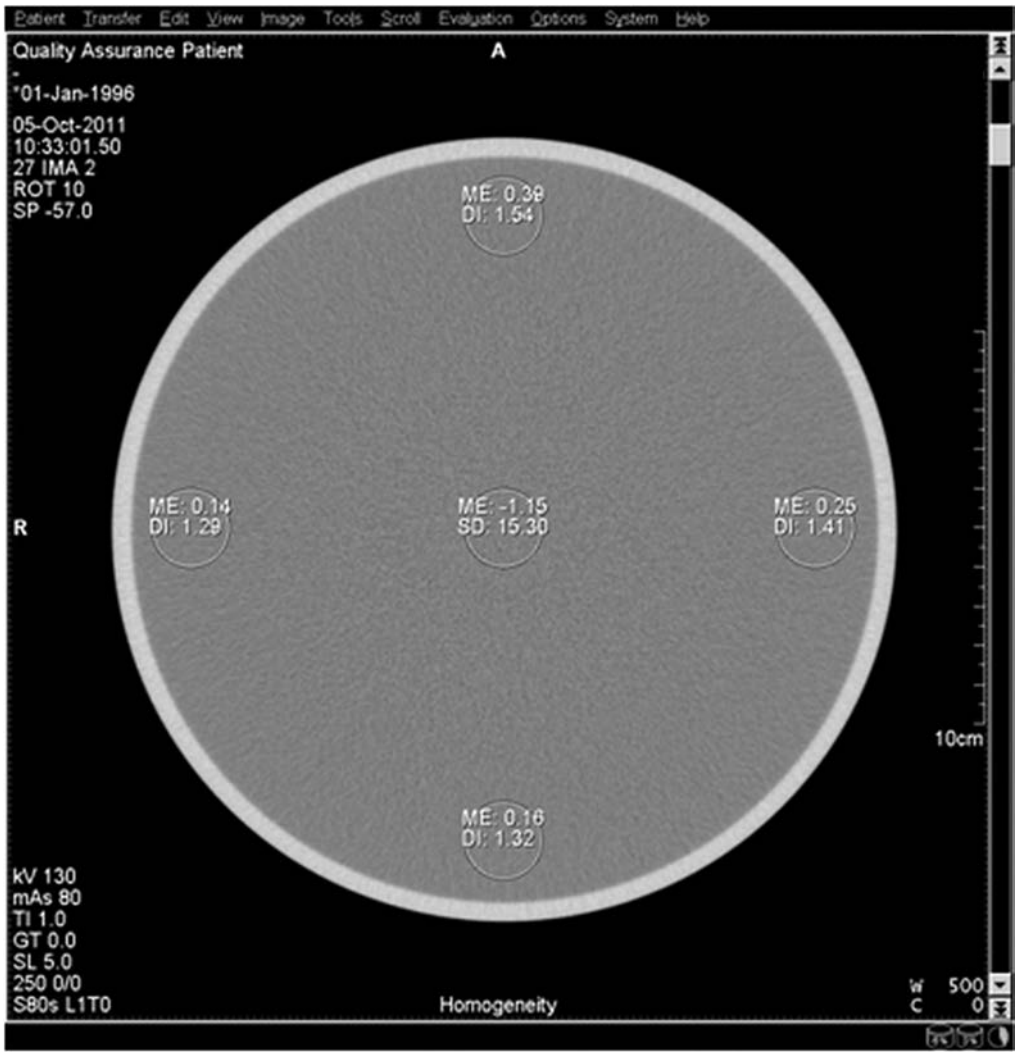

FIG. 26. CT image of the water filled phantom with ROIs drawn at different locations to determine the CT number uniformity.

image noise, and can be helpful in determining the effect different exposure parameters have on this measurement. For linearity, the CT numbers for water, air and acrylic (all part of the phantom) should be within expected ranges. In addition, the CT images of the phantom should be void of any artefacts.

3.3.3. CT dose assessment

In addition to the image quality evaluation, an assessment of radiation dose should be performed for the CT system. The dosimetric quantity for CT is the computed tomography dose index (CTDI), which, although not an actual dose figure, is a parameter which permits relative dose comparison among different scanners. Measurements require a polymethyl methacrylate cylindrical CTDI phantom and an ionization chamber (see Fig. 29). This test should be performed annually or following a CT X ray tube or detector array replacement. The CTDI phantom is placed at isocentre in the FOV of the scanner with the ionization chamber placed in the central hole of the phantom. A CT axial acquisition is then performed and the radiation exposure (or kerma) measured. This measurement is repeated for four different peripheral positions of the ionization chamber within the phantom. A weighted average of these five exposure (or kerma) measurements is used to calculate the CTDI value, which is then compared to the value reported by the scanner. The process is repeated for clinically relevant CT acquisition parameter combinations (kV and mAs). The measured and reported values should be similar to within manufacturers' specified deviations.

In addition, a review of the predetermined dose notification levels that have been set as part of each CT protocol may be performed. When a CT study is suspected to exceed the pre-set notification value, an alert

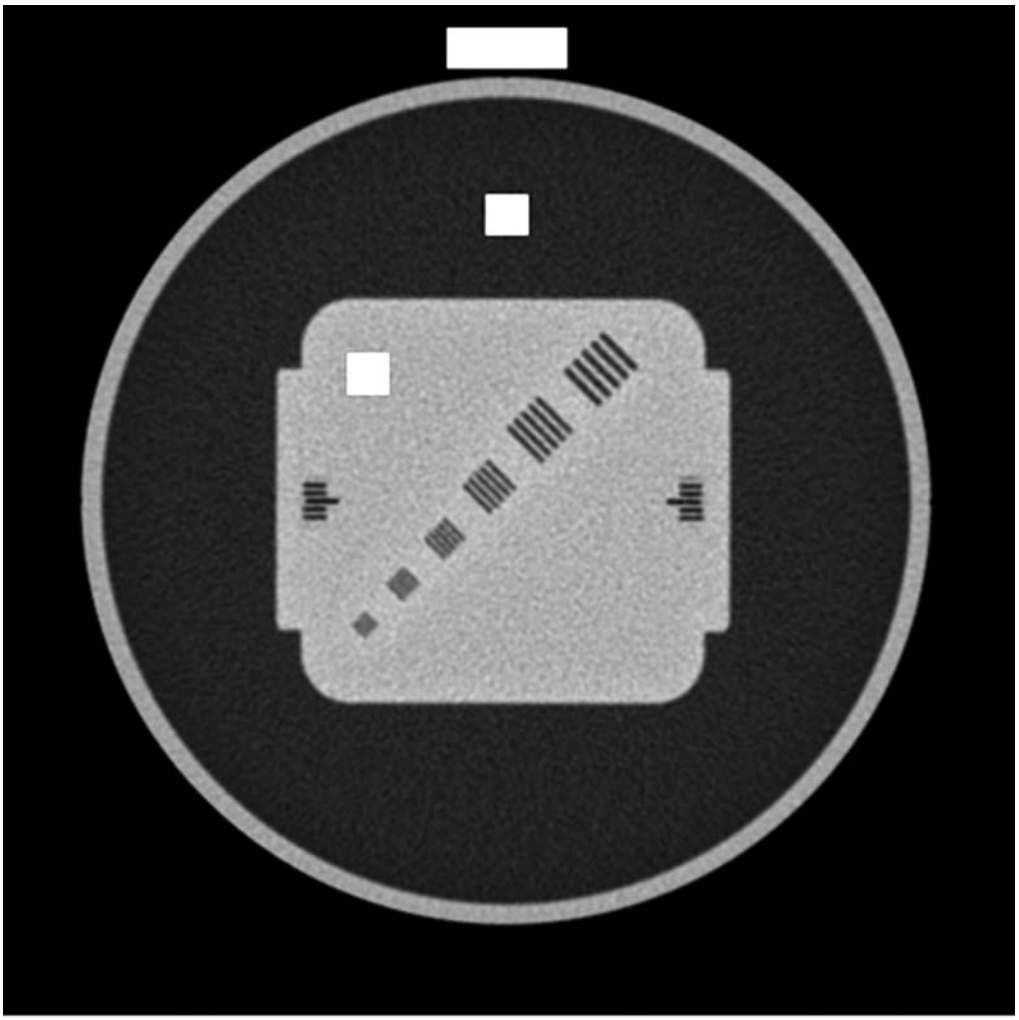

FIG. 27. CT image of the water filled phantom with ROIs drawn at different locations (white regions) corresponding to air, water and acrylic to determine the CT number linearity.

message is generated before the exam is acquired in order to allow the user to modify the acquisition parameters. This enables the user to reduce the patient dose, or override the alert if necessary. Furthermore, a dose alert (different from a dose notification level) value can also be programmed into new CT scanners to trigger a message when the cumulative dose at a location, plus the dose for the next planned and confirmed scan(s), is likely to exceed a preprogrammed value. It is important to note that dose alert values are applicable across all protocols on a scanner, while dose notifications are specific to protocols. These tools allow users to track patient CT doses and ensure they are within specified limits.

3.4. SPECT/CT TESTS

3.4.1. SPECT/CT registration

For hybrid systems, a SPECT/CT registration test should be performed to ensure that the two scanners are properly aligned. The motivation for SPECT/CT image registration is that spatial registration is critical for accurate SPECT image reconstruction using CTAC and the display of fused images for clinical interpretation. The standards of the AAPM [46] and the EANM [48, 49] are the only ones which describe this test. However, the AAPM recommends that the manufacturer's specific registration test phantom procedure and analysis tools be used to evaluate the spatial registration accuracy (see Figs 30 and 31). Alternatively, the AAPM also suggests visually

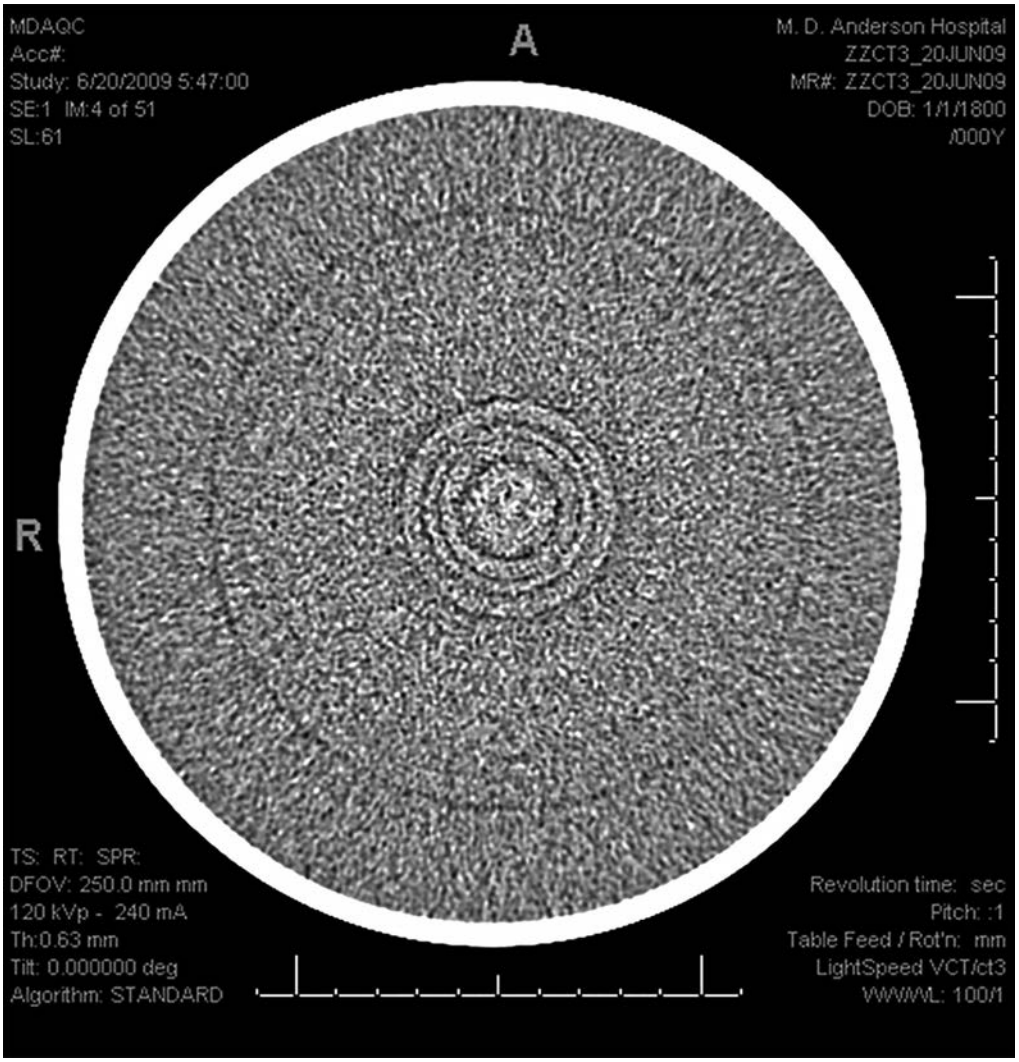

FIG. 28. CT image of the water filled phantom showing ring artefacts, which will necessitate a service call.

inspecting the SPECT/CT images of the SPECT performance phantom for spatial registration when acquired with and without any table loading (placement of >50 kg on the patient couch to simulate a patient; see Fig. 32) [46]. An optional procedure in which point sources placed on the SPECT phantom that are visible on both SPECT and CT images is also described. In this case, the alignment of the point sources on both images can be determined. Currently, there are no generally accepted criteria for alignment accuracy between the SPECT and CT images; however, an alignment mismatch that is less than the size of a SPECT image pixel should be acceptable.

3.4.2. SPECT/CT image quality

This test evaluates the overall SPECT/CT image quality when using CT based AC while all processing and reconstruction parameters that are recommended by the manufacturer for routine use in clinical SPECT/CT imaging (e.g. scatter corrections, iterative reconstruction parameters and resolution recovery, among others) are applied. The test uses the same SPECT performance phantom described in Section 3.4.1 with the resolution and sphere insets included except that, in this case, CTAC is applied. The phantom is first filled with about 740 MBq of activity and placed at isocentre in the FOV. CT and SPECT scans of the phantom are then acquired and reconstructed using standard clinical protocol parameters. The resultant images are then evaluated visually for uniformity, resolution and contrast in a manner similar to standard SPECT imaging. Alternatively, a NEMA PET image quality phantom could be used for this assessment, which is more applicable to body imaging.

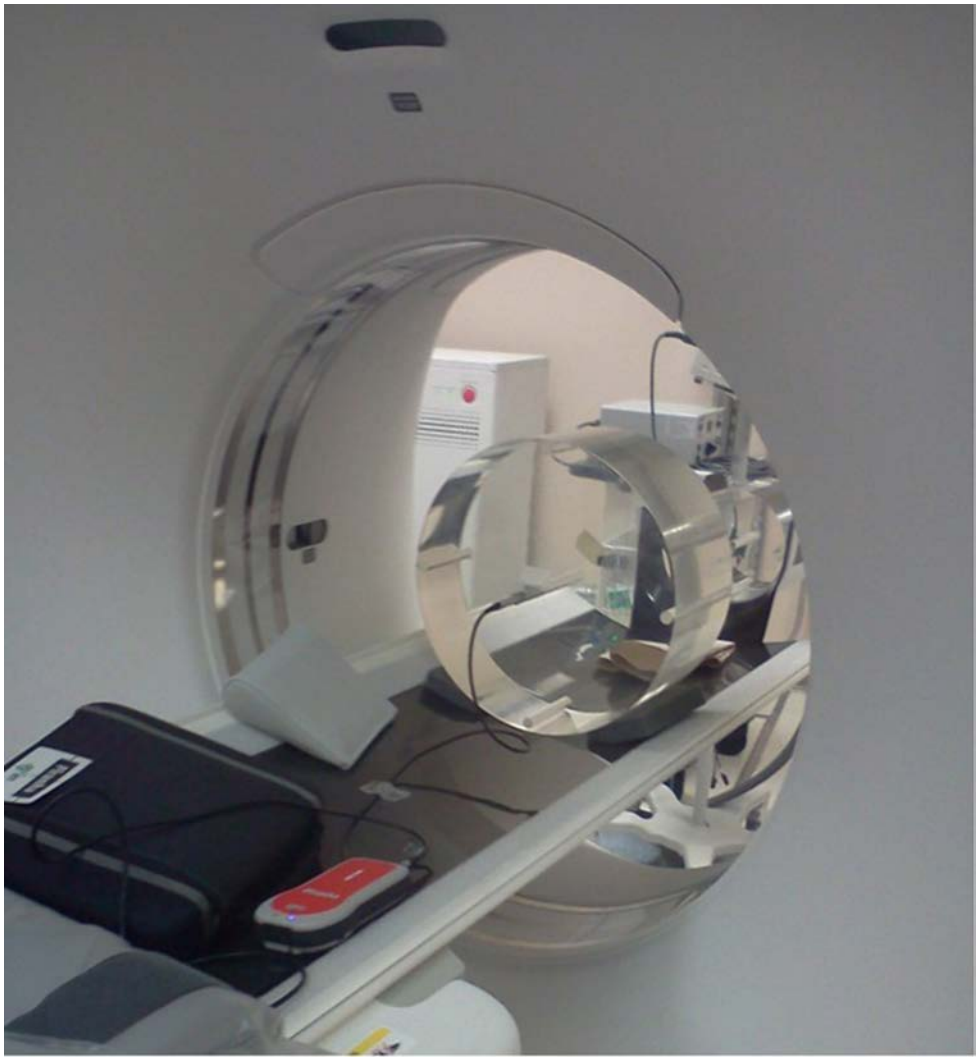

FIG. 29. CTDI phantom with an ionization chamber placed at the centre of the phantom and positioned at isocentre in the FOV of the scanner.

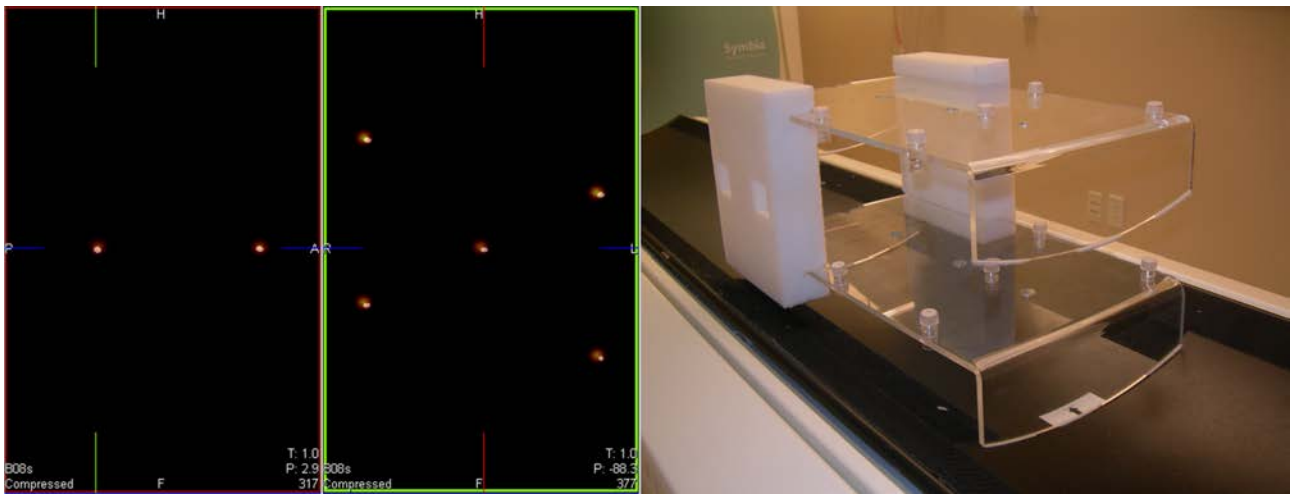

FIG. 30. SPECT/CT registration tool from a manufacturer, which includes ten point sources (right) seen in the fused SPECT and CT images (left and middle).

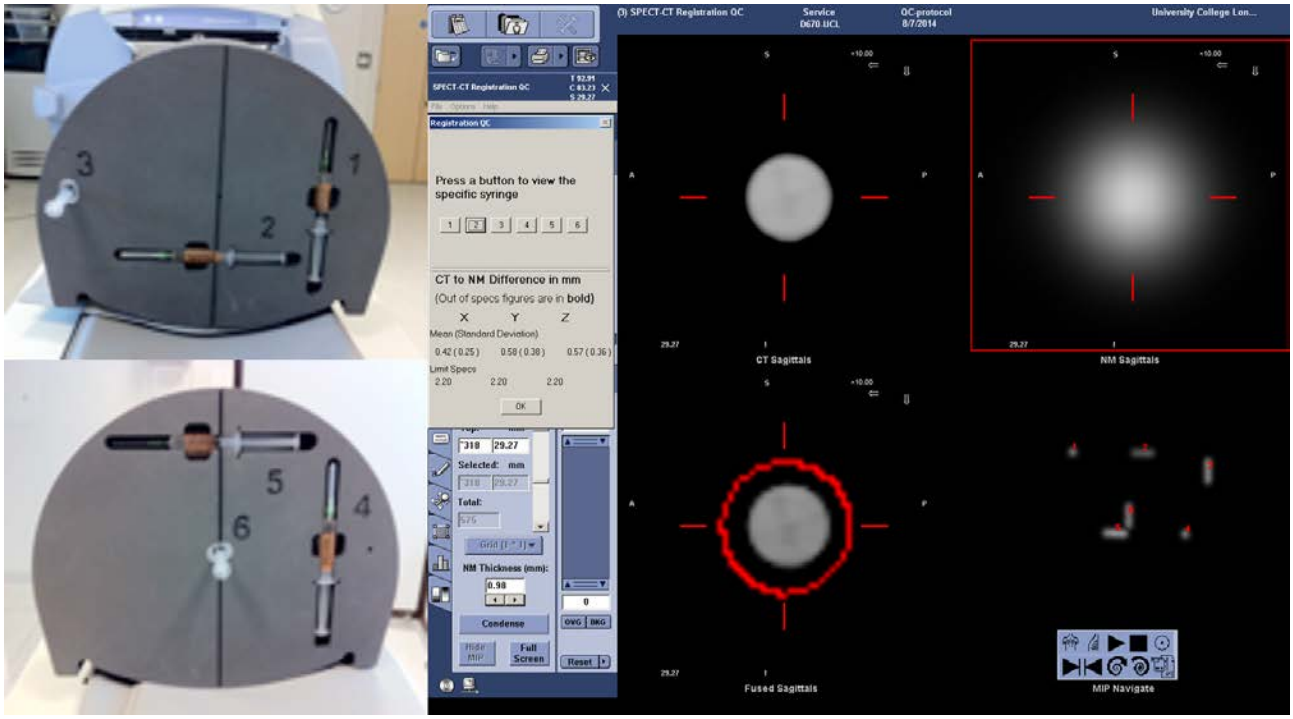

FIG. 31. SPECT/CT registration tool (left) from a manufacturer, which includes six line sources seen in the SPECT and CT images (right).

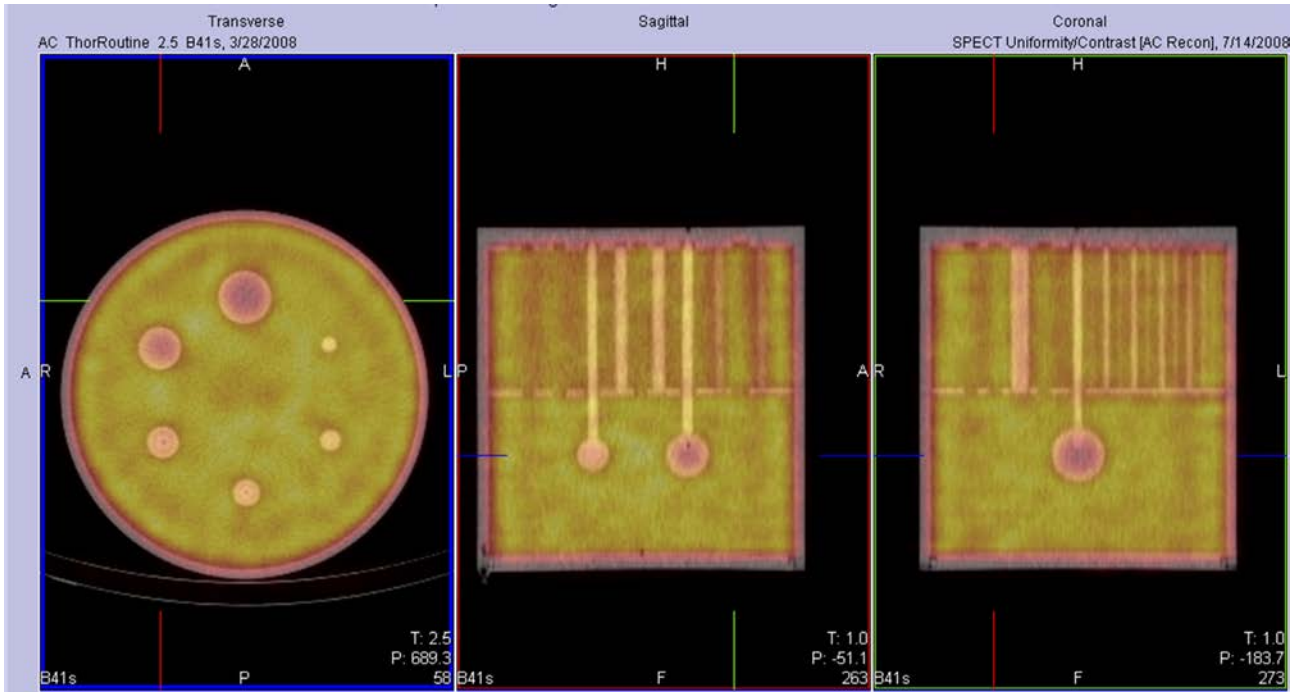

FIG. 32. Fused SPECT/CT images of a SPECT performance phantom that can be used for the assessment of the alignment of the SPECT and CT scanners of the hybrid system.

4. ARTEFACTS

Clinically useful diagnosis from SPECT and SPECT/CT imaging depends on accurate interpretation of the images and corresponding quantitative results. This means that nuclear medicine professionals should be acquainted with the different patterns associated with images of different organs or parts of the body being examined. However, possible image abnormalities or artefacts related to machine, user or patient factors might not be recognized by these professionals, which could hinder optimal patient management. This section provides examples of abnormal patterns and artefacts caused by errors owing to system, user and patient sources and their manifestation on resultant SPECT and SPECT/CT images. This section also describes methods to resolve these abnormalities and artefacts.

4.1. SYSTEM RELATED ARTEFACTS

In order to deliver good and quantifiable SPECT images, it is essential that artefacts related to system factors should not be present. These artefacts can manifest themselves as rings, which can be caused by, for example, detector non-uniform response, COR offset or the wrong uniformity correction map. Other factors such as inadequate energy peaking, head tilt, head to head registration, mismatched sensitivity and mechanical problems can also generate artefacts that might hamper both visual inspection and quantification of clinical data.

4.1.1. Non-uniformity of detector response

Background

The response of a scintillation camera when subject to a uniform flux of photons should be uniform over the whole FOV. When non-uniformities are present, full or partial ring artefacts will appear in the tomographic slices. These can be caused by one or more of, but not limited to, the following factors:

(a) Poor detector uniformity;
(b) Small differences in the responses from the photomultiplier tubes;
(c) Non-linearity of the detector and electronics;
(d) Defects in the collimator;
(e) Crystal hydration.

Gamma camera quality control tests (see Section 3 for more details) should be performed before SPECT studies, so that most non-uniformity artefacts can be detected and corrected for prior to tomographic acquisitions.

Case A

Projections of a Jaszczak phantom filled with ^{99m}Tc were acquired for a radius of rotation of 17 cm and using a 128 × 128 matrix. The 128 projections were reconstructed with FBP and Chang-AC. Figure 33 shows the reconstructed images presenting ring artefacts in three of the four slices in the uniform section, indicating the presence of detector non-uniformities.

Guidance

Poor detector uniformity may result in ring artefacts in the reconstructed SPECT slices, even when not noticeable in planar image, as the tolerances permitted are far less than those accepted in conventional planar imaging.

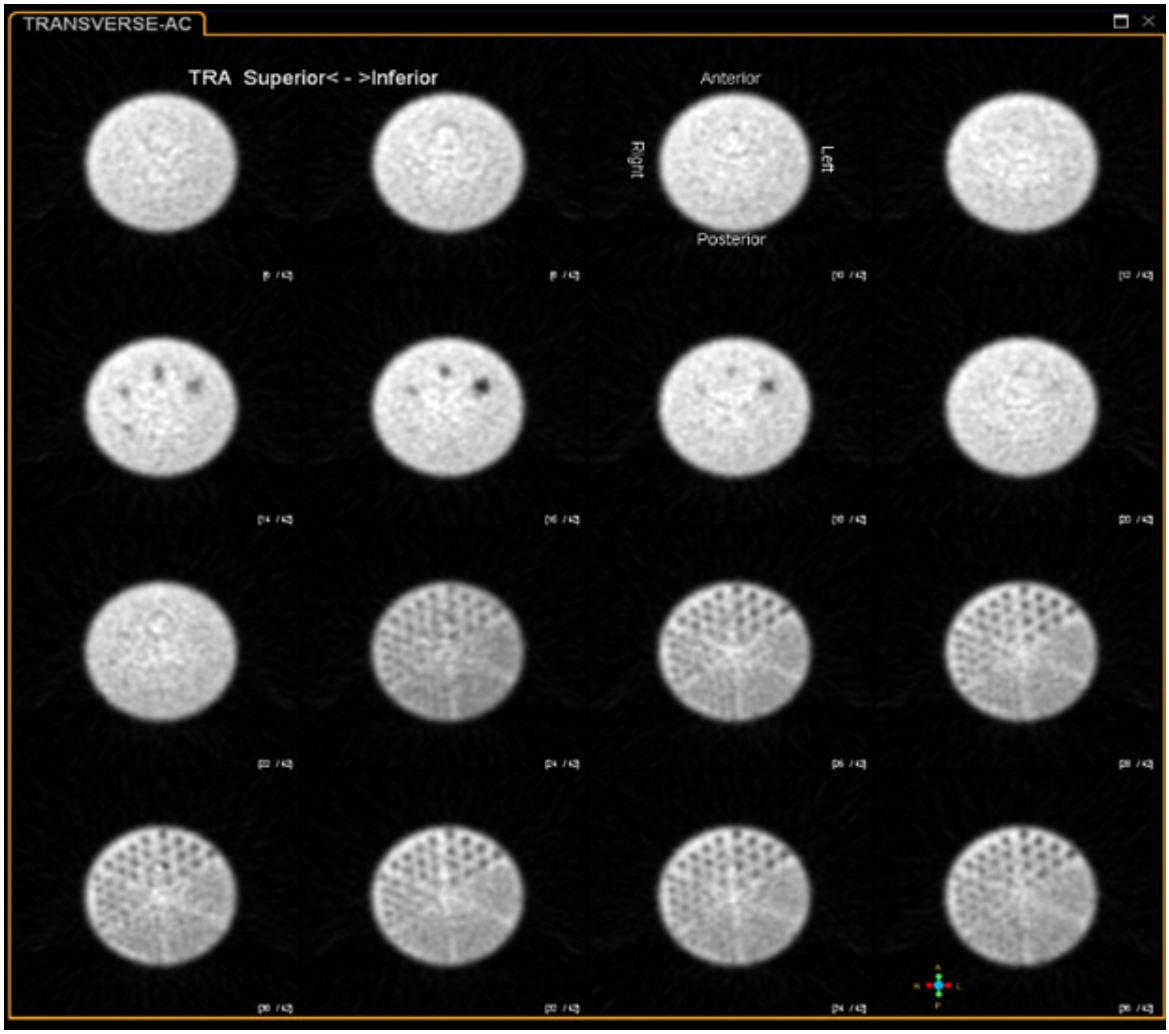

FIG. 33. SPECT images of a Jaszczak phantom showing ring artefacts in several slices, indicating detector non-uniformities.

Case B

SPECT image quality was tested using a SPECT performance phantom. Data were acquired with a low energy ultra high resolution (LEUHR) collimator, 128 × 128 matrix, 128 projections and 16 cm radius of rotation. FBP reconstructed slices presented ring artefacts, depicted in Fig. 34. Daily uniformity checks showed a degrading trend of the uniformity parameters, although still within recommended values by the manufacturer.

Guidance

When daily uniformity parameters tend to degrade (e.g. for an 'old' camera) even when they are within the manufacturer's recommended limits, poor planar uniformity is amplified by the reconstruction process. SPECT image quality tests should therefore be carried out in order to ensure that no damaging effects would affect the clinical results.

Case C

A myocardial perfusion study was performed on a patient using ^{99m}Tc labelled methoxyisobutylisonitrile (MIBI) and the stress images presented defects at the apex and anterior wall that were not consistent with the patient's clinical data (see Fig. 35). Daily routine tests were checked, and it was verified that one of the heads presented non-uniform response over part of the FOV, as shown in the top row of Fig. 36. The system was

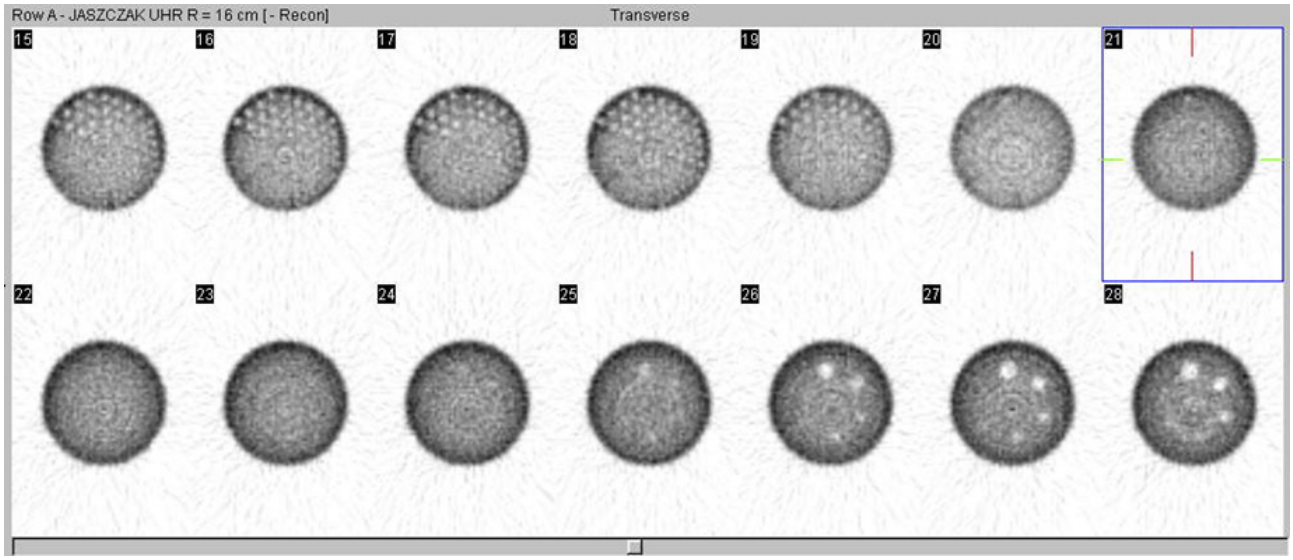

FIG. 34. Ring artefacts present in some of the FBP reconstructed Jaszczak phantom images, obtained with an LEUHR collimator.

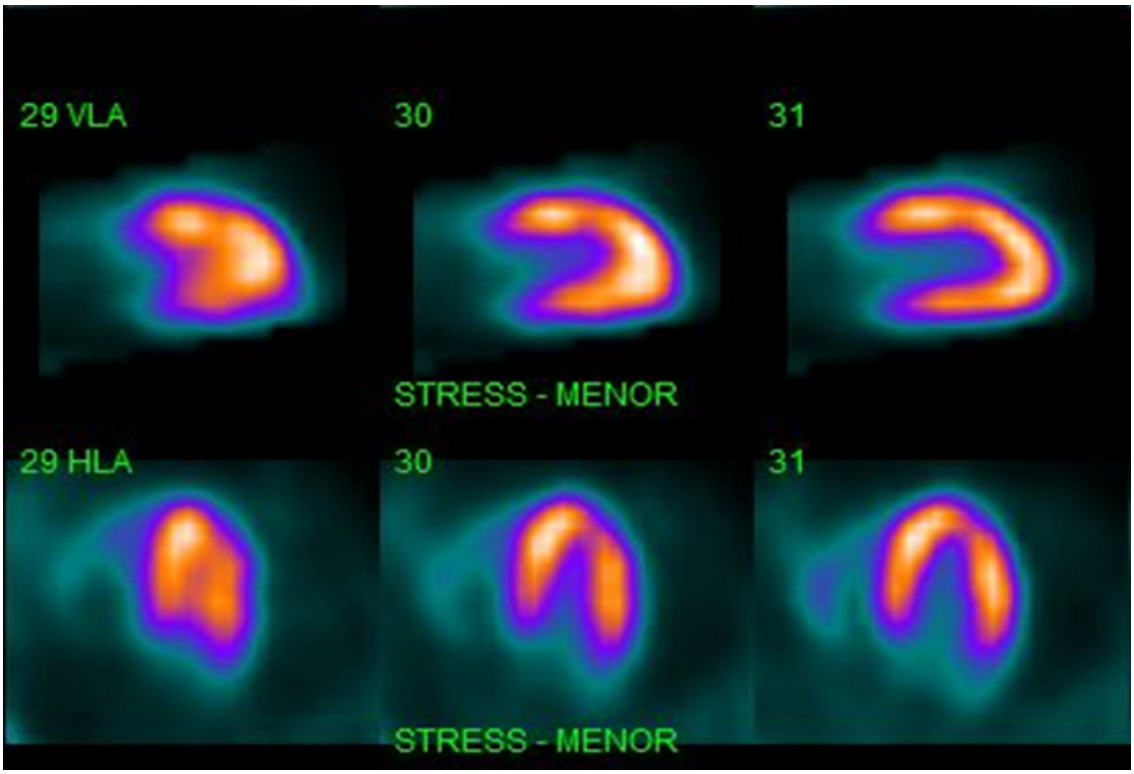

FIG. 35. ^{99m}Tc-MIBI myocardial perfusion results obtained with one detector of a dedicated cardiac system out of calibration.

recalibrated and the uniformity maps became normal, as indicated in the bottom row of Fig. 36. The patient study was repeated and the new images were in accordance with his clinical information (see Fig. 37).

Guidance

It is necessary to check carefully, both visually and numerically, the daily operational tests before starting clinical studies in order to avoid mistakes or repeating patient studies.

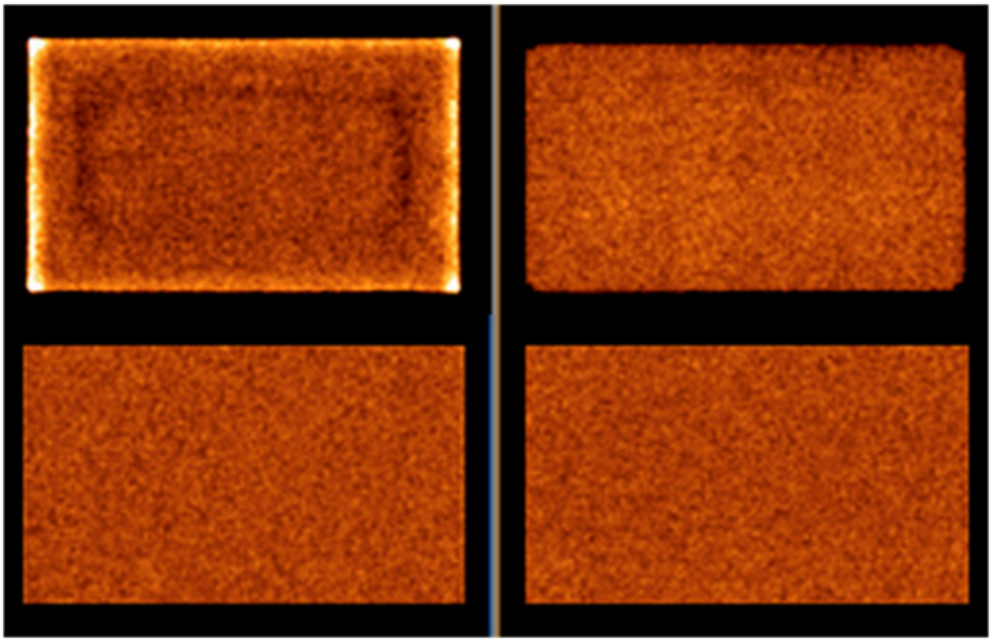

FIG. 36. Uniformity maps for both heads before recalibration (top) and after recalibration (bottom).

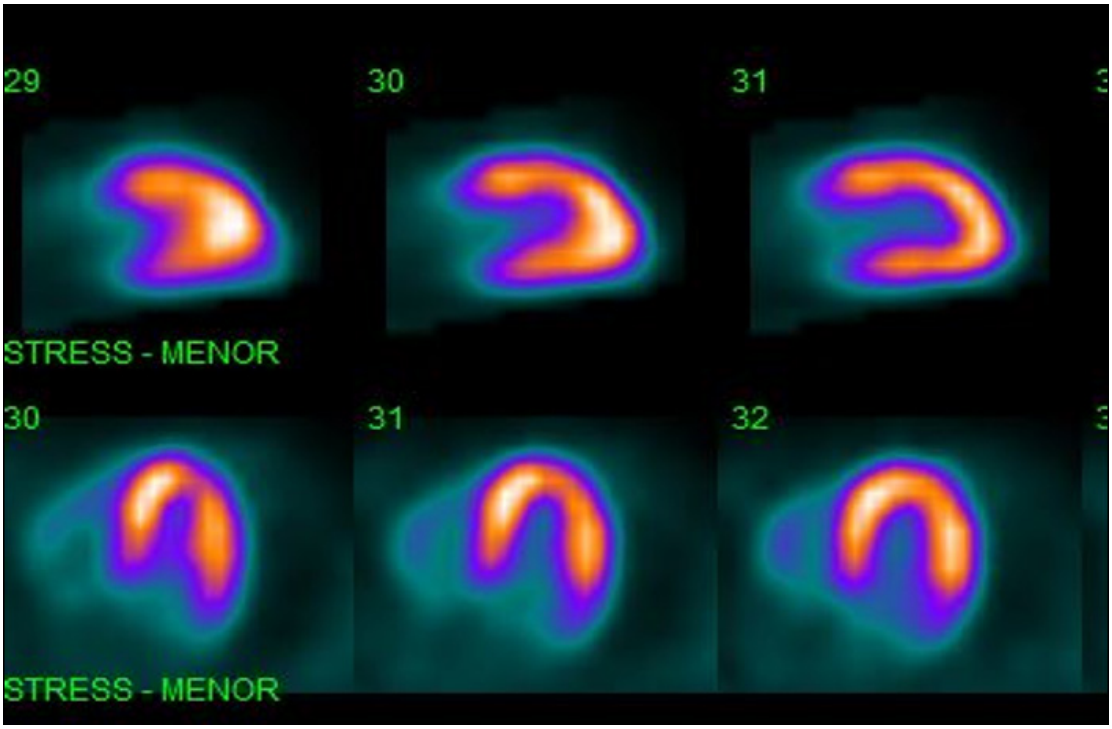

FIG. 37. ^{99m}Tc-MIBI myocardial perfusion results obtained for the same patient as in Fig. 35 after recalibration of the faulty detector.

4.1.2. Crystal hydration

Background

Crystal hydration is a rare event in gamma camera systems. When it occurs, however, it can have a large impact on both planar and SPECT images.

Case

After an incident involving a water leak in a SPECT scanning room, the SPECT system was tested and hydration was found in both crystals of a dual head camera (see Fig. 38). SPECT data of a NEMA PET image quality phantom is shown in Fig. 39. Data were acquired using a 128 × 128 matrix, 120 projections of 20 s and reconstructed without AC.

On-peak images show that the hydration is only visible on head 2. The non-uniformity of these two close cold spots form the half-ring artefact shown in the SPECT images. Once both crystals had been replaced, the system functioned properly.

Guidance

Off-peak hydration tests should be carried out when physical factors, such as water leaks, affect the environmental conditions in the room that houses the SPECT or SPECT/CT scanner. It is important to note that not all hydration spots visible in off-peak flood images result in on-peak image artefacts.

4.1.3. Poor correction maps

Background

Nuclear medicine imaging systems have both intrinsic and extrinsic uniformity maps that are used to correct for non-uniformities present in the detector and the collimated detector, respectively. The use of an appropriate correction map is essential if non-uniformity artefacts are to be avoided. When liquid flood phantoms are not mixed properly, or when collimators are exchanged between systems of the same scanner model, the uniformity maps might introduce artefacts in the SPECT images. Furthermore, outdated correction maps that do not match the current state of the detector can introduce image artefacts.

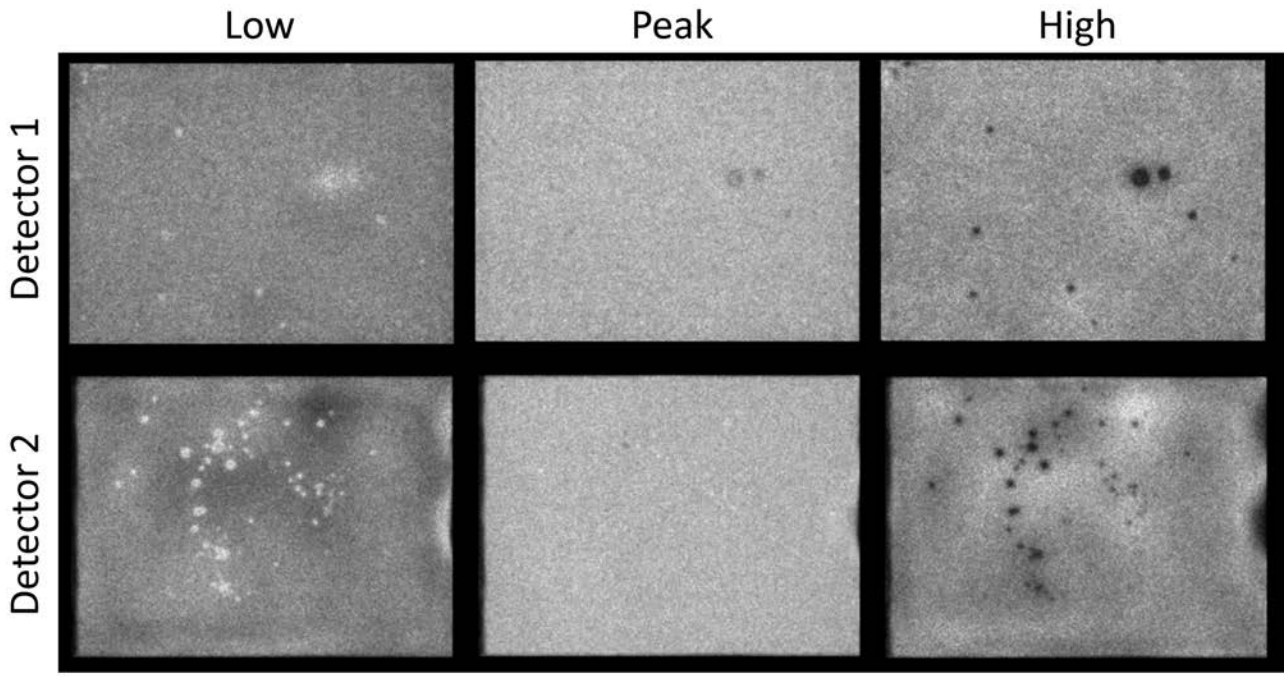

FIG. 38. Lower (126 keV) and upper (154 keV) off-peak (left and right) and on-peak (middle) flood images showing hydration spots in both crystals of a dual head SPECT system.

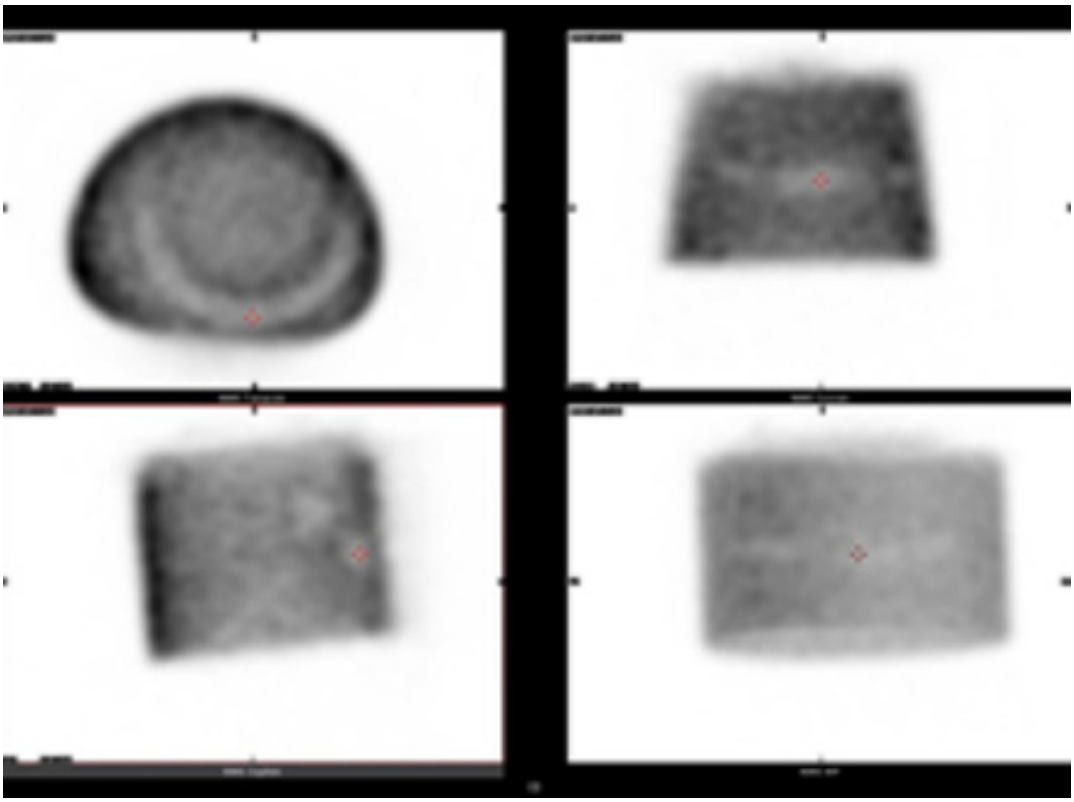

FIG. 39. Half-ring artefact caused by crystal hydration of a dual head SPECT camera.

Case A

SPECT uniformity test was performed with a Jaszczak phantom filled with ^{99m}Tc. FBP reconstructed and uniformity corrected slices presented ring artefacts (see Fig. 40). It was verified that this defect was created by a poorly mixed uniformity liquid flood phantom.

Case B

Uniformity corrected slices of a SPECT performance test phantom presented ring artefacts, as shown in the top row of Fig. 41. When uniformity correction was excluded from the reconstruction process, the artefacts disappeared (shown in bottom row). The loaded uniformity correction map was found to be outdated; and when the proper map was used, ring artefacts did not appear.

Guidance

When creating tomographic uniformity maps using a flood tank, it is important that the radioactive solution be properly mixed to ensure that the system correction map only corrects for varying detector performance. A prior planar image of the phantom can help to ensure that the phantom is properly mixed. Where a choice of uniformity maps is available, it is important that the correct map be chosen; and where collimators may be interchanged between systems, any system uniformity correction should be for the desired detector–collimator combination.

4.1.4. Centre of rotation offset

Background

Ring artefacts that can occur owing to COR errors are not clearly seen on clinical images but result in a loss of resolution or blurring in the reconstructed image. Therefore, evaluation using appropriate test phantoms, such as

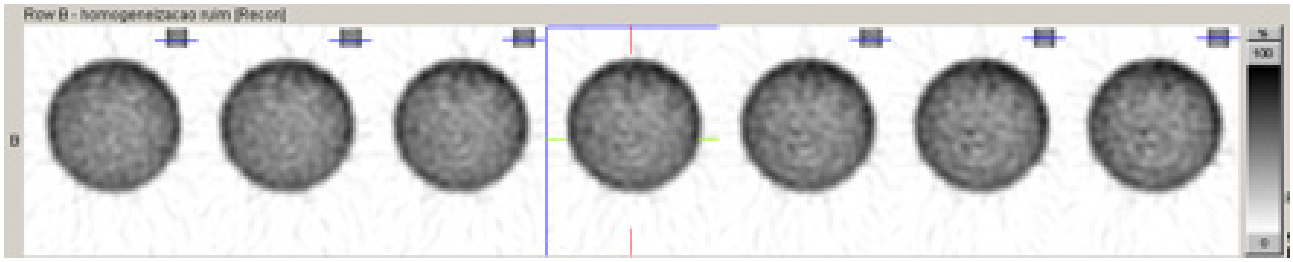

FIG. 40. Partial ring artefacts caused by a poorly mixed fillable flood phantom.

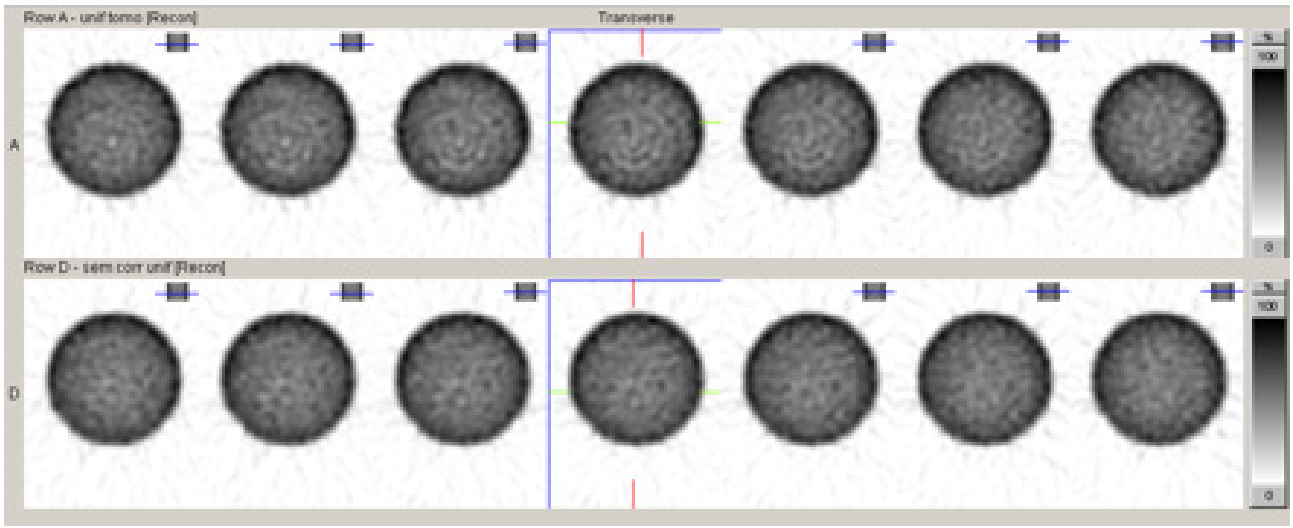

FIG. 41. Ring artefacts resulting from using an outdated uniformity map (top row) and reconstructed slices without uniformity correction (bottom row).

multiple point sources, should be carried out according to manufacturer's recommendations. COR testing aims to guarantee correct alignment of the physical COR with the reconstruction COR.

Case

A SPECT performance phantom filled with ^{99m}Tc was imaged with a 128 × 128 matrix and 128 projections. FBP reconstruction and Chang-AC were performed. Figure 42 depicts the slices presenting ring artefacts in all of them, indicating offset error (i.e. a shift of the physical COR in relation to the centre of the matrix of reconstruction).

Guidance

A periodic check of COR offset is essential in order to ensure that no distortions or ring artefacts be introduced in SPECT studies, even if planar uniformity maps do not present inhomogeneities.

4.1.5. Energy peaking

Background

Before acquiring a SPECT image, it is important to ensure that the correct radionuclide be selected and that the camera be peaked correctly on the chosen radionuclide.

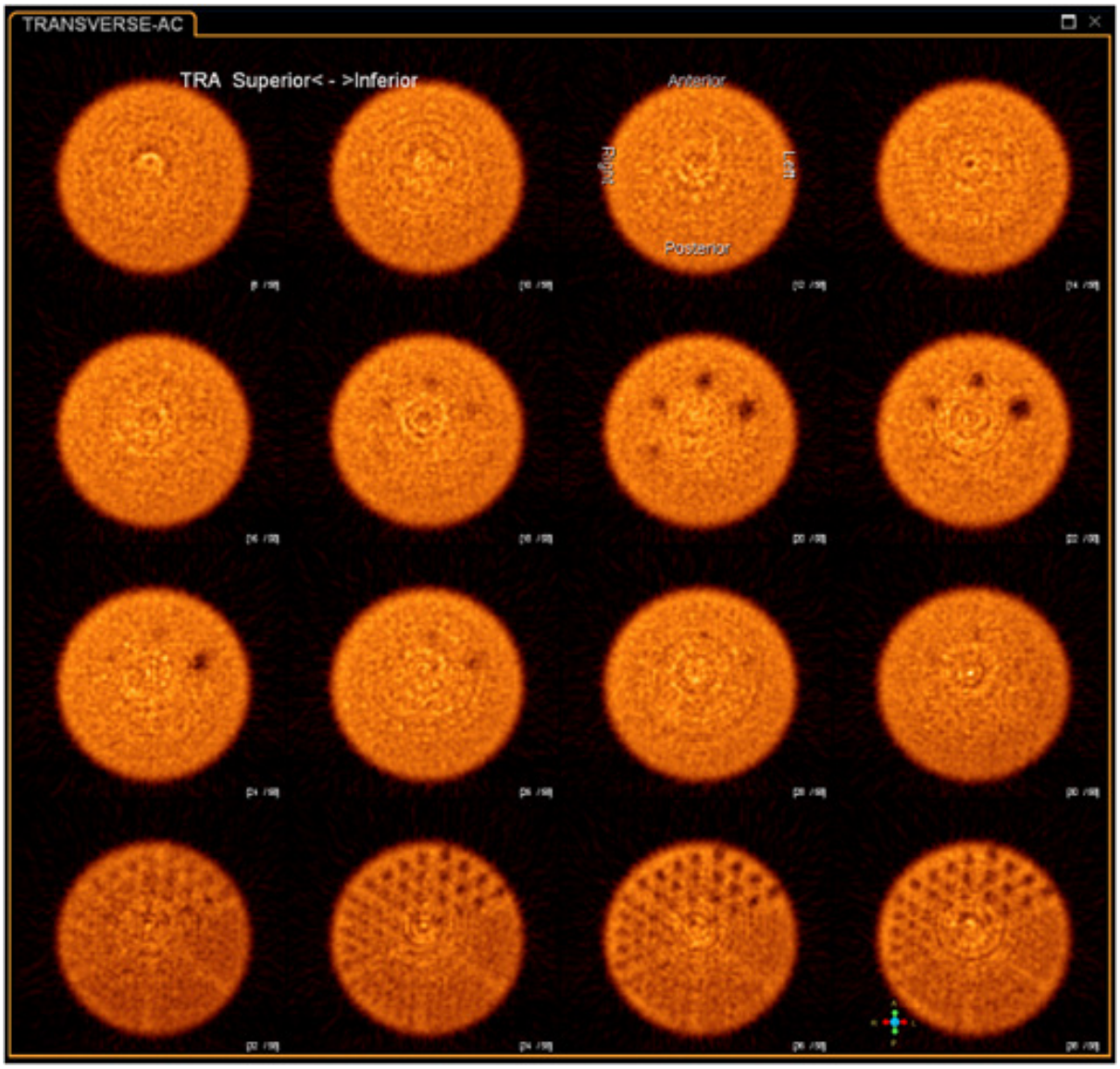

FIG. 42. Ring artefacts in a sequence of SPECT images of a performance test phantom owing to COR error. The centre of the rings corresponds to the axis of rotation

Case

Two ^{99m}Tc-MIBI myocardial perfusion studies were performed. Patient (a) was acquired on-peak (centred at 140 keV) and at low off-peak (centred on 125 keV), as shown in Fig. 43(a). Patient (b) was acquired on-peak and at high off-peak (centred on 155 keV), as shown in Fig. 43(b). If the energy window is placed too low, more scatter radiation will be acquired in the projections, diminishing the contrast (see Fig. 43(a)). Conversely, with the energy window placed high, less scattered radiation is present and borders are better defined, albeit at the cost of a lower count rate. The resulting SPECT slices are shown in Fig. 44.

Due to the increase of scatter in the low off-peak images, resolution and contrast are compromised with thicker myocardial walls and more non-myocardial uptake respectively. Using a high off-peak energy window improves contrast — but with more noise — although this appears to be minimal in this example owing to high acquired counts.

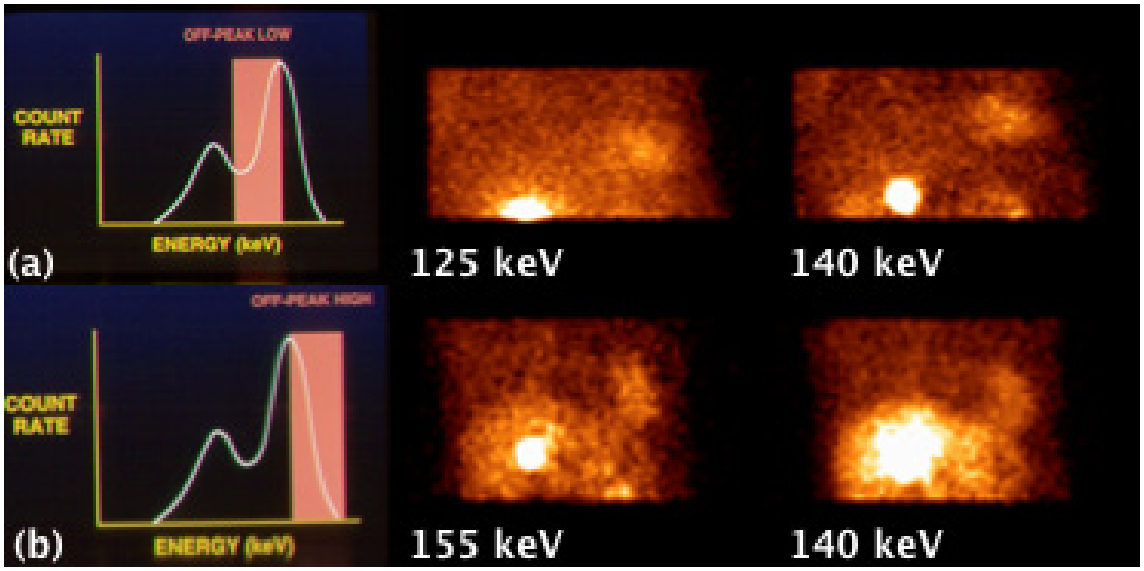

FIG. 43. Projection views of a myocardial perfusion study (a) imaged at 125 keV and 140 keV with the lower energy window used and (b) energy peak and projection views at 155 keV and 140 keV using the higher energy window.

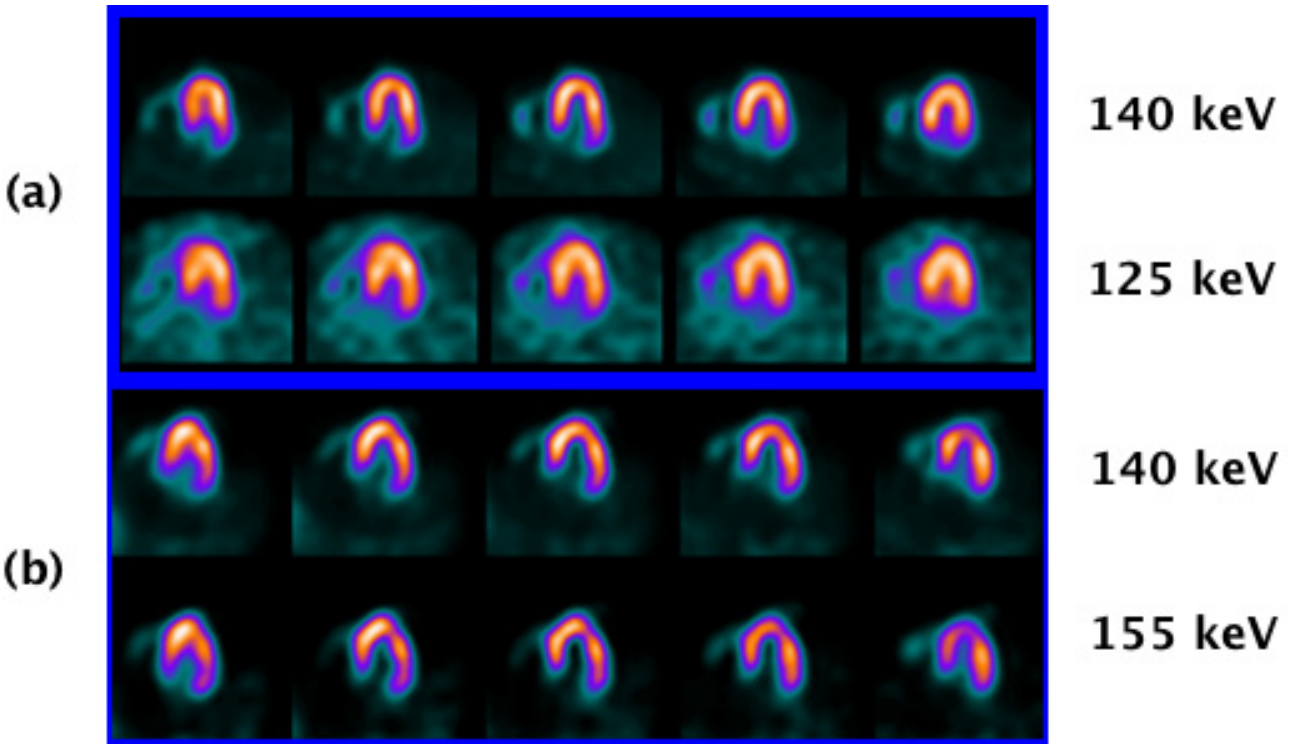

FIG. 44. Projection views of two myocardial perfusion studies: patient (a) imaged at low off-peak and on-peak; and patient (b) imaged at high off-peak and on-peak. The centre of the energy window settings is also shown for each image.

Guidance

The energy window needs to be well centred in order to produce good contrast, high resolution and low noise images. In the case of a large contribution of scattered radiation, the window can be shifted towards the high energy end, with the acquisition time per projection increased in order to keep an acceptable noise level.

4.1.6. Head tilt

Background

COR artefacts typically present as ring artefacts that show throughout every slice of a tomographic dataset. In some instances, however, a ring artefact might only be present in a small number of slices. While this may be due to detector non-uniformity, another cause for this type of artefact is head tilt (i.e. detector sag in the axial (Z) plane). With head tilt, the COR might only be correct for some, but not all, slices, giving the slice dependent COR ring artefact.

Case A

Ring artefacts can be observed in reconstructed slices from a dual detector SPECT system (see Fig. 45). As the uniformity maps for both detectors did not have noticeable inhomogeneities (see Fig. 46(a)), COR offsets were checked and found to be within the manufacturer's limits (see Fig. 46(b)). Once the head tilts were adjusted and a new calibration performed, all slices were brought within tolerance, and ring artefacts were not seen in the resulting uniformity transverse slices (see Fig. 47).

Case B

The reconstructed slices of a myocardial perfusion study showed abnormal shapes in all projections. It was verified that the detectors were tilted, converging towards the gantry. The heads were repositioned and new rest study was performed. The top row of Fig. 48 shows the tilted head slices, while the bottom row shows the corrected ones.

Guidance

When ring artefacts are present in uniform phantom slices, with planar uniformity not showing inhomogeneities and COR testing within acceptable limits, head tilt can be suspected as the cause of the artefact.

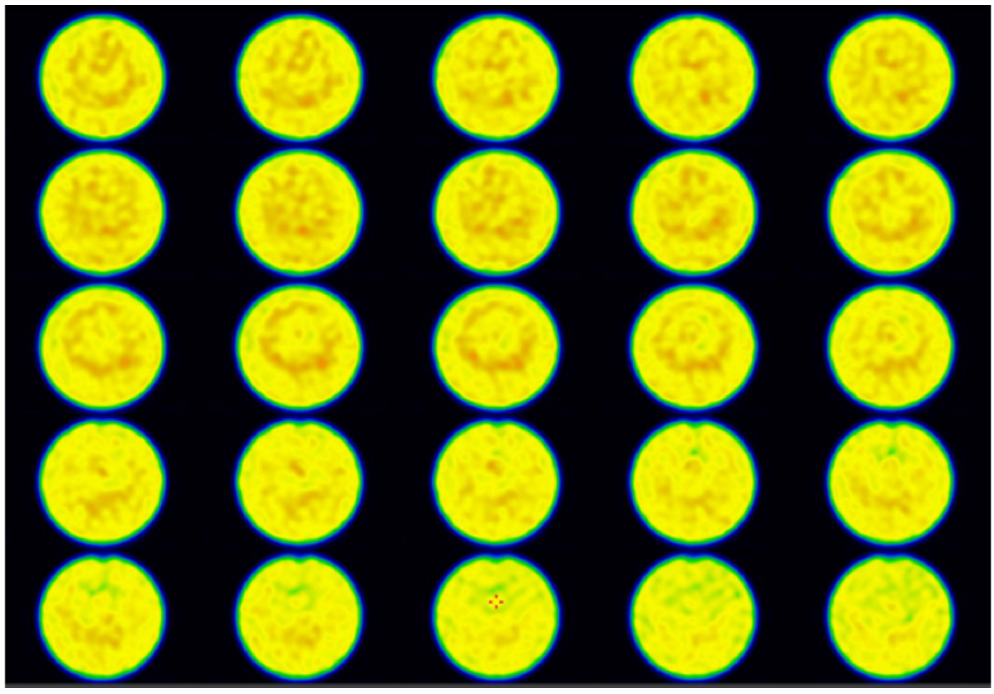

FIG. 45. Ring artefacts present in the slices further away from the centre along the AOR of a uniform cylinder.

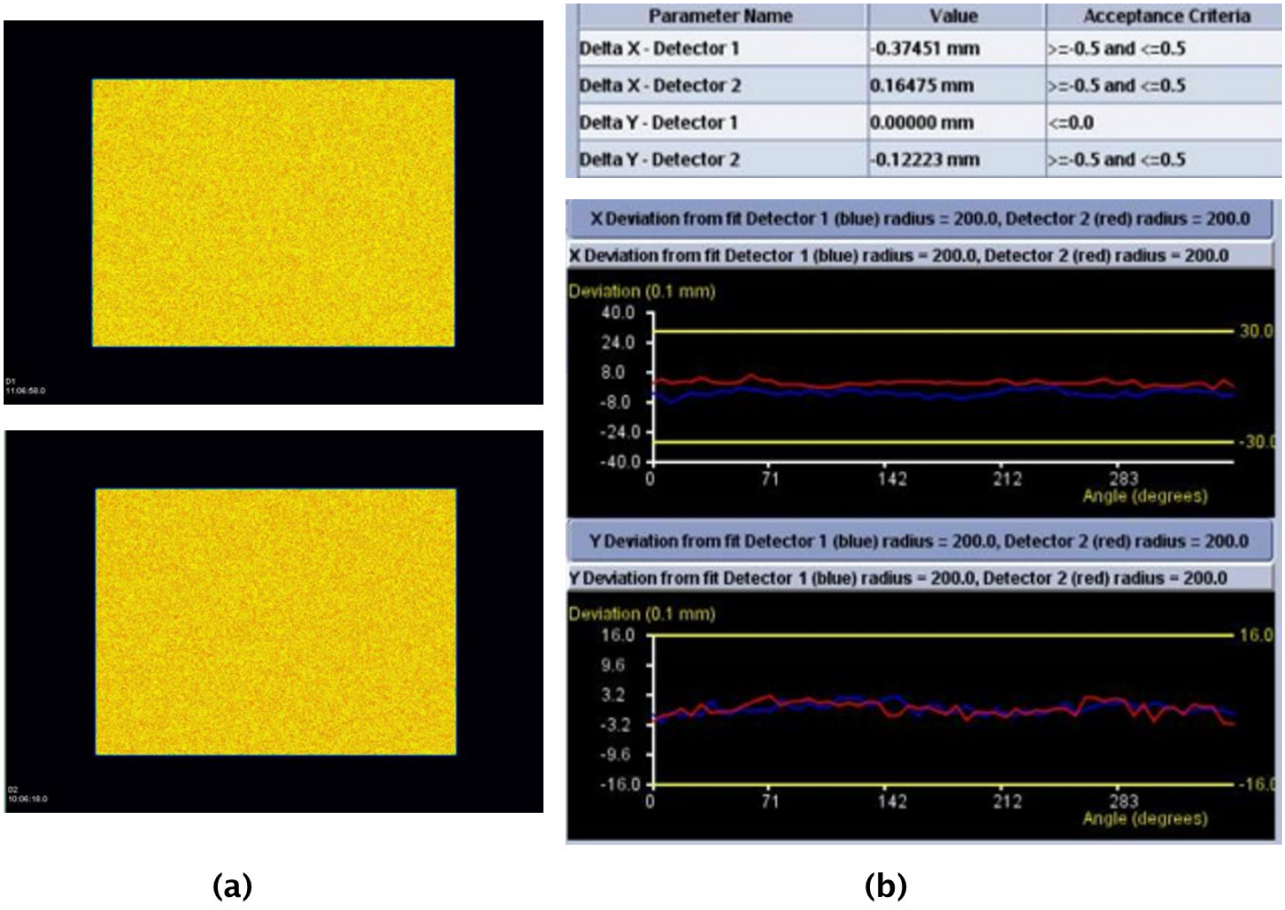

FIG. 46. Acceptable uniformity and COR corrections suggesting that SPECT artefacts are not associated with uniformity or COR.

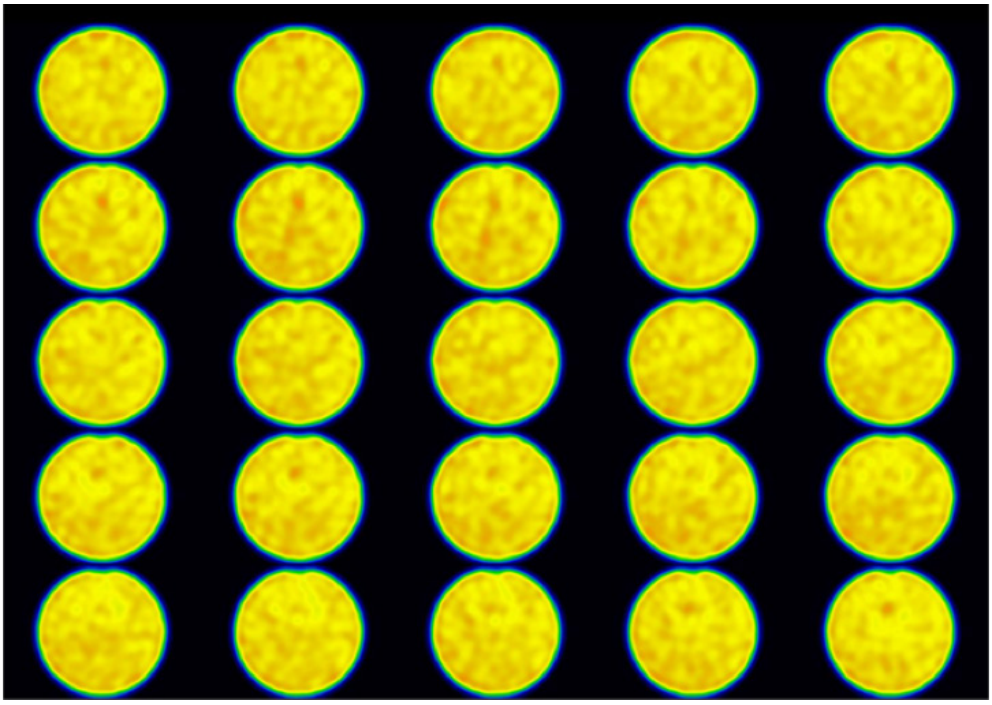

FIG. 47. Reconstructed slices of the uniform cylinder after adjusting COR deviations.

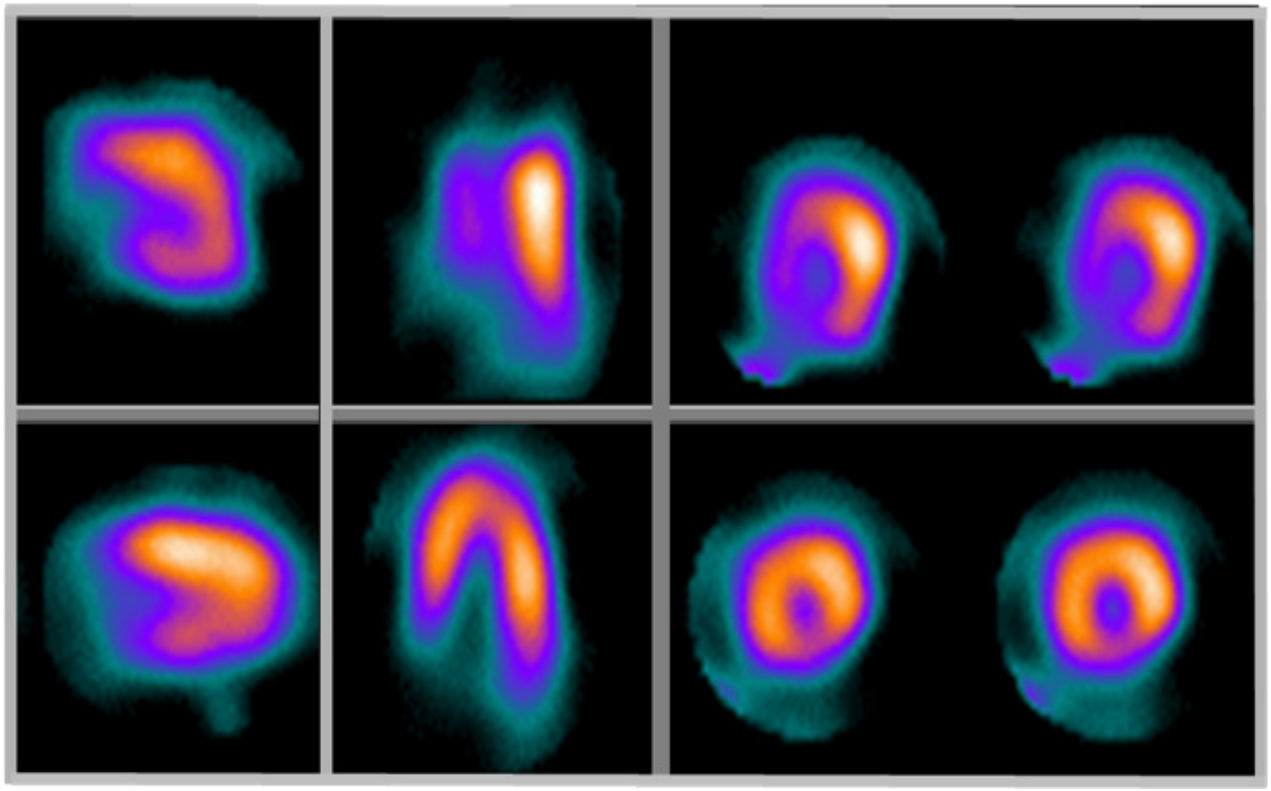

FIG. 48. Myocardial perfusion study reconstruction with tilted head (top row) and with no tilt (bottom row).

Improved COR calibrations can resolve the issue. If this is not successful, the manufacturer's engineer may need to be called to fix the head tilt.

4.1.7. Mismatched sensitivity

In poorly performing systems, there may be a change in detector sensitivity as the scanner rotates around the patient. It is expected that this could have an adverse effect on image quality.

Case

A Jaszczak phantom filled with a ^{99m}Tc solution was imaged while positioned on the imaging couch of a SPECT/CT system (see Fig. 49). Because the couch attenuated the signal from posterior projections as demonstrated in the figure, this acquisition simulates a potential change in sensitivity of a SPECT system with acquisition angle.

Images showing the uniform section of the phantom with different reconstructions, together with a vertical profile through this slice with each reconstruction is shown in Fig. 50. Using FBP and OSEM reconstructions without AC, the profile displays a slight (~15%) reduction in counts between the bottom edge of the phantom compared to the top edge. A small difference can also be seen visually in the rim of these phantom images. This would be expected given that the projection counts were reduced in these posterior stations. No significant difference was seen between the iterative and FBP methods.

Once Chang-AC is applied, this difference is less apparent (but still visible because it does not account for bed attenuation) in both the image and profile data. For reference, the data iteratively reconstructed with OSEM and CTAC, accounting for the bed attenuation, are given as truth for the phantom data. It shows no difference between upper and lower phantom rims, signifying that any difference found in the other reconstructions are real. Interestingly, there is also a bias between CT and Chang-AC, which is likely augmented by the inappropriate choice of a linear attenuation coefficient for this phantom.

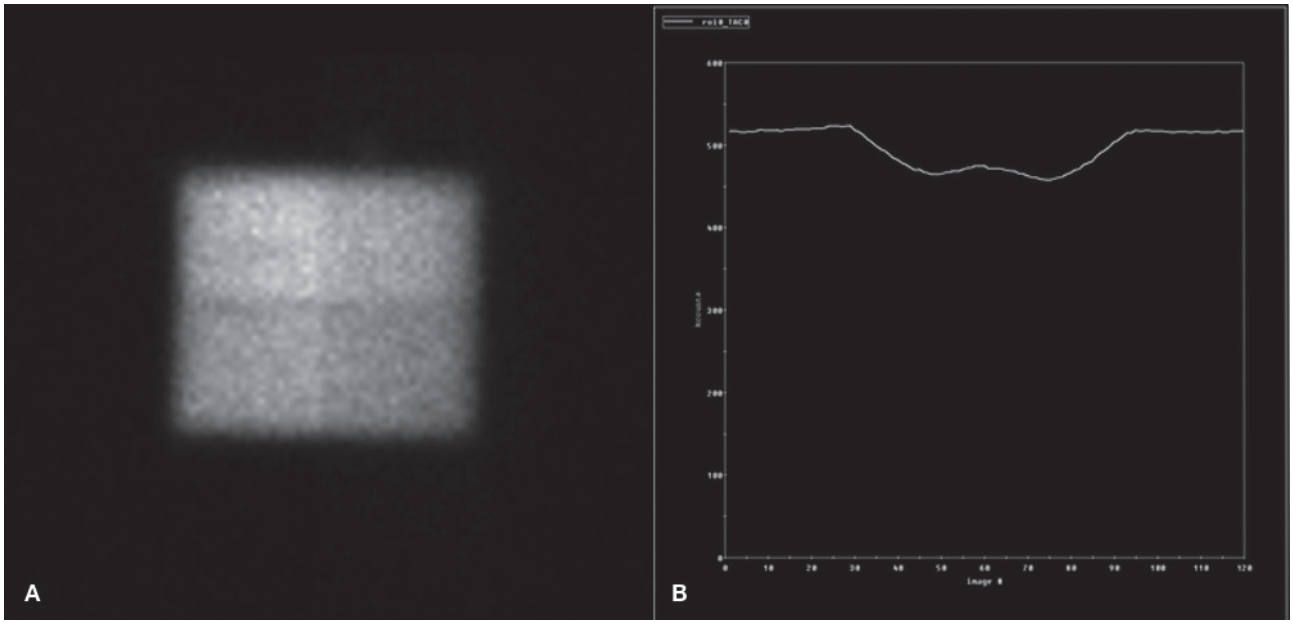

FIG. 49. (A) Projection from an acquisition of a Jaszczak phantom clearly showing a reduction in counts from imaging couch attenuation and (B) the change in total counts acquired for each projection.

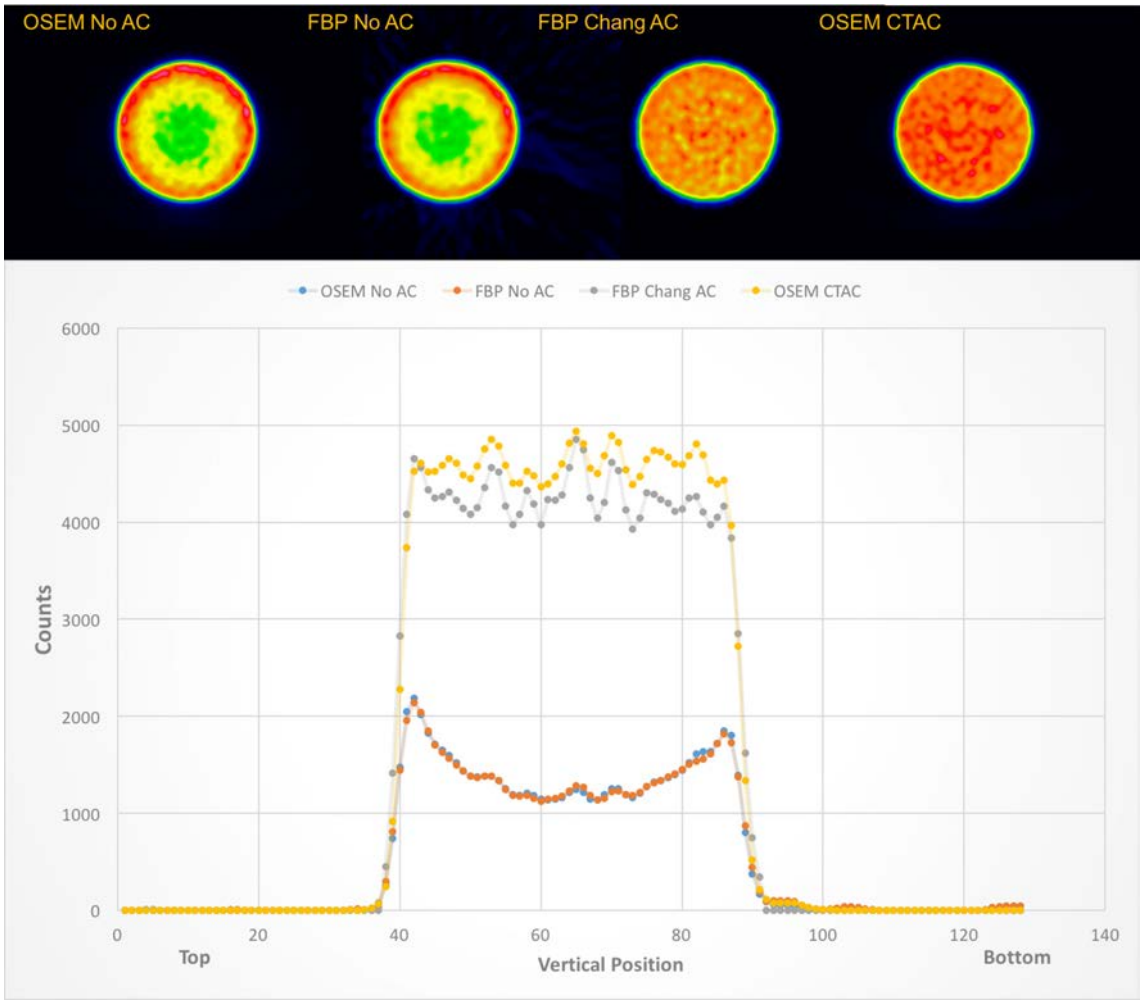

FIG. 50. Uniform slice from the Jaszczak phantom reconstructed with four reconstructions: (left to right) OSEM with no correction for attenuation; FBP with NAC; FBP with Chang-AC; and iterative CTAC. The profiles from each reconstruction are also shown.

Guidance

Although SPECT reconstructions are relatively tolerant of detectors with changing sensitivity at different angles, all efforts should be made to ensure that detector sensitivity is not affected by detector angle, particularly if quantification is to be performed.

4.1.8. Phantom related artefacts

Background

When a phantom is used to test the characteristics and performance of a SPECT system, high activity spots may be present in the reconstructed slices if radioactivity adheres to the phantom edges or its internal structures. Conversely, cold spots may indicate the presence of air bubbles in the mixture. In addition, ring patterns may appear if there are defects in the phantom.

Case

A dual head SPECT system was testing using a Jaszczak phantom with a 128 × 128 acquisition matrix, 800 kcounts per projection, OSEM reconstruction with 8 subsets and 3 iterations, and a Butterworth filter order 5 and 0.7 cut-off frequency. Chang-AC was applied with $\mu = 0.12\ cm^{-1}$. Figure 51 shows reconstructed images across all slices of the phantom, with a ring located at half the radius in the resolution rods section that is not observed in the uniform section of the phantom. This defect was caused by damage to the rods section when it was dropped onto the floor.

Guidance

The condition of a SPECT testing phantom should be carefully checked when used to verify the image quality of a SPECT system, as damage to the phantom can hamper the results of the test.

4.2. ACQUISITION RELATED ARTEFACTS

Several acquisition parameters can be selected during a SPECT image acquisition, including: collimator type, number of projections, time or counts per projection, matrix size, FOV and zoom factor, which define the pixel size, rotation direction, type of orbit, radius of rotation and detector head orientation. All of these parameters should be optimized in order to minimize image artefacts. In general, data are acquired over 360 degrees, with the number of projections chosen depending on the detector FOV and the linear sampling interval. In cardiac studies, however, data are acquired with the detectors positioned in 90 degrees and over a 180 degree arc, from RAO to LPO projections.

4.2.1. Matrix and pixel size

Background

Pixel size is determined by dividing the camera's FOV by the matrix dimension. Images with large pixel size are characterized by lower image resolution. Conversely, smaller pixel size produces images with potentially better resolution at the expense of a higher noise level. Zoom factors can be applied during acquisition to increase the image area occupied by the same region of an object in the unzoomed mode, resulting in a better resolution.

Case A

A ^{99m}Tc filled Jaszczak phantom was imaged with a dual head SPECT system with a low energy high resolution (LEHR) collimator, a radius of rotation of 20 cm, 120 projections with 800 kcounts per projection and acquisitions

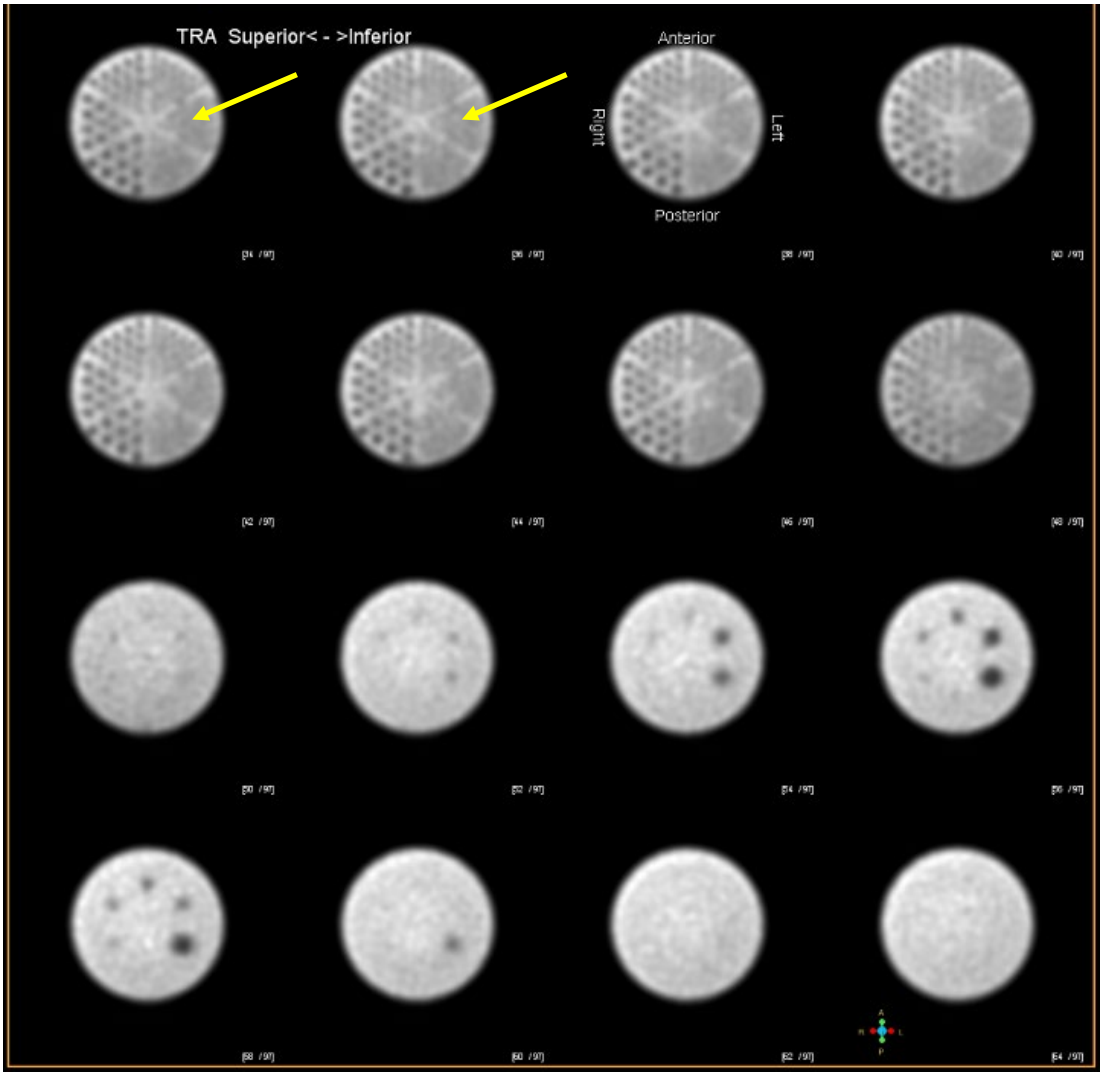

FIG. 51. Ring artefacts in the rods section from damage to the SPECT performance phantom.

matrices equal to 64 × 64, 128 × 128, 256 × 256, and 128 × 128 with a zoom factor of 1.33. Image reconstruction was performed with FBP with a ramp filter (cut-off at 0.5 Nyquist frequency) and Chang-AC ($\mu = 0.12$ cm^{-1}). Representative slices in the cold rods and spheres sections are shown in Fig. 52, where improvement in image resolution with decreasing pixel size, at the expense of noise level, can be verified. More specifically, in the rods the 256 × 256 acquisition and the 128 × 128 acquisition with a zoom factor of 1.33 resulted in four sections resolved, in contrast to three sections in the 128 × 128 unzoomed acquisition.

Guidance

The appropriate choice of matrix size and filter cut-off frequency is essential to preserve the resolution of the imaging system and to keep the details present in the object. When appropriate, zoom factor applied during acquisition can be used to enhance spatial resolution. However, attention should be paid to the number of acquired counts to maintain an acceptable image noise level.

Case B

A striatal phantom was imaged with a radius of rotation of 15 cm, 128 × 128 matrix, 120 projections and a pixel size of 2.1 mm. Figure 53(a) shows a FBP Butterworth (cut-off at 0.45 Nyquist frequency and order 10)

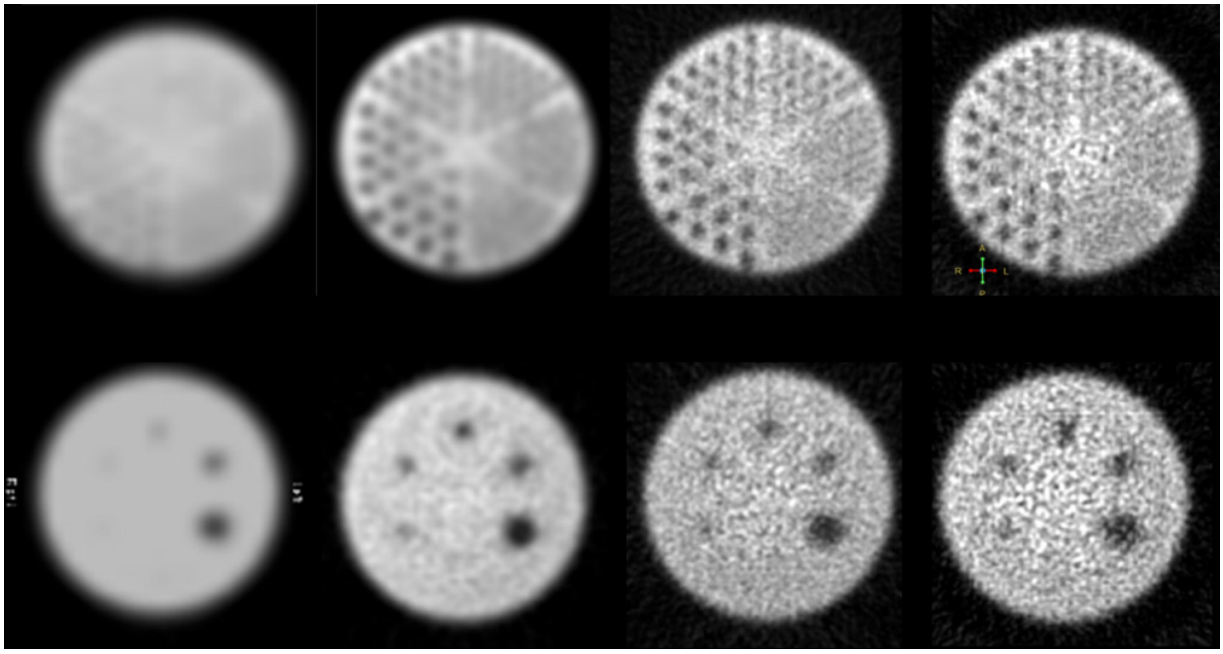

FIG. 52. Cold rods (top row) and cold spheres (bottom row) sections reconstructed slices of a ^{99m}Tc filled Jaszczak phantom, with different matrix size, pixel size and reconstruction filter cut-off fixed at 0.5 Nyquist frequency: (left to right) 64 × 64, 8.84 mm, 0.028 cycles/mm; 128 × 128, 4.42 mm, 0.057 cycles/mm; 256 × 256, 2.21 mm, 0.113 cycles/mm; and 128 × 128 with zoom factor = 1.33, 3.32 mm, 0.075 cycles/mm.

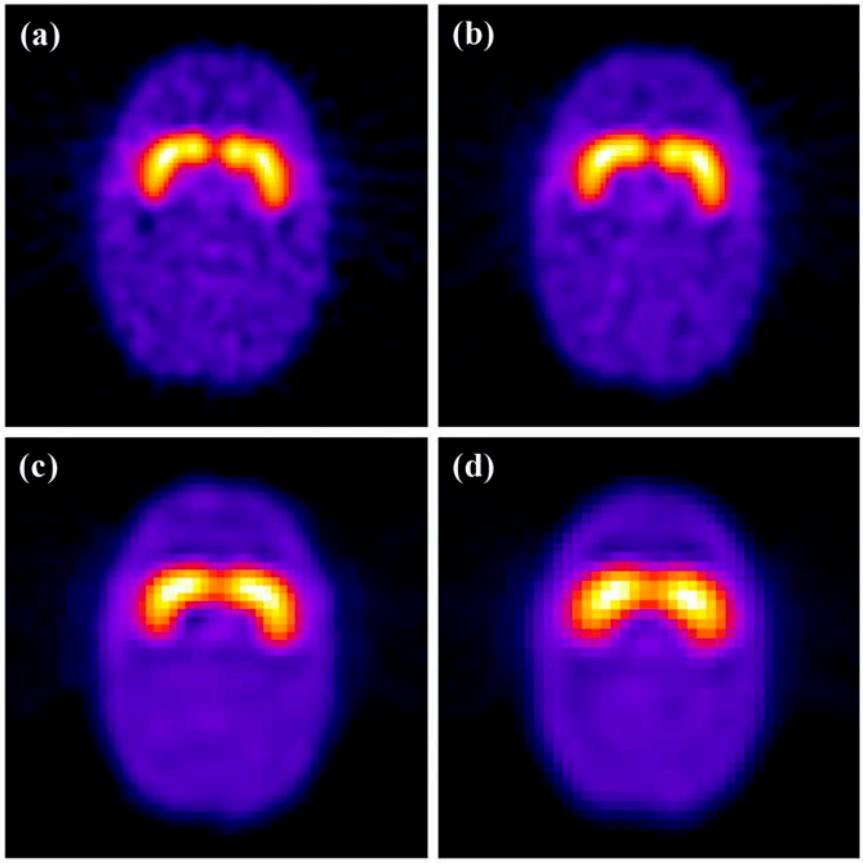

FIG. 53. Striatal phantom imaged with different pixel sizes (spatial frequencies): (a) 2.4 mm (0.094 cycles/mm); (b) 2.7 mm (0.083 cycles/mm); (c) 3.9 mm (0.058 cycles/mm); and (d) 4.8 mm (0.047 cycles/mm).

reconstructed slice, after Chang-AC, where both caudate nuclei and putamina can be distinguished (dimensions 7–15 mm). When the pixel size is enlarged from 2.1 mm to 4.8 mm (see Fig. 53(b–d)), the separation between the four structures decreases until almost forming one sole structure. The images also show that the noise level in the background has smoothed out during this process. Note that the cut-off frequency has been maintained fixed at 0.45 Nyquist frequency. So, in terms of cycles/mm, it increases with decreasing pixel dimension. This also has an influence on spatial resolution, improving it with decreasing pixel size.

Guidance

Proper selection of pixel size according to the object of interest dimensions will preserve the information collected. Note that filter cut-offs defined as a fraction of the Nyquist frequency may need to be altered to keep the same noise and resolution characteristics.

4.2.2. Number of projections

Background

Increasing the number of projections improves image quality while increasing acquisition time for a fixed dwell time per projection. Decreasing the number of projections degrades the image quality, particularly at the edges of the FOV because of the poorer spatial sampling in this area. Although spatial resolution is a function of distance to the collimator, at the centre of the FOV it is not highly dependent on the number of projections.

Case A

SPECT performance tests were obtained with a Jaszczak phantom, using a 128 × 128 matrix and different angular samplings for a circular orbit with a radius of 20 cm. Figures 54–56 show reconstructed slices for 120,

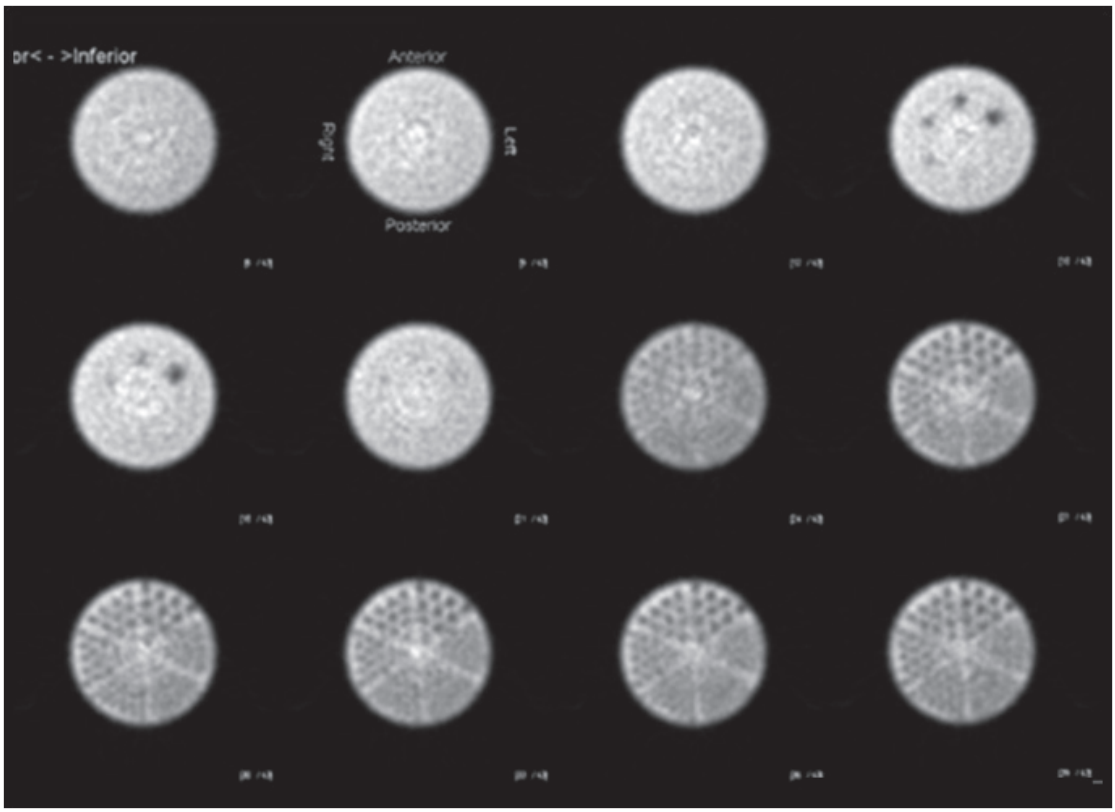

FIG. 54. Matrix size: 128 × 128, 120 projections.

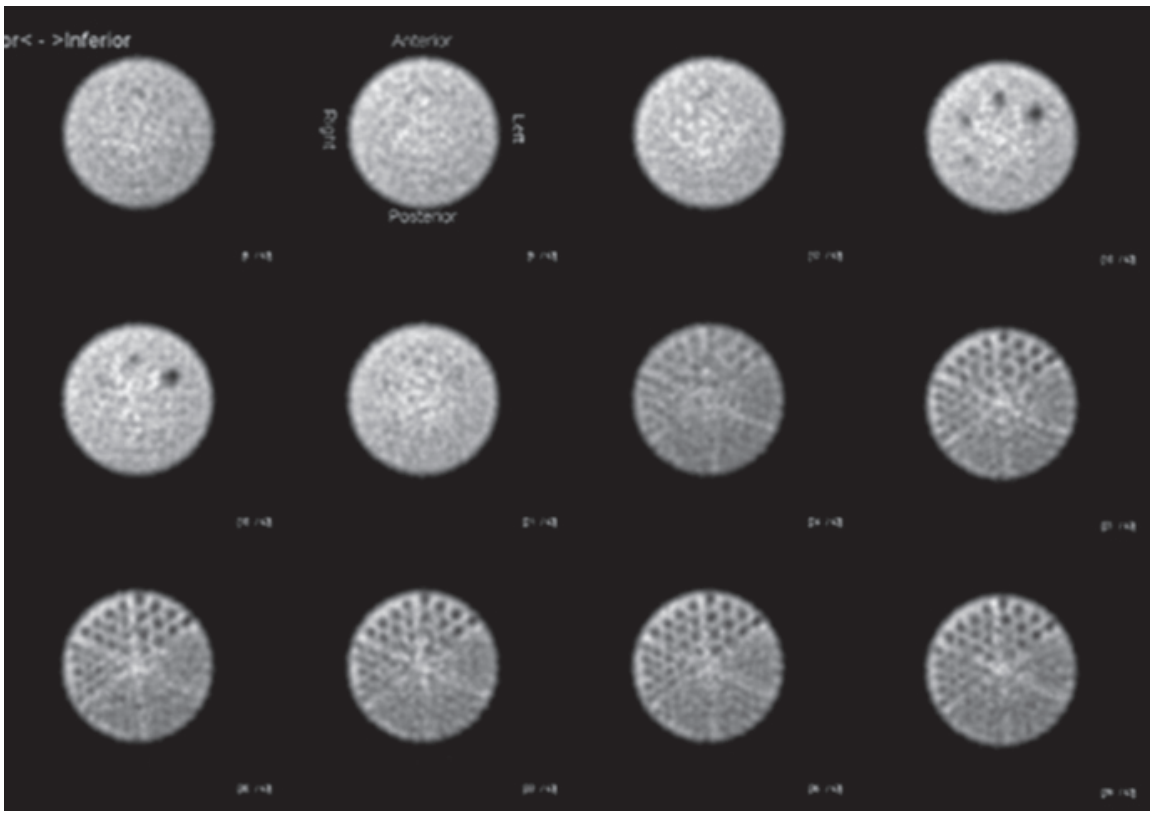

FIG. 55. Matrix size: 128 × 128, 60 projections.

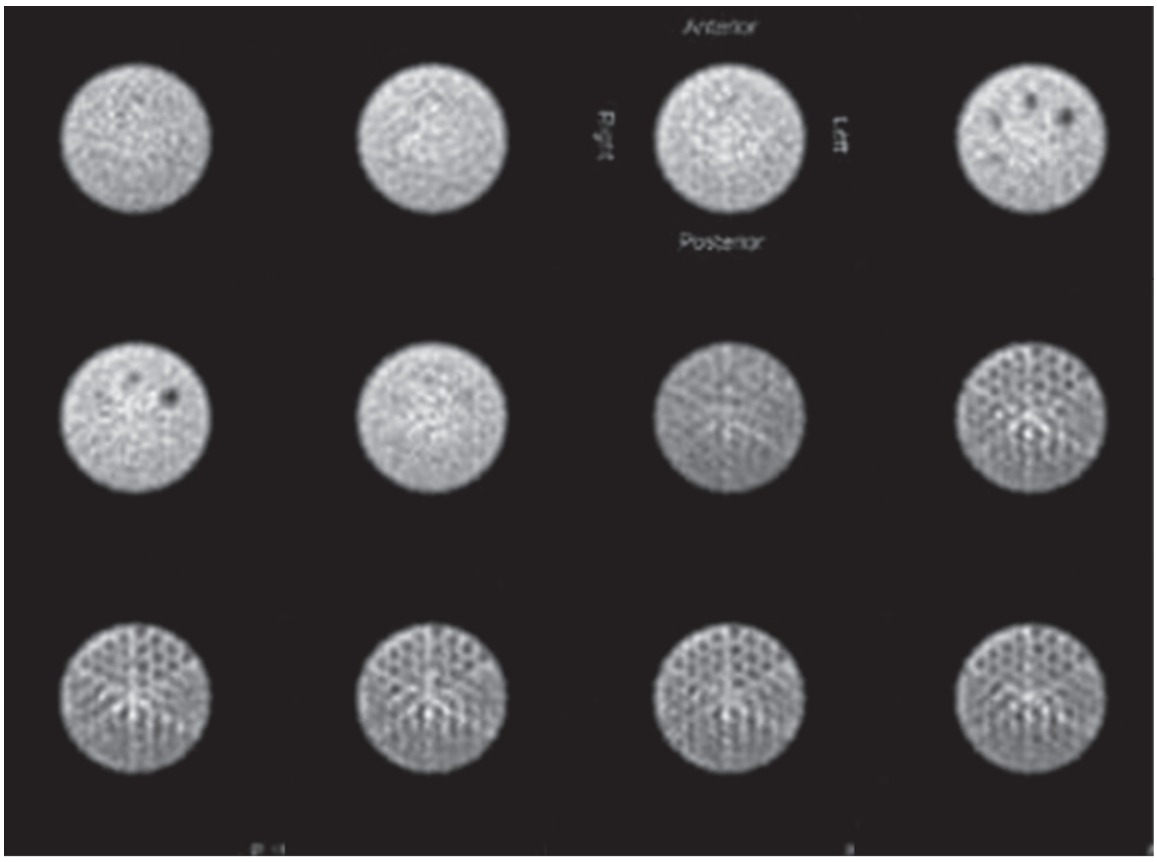

FIG. 56. Matrix size: 128 × 128, 30 projections.

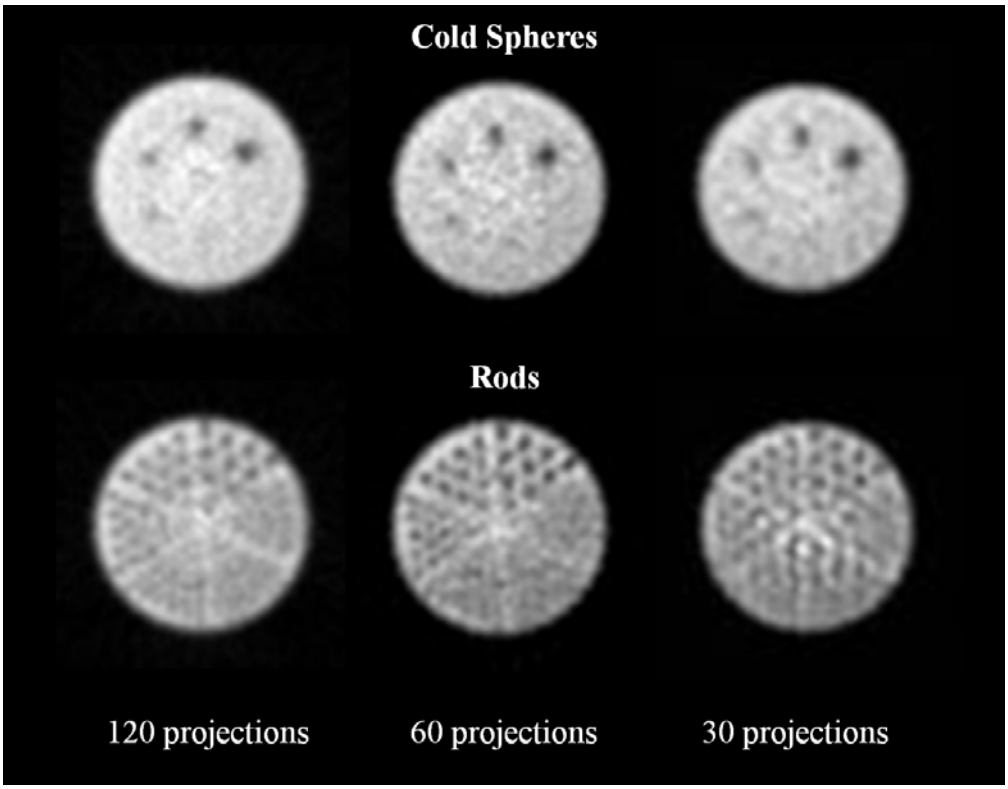

FIG. 57. Slices in the cold spheres and rods sections for all angular samplings, showing differences in resolution.

60 and 30 projections, respectively. Figure 57 illustrates corresponding slices in the cold spheres and the rods sections for all angular samplings. The same number of counts per projection was used in all acquisitions, so total counts in the images differ. The degrading effect in resolution with decreasing number of projections can be seen in both the cold spheres and the rods sections of the phantom. The effect of variable count density on the visualization of a non-uniformity ring artefact is also evident in some slices.

Case B

A striatal phantom was imaged at a radius of rotation of 15 cm, matrix with 3.3 mm pixel size and the same total counts, for angular samplings of 30, 64, 90 and 128 projections. Figure 58 shows the results of Chang-AC FBP reconstruction with a Butterworth filter cut-off frequency set at 0.45 Nyquist frequency and order 10. Streaks are more prominent in the 30 projections slice than in the 64 projections slice and are not present in the higher sampled images.

Guidance

An adequate choice of linear and angular samplings will preserve the imaging system's resolution and produce tomographic images with fewer distortions.

Case C

SPECT performance tests were obtained with a Jaszczak phantom, using a variety of angular and linear samplings (matrix sizes) for a circular orbit with a radius of 20 cm. The same total counts were acquired in all studies. Figure 59 shows reconstructed slices for cold spheres and rods sections for 64 × 64, 128 × 128 and 256 × 256 matrix sizes with 120 projections. In addition, 30 and 60 projections data were also acquired for the 128 × 128 matrix.

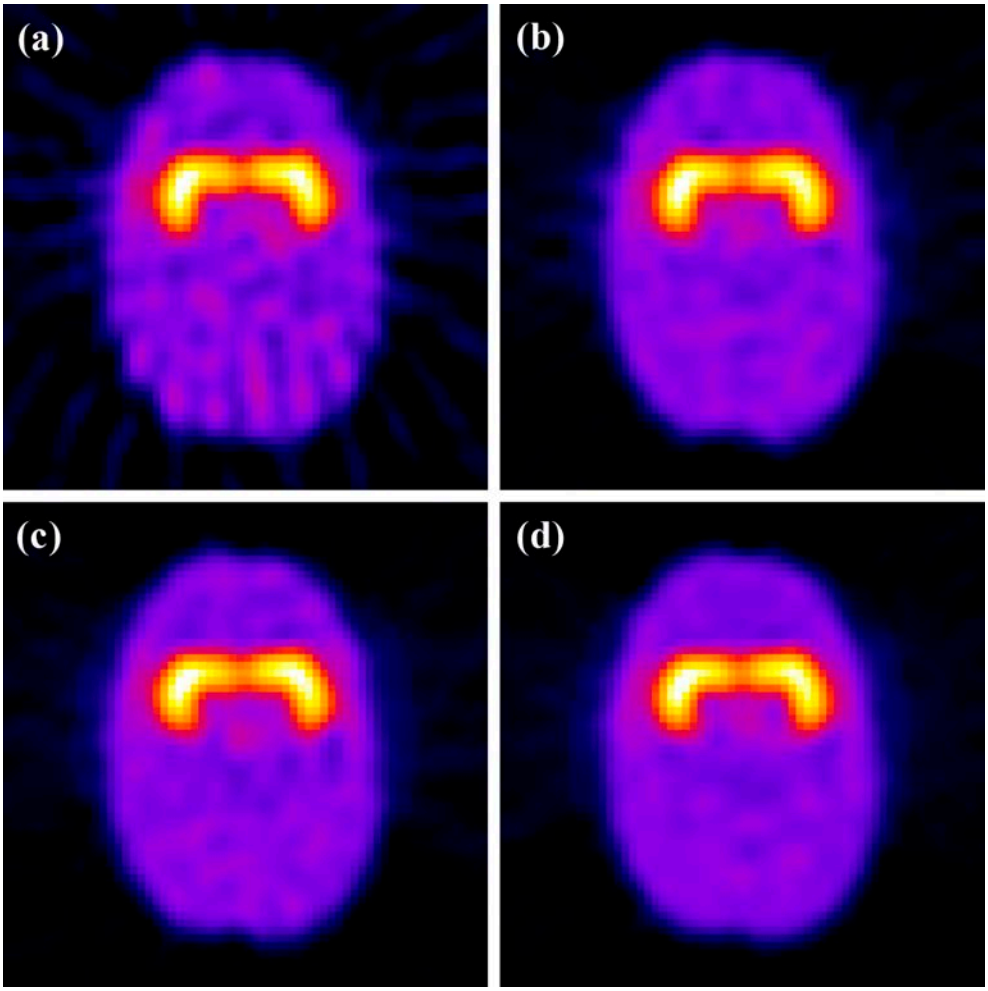

FIG. 58. Striatal phantom imaged using the same number of total counts but with different angular sampling: (a) 30, (b) 64, (c) 90 and (d) 128 projections. Butterworth filter cut-off frequency fixed at 0.45 Nyquist frequency and order 10.

The degrading effect in resolution with decreasing number of projections can be seen more clearly in the rods section slices. It can also be noticed that better image resolution and less distortion are achieved when the number of projections is close to the matrix size, as in the case of 128 × 128 matrix with 120 projections. Furthermore, there is no advantage in using a larger matrix, 256 × 256, due to the spatial resolution of the system and the higher noise level.

Guidance

An adequate choice of linear and angular samplings will preserve the imaging system's resolution and produce tomographic images with fewer distortions. Attention should be paid to the number of counts to be collected, as the image noise level is affected by the matrix size.

Case D

A Jaszczak phantom was placed under a dedicated cardiac study camera, with the two heads positioned at 90 degrees, and projections were obtained with 32 × 32 × 32, 64 × 64 × 64 and 128 × 128 × 64 matrix size and projections. FBP reconstruction with Chang-AC was performed, and the results for a slice in the rods section are shown in Fig. 60. Geometric distortions are seen at the border region of the half of the phantom that was imaged, while strong blurring is present at the other half that was not directly imaged.

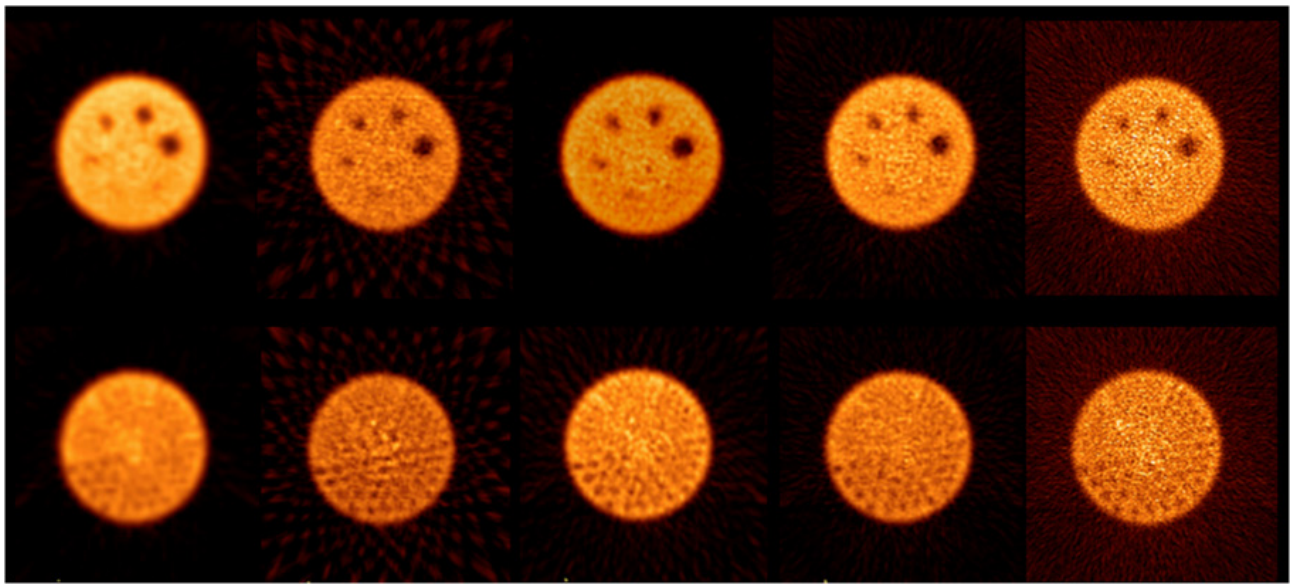

FIG. 59. Jaszczak phantom acquired with same total counts: (left to right) 64 ×64 × 120, 128 × 128 × 30, 128 × 128 × 60, 128 × 128 × 120, 256 × 256 × 120.

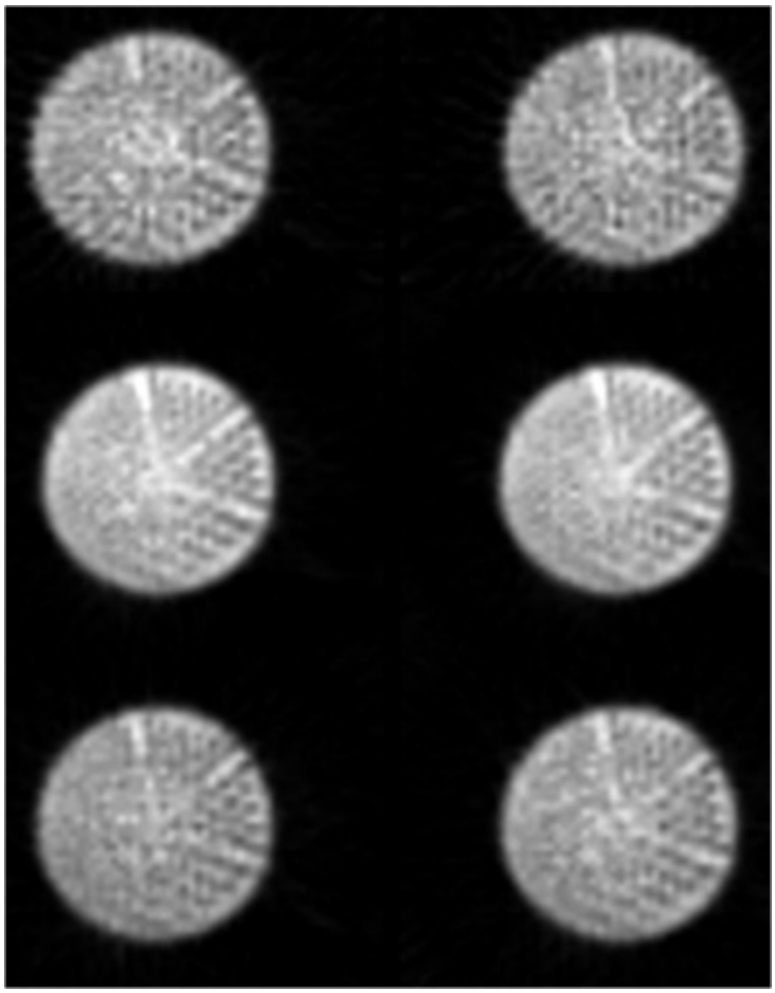

FIG. 60. Rods section slices obtained with a dedicated cardiac SPECT scanner (90 degree detector configuration, using a 180 degree arc acquisition from LPO to RAO) reconstructed with FBP and Chang-AC: (top row) 32 × 32, 32 projections; (middle row) 64 × 64, 64 projections; (bottom row) 128 × 128, 64 projections.

Guidance

In cardiac studies, incomplete 180 degree angular sampling is adopted despite the fact that it introduces geometrical distortion, as the contrast is improved when compared to 360 degree acquisition and the study time is shortened. It should be noted that the patient can be positioned in either supine or prone positions (see Section 4.4.3).

4.2.3. Counts per projection

Background

As with planar nuclear medicine imaging, reducing counts per projection will result in increased noise, while longer scan times can reduce noise and improve image quality.

Case A

A ^{99m}Tc filled Jaszczak phantom was imaged using 128 projections, a 128 × 128 image matrix and a range of 100–1200 kcounts per projection. Data were reconstructed using FBP with the same reconstruction filter and Chang-AC (see Fig. 61). There is a clear difference between 100 and 1200 kcounts per projection, although in this instance, the improvement in image resolution and contrast between 800 and 1200 kcounts per projection is limited.

Case B

Another ^{99m}Tc filled phantom shows no clear ring artefacts at low (100) kcounts per projection, but does show a non-uniformity artefact at high (1200) kcounts per projection (see Fig. 62). The two sets of data were acquired one after the other on the same system.

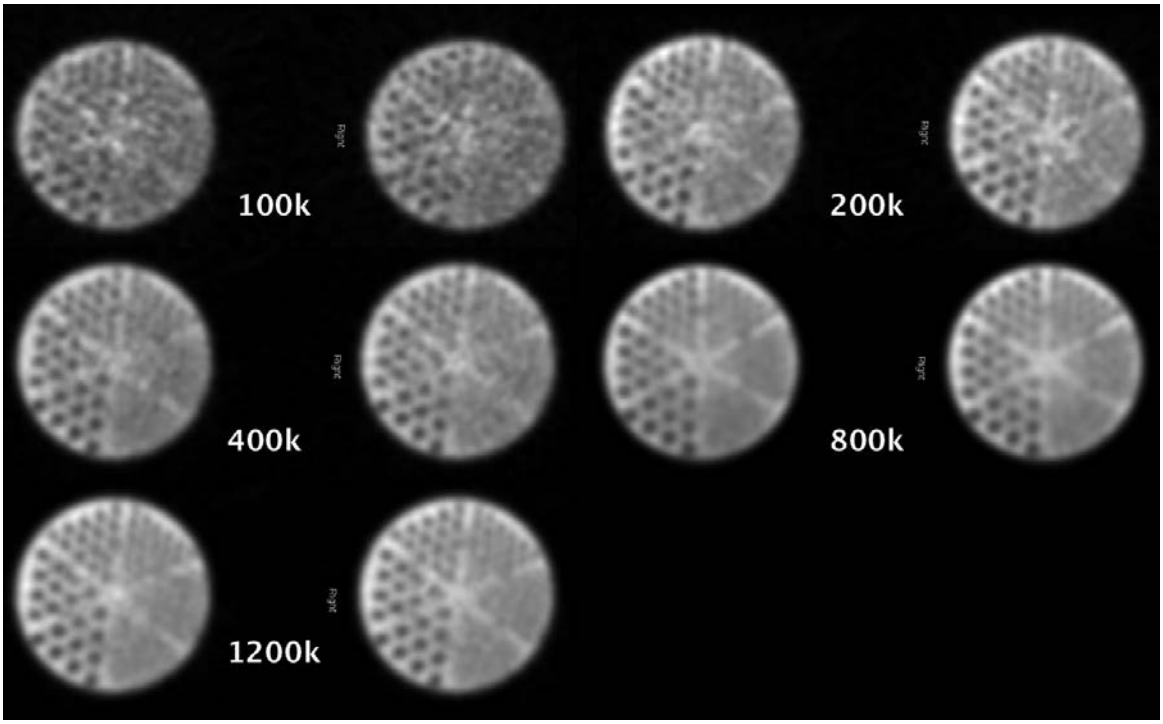

FIG. 61. Transaxial slices through the rods section of a Jaszczak phantom at different numbers of counts per projections.

Case C

A patient was referred for a ^{123}I-ioflupane scan to distinguish between idiopathic Parkinson's disease and essential tremor. Three hours following the injection of 185 MBq of ^{123}I-ioflupane, the patient was imaged for 40 s per projection using a 3 mm voxel size and reconstructed using OSEM iterative reconstruction. Using Poisson resampling techniques, it is possible to derive images of different counts levels. In Fig. 63, images with between 4 and 40 counts per second are shown. Once more, there is a clear difference between the lowest (4 s) and highest (40 s) times per projection; although in this example, there is no clear benefit of imaging beyond 24 s per projection.

Guidance

The number of acquired counts per projection should be chosen to match acceptable noise levels for the specific application. For quality control purposes, using a Jaszczak phantom with very low levels of noise is preferred, particularly to identify underlying problems leading to artefacts, whereas for clinical imaging, a higher level of noise may be acceptable. Nevertheless, whichever application is used, there comes a point where increasing the acquired counts per projection brings very little extra benefit to the imaging task.

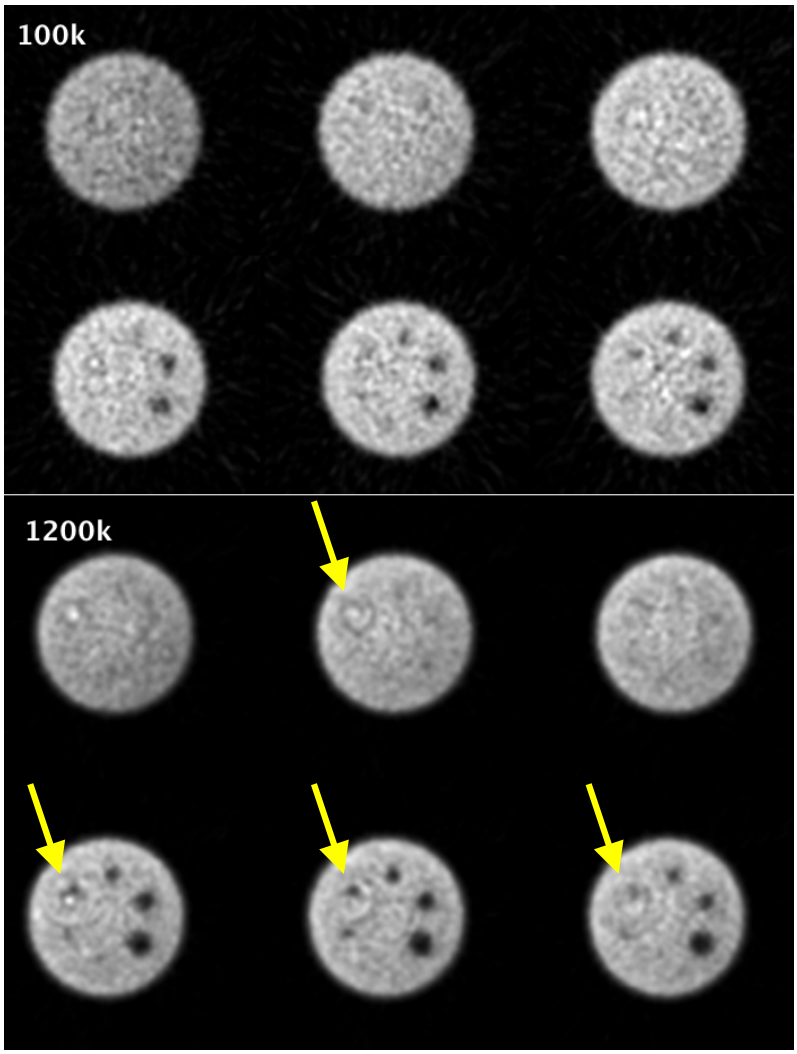

FIG. 62. Ring artefact caused by detector non-uniformity which is visible at high (1200) kcounts per projection but barely visible at low (100) kcounts per projection.

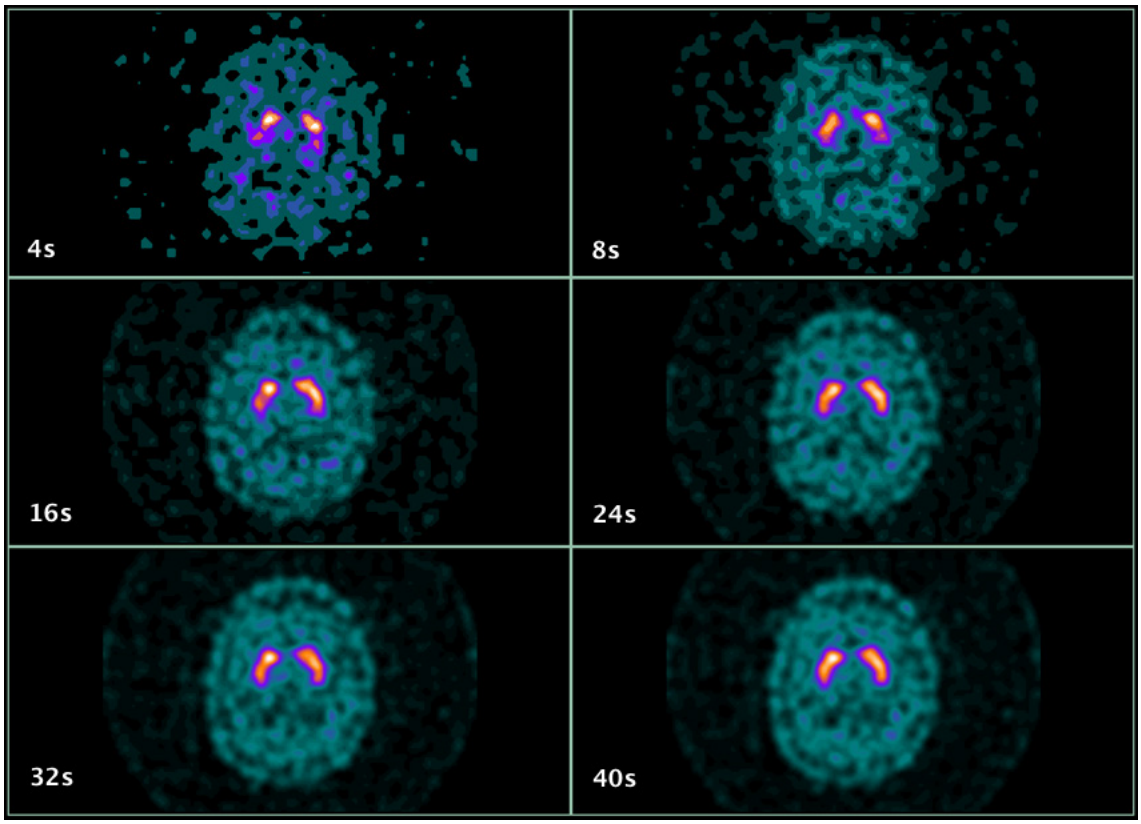

FIG. 63. ^{123}I-ioflupane imaging with varying levels of acquired counts per projection.

4.2.4. Acquisition arc

Background

In general, tomographic slices are reconstructions of projections acquired over 360 degrees around the patient. However, for organs localized mainly on one side of the body, such as the heart, partial arc acquisition is performed in order to improve the spatial resolution of the image by excluding projections that are further away from the organ. Acquisitions typically use the two detectors positioned in a fixed 90 degree configuration moving from the RAO to LPO position.

Case A

A Jaszczak phantom was placed at the centre of a dedicated cardiac SPECT system with a fixed 90 degree head configuration, and both 180 degree and complete 360 degree arc acquisitions were obtained. Figure 64 shows the reconstructed slices from the half circle acquisition (top row) and those from the complete circle (bottom row). The top row clearly shows the distortions from the incomplete data in the rods section of the phantom, as well as improved contrast in proximal regions due to improved resolution when compared to the results in the bottom row.

Guidance

With the exception of imaging organs localized mainly on one side of the body, acquiring SPECT data over a 360 degree arc should be performed in order to minimize image distortion and to improve image resolution and contrast.

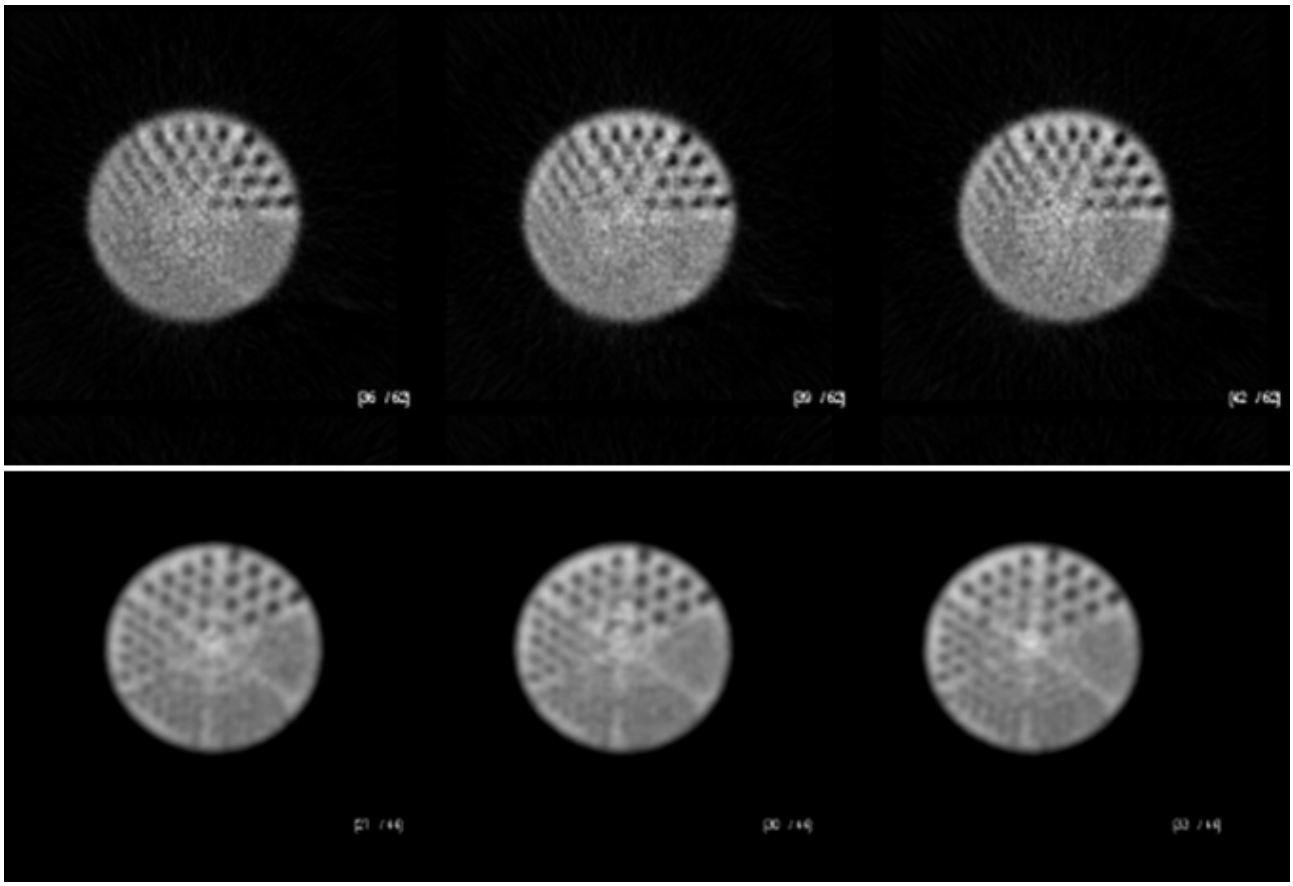

FIG. 64. Reconstructed slices of the rod section of a Jaszczak phantom from an LPO to RAO 180 degree acquisition (top row) and a 360 degree acquisition (bottom row).

4.2.5. Collimator

Background

The ability of an imaging system to distinguish two identical point sources is described by its spatial resolution. The collimator is one of the most important components that defines the spatial resolution of a gamma camera. The choice of collimator depends on the radionuclide, and the compromise of sensitivity and spatial resolution required for the underlying application.

Case

A striatal phantom was imaged with ^{99m}Tc, using a pixel size of 3.3 mm, with 120 projections and a radius of rotation of 15 cm. In this instance, the time of acquisition was kept constant. Data were reconstructed with FBP using a Butterworth filter with cut-off at 0.45 Nyquist frequency and order 10, and Chang-AC. Figure 65 shows the results when imaging was done using collimators of the type: (a) LEUHR; (b) LEHR; and (c) medium energy general purpose (MEGP).

The loss of spatial resolution varies with the type of collimator used. An LEUHR collimator may be used for optimal spatial resolution but with the penalty of reduced system sensitivity and potential image artefacts due to reduced count density. MEGP collimators typically have wider holes to offset losses in sensitivity caused by increased septal thickness and therefore have poorer spatial resolution than low energy collimators.

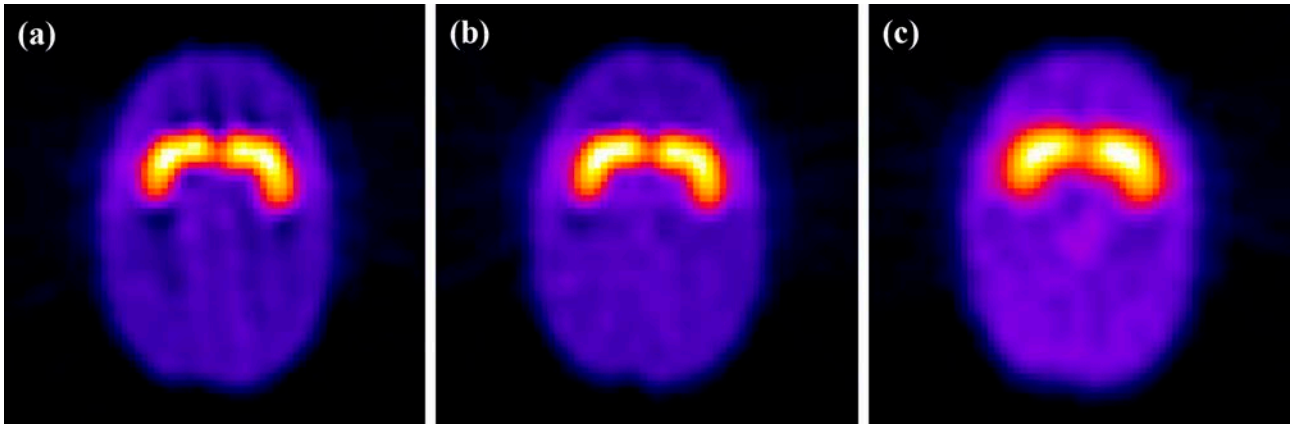

FIG. 65. Striatal phantom imaged with different collimator types (a) LEUHR, (b) LEHR and (c) MEGP.

Guidance

The appropriate collimator should be used for the application and radionuclide being used. In modern systems, resolution modelling in the reconstruction could be used to compensate for resolution losses on more sensitive collimators (poorer spatial resolution). MEGP collimators are (as the name indicates) intended for nuclides with an energy higher than ^{99m}Tc (e.g. ^{111}In, ^{177}Lu and to some extent ^{123}I).

4.2.6. Radius of rotation

Background

Image resolution in SPECT degrades with distance from the detector head. Increasing the radius of rotation of the camera heads will therefore cause a loss of spatial resolution.

Case

A striatal phantom was imaged with ^{99m}Tc, using an LEHR collimator and pixel size of 3.3 mm, with 120 projections. Five radii of rotation were used, with the resulting images shown in Fig. 66. In addition, the FWHM of a line source placed centrally in the FOV of the SPECT scanner and imaged with increasing radius of rotation is plotted in Fig. 67. The phantom images and plot clearly show the non-linear resolution losses with increasing radius of rotation.

Guidance

All efforts should be taken to minimize the radius of rotation used for SPECT imaging. The use of non-circular orbits is often advantageous, except when imaging the brain on account of its shape and safety considerations.

4.2.7. Orbit effects

Background

In the human body, the length of the anterior–posterior axis is usually smaller than the left–right one. Consequently, circular orbits will collect anterior and posterior projections further away from the patient than the lateral views. As illustrated in Section 4.2.6, the spatial resolution of a gamma camera degrades with the distance of the object to the collimator. Therefore, to improve spatial resolution, non-circular orbits, such as elliptical or body contoured, are preferable.

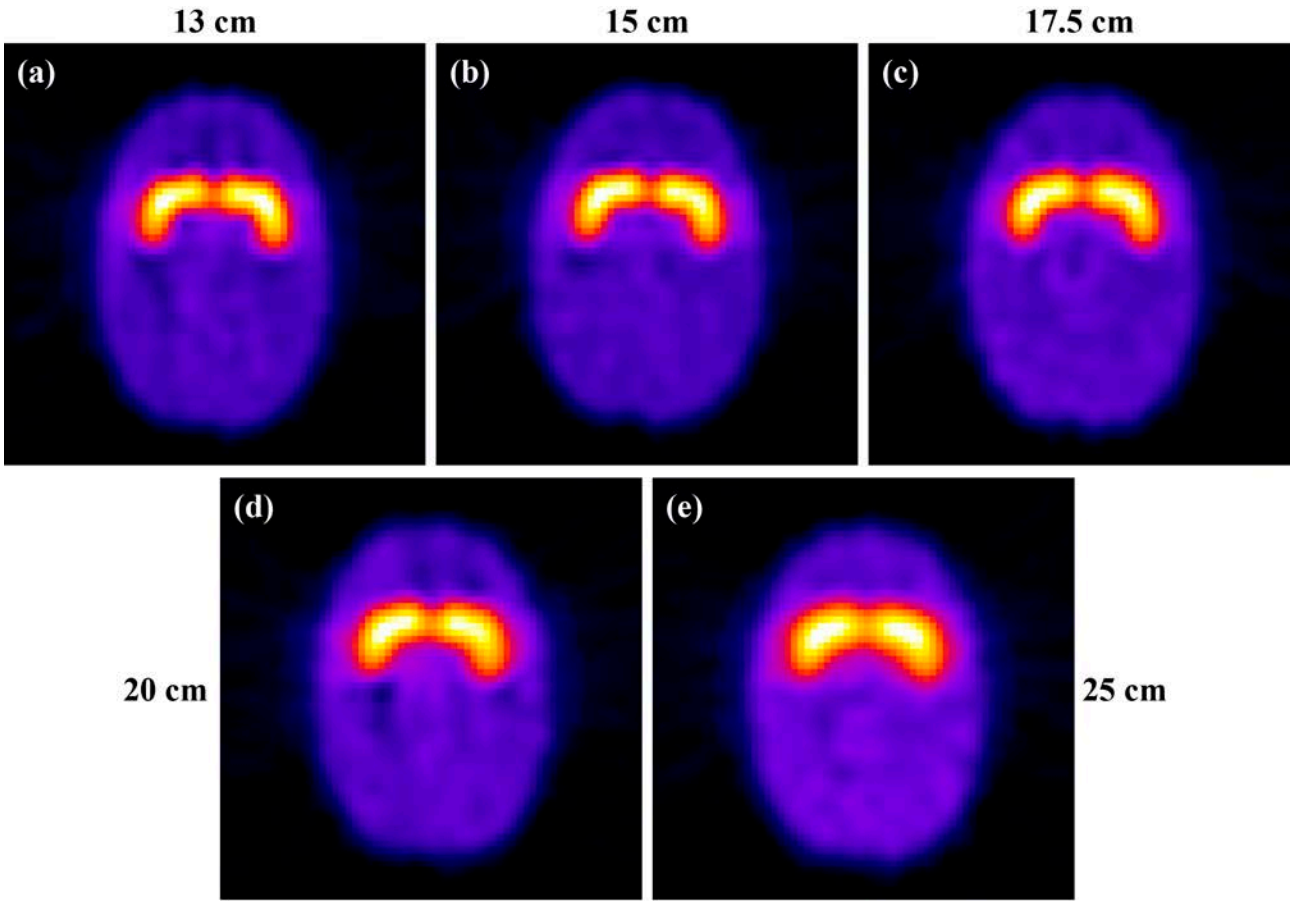

FIG. 66. Striatal phantom images with increasing radii of rotation showing degrading image resolution with increasing radius of rotation.

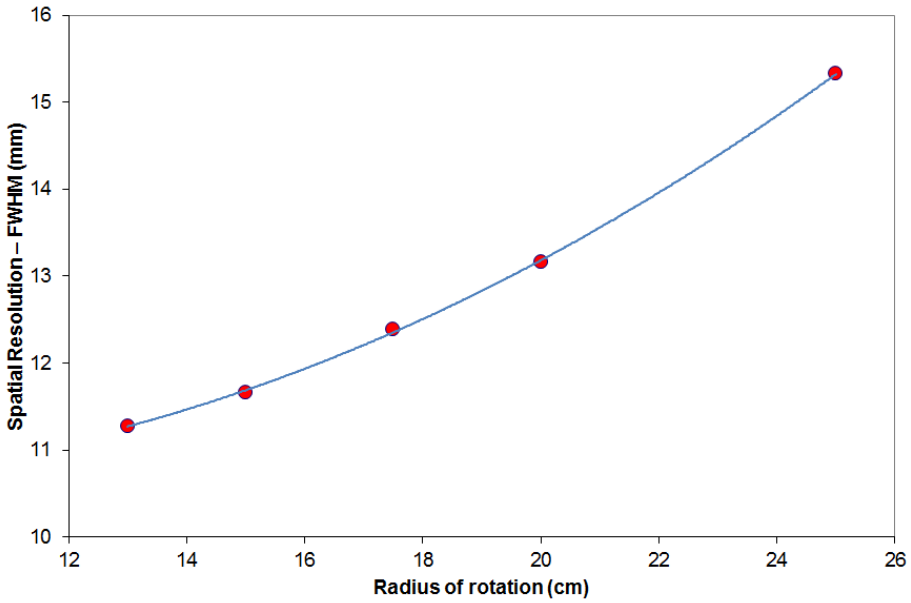

FIG. 67. Variation of spatial resolution with radius of rotation for a parallel hole collimator.

Case

A heart and lung torso phantom was used, with an anterior–posterior length of 20 cm and a left–right length of 29.6 cm. In order to verify the effects of the different acquisition orbits with a dual head SPECT camera, the heart was replaced by a set of two thick (2.5 cm in diameter) and two thin (1.5 cm in diameter) rods, mounted at different depths (3.0 cm and 11.4 cm from the anterior wall of the phantom), and two saline bags were attached on each side, simulating patient arms (see Fig. 68). A solution of 1.26 GBq of ^{99m}Tc diluted in 4 L of water filled the phantom cavity. Projections were collected with LEHR collimators, 256 × 256 matrix and 120 angular samplings for both circular (radius of 26.5 cm) and body contour (anterior–posterior radius of 21.9 cm and lateral radius of 26.5 cm) orbits, with a total of 117.7 Mcounts and 115.3 Mcounts, respectively, and a zoom factor of 1.33.

Figure 69 shows the SPECT transverse and sagittal slices of the phantom inserts, depicting the rods at different depths. Reconstruction was performed without AC, using OSEM (8 subsets and 5 iterations, Butterworth filter with cut-off frequency at 0.7 Nyquist frequency and order 5) and FBP (ramp filter with cut-off frequency at 0.6 Nyquist frequency). Figure 70 shows the transverse slices for both reconstructions. Some loss of spatial resolution and contrast in the circular orbit acquisition is visible for both reconstructions. Note also that OSEM preserves the geometry better than FBP, as well as dealing with the noise level in the image.

Four transverse slices were summed and count profiles were drawn for double lines passing through the centres of both anterior and posterior rods (see Fig. 71). Body contour orbit data provided a more consistent result, especially for the deeper structures, because the cameras were closer to the phantom at the anterior and posterior projections, when the radius of rotation was 21.9 cm, than in the case of circular orbit, where this distance was 26.5 cm, equal to the lateral radius in body contour orbit.

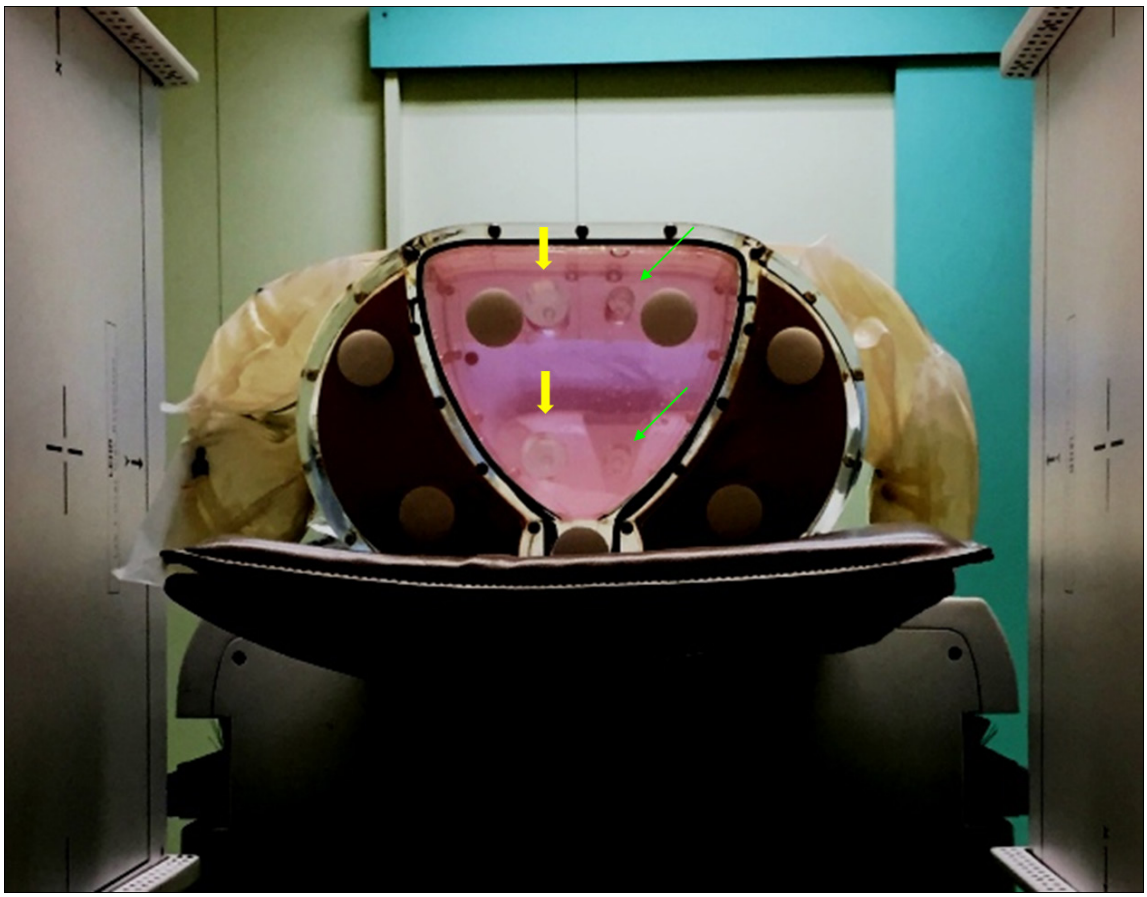

FIG. 68. Torso phantom with rod inserts on the imaging table with two saline bags attached to each side simulating patient arms. Thick yellow arrows indicate the thick rods, and thin green arrows indicate the thin rods.

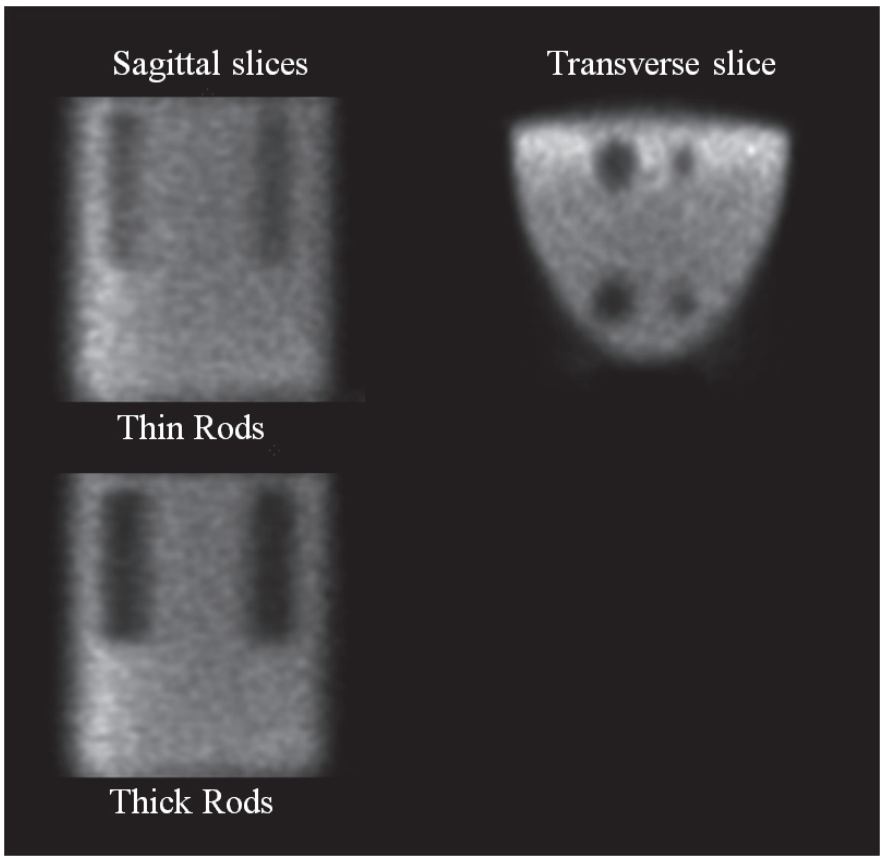

FIG. 69. SPECT transverse and sagittal slices depicting the thin and thick rod inserts in the thoracic phantom.

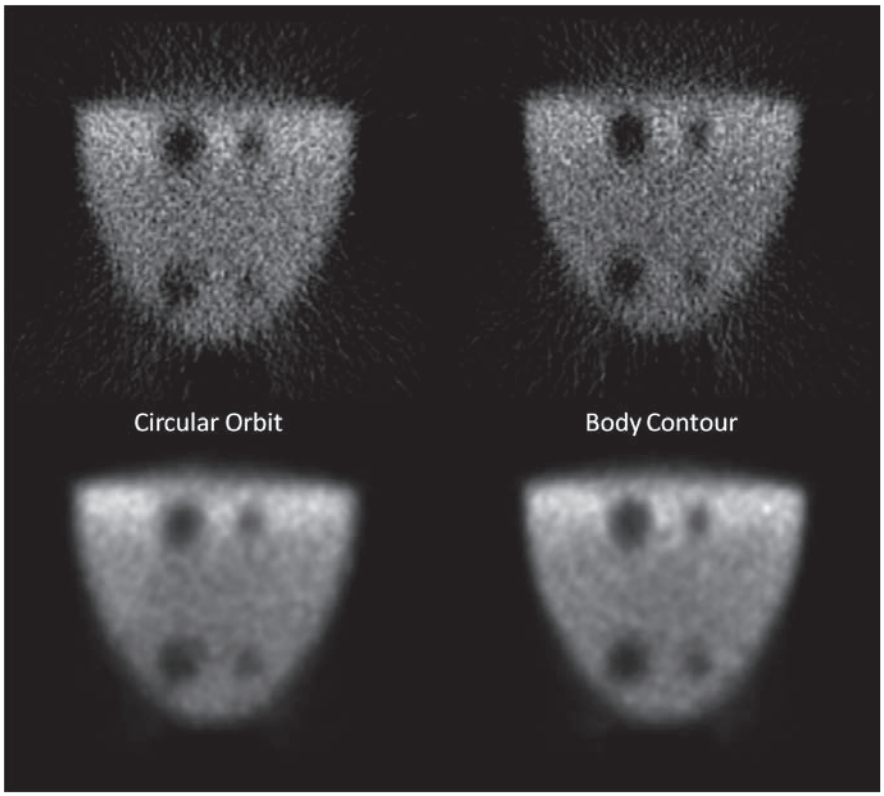

FIG. 70. FBP (top row) and OSEM (bottom row) reconstructed cold rod inserts transverse slices for both body contour and circular orbits. Some loss of resolution and contrast is more noticeable in the FBP reconstructed images.

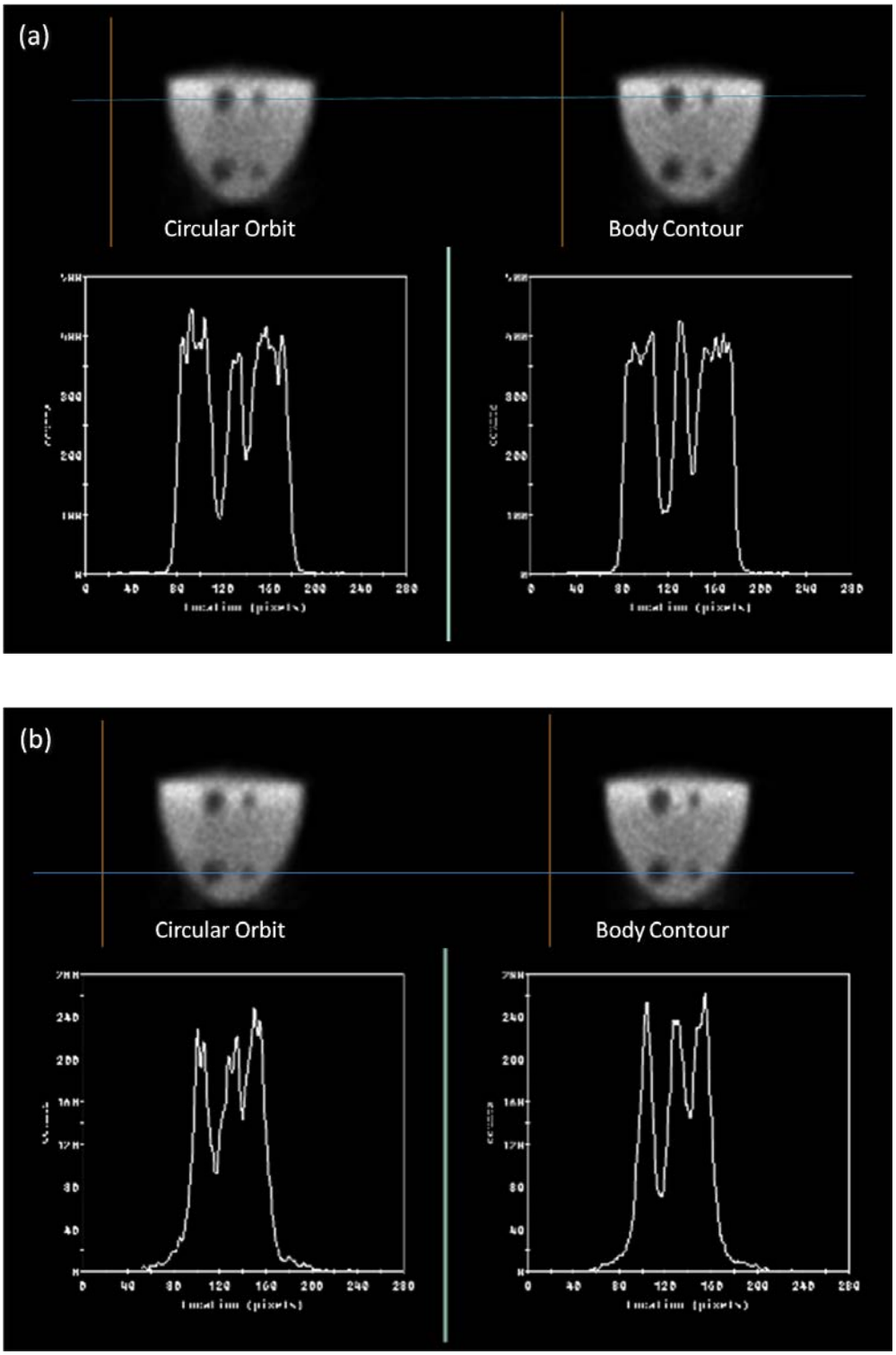

FIG. 71. OSEM reconstructed transverse slices for both circular (left) and body contour (right) orbits. Profiles were drawn for a double line across the centres of the (a) anterior and (b) posterior rods.

Guidance

On account of the geometry of the human body and whenever feasible, body contour (or elliptical) orbits should be used for tomographic acquisition to keep the camera as close as possible to the body, minimizing any loss of spatial resolution and contrast.

4.3. RECONSTRUCTION ARTEFACTS

The formation of a three dimensional dataset from two dimensional projection data is achieved by reconstruction, either by FBP or by iterative reconstruction methods such as OSEM (see Section 2.1.3). FBP is a direct, fast and linear method, but often results in high noise levels, including streaking artefacts. Iterative methods offer a better control of noise levels, but are non-linear and their results depend on the number of iterations and subsets (for OSEM) used and the corrections included (e.g. resolution recovery). Quantitative results of reconstructions may depend on the choice of method, filters and parameters for AC (e.g. by the Chang method).

4.3.1. Filtered back projection streak artefacts

Background

In FBP, data are back projected into image space to form the image. While this is a fast and direct method to derive the tomographic data, it can cause streak artefacts — particularly where there are areas of high uptake in a low uptake background.

Case A

This patient was referred to assess orthopaedic pain around the knee. SPECT/CT was performed following the injection of ^{99m}Tc-HDP (see Fig. 72). Although the salient features of the FBP reconstructed data within the knee are the same as those reconstructed using OSEM, the FBP data have clear streak artefacts coming from the back projection process which are not visible with OSEM. The reconstruction filter and scaling of both images are the same.

Case B

Myocardial perfusion SPECT and ^{123}I-ioflupane SPECT images reconstructed using FBP are shown in Fig. 73. In the two images, streak artefacts are still clearly visible within and outside the patient boundary, but they do not adversely affect the diagnostic quality of the data.

Guidance

FBP reconstructions create streak artefacts in the reconstructed data. Although this form of reconstruction does not necessarily produce image data of inferior diagnostic quality, the streak artefacts mean it is not preferred for imaging small areas of high uptake in a low uptake background.

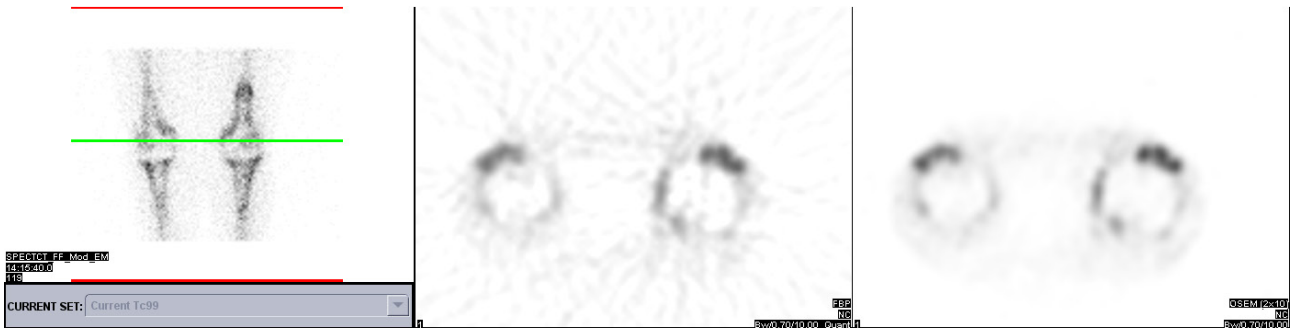

FIG. 72. Anterior projection (left) showing the position of a transaxial slice reconstructed using FBP (middle) and OSEM iterative reconstruction (right).

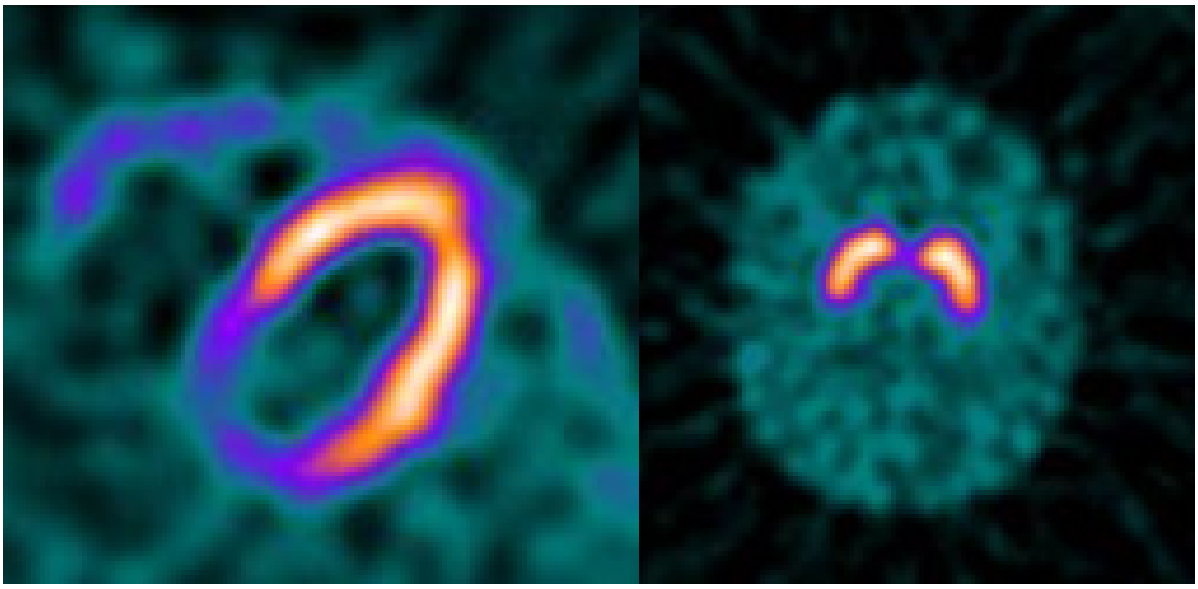

FIG. 73. Myocardial perfusion SPECT (left) and ^{123}I-ioflupane SPECT (right) reconstructed using FBP.

4.3.2. Filters

Background

Image resolution in SPECT changes with the type of filter used and its corresponding parameters. Increasing image smoothing reduces image noise but at the expense of degrading image resolution.

Case

A striatal phantom was imaged with ^{99m}Tc, using an LEHR collimator and pixel size of 3.3 mm, with 120 projections. Data were reconstructed with FBP using a Butterworth filter order 10 and with increasing cut-off from 0.30 to 0.60 Nyquist frequency (decreasing smoothing) with a 0.15 increment. In all cases, Chang-AC was applied. The results are shown in Fig. 74, which clearly shows that as cut-off frequency increases (decreasing image smoothing), image resolution improves but at the expense of increasing image noise.

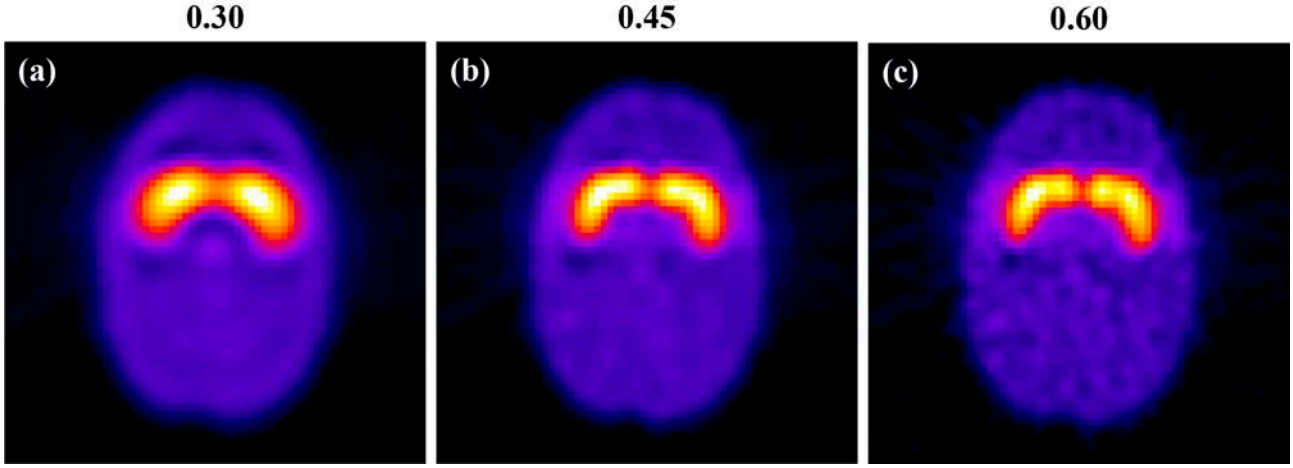

FIG. 74. Representative striatal phantom images reconstructed using FBP with a Butterworth filter order 10 with increasing cut-off from 0.3 (left) to 0.6 Nyquist frequency (right), showing improvement of image resolution but at the expense of increasing image noise.

Guidance

The choice of filter type and associated cut-off frequency should be balanced between image resolution and noise. Increasing image smoothing reduces image noise but degrades image resolution.

4.3.3. Iterations and subsets

Background

Iterative reconstruction using expectation maximization methods such as MLEM make many attempts at matching an estimated image to the measured projections, using the differences in the current estimate to help to improve the following estimate. As a consequence, the estimated image becomes a better representation of the true activity distribution with increasing number of iterations.

This process can be accelerated by using OSEM, where the estimated image is only compared with a subset of projections each time. With OSEM, the number of iterations and subsets are defined. The number of subsets equals the number of projections divided by the subset size. One iteration is defined as a pass through all subsets.

Case

A thorax phantom with myocardial, liver and background compartments were filled with a solution of ^{99m}Tc and imaged using a SPECT system with transmission AC. Figure 75 shows the image becoming more defined with

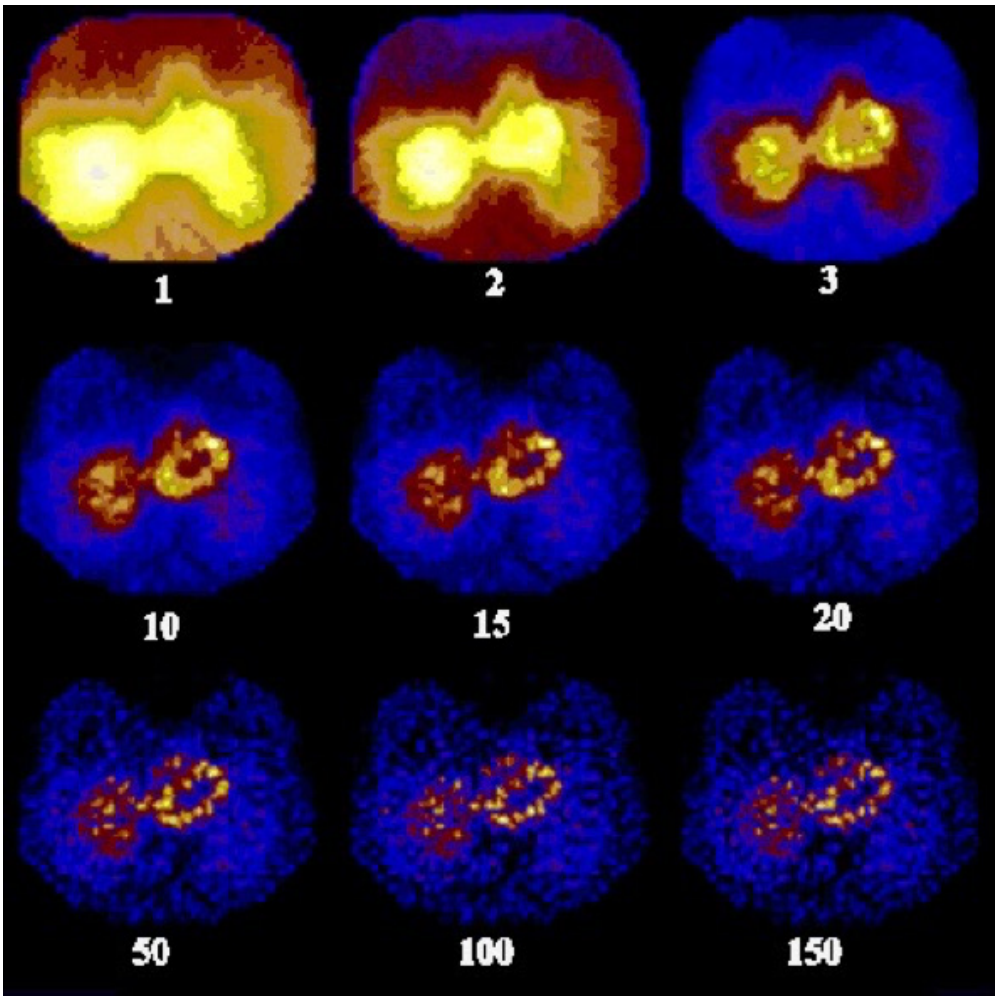

FIG. 75. Thorax phantom data reconstructed using MLEM reconstruction with between 1 and 150 iterations.

increasing numbers of MLEM iterations. At a high number of iterations, the noise becomes amplified — a known effect of iterative reconstruction.

Figure 76 demonstrates how OSEM can speed up the iterative reconstruction process. The left column shows a reconstruction with 30, 60 and 120 MLEM iterations. Sixty projections were collected in the SPECT acquisition. A subset size of 4 therefore corresponds to 15 (= 60/4) subsets. The middle column clearly shows that: 2 iterations of 15 subsets are equivalent to 30 MLEM iterations; 4 iterations of 15 subsets are equivalent to 60 MLEM iterations; and 8 iterations of 15 subsets are equivalent to 120 MLEM iterations — each leading to a huge saving in reconstruction time. The right column shows that even a subset size of 2 giving 30 subsets can be used. The equivalence of 1, 2 and 4 iterations with these 30 subsets correspond to similar image features derived from 30, 60 and 120 MLEM iterations, respectively.

Guidance

The formation of tomographic data using iterative reconstruction is defined using iterations in the case of MLEM and iterations and subsets with OSEM. The number of iterations has an impact on image quality and on the quantitative accuracy of the activity distribution. With OSEM, significant savings in reconstruction time can be achieved using subsets of projections and the corresponding much reduced numbers of iterations.

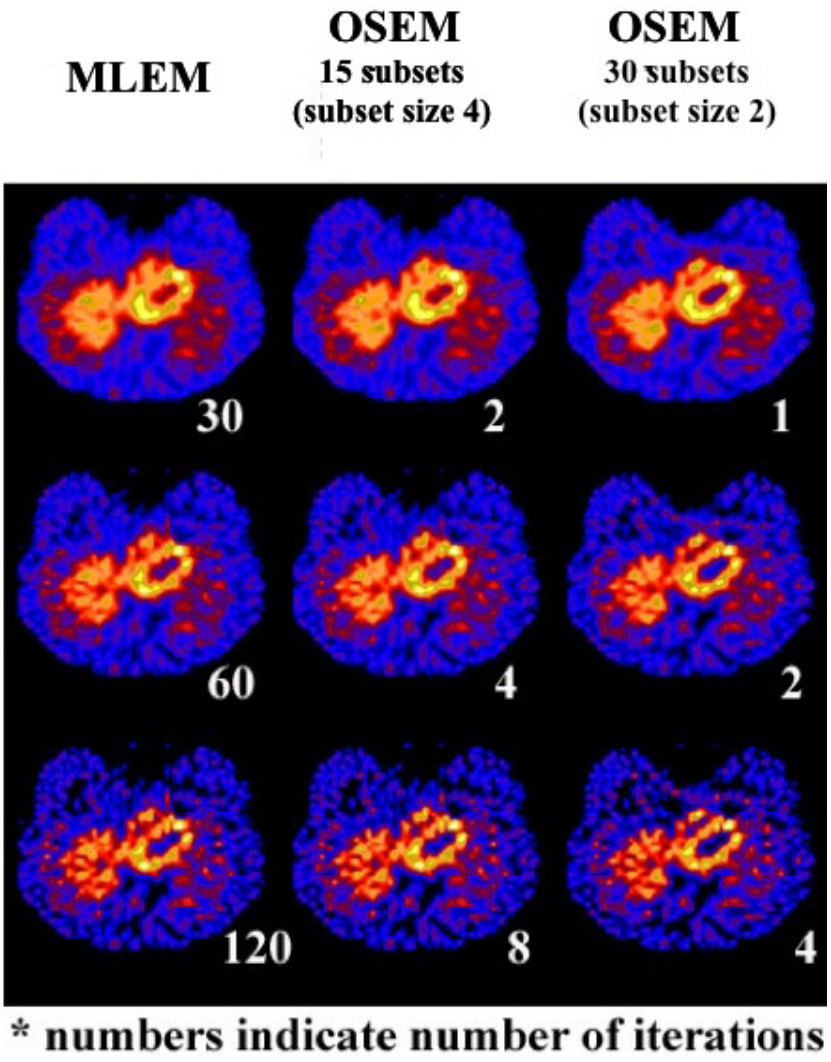

FIG. 76. Thorax phantom data reconstructed using MLEM and OSEM reconstruction showing the equivalence and improvement in reconstruction times using OSEM with a subset size of 4 and 2 (corresponding to 15 and 30 subsets, respectively).

4.3.4. Use of resolution modelling

Background

Accounting for losses in spatial resolution within iterative reconstruction is an option available in most modern SPECT/CT systems (see Section 2.1.4). Much of the focus on these algorithms is their ability to reduce noise in an image, and in doing so provide an opportunity to reduce acquisition time and/or injected activity [50]. However, by using resolution modelling which incorporates point spread function (PSF) information, it is also possible to resolve small lesions that might be undetectable using standard reconstruction approaches. Unfortunately, resolution modelling can also produce overshoot artefacts (also known as Gibbs artefacts), which can overestimate activity and produce apparent cold spots in larger lesions. Such artefacts are particularly prevalent in areas of high contrast (i.e. where there are large changes in activity).

Case A

A transaxial slice from a ^{99m}Tc filled NEMA image quality phantom reconstructed using OSEM with and without resolution modelling is shown in Fig. 77. In the largest sphere, the overshoot effect of resolution modelling is represented by overestimation of activity at the edge of the sphere and underestimation in the centre. In the smaller sphere highlighted in the profile, the overshoot artefacts superimpose, artificially elevating the counts in the sphere. Although potentially helpful in visualizing lesions, it may overestimate the relevance of the lesions. Furthermore, if quantification is required, the use of resolution modelling can adversely affect the values recorded.

Case B

Figure 78 shows contrast recovery curves from a ^{99m}Tc filled NEMA image quality phantom highlighting maximum sphere count, and contrast ratio (maximum sphere count to average count concentration) for spheres in a phantom filled with a sphere to background ratio of 5:1. Clearly the use of resolution modelling increases the maximum count in each of the spheres compared to standard reconstruction for all sphere sizes. In terms of contrast, this difference is reduced given that the background counts increase, too. However, it can be seen that the filling contrast ratio of 5:1 is overestimated using resolution modelling, while for standard reconstruction the result in the largest sphere converges to 5:1. Note that for smaller spheres, the partial volume effect limits the recovery of the true contrast.

Guidance

Although the use of resolution modelling within reconstructions can improve the noise characteristics of the data and lead to better visualization of small features, overshoot artefacts from these reconstructions can

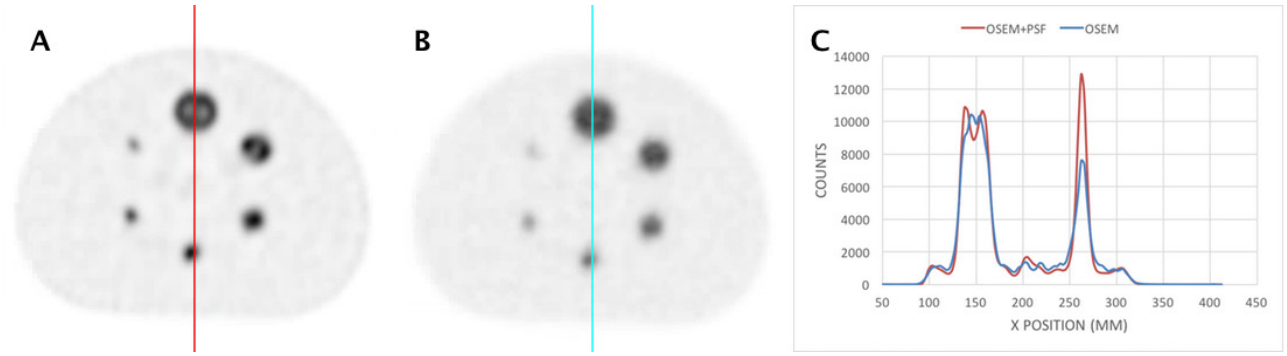

FIG. 77. A transaxial slice of a ^{99m}Tc filled NEMA image quality phantom (A) with resolution (PSF) modelling and (B) without resolution modelling. (C) Profiles through each image highlighting the effects of resolution modelling. All reconstructions also include correction for attenuation and scatter.

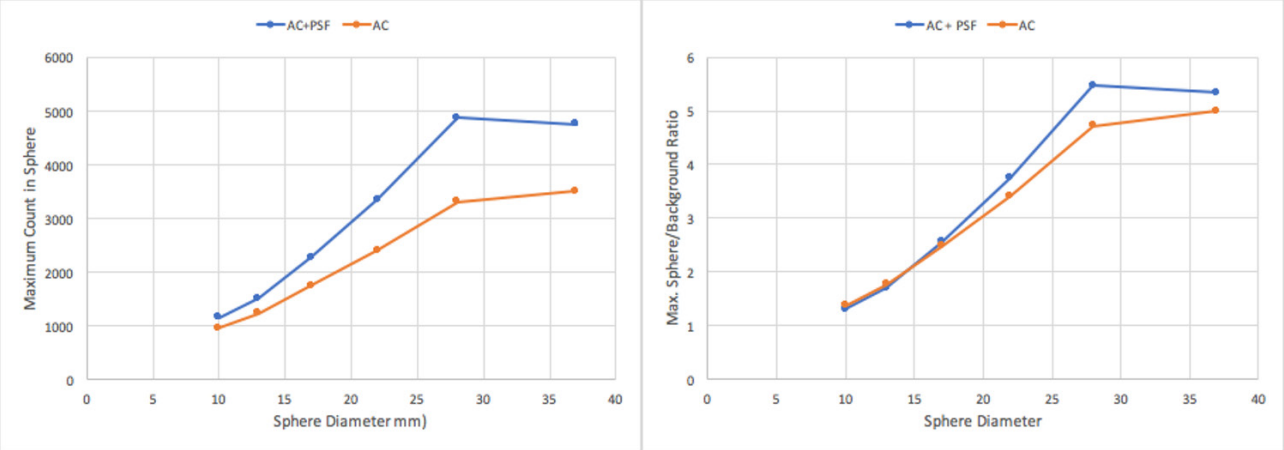

FIG. 78. Contrast recovery curves from a ^{99m}Tc filled NEMA image quality phantom: (left) maximum counts in each sphere of the phantom with a sphere to background ratio of 5:1; (right) contrast ratios in each sphere represented as the maximum count to average count concentration in the background compartment of the phantom. Reconstructions were corrected for attenuation (AC) and corrected for attenuation and resolution losses using resolution modelling (AC + PSF).

lead to overestimated activity concentrations and 'cold' centres to larger features. Visualization of data with and without resolution modelling can help to understand when these artefacts occur. It has to be noted, however, that quantification with these techniques is prone to overestimate, or under certain circumstances underestimate, activity. Reducing the numbers of iterations used in the reconstruction can help to mitigate these artefacts, although resolution modelling typically takes many more iterations to converge compared to regular OSEM reconstruction.

4.3.5. Chang attenuation correction

4.3.5.1. Bad contouring

Background

SPECT images of uniform phantoms can be attenuation corrected using the Chang technique. This technique requires that an ROI be defined around the boundary of the phantom. The correction then assumes a uniform attenuation value in every pixel within the defined region and uses that to perform the AC.

Case

SPECT images of a ^{99m}Tc filled Jaszczak phantom were acquired and reconstructed using Chang-AC. Four different boundaries were created (see Fig. 79). One of which matched the phantom boundary and is considered the gold standard, one larger than the phantom, one smaller than the phantom and one that is offset with respect to the phantom.

The effects of the different boundaries are very clear in the image. The images are improved when using Chang-AC compared to NAC images. However, an overly large contour will produce central areas of the phantom with relatively fewer counts, while boundaries that are too small will result in relatively elevated counts in central regions. A shifted boundary introduces a gradient of counts across the images.

Guidance

Boundaries that are badly defined in Chang-AC will result in artefacts in the AC images. Care should be exercised to ensure that object boundaries are defined correctly.

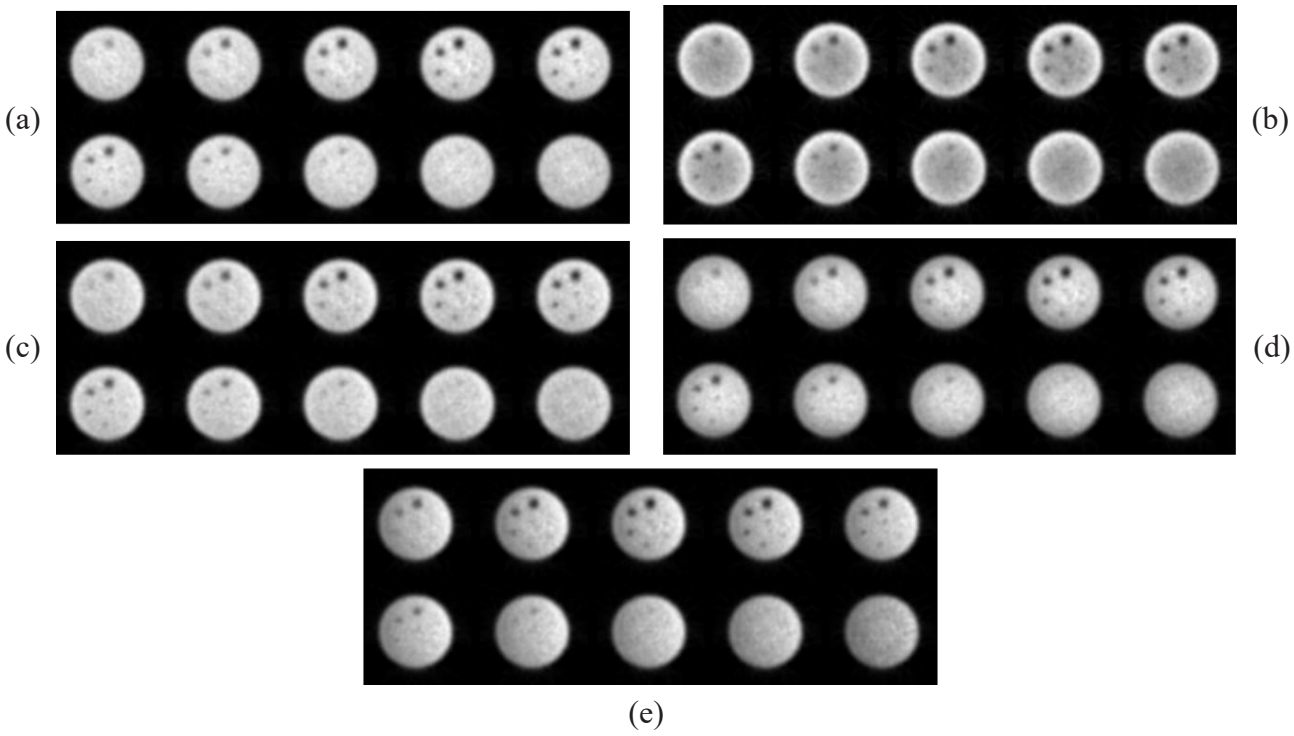

FIG. 79. SPECT phantom images with Chang-AC using different boundaries: (a) correct boundary; (b) without AC; (c) large boundary, showing an enhancement of the edges with respect to the central region; (d) small boundary, showing increased counts in the central region; and (e) offset boundary showing non-uniform counts across the images.

4.3.5.2. Effect of different μ values

Background

The Chang-AC approach assumes a constant attenuation coefficient within the imaged object. This constant value is dependent on the tissue density of the object and the energy of the incident photon. For soft tissue or water at 140 keV (^{99m}Tc), many camera systems use a default value of 0.11 cm^{-1}, compared to the narrow beam definition of 0.15 cm^{-1}, in an attempt to correct for scattered photons.

Case

A cylindrical SPECT phantom filled with a solution of ^{99m}Tc was imaged in a SPECT scanner. The acquired data were reconstructed using Chang-AC with different μ values in the range of 0.07–0.15 cm^{-1}. The reconstructed images are shown in Fig. 80, which shows that too low a value and the count density in central areas will be underestimated, while too high a value and the count density will be overestimated. Interestingly in this example, the optimal linear attenuation coefficient for image flatness is 0.09 cm^{-1}. This is a consequence of the acrylic walls of the phantom and also the scatter environment in the phantom, with the lower value giving a flatter profile, but not necessarily a more accurate value of count density. A similar effect may be seen in brain imaging owing to the higher density and therefore attenuation of the skull. It should also be noted that the narrow beam value of 0.15 cm^{-1} is not appropriate for this wide beam source arrangement.

Guidance

The use of an adequate μ value for Chang-AC of SPECT images is essential for good quality and more accurately quantitative images. However, because no phantom or human brain has the same attenuation throughout, the value of linear attenuation coefficient chosen to create the flattest image may not result in the most accurate value of count density.

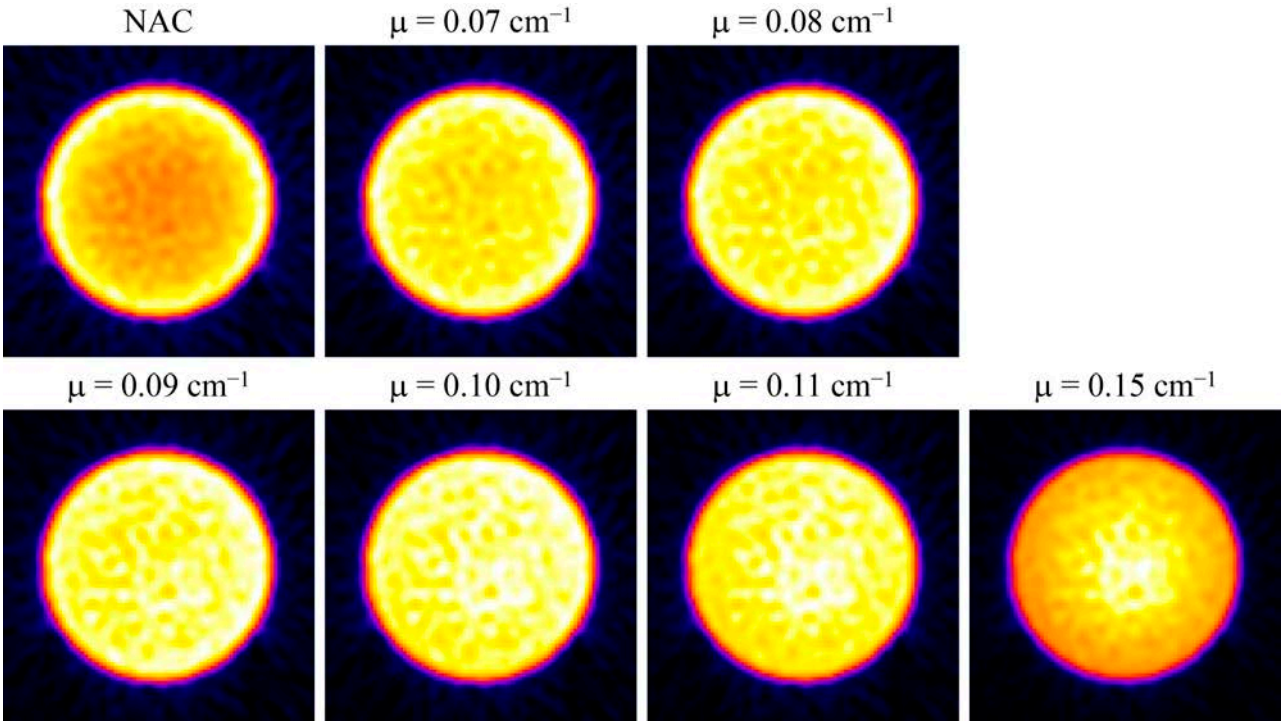

FIG. 80. Images through the uniform area of a Jaszczak phantom using Chang-AC with different values of linear attenuation coefficient.

4.3.5.3. Non-uniform attenuation

Background

Chang-AC assumes a uniform attenuation of photons within the imaged object. However, if the object is composed of different materials with different attenuation coefficients then the application of the Chang technique will result in errors.

Case

A uniform phantom containing three cylindrical inserts of different materials (air, water and teflon) was imaged in a SPECT/CT scanner (see Fig. 81). The acquired data were reconstructed using CTAC as well as Chang-AC with a μ value of 0.11 cm^{-1}. The CTAC SPECT image is used as the gold standard, since CT can account for the different attenuating material during the SPECT image reconstruction. In addition, the data were reconstructed without AC. None of the cylindrical inserts contained radioactivity and hence the resultant images should show no counts in these regions. As can be seen from the images, the use of Chang-AC resulted in image artefacts and large errors in quantification (see Section 4.7) particularly in the air insert. The image without AC also showed more counts at the phantom boundaries as well as low counts in the central region which are characteristic of uncorrected images.

Guidance

The use of Chang-AC should be restricted to objects of uniform attenuation; otherwise image artefacts will appear in the resultant images.

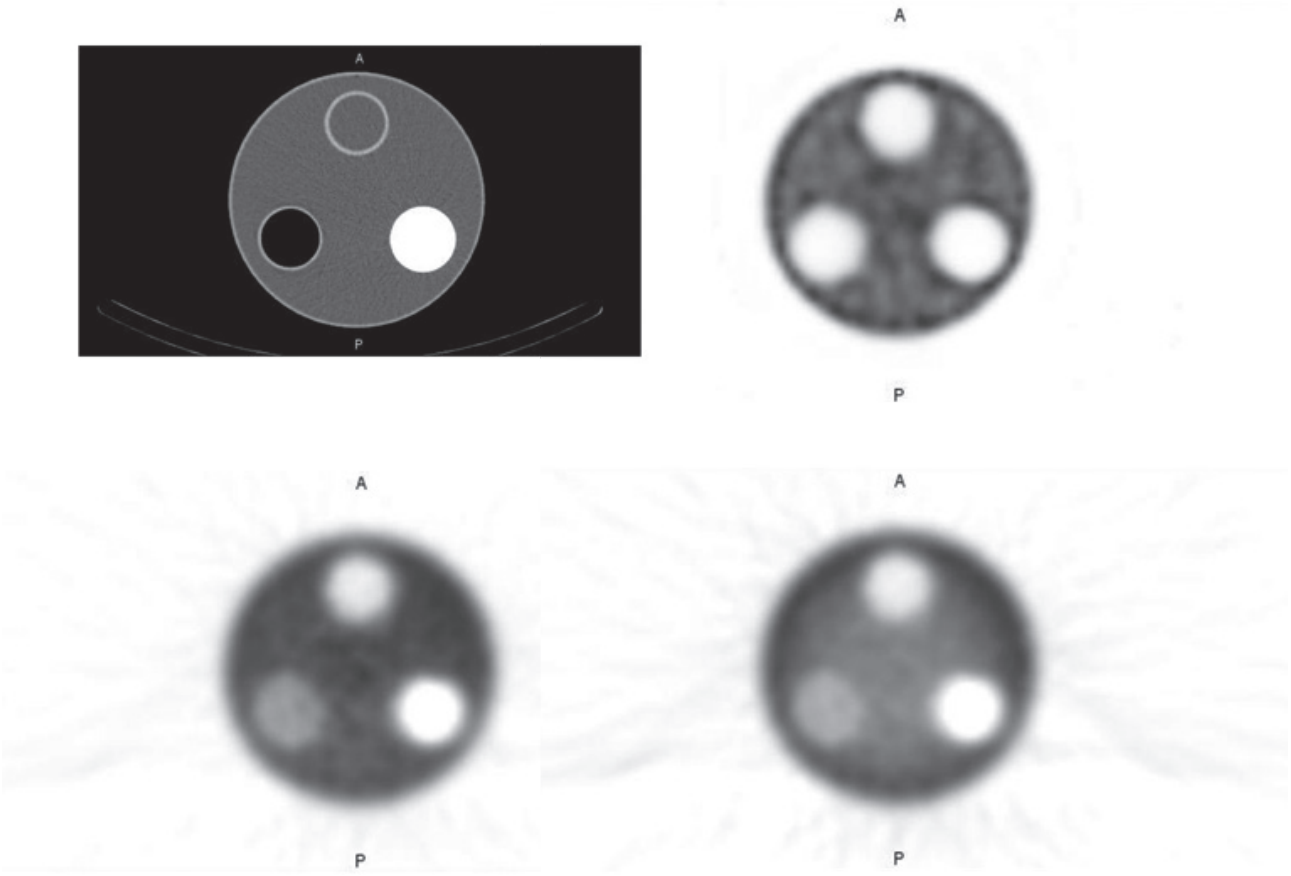

FIG. 81. SPECT and CT images of a uniform phantom with three cylindrical inserts: (top left) CT image with inserts clockwise from top of water, teflon and air; (top right) iterative reconstruction with CTAC; (bottom left) FBP with Chang-AC; (bottom right) FBP with NAC.

4.4. PATIENT RELATED ARTEFACTS

Image artefacts may be generated not only by system related factors, but also by the patients themselves. This section includes patient motion (voluntary as well as involuntary cardiac motion), injection problems or residual of tracer from previous examinations or treatments, together with specific problems in positioning and related attenuation effects.

4.4.1. Voluntary patient motion

Background

In general, compared to planar imaging, SPECT requires a greater number of acquired counts to produce robust, low noise diagnostic images. Ethical limitations to the injected activity that can be given to a patient mean that high level of counts need to be achieved by relatively long scan times — normally between 15 and 45 minutes. This obviously places a greater demand on the patient to remain still during the acquisition of image data. Although for most patients this is achievable, in some cases long scan duration results in patient motion. This can make the reconstructed data difficult, or even impossible to use, for diagnosis.

Case A

A 50 year old male with drug resistant frontal lobe epilepsy was referred for an ictal cerebral blood flow study to help localize an epileptogenic focus. Immediately following the onset of an epileptic seizure, 485 MBq of

^{99m}Tc-hexamethylpropyleneamineoxime (HMPAO) was injected, with imaging performed 2.5 hours later. Twenty minutes after the start of imaging, the patient suffered another seizure, moved and left the scanner FOV at angles of 114 and 117 degrees, respectively. The consequences of the motion and empty projections reconstructed with FBP and OSEM are shown in Fig. 82.

In Fig. 82(a), the artefact caused by the incomplete projection data is seen in the FBP reconstruction. With iterative reconstruction, the study might not be recognized as being artefactual if the reconstructed data were shown in isolation. However, the lack of counts in the lower left and the upper right of the transaxial image are caused by the missing projection data.

Case B

A rest myocardial perfusion study was performed using ^{99m}Tc-MIBI. In the left panel of Fig. 83, the linogram shows that the patient moved during the study. Motion correction was applied to the data to produce the linogram in the right panel. The bullseye plots from uncorrected and corrected data show that on the uncorrected data, the perfusion deficit is at a 9–10 o'clock position, representing the anterior wall of the heart. Once corrected, the perfusion deficit moves to the apex of the heart (centre of the bullseye plot).

Guidance

During SPECT studies, it is important that the technologist fully explain the procedure and its duration prior to patient set-up. When positioning the patient, it is equally important to ensure that the patient is comfortable, and that appropriate immobilization straps are used to minimize any potential patient motion. It is important that the doctor writing the report of the images be made aware that motion has occurred. Although it is always possible to perform quality control for motion in projection or sinogram data, it may not always be possible to spot in the reconstructed data that the patient has moved. Therefore, the projection images should be checked before releasing the patient.

4.4.2. Involuntary patient motion

Background

A SPECT acquisition can take anywhere between 10 and 40 minutes. Consequently, any image of the mediastinum will create a time averaged image of uptake within the heart, unless that acquisition is ECG gated. However, because the heart spends most time in or close to the end diastolic phase, the myocardial uptake is relatively well defined and not grossly affected by cardiac motion.

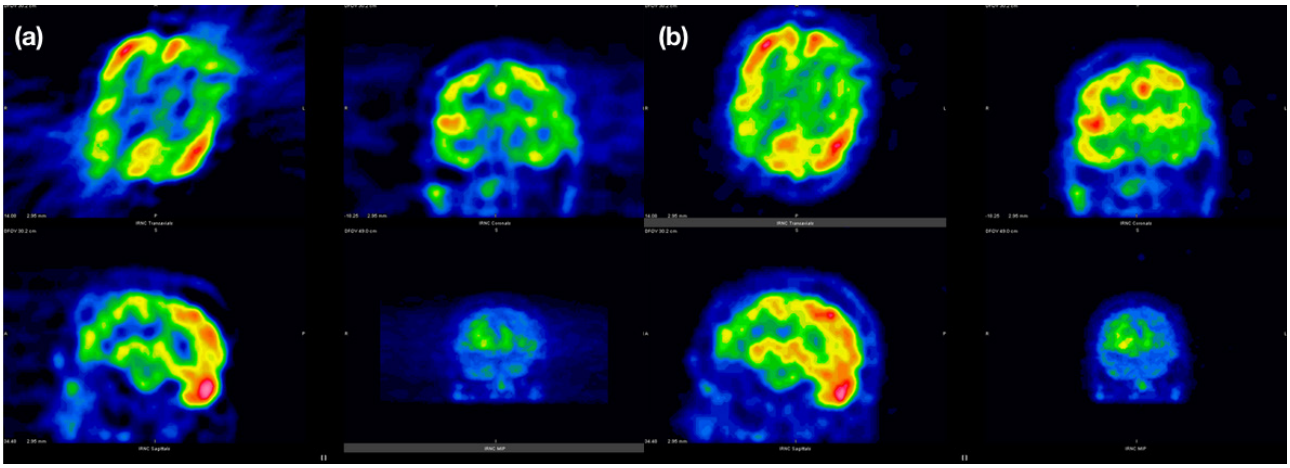

FIG. 82. Cerebral blood flow study showing an artefact caused by incomplete projection data: (a) FBP reconstruction; and (b) iterative reconstruction (OSEM).

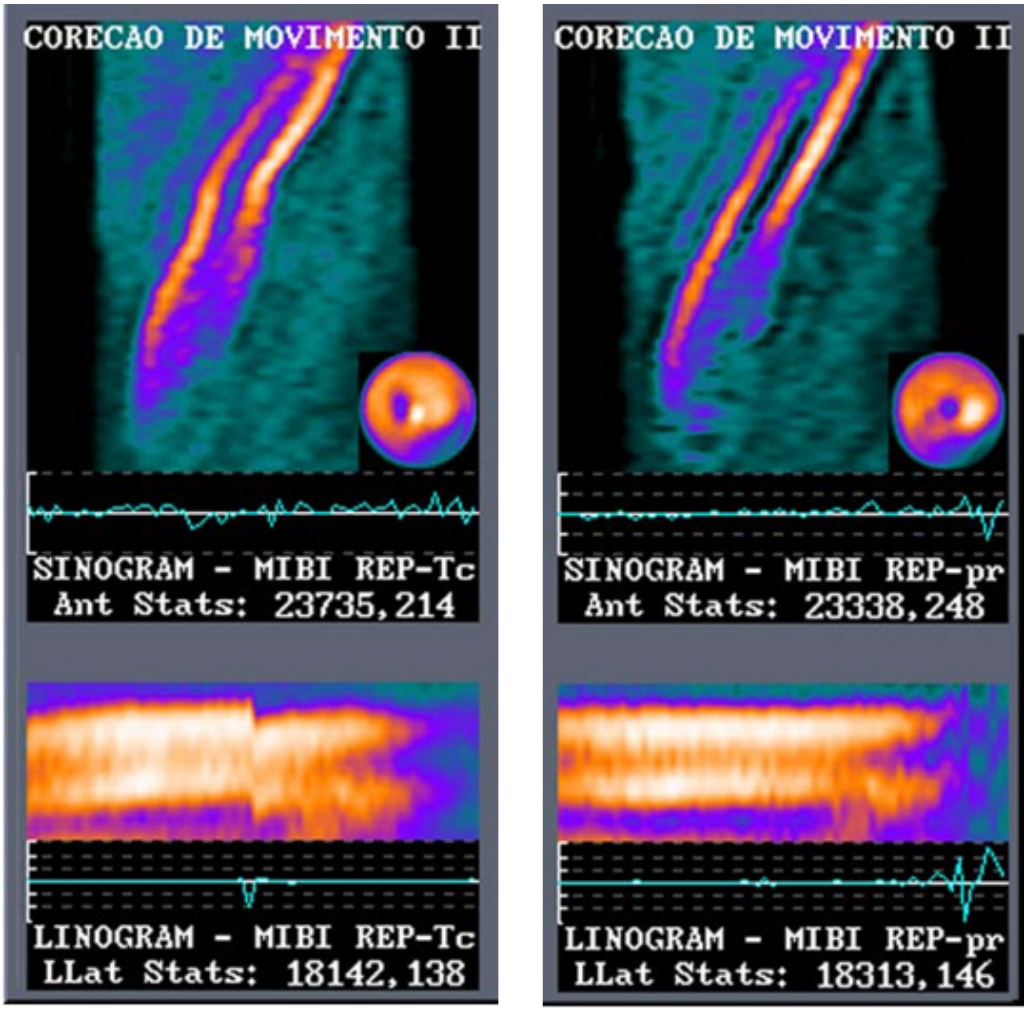

FIG. 83. A rest myocardial perfusion study: (left) sinogram and linogram showing patient movement during the SPECT acquisition which, before correction, presents with a perfusion deficit in the patients' anterior wall; (right) after motion correction of the sinogram data, the sinogram and linogram now appears uninterrupted and the perfusion deficit moves to the apex.

Since the myocardium is relatively thin in the diastolic phase, the limited spatial resolution of SPECT systems can produce partial volume artefacts, where the measured signal is less than the true signal. Indeed, this artefact is actually used for clinical interpretation of myocardial perfusion imaging. The diastolic phases are significantly affected by the partial volume effect, while in the systolic phases the myocardial wall thickens, which, with the reduced effect of partial volume, increases the myocardial count level to produce the measure of 'wall thickening'.

Case

A 54 year old man who was being assessed for coronary artery disease had a stress myocardial imaging study using ^{99m}Tc-MIBI and adenosine pharmacological stress. The resultant images from ungated data show well defined myocardium (see Fig. 84(a)). In the gated study (see Fig. 84(b)), the end diastole myocardial wall thickness is similar to that shown in the ungated data, as would be expected given that the heart is mostly in this phase. At end systole, the wall thickens, reducing the effects of partial volume artefacts and giving a relative increase in uptake signal which is used to derive the 'wall thickening' metric.

Guidance

Non-voluntary motion from the heart can lead to some motion blurring, although in practice, since the heart is mostly in the end diastolic phase, a time averaged image mostly represents the heart in the ventricle filling phase.

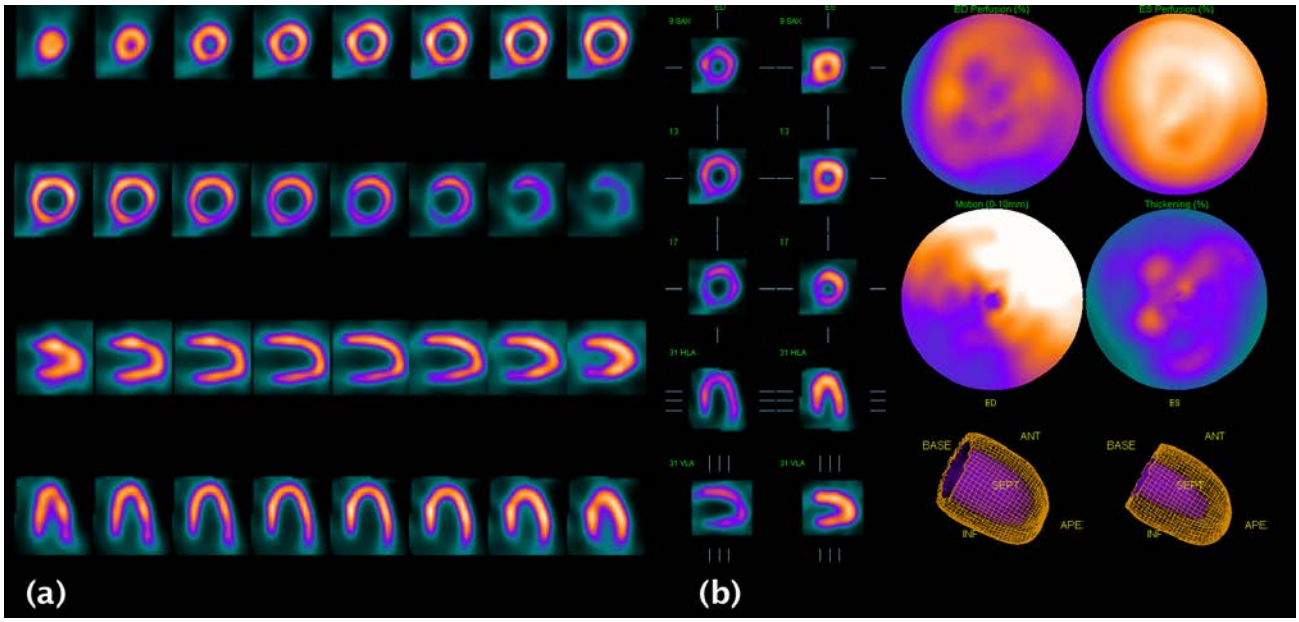

FIG. 84. (a) Ungated studies showing a uptake of ^{99m}Tc-MIBI in the myocardium and (b) a gated study showing the end diastolic phase and end systolic phase, together with the concept of 'wall thickening'.

4.4.3. Postural and positional artefacts

Background

On some dedicated cardiac SPECT scanners, there is the ability to perform scans in an erect or semirecumbent position instead of the standard supine position. In the absence of AC, using a different position for SPECT scanning can lead to different attenuation effects.

In some centres, to tackle attenuation artefacts in SPECT only scans of the myocardium (see Case B below), patients can be positioned prone rather than the more traditional supine position. Although uncomfortable for some, the prone position can compact (e.g. breast tissue) leading to a less attenuated signal.

Case A

A 59 year old man presenting with breathlessness and showing coronary artery calcifications on a recent chest CT was referred for a myocardial perfusion scan. Under adenosine pharmacological stress, 1052 MBq of ^{99m}Tc-MIBI was injected intravenously, with imaging performed in both a semirecumbent and supine position using a dedicated solid state imaging system. No attenuation correction was performed.

Figure 85 shows differences in image appearance with the patient in a semirecumbent and supine position. Due to gravity, diaphragmatic attenuation is less of an issue with the patient semirecumbent, which is highlighted by better perfusion in the inferior wall when compared to supine imaging. However, spill-in of activity from neighbouring gastrointestinal activity into the myocardium is also more problematic in this patient when semirecumbent. Perfusion in the septum is reduced in semirecumbent imaging compared to supine imaging, which, in this instance, is due to the preferable attenuation environment found in the supine position.

Case B

A SPECT only myocardial perfusion study was performed using ^{99m}Tc-MIBI on a male patient. In the supine image shown at the top of Fig. 86, there is a clear inferior wall attenuation artefact. When the patient was imaged prone (bottom), this artefact disappeared.

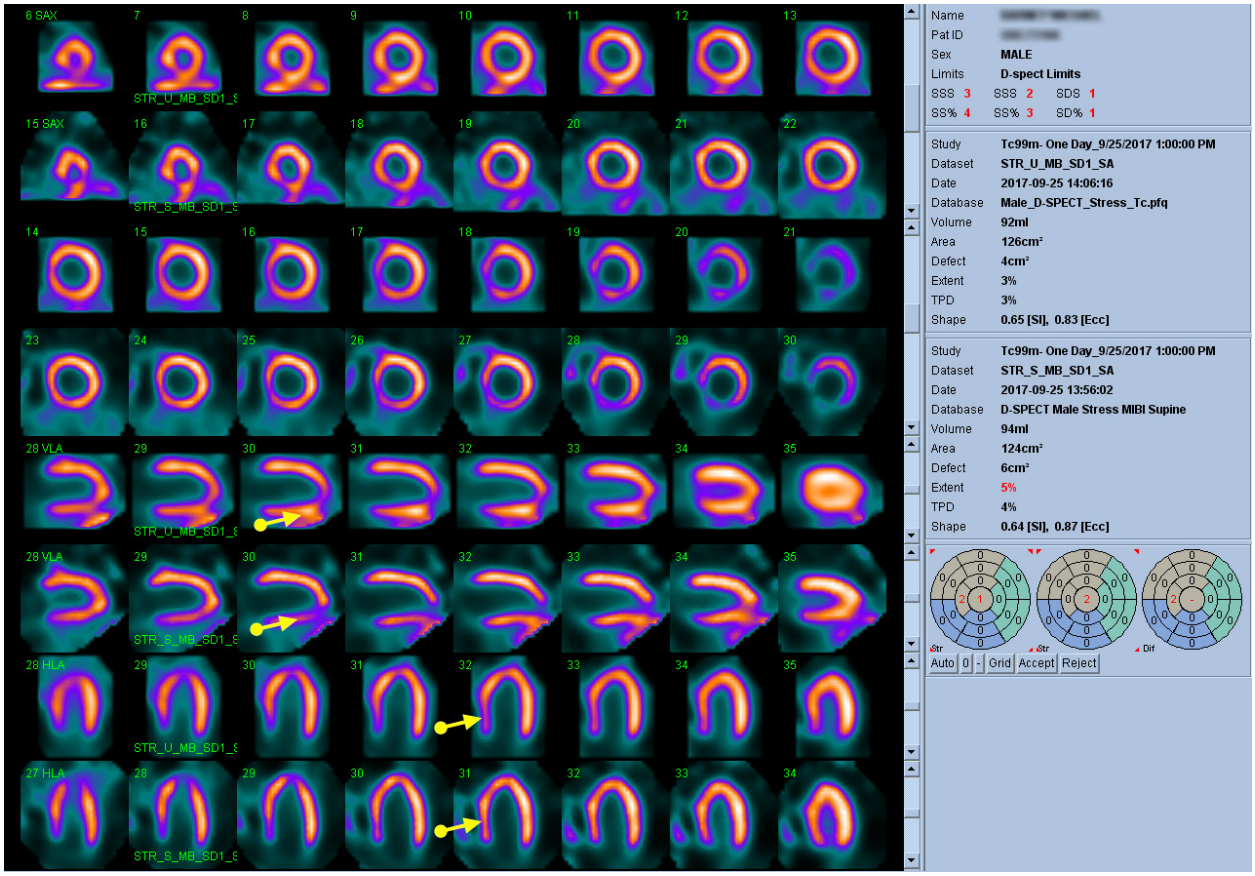

FIG. 85. Semirecumbent (upper row of each pair) and supine (lower row) stress ^{99m}Tc myocardial perfusion images. Yellow arrows show postural differences in uptake in the inferior wall and septum.

Guidance

Posture related artefacts can be reduced by using transmission based AC or by using prone imaging where possible. When this is not possible, the reporting doctor should be made aware of the patient's posture during scanning to take account of attenuation artefacts. Dual scanning in multiple positions may also be helpful in some instances.

4.4.4. Incomplete injection

Background

During injection of a patient, a drop of injectate may be left in the injection line if not properly flushed. In that case, image distortions of different types may appear, depending on the method of reconstruction and the selection of image display parameters. Similar results may appear in the case of a (partial) subcutaneous injection.

Case

A body phantom (volume 9.7 L) was filled with a concentration of ^{99m}Tc of 50 MBq/L and 'arms' consisting of 1 L infusion bags with the same activity concentration were placed along each side (see Fig. 87). A droplet of 10 MBq 'injectate' (2%) in a test tube was placed at the left arm to simulate the injection site. SPECT/CT was performed on a Philips Precedence 16. Acquisition parameters of a low energy general purpose (LEGP) collimator, 128 angles, 128 × 128 matrix, 60 s per angle; and reconstruction parameters of (left) FBP (NAC), Hamming filter with cut-off frequency at 0.5 Nyquist frequency and (right) iterative method (OSEM: PSF, 4 iterations 16 subsets, CTAC).

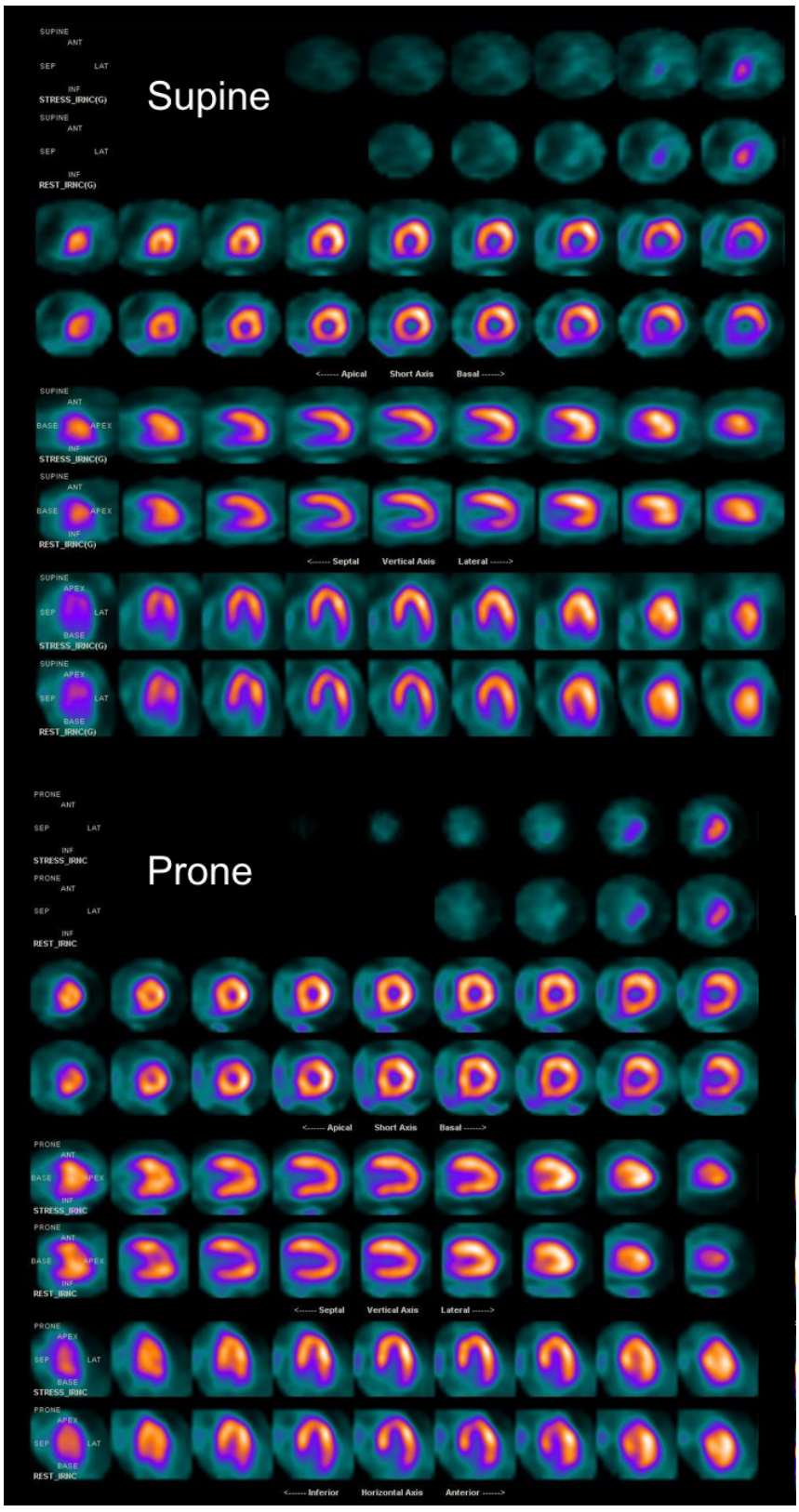

FIG. 86. ^{99m}Tc-MIBI scan of a patient scanned in supine and prone positions. The inferior wall attenuation artefact seen in the supine image is resolved when the patient is imaged in the prone position.

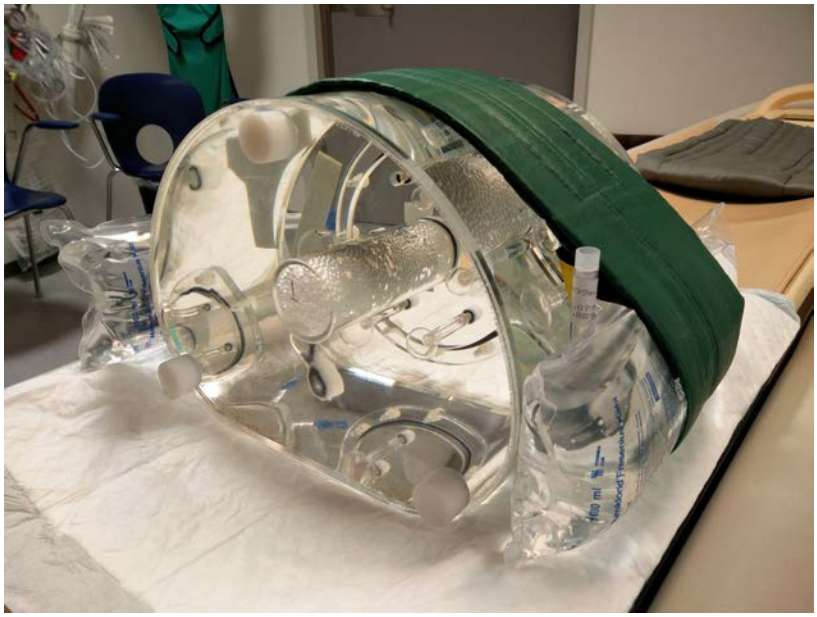

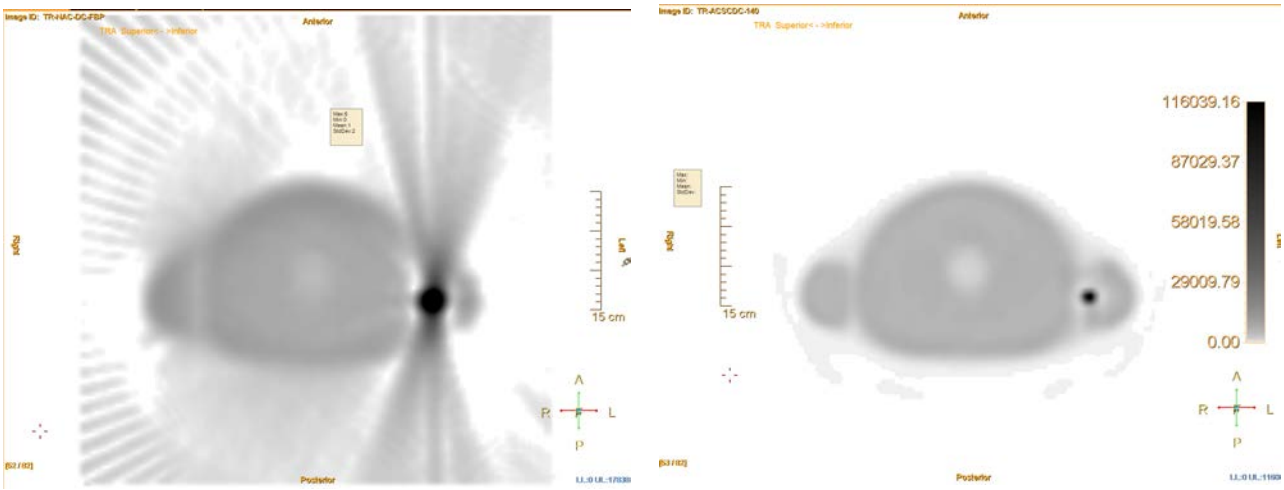

FIG. 87. Body phantom with 'arms' attached and a test tube placed between the 'body' and the 'left arm' with a hot droplet simulating an injection site: (bottom left) FBP reconstruction (NAC); (bottom right) iterative reconstruction with CTAC. The grey scale in both cases is logarithmic in order to represent the large dynamic range of the image contents.

Guidance

Injection problems may cause small spots of very high activity concentration. FBP reconstruction (NAC) exhibits large artefacts, while the iterative method is able to handle the situation reasonably correctly. The dynamic range may require that the images be shown in a logarithmic scale. Accepting an overflow at the 'point source' in a linear scale can bring out the main information, but it can also result in the main part of the image being displayed with very few levels of grey, resulting in a loss of information.

4.4.5. Radiopharmaceutical cross-contamination

Background

Gamma camera collimators are designed for a certain range of photon energies and are often referred to as low, medium or high energy. If the upper limit is exceeded, the photons will penetrate the collimator septa to

an unacceptable degree, leading to a diffuse image blur or a streak pattern that will impair image resolution and general quality. In SPECT, reconstruction of inconsistent projections may lead to further errors.

Case

A 50 year old woman was referred for a bone scintigraphy and SPECT and was injected with 545 MBq of ^{99m}Tc-HDP. An examination was performed on a Siemens Symbia 16 with low energy collimators. The images showed an unexpected pattern (see Figs 88 and 89), and it was recognized that there was an apparent high activity in the neck region (front). An investigation revealed that four weeks earlier in another hospital, the patient had been given a ^{131}I treatment with 400 MBq for a benign thyroid disease. The amount of ^{131}I remaining was not measured but estimates were about 1–2 MBq.

Guidance

It is important to be informed about a patient's previous nuclear medicine examinations and radionuclide treatments. Of particular importance are nuclides used in therapy with higher energy and long half-lives, such as

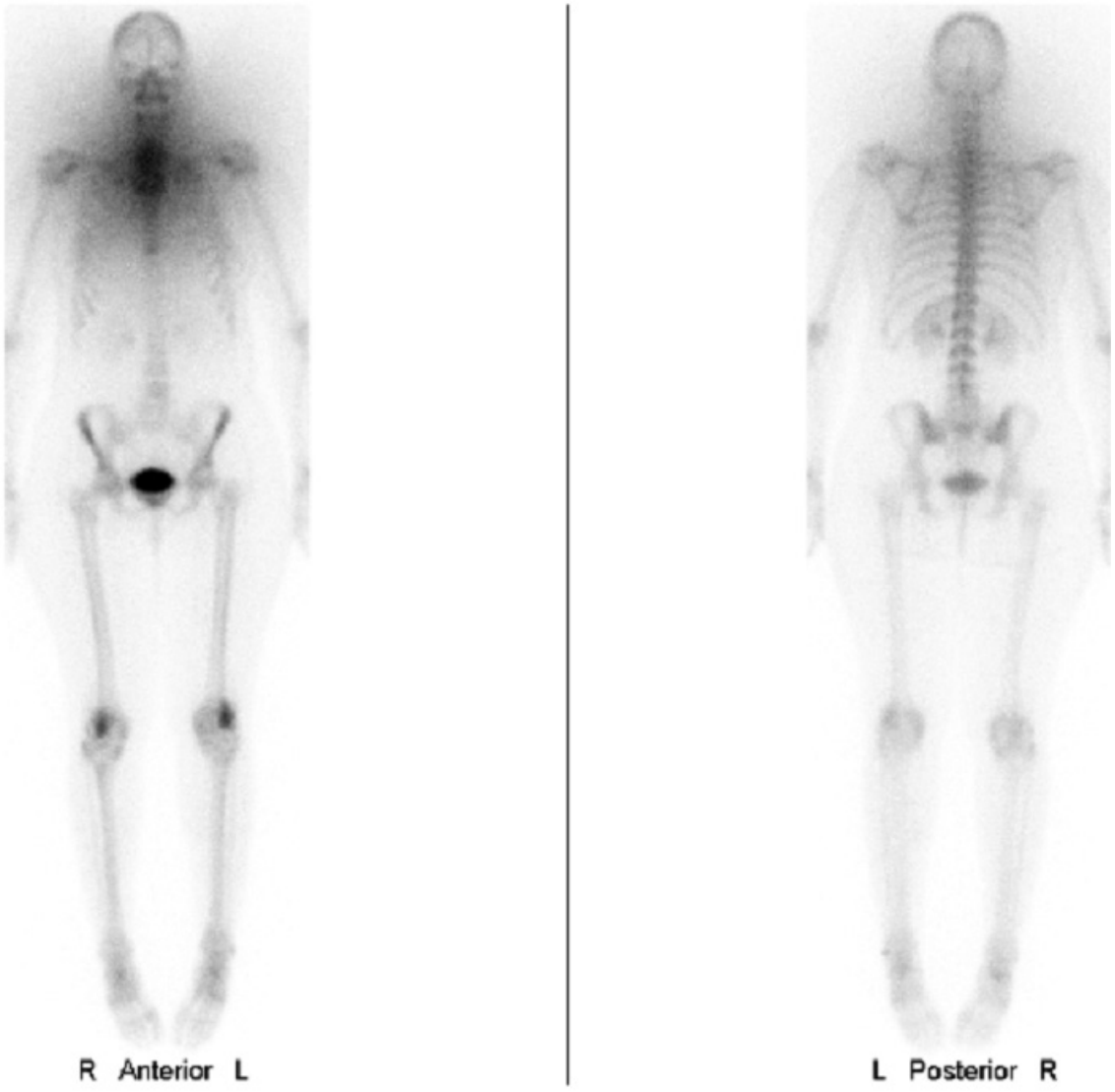

FIG. 88. Planar bone scintigraphy (^{99m}Tc-HDP) of a 50 year old woman who had received ^{131}I treatment with 400 MBq four weeks earlier.

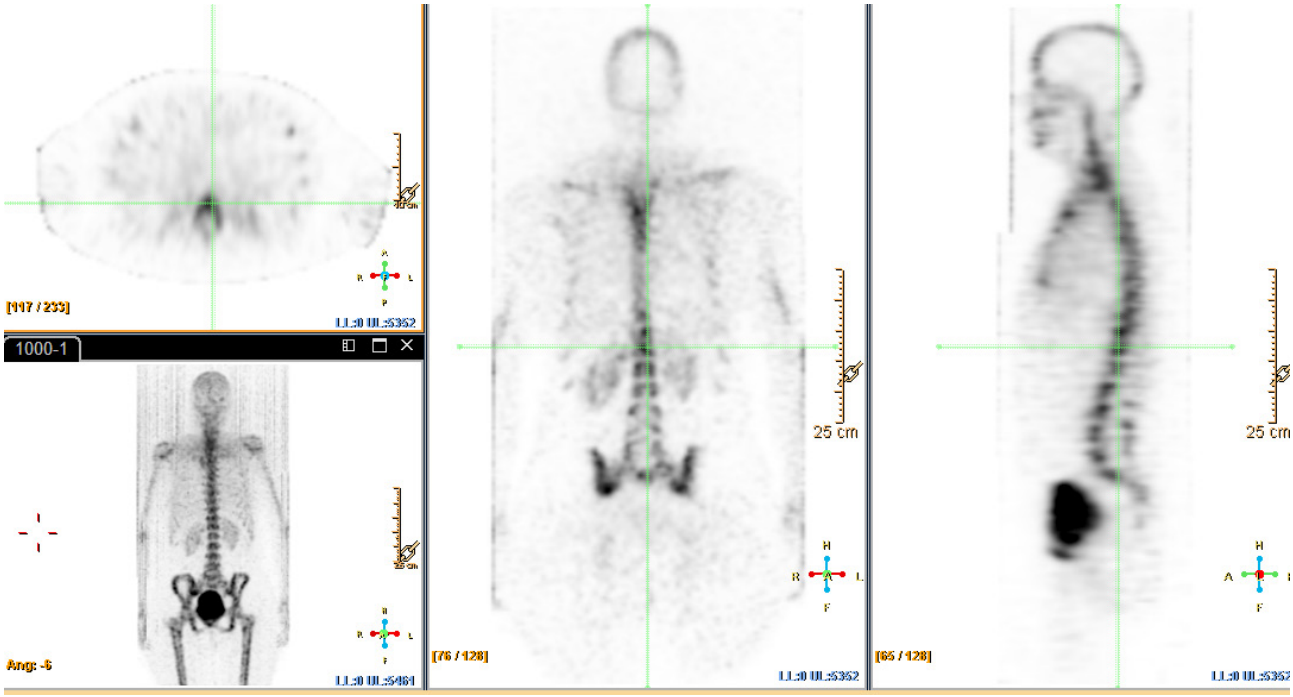

FIG. 89. SPECT (^{99m}Tc-HDP) of 50 year old woman who had received ^{131}I treatment four weeks earlier.

^{131}I or ^{177}Lu, but also PET isotopes with an energy of 511 keV can even in small amounts seriously disturb SPECT imaging at lower energies owing to collimator penetration.

4.4.6. Patient attenuation

Background

When SPECT data are acquired without CTAC, attenuation artefacts can be present in the reconstructed image. For many SPECT studies, attenuation artefacts do not strongly affect clinical interpretation of the images. However, for myocardial perfusion SPECT, the semiquantitative nature of the data, and the fact that stress and rest images may be compared can lead to attenuation related artefacts causing problems in clinical interpretation.

Case A

A common attenuation artefact found in myocardial perfusion imaging is that caused by attenuation of projection data by breast tissue — particularly in women with large breasts. In Fig. 90, short axis together with horizontal and vertical long axis data from a myocardial perfusion study are shown highlighting breast attenuation in the anterior wall (upper row). In the lower row, the breast tissue was strapped and compressed, resulting in a reduction of the attenuation artefact.

Case B

Typically, when performing a myocardial perfusion study, patients are asked to put their arms above their heads to avoid unwanted attenuation of the projection signal. For some patients, however, this position can be difficult to achieve. For these patients, data are to be acquired with arms down. In Fig. 91(a), the sinogram in the top row shows attenuation artefacts from an arm down by the patient's side. In the bottom sinogram image, the patient's arm is moved above the head and there are no attenuation artefacts. In the reconstructed data in (b), the upper rows show an apical–lateral artefact related to arm attenuation, which disappears once the arm is moved above the patient's head.

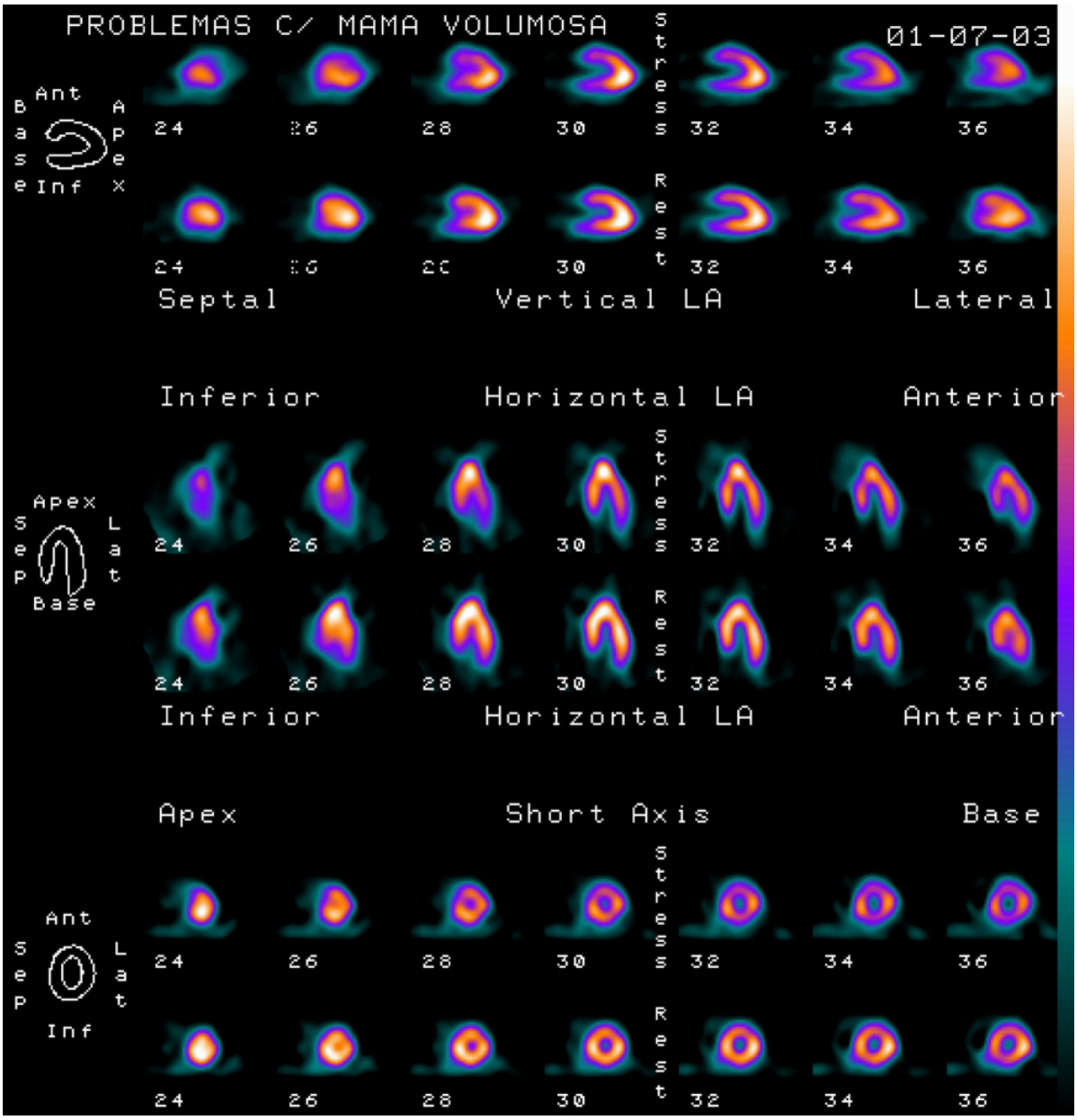

FIG. 90. Myocardial perfusion study with breast attenuation artefact (upper row), and with breast tissue strapped to reduce the attenuation artefact (lower row).

Guidance

Attenuation artefacts can cause problems in uncorrected SPECT data when quantification, semiquantitative or comparative data are required. The simple way to address these issues is to perform CTAC if it is available. If this is not an option, all steps should be taken to minimize attenuation issues before SPECT data are acquired.

4.5. CT ISSUES

CT image quality may be limited by a number of factors in the scanner design or the choice of imaging parameters. This section includes some examples that relate to the use of CT with SPECT.

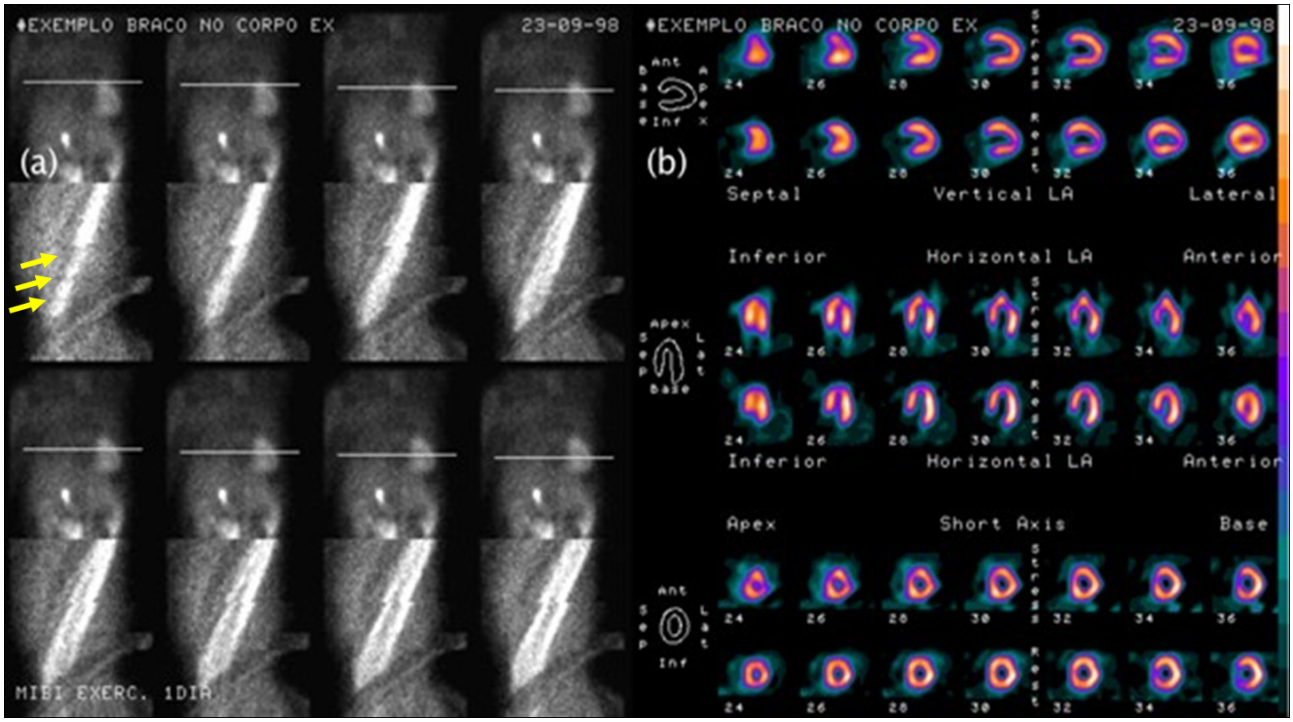

FIG. 91. Myocardial perfusion study. (a) Top sinogram shows reduced signal at the lower part of the sinogram because of arm attenuation. In the bottom row the intensity of the signal is maintained with the patients' arms raised. (b) An apical–lateral artefact seen with arms down (upper row) disappears once the patients' arms are raised (lower row).

4.5.1. CT slice thickness

Background

CT scanners can acquire data in helical or axial mode. In helical mode, there is a high degree of flexibility in slice thickness because of the interpolation of helical data into transaxial slice bins. However, in axial mode the transaxial slice thickness is set by the configuration of CT detectors. In modern multislice scanners, slice thickness can vary from tenths of a millimetre to several millimetres. In some older systems, particularly SPECT/CT systems, the transaxial slice thicknesses can be limited to 5–10 mm. As a consequence, although data within a transaxial slice demonstrate good spatial resolution, in coronal and sagittal planes the spatial resolution is severely compromised. This can cause problems when measuring feature dimensions across reconstructed slices.

Case

An abdominal CT from an early SPECT/CT system with a 1 cm slice thickness is shown in Fig. 92. While spatial resolution within the transaxial plane is adequate, the 1 cm slice thickness creates partial volume effects in coronal and sagittal views, which limits their usefulness.

Guidance

On modern multislice SPECT/CT systems, the issue of large slice thicknesses has virtually disappeared. If such limits are applicable in a SPECT/CT system, the use of helical mode should be considered.

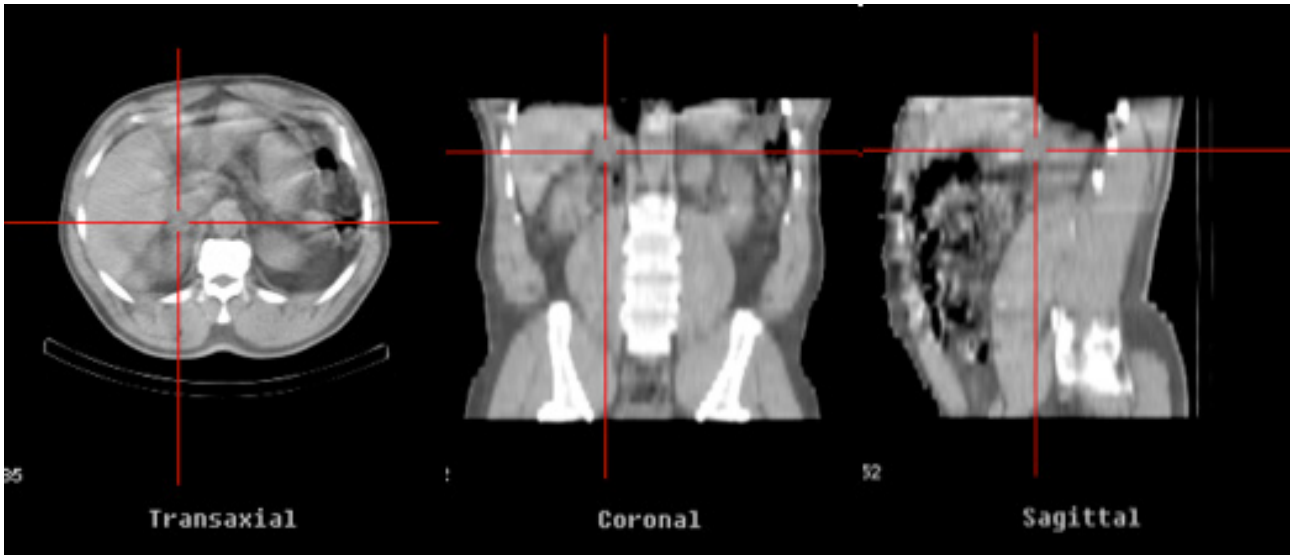

FIG. 92. Transaxial, coronal and sagittal slices through the abdomen using a 1 cm slice thickness. The large slice thickness results in step like features in sagittal and coronal views.

4.5.2. CT helical pitch

Background

The use of helical CT is very common in SPECT/CT. This is primarily due to dose savings when high levels of pitch are used. While this may be acceptable in areas where there are no rapid changes in the morphology of anatomy, in some instances the use of a high pitch CT may break the assumptions required to interpolate missing data used for reconstruction.

Case

A high pitch (1.375:1) helical CT of a patient's arm was acquired (see Fig. 93). Due to the oblique position of the arm, the interpolation used on the helical CT reconstruction produces a wave pattern in the bony structures of the arm.

Guidance

Wave like artefacts in CT images can be avoided by placing anatomical structures in a straight position. If an oblique position cannot be avoided, a lower pitch CT should be considered together with a reduced tube current to maintain a similar patient dose.

4.5.3. Noise

Background

The choice of CT image quality (noise content) could in principle affect the SPECT image quality and quantification when the CT image is used for the AC of the SPECT data.

Case

Figure 94 shows CT and corresponding SPECT scans of an anthropomorphic thorax phantom filled with ^{99m}Tc. CT scans with three different dose levels ($CTDI_{vol}$: 21, 10, 0.5 mGy) were acquired and then used to correct the SPECT data for attenuation. The results show that with decreasing CT dose level, the CT images become noisier

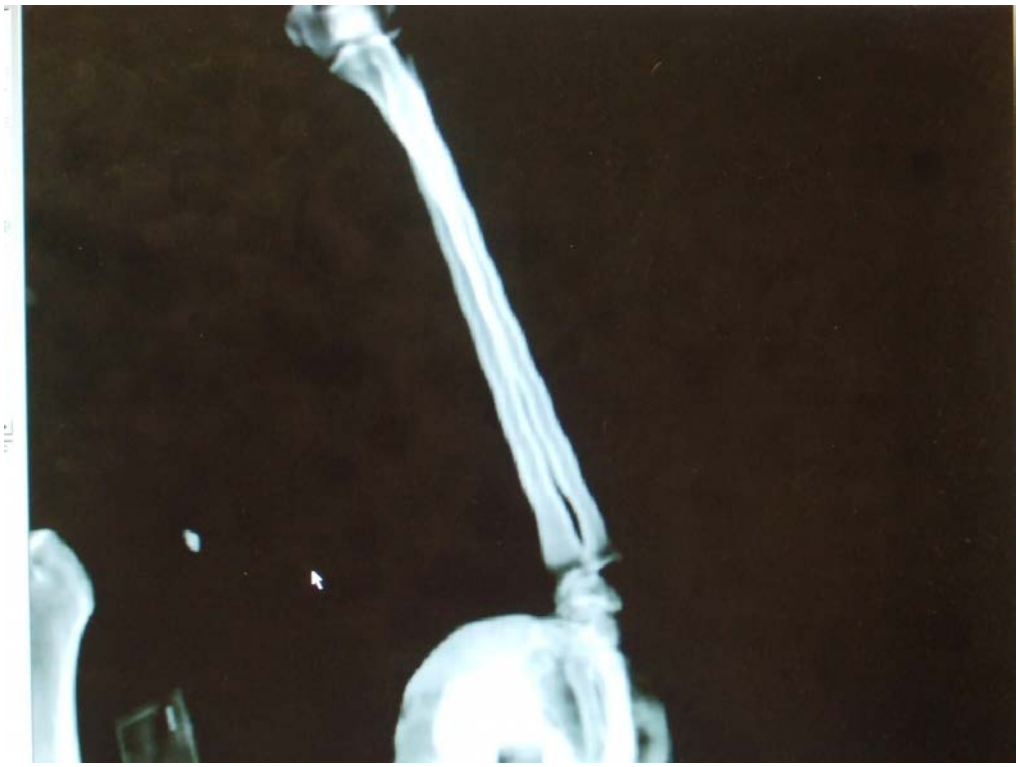

FIG. 93. Coronal slice of an obliquely positioned arm acquired with high pitch helical CT produces wave like patterns in the structures of the arm.

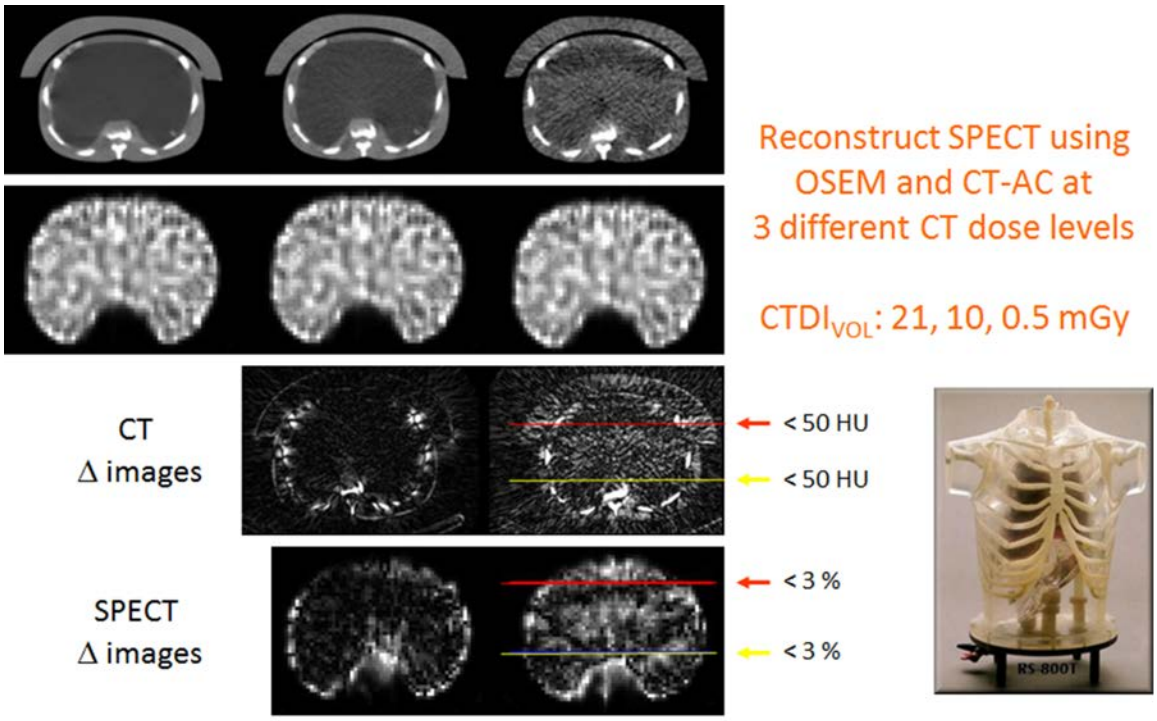

FIG. 94. The effect of CT noise on SPECT image quality of an anthropomorphic thorax phantom filled with ^{99m}Tc. The top row shows CT scans of increasing noise content (left to right). The second row shows the corresponding SPECT scan when reconstructed with these different CTs. The third and fourth rows show CT and SPECT subtraction images, respectively, to highlight the effect of CT noise on the resultant images. Even with large decreases in CT dose levels, the effect on the CT HU were less than 50 HU and the corresponding quantitative difference on the SPECT images were less than 3% (red and yellow lines).

and the corresponding HU changes. This change, however, has minimal impact on the SPECT image quality and quantification, as seen in Fig. 94. It is important to note that a large change in CT dose (21 to 0.5 mGy: 2% of the original dose) resulted in a change of only less than 3% in the SPECT image quantification. The reason for this small change is primarily due to image smoothing which is applied to the CT images before they are used for AC of SPECT data.

Guidance

A decrease in CT dose results in noisier CT images but has very little impact on the SPECT image quality and quantification.

4.5.4. Slow rotation time CT

Background

In some SPECT/CT systems, CT data are acquired with rotation speeds of several seconds. This can cause problems with patient motion being captured during the tube rotation, which results in inconsistent projection data, for example the anatomical distribution in the patient changes as the projection data are being acquired. A common artefact from this effect is seen in the abdomen, where gas in the gastrointestinal tract moves during tube rotation.

Case

Figure 95(A) illustrates an axial abdominal CT acquired on a slow rotation CT system. Involuntary patient movement during the scan has led to inconsistent projections, some of which originates from moving pockets of gas within the gastrointestinal tract. As a result, 'streak' type artefacts are seen in the transaxial data. Fortunately, when used for AC, the CT data are smoothed (B) to reduce the level of noise translated into the SPECT data so the streaks are not seen in the reconstructed emission data.

Guidance

In slow rotation CT systems, these artefacts are difficult to avoid. Faster rotation CT scanners are unlikely to create this type of artefact.

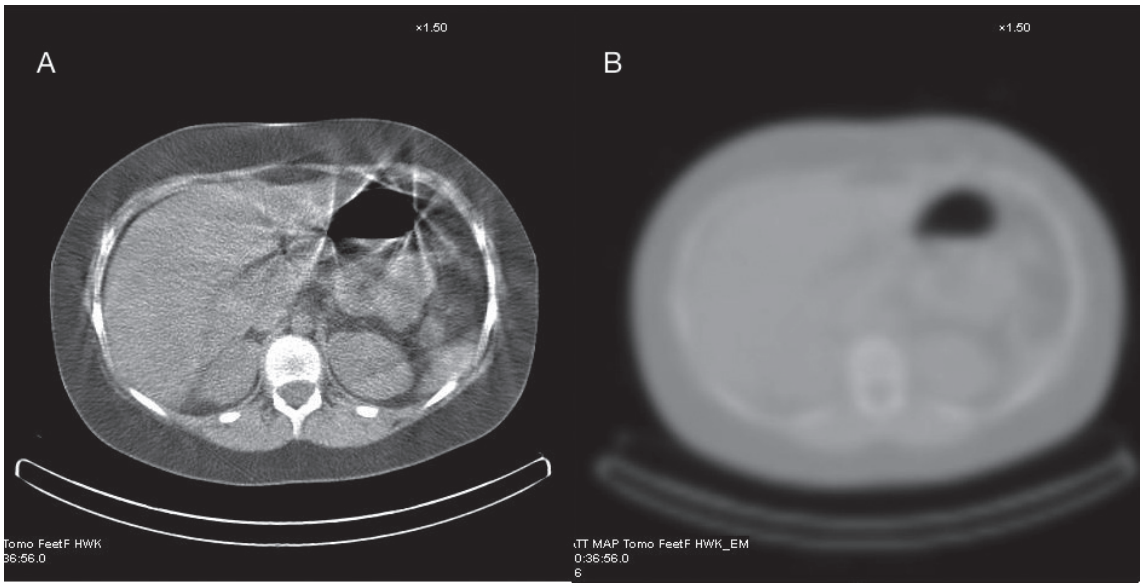

FIG. 95. (A) Transaxial CT data from a slow rotation CT scan of the abdomen and (B) data are smoothed for AC and loses the streak artefacts.

4.6. SPECT/CT ARTEFACTS

The introduction of SPECT/CT imaging has brought several advances to SPECT imaging, such as anatomical localization, AC and more recently quantification of SPECT data. However, the advent of this technology has also introduced several artefacts primarily arising from the use of CT images for AC of SPECT data. Examples of such artefacts include CT beam hardening due to high density material in the CT X ray beam such as metal objects or bone, CT contrast media, truncation, and misregistration between the CT and SPECT data.

4.6.1. Beam hardening artefacts

4.6.1.1. External metal objects

Background

As described in Section 2.3.2, metal objects will often create artefacts in CT owing to beam hardening and excess loss of photons (photon starvation). They will also erroneously reduce counts in the emission projection data, and these errors can propagate into the final SPECT images depending on the reconstruction algorithm's use of CTAC. In this section, such artefacts are demonstrated based on a phantom experiment.

Case

The experiment was performed on a Philips Precedence 16, with a NEMA image quality phantom with approximately 400 MBq of ^{99m}Tc in the background (40 kBq/cm^3), spheres and lung insert were left empty for simplicity. Several high density objects were used and they are listed in Table 3.

TABLE 3. METAL OBJECTS IMAGED

Object	Mass (g)	Material composition
(a) 2 euro coin	8.5	75% Cu, Zn, Ni
(b) Belt buckle	—*	—*
(c) Euro cent coins	14.6	Fe, Cu
(d) Gold earring	0.42	59% Au (Ag)
(e) Silver earring	0.28	Ag
(f) Gold ring	3.7	59% Au (Ag)
(g) Silver ring	5.0	Ag

* —: data not available.

The objects were attached to the sides of the phantom at different locations (see Fig. 96). A preview scan was performed at 120 kV followed by two CT scans, one at the lower and one at the upper bounds for the system X ray tube energy (90 kV (300 mAs) and 140 kV (200 mAs)). SPECT data were then acquired with 120 projections, 20 s per projection, in a 128 matrix. Images were reconstructed first with NAC and then using the two CT scans for AC including scatter correction and resolution recovery (Astonish kernel). No specific corrections were performed for the presence of metal. High CT values were clipped at 3000 HU.

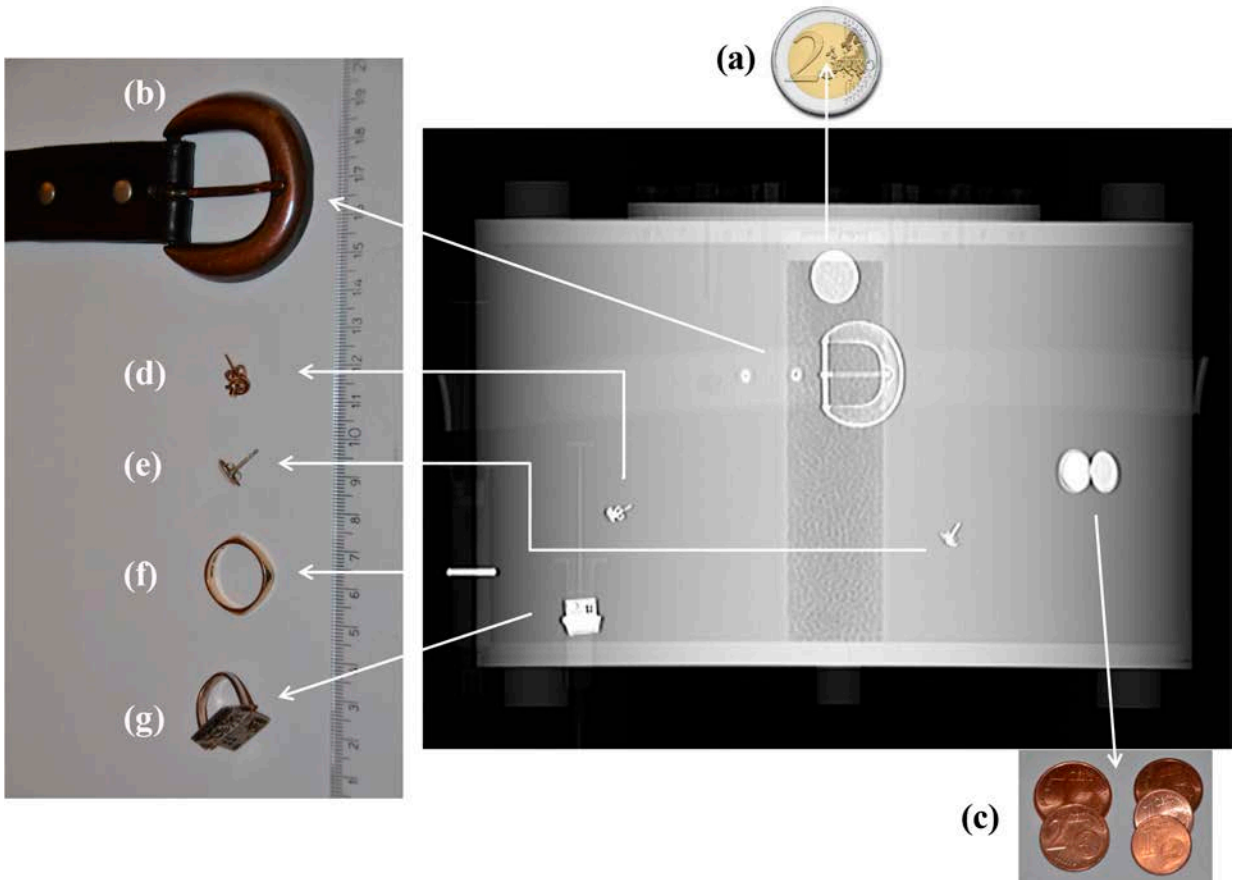

FIG. 96. Preview scan of the phantom with seven metal objects attached, all easily detectable. The finger rings (f) and (g) were mounted on water filled syringe 'fingers'. The remaining objects were taped directly to the surface of the phantom.

Figures 97–103 show a single slice of the NEMA image quality phantom at the location of each of the high density objects from Fig. 96. In each figure, the top row shows the NAC image. The other two rows display the AC SPECT images with their respective CTs at two different tube voltages: low (middle row) and high (bottom row).

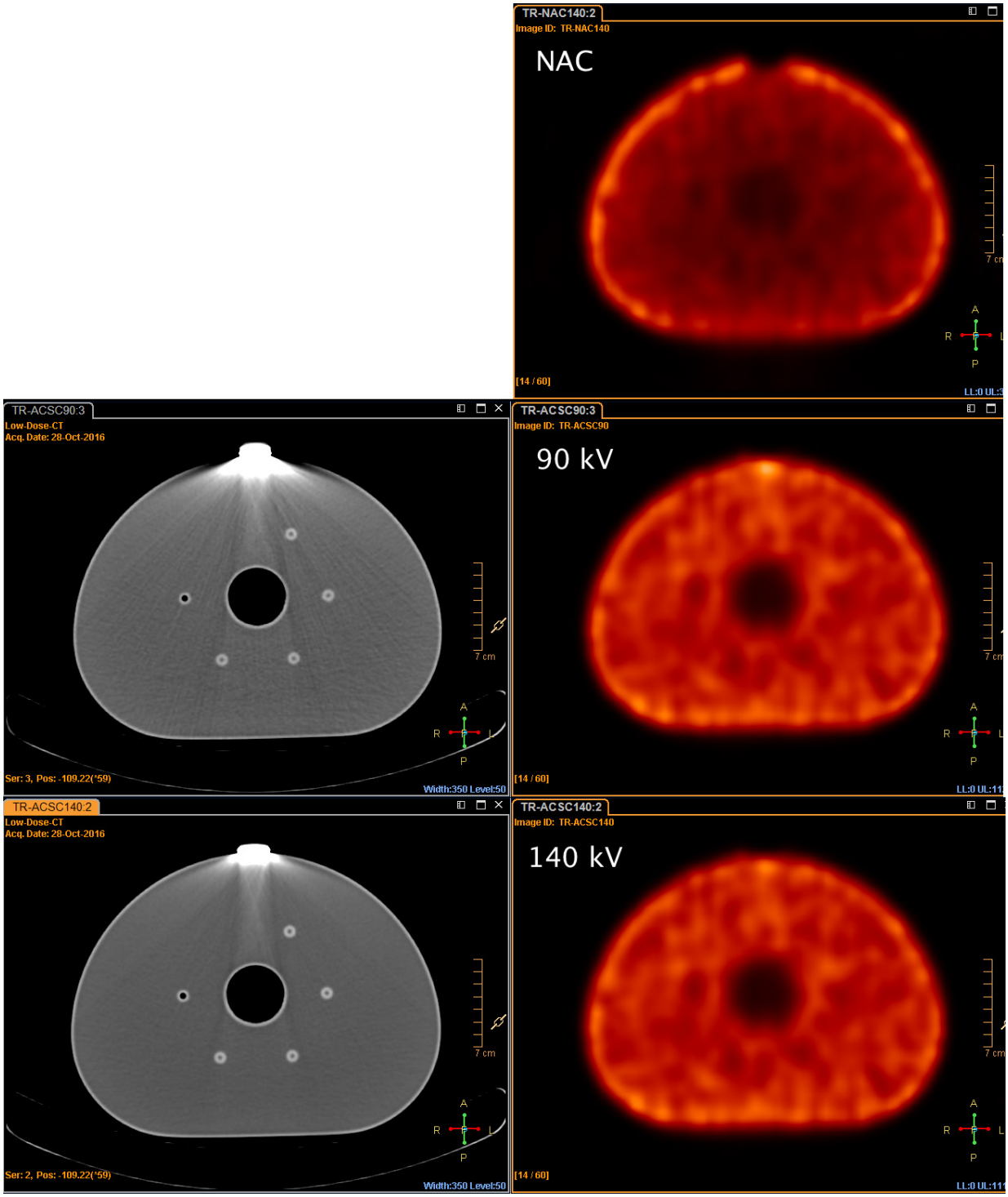

FIG. 97. A 2 euro coin on the surface of a ^{99m}Tc filled phantom.

In Fig. 97, the NAC image shows a lack of counts at the position beneath the coin. The metal is clearly visible on the two CT scans with some streak artefacts, more prominent at 90 kV than 140 kV. The AC images on the right displays a hot spot from overcorrection of the attenuation, more pronounced at 90 kV than at 140 kV (see also Fig. 13, Section 2.3.1, and Table 1).

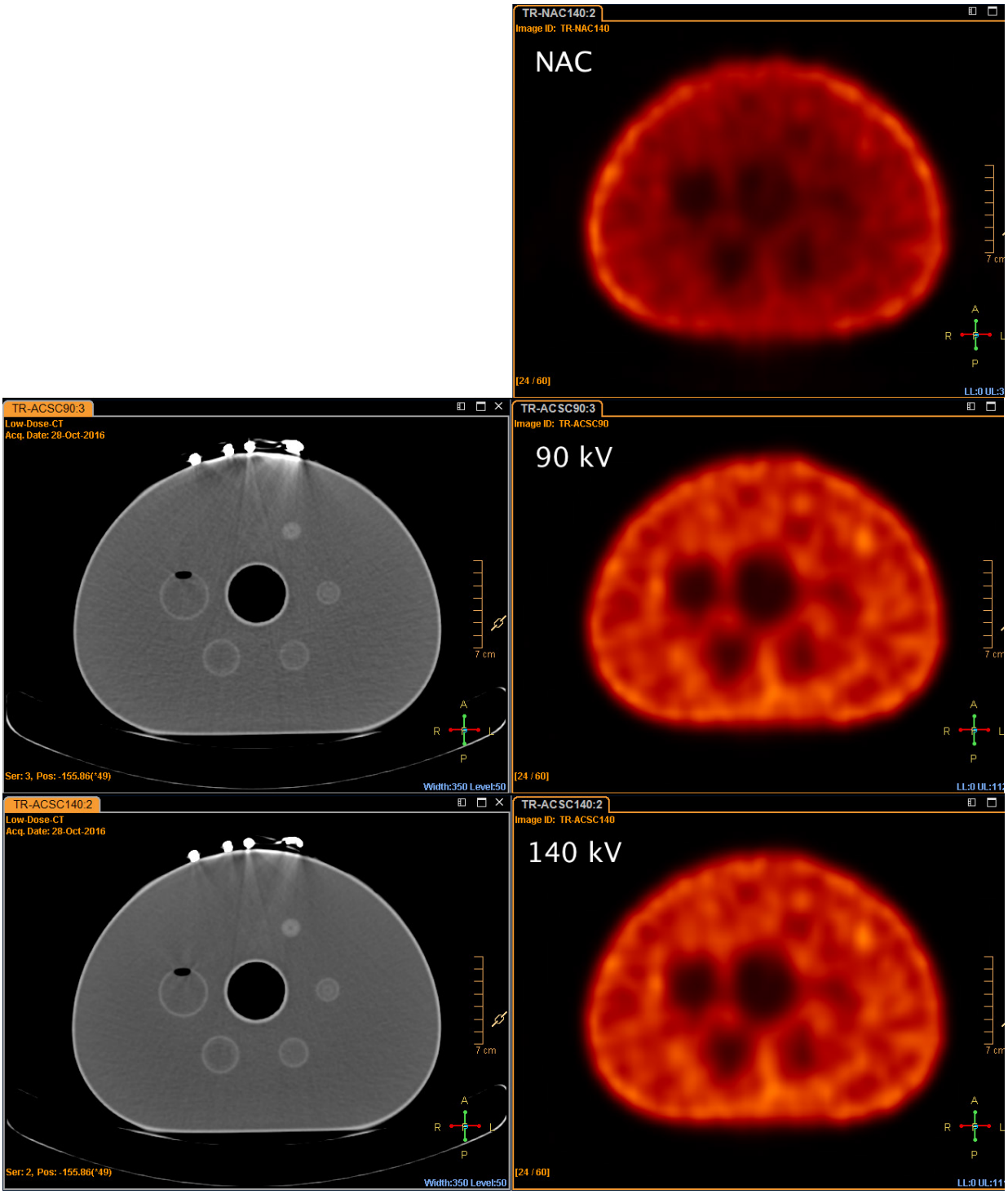

FIG. 98. A belt buckle on the surface of a ^{99m}Tc filled phantom.

In Fig. 98, the NAC image looks rather unaffected by the presence of the belt, presumable made of rather light materials. The metal parts, however, are clearly visible on the two CT scans with weak artefacts, more prominent at 90 kV than 140 kV. The AC images on the right do not show clear indications of artefacts.

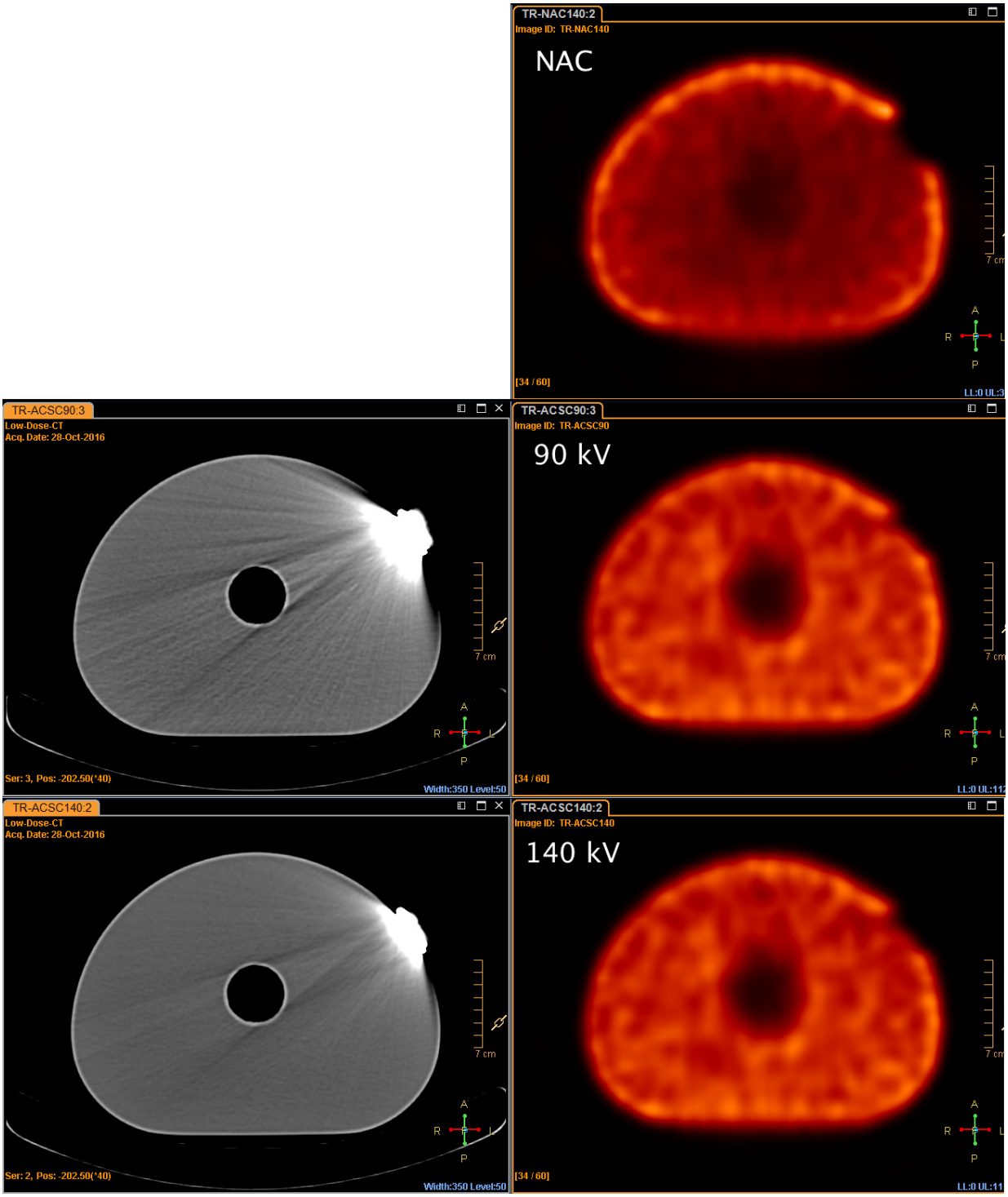

FIG. 99. Euro cent coins on the surface of a ^{99m}Tc filled phantom.

In Fig. 99, the NAC image shows a significant lack of counts at the position beneath the coins. The metal is clearly visible on the two CT scans with strong streak artefacts, more prominent at 90 kV than 140 kV. The AC images to the right still displays a count deficit, not entirely corrected by the CTAC.

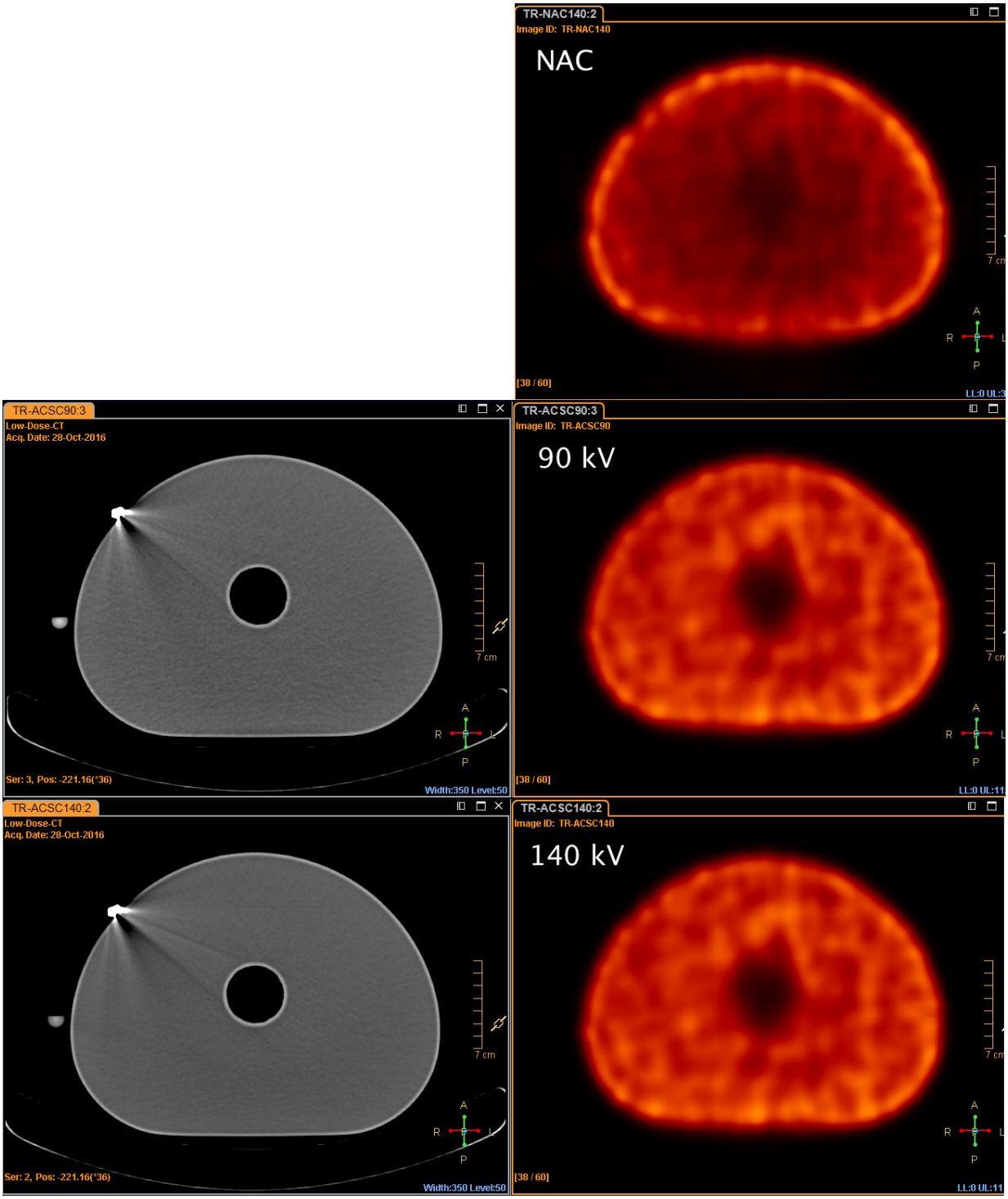

FIG. 100. Gold earring on the surface of a ^{99m}Tc filled phantom.

The tiny object of a gold earring is barely visibly in the NAC image in Fig. 100. The metal creates local streak artefacts on the two CT scans with little or no difference between 90 kV and 140 kV, which may be explained by the abrupt change in absorption properties of gold changing at the K edge (80 keV) (see also Fig. 13 and Table 1). In the AC images on the right, no artefact is visible.

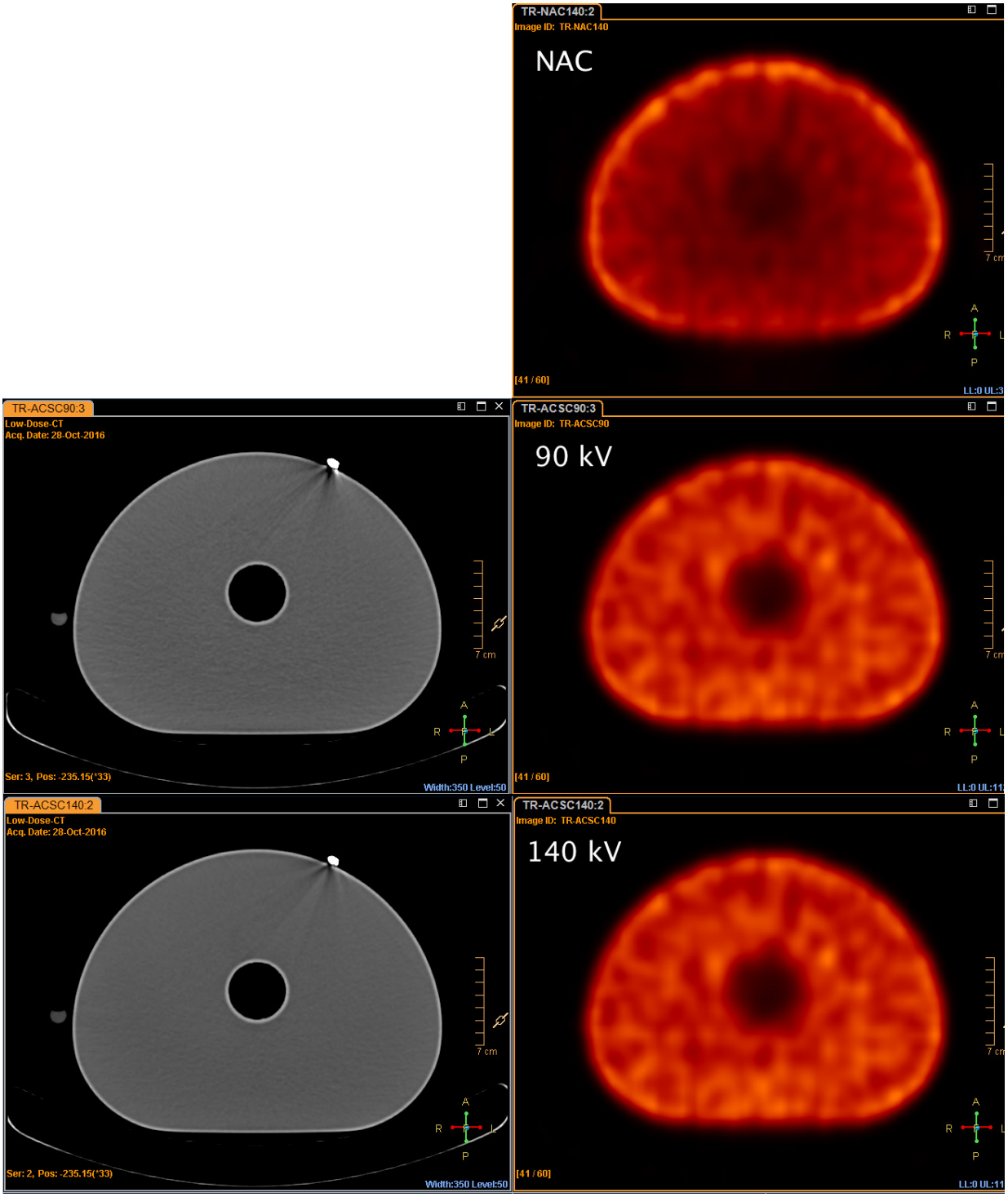

FIG. 101. Silver earring on the surface of a ^{99m}Tc filled phantom.

Similarly, with the silver earring in Fig. 101, the tiny object is barely visibly on the NAC image. The metal creates weak local streak artefacts on the two CT slightly worse with 90 kV than with 140 kV, and an artefact is not visible in the AC images on the right.

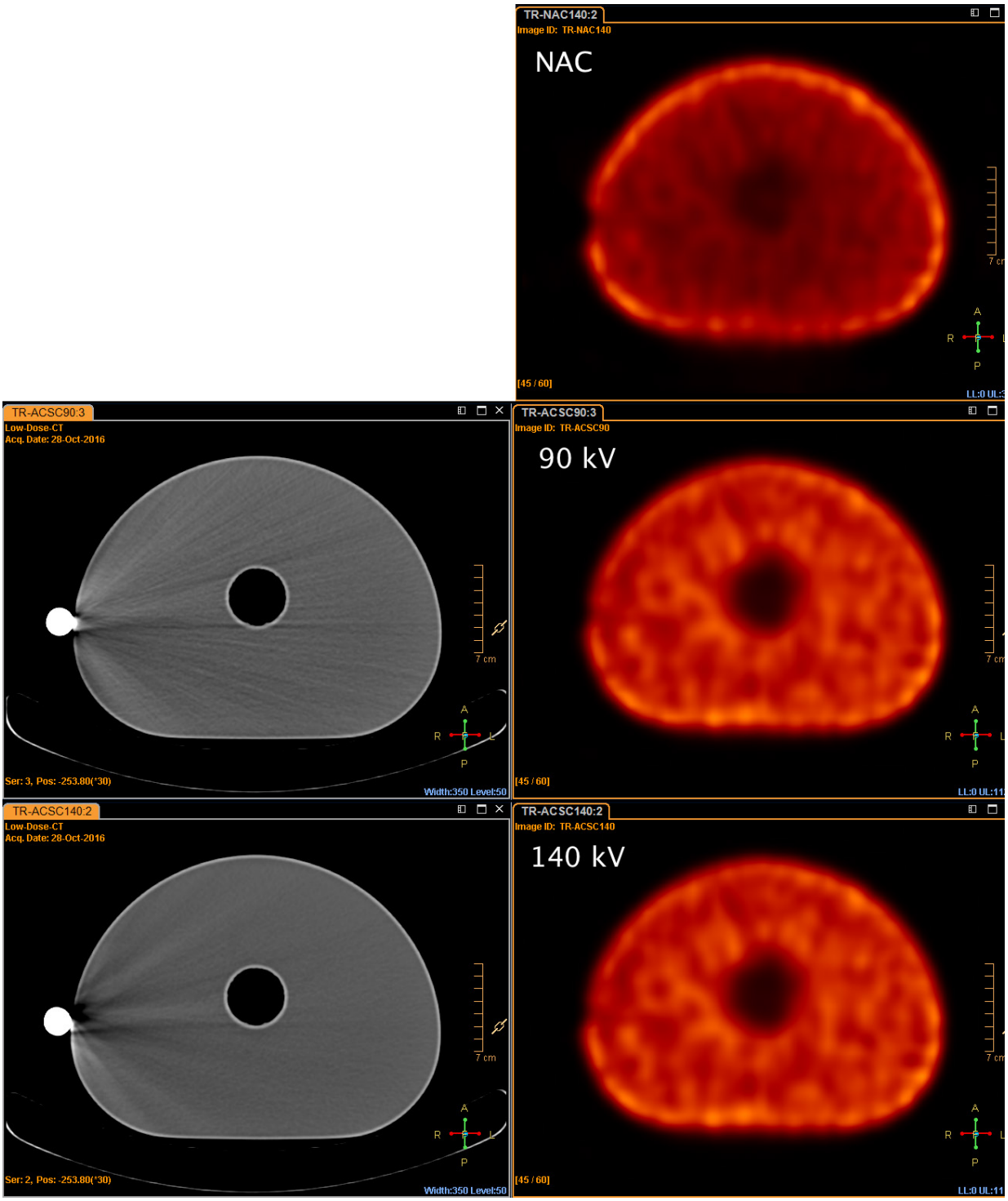

FIG. 102. Gold ring on the surface of a ^{99m}Tc filled phantom.

The gold ring creates a surface 'hole' in the NAC image in Fig. 102. The metal creates strong streak artefacts on the two CT scans with little difference between 90 kV and 140 kV which, again, may be understood from the absorption properties of gold (see Fig. 13). The count loss is partially corrected by the CTAC images to the right.

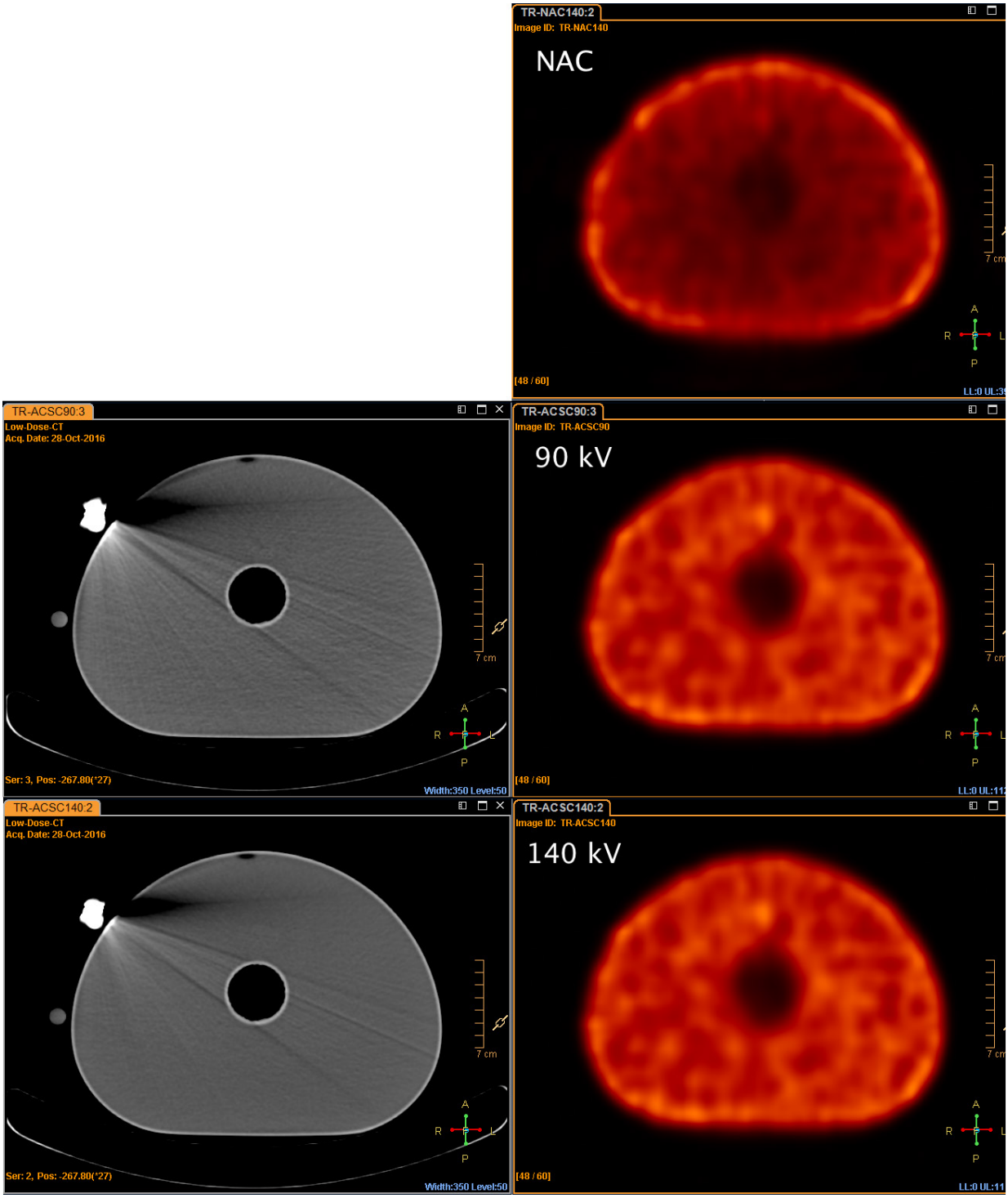

FIG. 103. Silver ring on the surface of a ^{99m}Tc filled phantom.

The silver ring is hardly visible in the NAC image in Fig. 103. Yet, the metal creates strong streak artefacts on the two CT scans, more evident at 90 kV than at 140 kV. The artefacts do not propagate into the CTAC images in a visible manner.

Guidance

The preview scan should be inspected for any kind of metal objects to be removed if possible, even if quite small. The effect on both CT as well as the final corrected SPECT images is difficult to predict, since it depends on the size, material composition and geometry of the object as well as the CT energy chosen and the activity distribution (not included in this simple simulation).

4.6.1.2. Prostheses

Background

In some patients, it is impossible to avoid CT beam hardening effects when performing SPECT/CT studies. Indeed, in some orthopaedic referrals, it may be the prosthesis itself that is the reason for the SPECT/CT study. The presence of prostheses can affect both CT and SPECT images.

Case A

Imaging of bone surrounding prostheses is a common referral for SPECT/CT. In Fig. 104, the upper and lower parts of a knee prosthesis in the right knee (left side) can be seen. In Fig. 105(A), a transaxial slice through the lower part of the leg shows radial streak artefacts coming from the very dense centre of the prosthesis, which extend into the opposite leg — a known metal beam hardening artefact. Figure 105(B) shows the bone SPECT image from the same patient, together with the count profile from NAC reconstructed data (blue) and the ratio of CTAC to NAC counts in red.

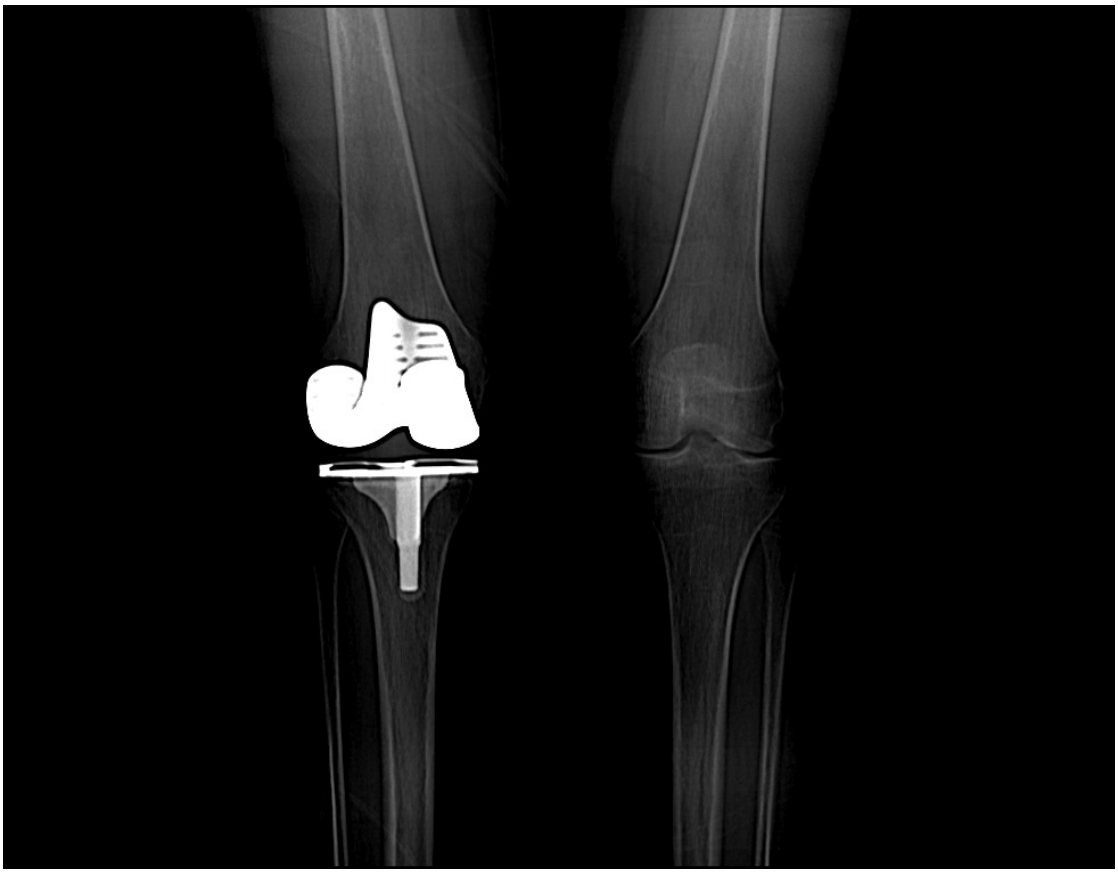

FIG. 104. Knee prosthesis in situ in an X ray preview scan.

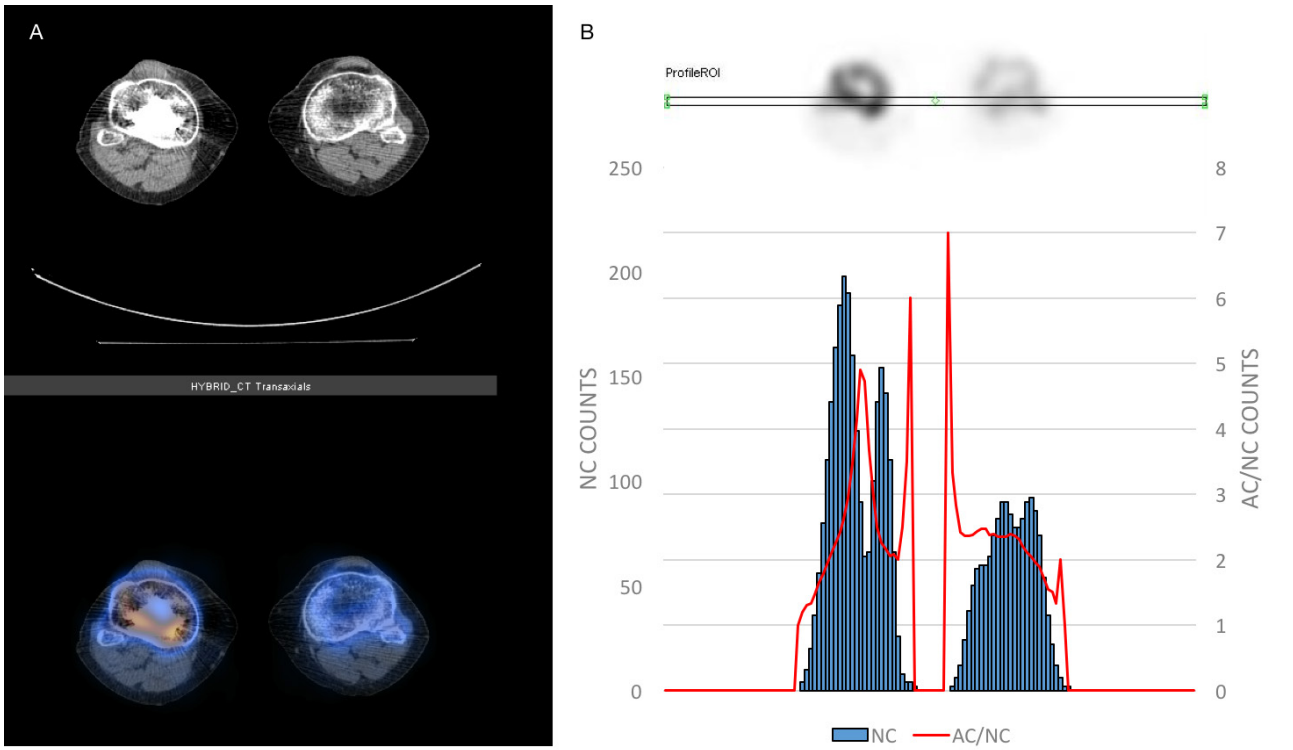

FIG. 105. (A) CT and fused bone SPECT/CT images through the lower part of the knee prosthesis and (B) bone SPECT profile showing the NAC counts (blue) and the ratio of CTAC to NAC counts (red).

The two central red peaks and the smaller, right most peak corresponding to the outside of the leg represent some misregistration between the emission and CT for AC — possibly due to patient movement. The dip between these peaks is a consequence of there being no counts between the legs in the uncorrected image, leading to a void in the plot. The centre of the knee prosthesis displays a clear reduction in counts because of the lack of bone tissue, but the AC attempts to correct for the high attenuation in this area. Whether this correction is adequate for a material that is very dense and outside the typical HU range is unknown, but it is unlikely to be under corrected for attenuation. The smoothness of the profile through the rest of the knee suggests that the streak beam hardening artefacts have not significantly degraded the AC.

Case B

A patient who had undergone spinal surgery was referred for a bone SPECT/CT scan to better understand the source of the patient's pain. A CT preview scan of the patient highlights two thin spinal prosthesis spanning from the upper thoracic to upper lumbar vertebrae (see Fig. 106). In Fig. 107(a), a metal artefact can be seen with dark streaks (green arrows) occurring along the lines of greatest attenuation and emanating from the two spinal prostheses. The reconstructed emission data in Fig. 107(b) together with the profile of NAC counts (blue) and ratio of CTAC to uncorrected counts show that overcorrection of counts in the small of the back (the lower curved part of the back) can again be seen because of movement causing misalignment between emission and CT scans. Furthermore, correction over the spinal prosthesis shows a step reflecting the correction for the dense prosthesis material.

Guidance

When imaging areas that contain metal prosthesis, there is an effect on CT image quality. As a consequence, there can also be an effect on SPECT image appearance and quantitative accuracy. However, the use of heavy

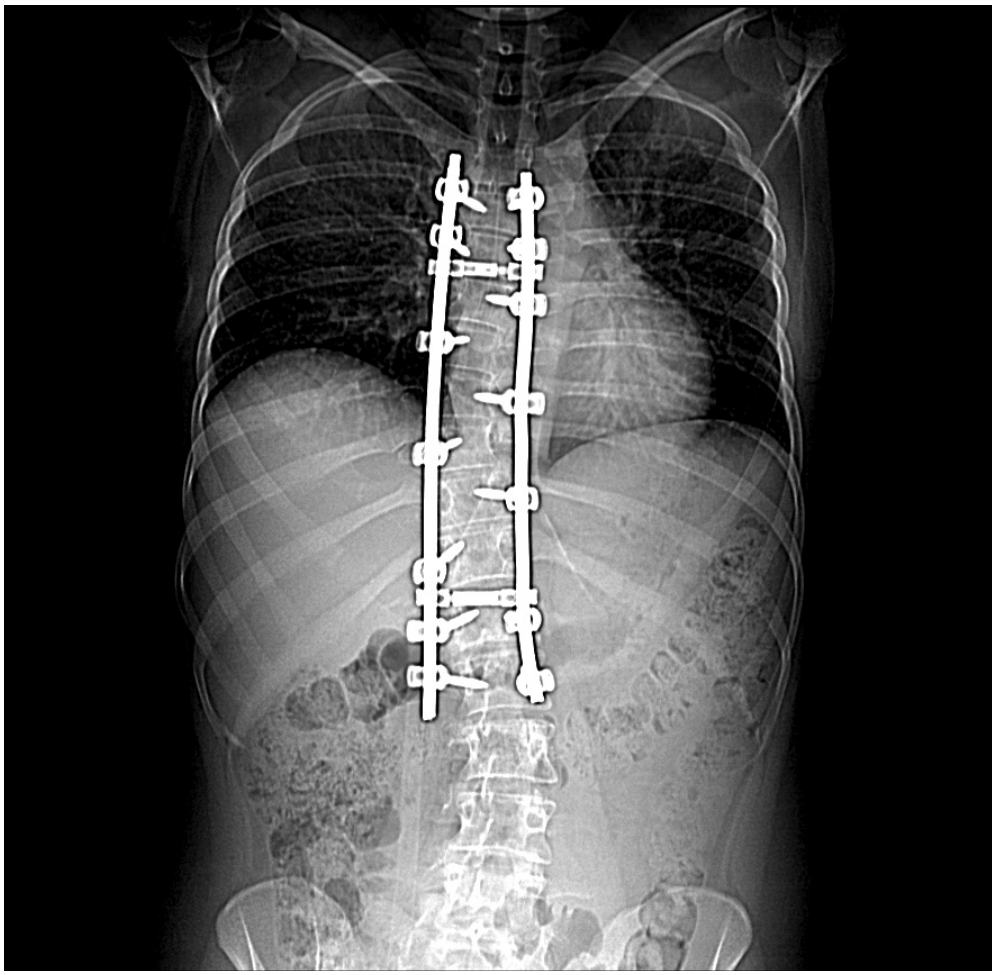

FIG. 106. X ray preview scan of the spine with spinal prosthesis in situ.

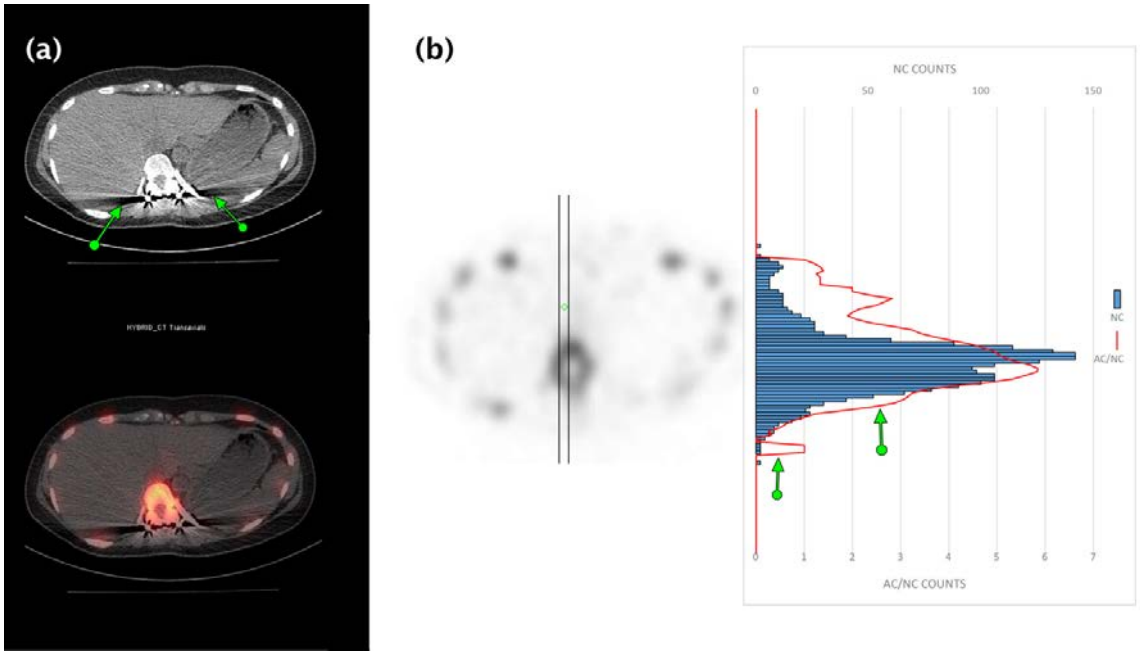

FIG. 107. (a) CT and fused bone SPECT/CT images through the spine and prosthesis and (b) bone SPECT profile showing the NAC counts (blue) and the ratio of CTAC to NAC counts (red).

smoothing kernels during the CTAC process can remove most small metal artefacts, and the use of extended HU scales can minimize the under correction for attenuation of SPECT.

4.6.1.3. Arms down versus arms up

Background

Whenever possible, patients undergoing a SPECT examination of the thorax or abdomen should be positioned with their arms above the head to minimize attenuation. The attenuation of one arm may well constitute a half value layer at the photon energies applied in both CT and nuclear medicine. Excess attenuation can result in photopenia and beam hardening artefacts in CT that may influence the resulting SPECT images.

Case

The effect is here exemplified in a phantom study using a body phantom with 1 L infusion bags attached to simulate the arms (see Fig. 108), and ^{99m}Tc was added to the phantom and the infusion bags to a concentration of approximately 40 MBq/L (total of 500 MBq). The phantom was scanned on a Siemens Symbia SPECT/CT and a selection of CT parameters was applied to simulate low dose as well as diagnostic scans (see Figs 109–112). SPECT was performed over an hour to improve statistics and thereby also improve the visibility of potential effects implied by the CTAC. Reconstruction was made with Flash3D (8 iterations, 4 subsets), including scatter correction.

Guidance

For SPECT image quality, it is generally better if the patient can keep the arms above the head for the duration of the examination, avoiding the excess attenuation from the arms. If this is not possible in a SPECT/CT study, the CT settings should be sufficient to provide the information requested.

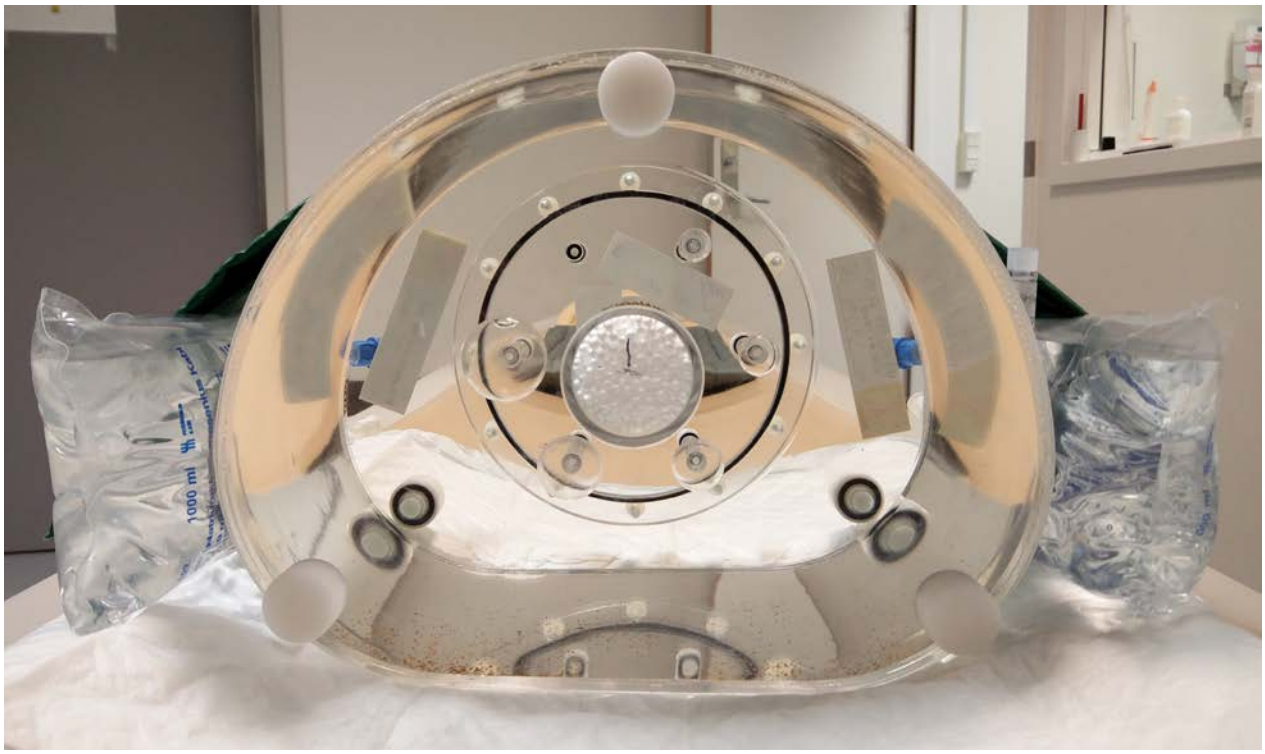

FIG. 108. Body phantom with 'arms' attached.

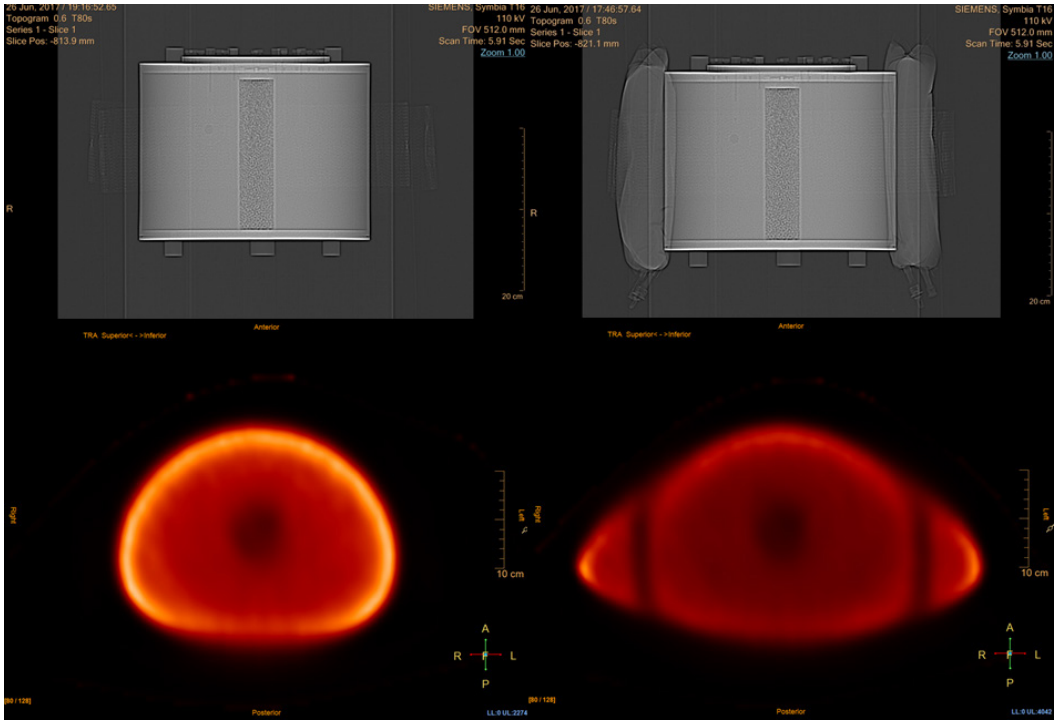

FIG. 109. Preview of the body phantom without and with arms attached in the form of infusion bags (top row); NAC reconstruction of phantom without and with attachments (bottom row).

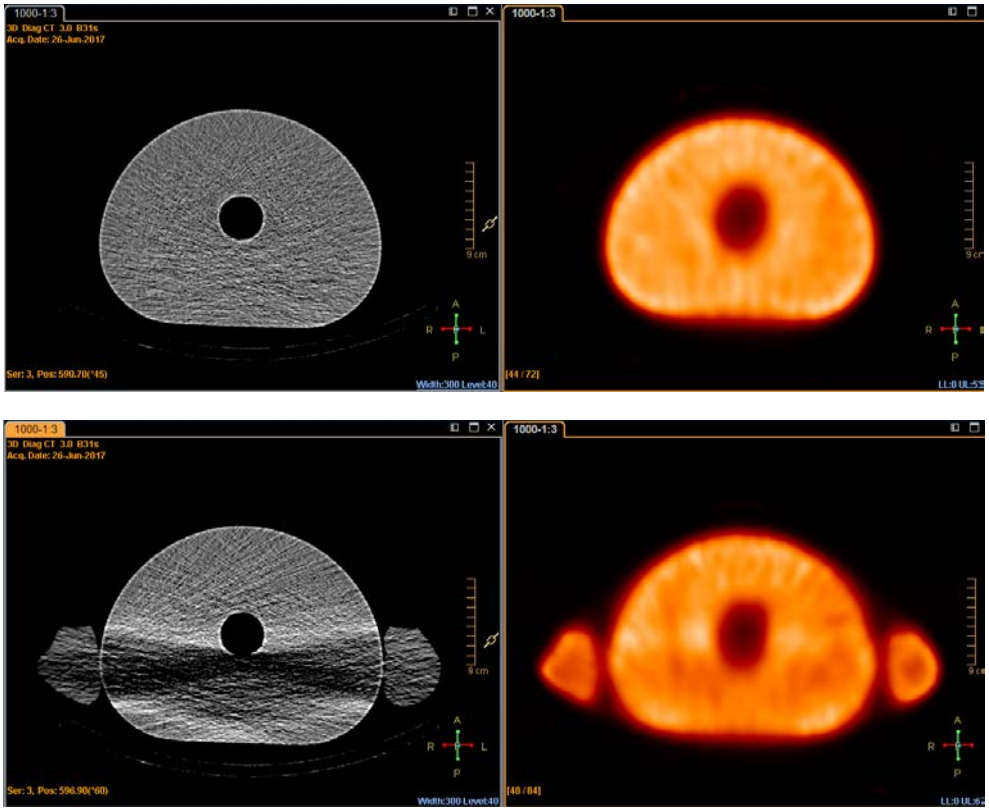

FIG. 110. CT scan of 80 kV and 10 mAs, significant beam hardening artefacts are observed in the CT image when the arms are down along the body. The influence in the SPECT image is visible.

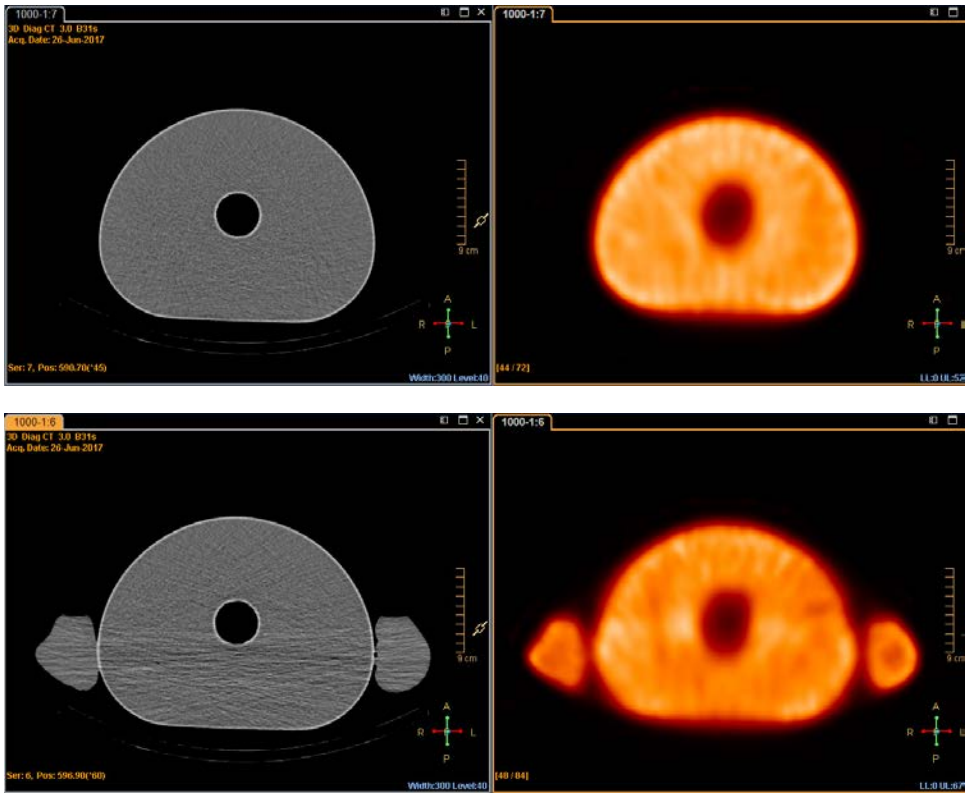

FIG. 111. CT scan of 80 kV and 100 mAs, artefacts are still visible in the CT images with the arms down. Owing to the soft filter applied to CT before the calculation of CTAC, the streaks do not propagate into the SPECT image, but quantitation is affected.

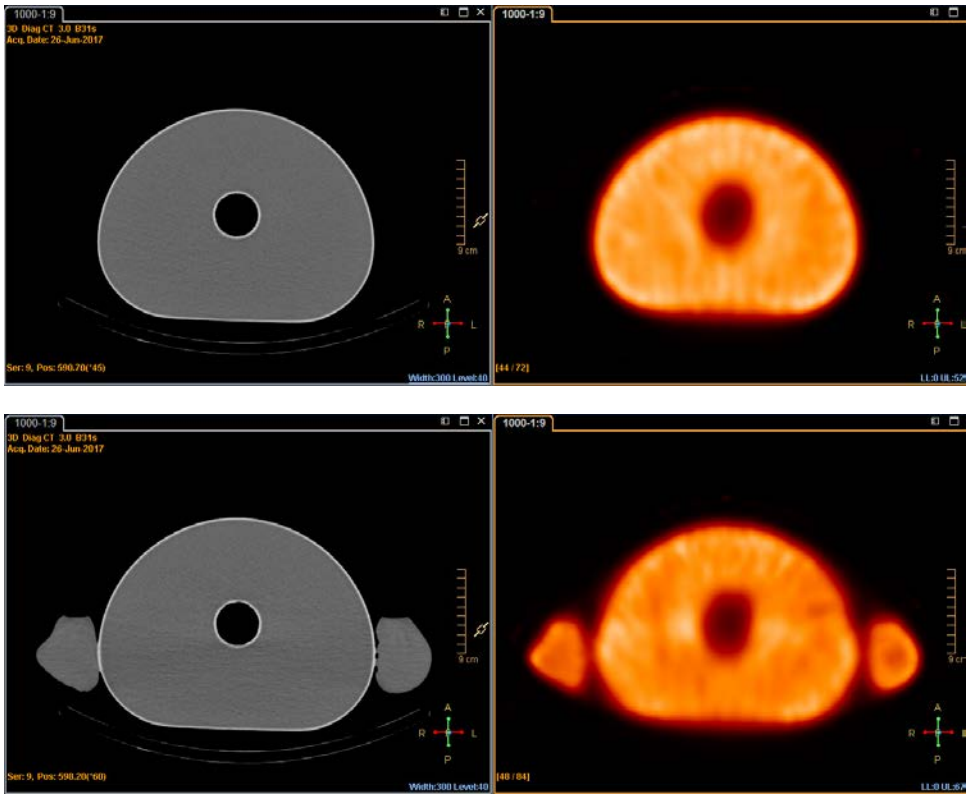

FIG. 112. CT scan of 130 kV and 170 mAs only a faint shadow is observed in the CT image, even with the arms down, and the influence on SPECT is negligible.

4.6.2. Contrast CT: Negative contrast

Background

In SPECT/CT imaging, negative contrast such as gas pockets can cause image artefacts owing to the transition of the gas pocket in the gastrointestinal tract between the time of the CT and SPECT data acquisition (see Fig. 95, Section 4.5.4).

Case

In Fig. 113, a CT scan (A) and corresponding attenuation map (B) illustrate an example of an air pocket present in the CT scan which is not present in the SPECT acquisition (C) due to the transition of the air pocket

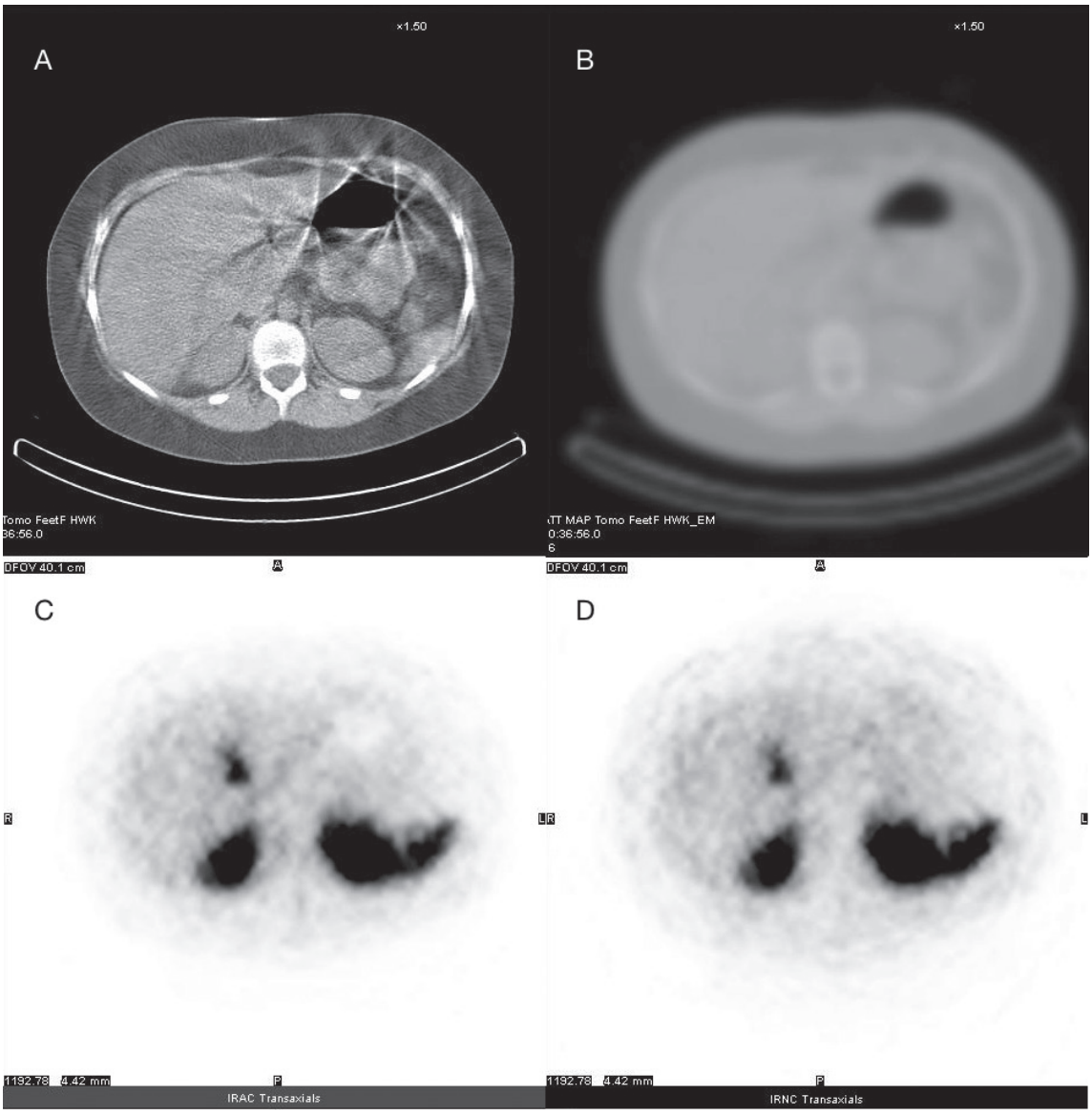

FIG. 113. (A) Transaxial CT data from a slow rotation CT scan of the abdomen showing an air pocket in the gastrointestinal tract and (B) corresponding CT attenuation map clearly showing the air pocket. (C) The AC SPECT slice clearly shows the air pocket indicating that the erroneous presence of the air pocket in the image is due to the AC process. (D) The corresponding uncorrected SPECT slice shows the absence of the air pocket indicating that the air pocket had transitioned between the acquisition of the CT and SPECT data.

in the abdomen/gastrointestinal tract between the CT and SPECT data acquisition times. As a consequence, the AC data (D) show an area of reduced counts (photopenic area) at the position of the gas pocket. This reduction in counts is not seen in the uncorrected data (C), indicating that the effect was introduced by AC.

Guidance

The transition of air pockets between CT and SPECT acquisitions can lead to artefacts that manifest as photopenic areas in the reconstructed SPECT images. Unfortunately, such artefacts are unavoidable in SPECT/CT imaging.

4.6.3. Truncation

Background

On SPECT/CT systems, the CT transaxial FOV is typically limited to a maximum diameter of 50 cm because of the geometry of the CT tube and detector array used in CT scanners. On some occasions, the CT scan might be truncated (i.e. part of the patient may be outside the CT FOV). This can occur with patients with large body habitus with diameters greater than 50 cm, or when patients are mispositioned in the CT scanner so that parts of the body fall out of the FOV.

Case A

In the bone SPECT/CT study of the neck and shoulder area shown in Fig. 114(A), it is clear that there is truncation of CT data on both shoulders (red arrows). This truncation is due to the position of the patient being too low in the CT FOV. A transaxial slice of SPECT data through the same area is also shown (B), with the count profile from NAC reconstructed data (blue) and the ratio of CTAC to NAC counts in red. In the areas of truncation, there is clear underestimation of counts — best seen in the AC transaxial image shown and the sharp drop at the

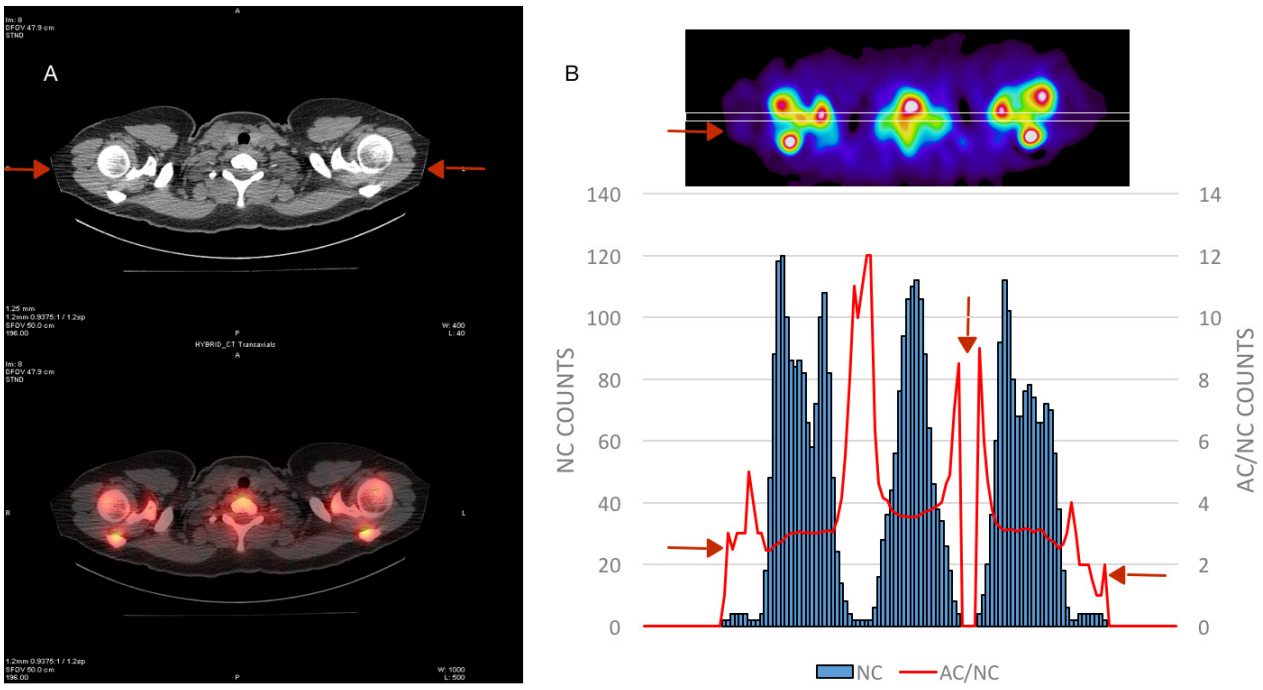

FIG. 114. (A) A CT and fused SPECT/CT image of the neck and shoulder area showing truncation in both shoulders on the CT data, and (B) bone SPECT profile showing the NAC counts (blue) and the ratio of CTAC to NAC counts (red).

very edge of the AC/NAC ratio on the right shoulder (left side). There is also a small amount of motion in the left shoulder (right side), which is shown as a peak on the other side of the AC/NAC ratio. In the space between the neck and the left shoulder, the peaks and sharp drop in the AC/NAC ratio are a consequence of the lack of counts in this area with NAC (zero), which if counts were present would match the profile seen on the opposite side because of the bone present in this area.

Case B

A coronal view of an ^{111}In labelled monoclonal antibody radiotracer SPECT/CT scan of a patient showing truncation along both arms of the patient is shown in Fig. 115. The CT truncation results in large CT numbers adjacent to the truncated anatomy (red arrows), which in turn also results in an artificial boosting of the radioactivity uptake in these areas (white arrows).

Guidance

CT truncation has an effect on AC emission data and should be avoided wherever possible by positioning patients centrally in the FOV. Some systems offer the ability of extended CT FOV reconstruction, which uses non-truncated projections to estimate the signal outside the standard FOV [51]. Iterative CT reconstruction may also offer better solutions with truncated CT data than FBP. Nevertheless, these CT reconstructions are estimates and truncation should be avoided wherever possible.

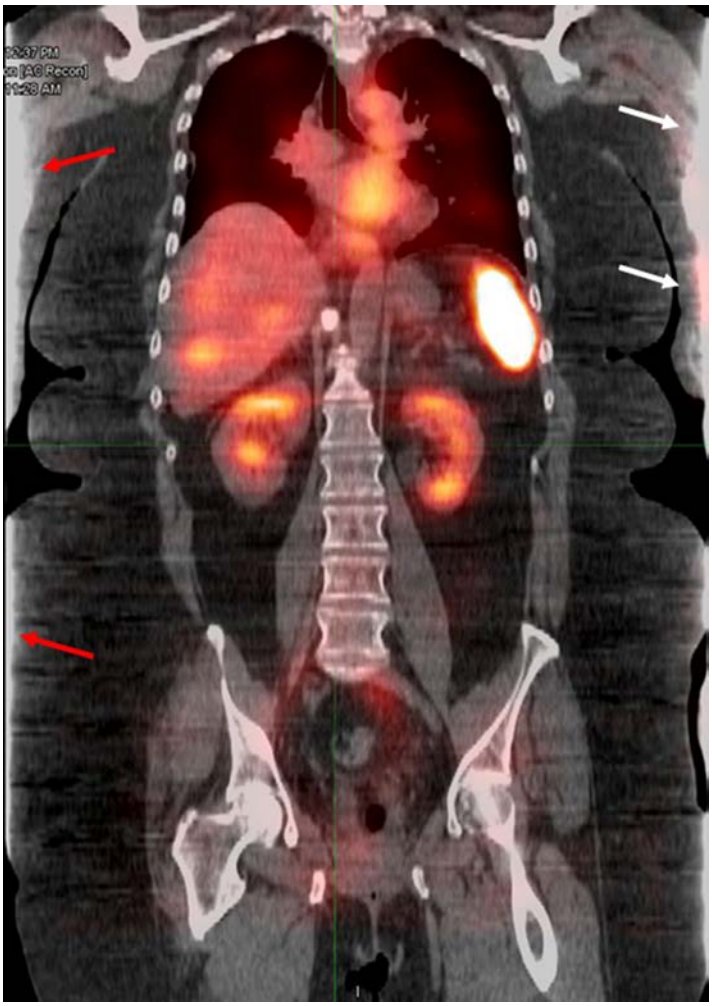

FIG. 115. A coronal view of an ^{111}In labelled monoclonal antibody radiotracer SPECT/CT scan of a patient showing truncation along both arms of the patient.

4.6.4. Misregistration

4.6.4.1. Cardiac

Background

In many centres, when performing myocardial perfusion SPECT imaging, it is common to acquire a CT in the same examination to correct for photon attenuation. This can be helpful to deal with attenuation from breast tissue in women or diaphragmatic attenuation in men, both of which can lead to the false positive reporting of myocardial ischemia or infarction. However, since SPECT and CT are performed sequentially on SPECT/CT systems, there is the possibility for mismatch in the emission and AC data. This is particularly problematic in the thoracic region where the heart is located. Breathing can easily lead to the misregistration of data in this region because the SPECT images are an average representation of uptake through the respiratory cycle, while the CT is a snapshot of anatomy at a particular respiratory phase. Misregistration of SPECT and CT data can induce artefactual changes in the displayed myocardial blood flow polar map.

Case A

A 66 year old women with previous myocardial infarctions and stents was referred for a myocardial perfusion study after complaining of dizziness and chest pain. A pharmacological stress myocardial perfusion SPECT/CT imaging study was performed after the injection of 866 MBq of ^{99m}Tc-MIBI.

Figure 116(A) shows the position of the CT in relation to the SPECT data, with clear misregistration in the apex of the heart. This leads to a mild apical defect (B). When the misregistration is corrected (C), the appropriate AC is applied, and the severity and extent of this apical defect changes slightly.

Guidance

In cardiac SPECT/CT imaging, misregistration of emission and AC data from patient breathing is possible. There is no easy method of reducing the likelihood of this artefact. Software postprocessing of the data to correct for misregistration should be performed before reporting to ensure that the images can be interpreted correctly, although any significant difference in the shape of the liver or spleen cannot be corrected for.

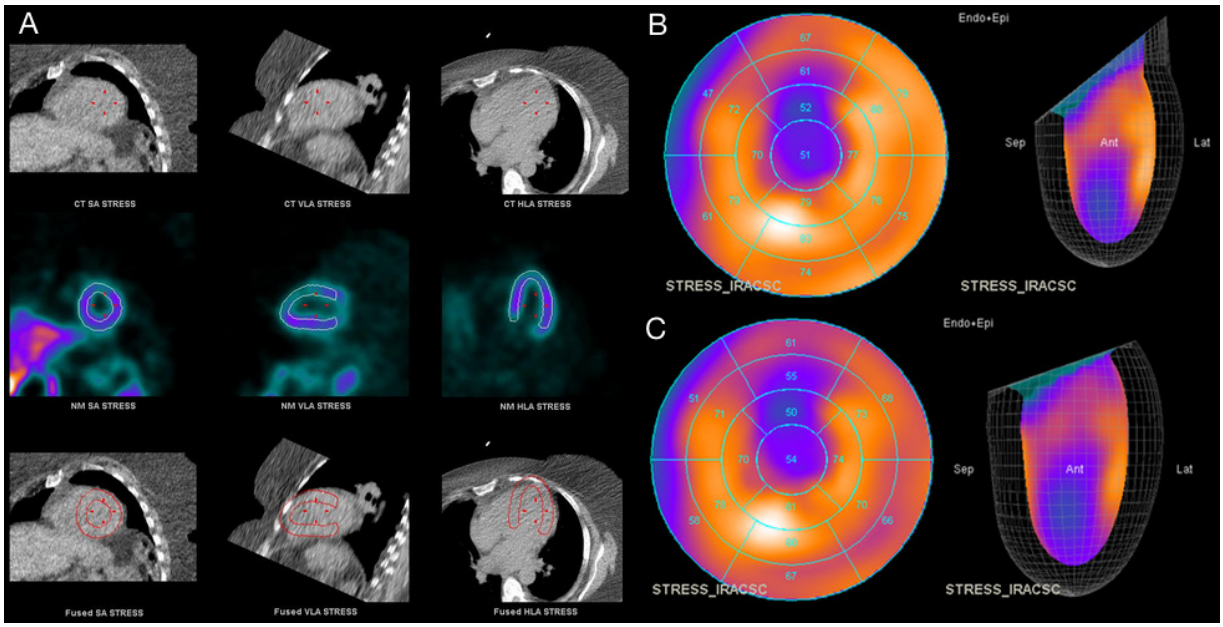

FIG. 116. Stress myocardial perfusion SPECT/CT study showing (A) misregistration of SPECT and CT data that results in (B) a small apical defect. (C) Once the misregistration is corrected, the severity and extent of the apical defect changes.

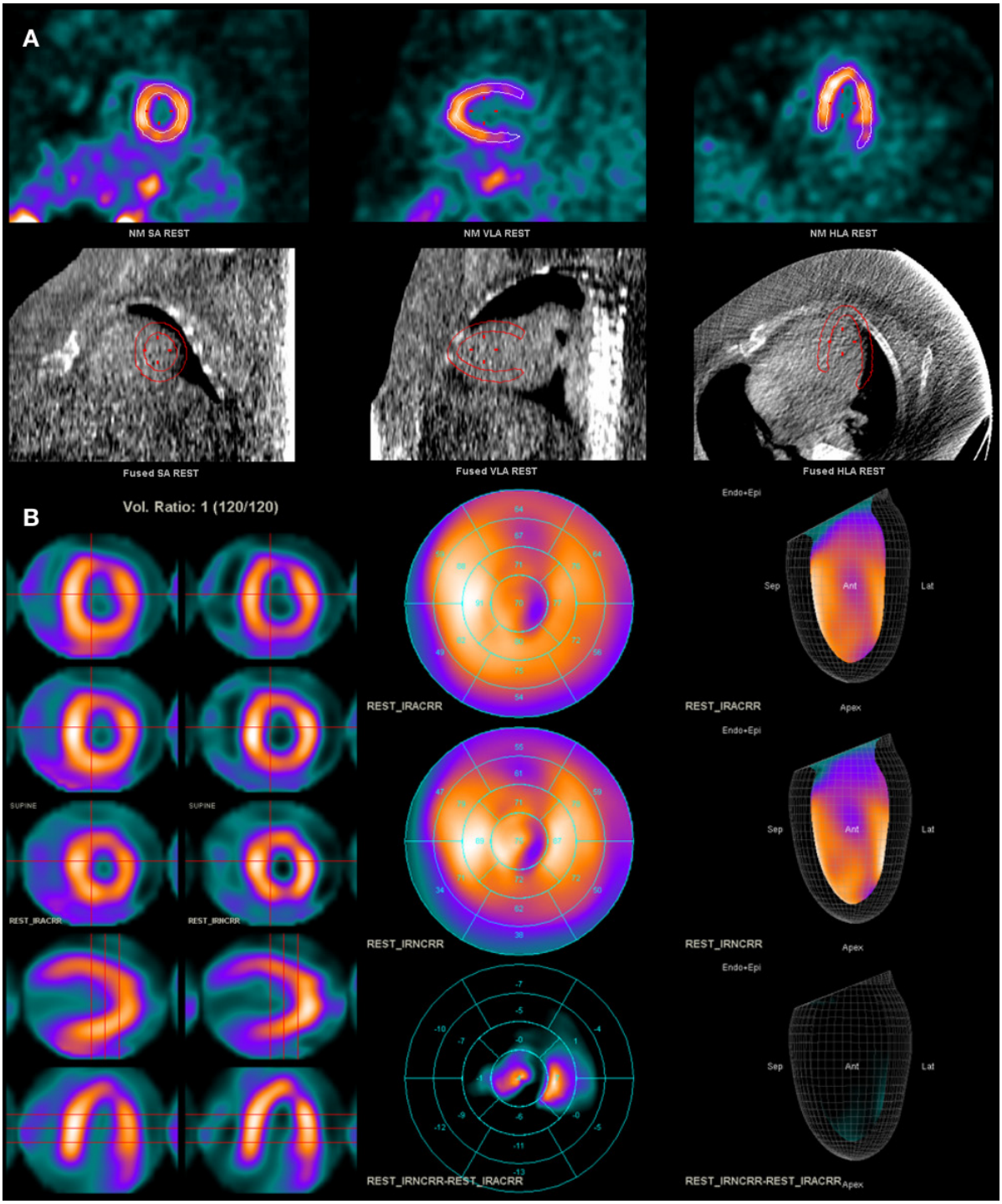

FIG. 117. (A) Myocardial perfusion SPECT/CT study showing misregistration between the emission and CT for attenuation scan and (B) the resulting AC images and polar maps from this misregistration (IRACRR) together with NAC (IRNCRR).

Case B

In Fig. 117(A), the misregistration of emission data with CT data can be seen, showing the apex of the heart on the emission data encroaching beyond the chest wall, and the lateral wall of the myocardium on SPECT positioned in the lung on the CT. The consequences of this misregistration are shown in Fig. 117(B), where slice and polar plot AC (IRACRR) data, and NAC (IRNCRR) data are shown.

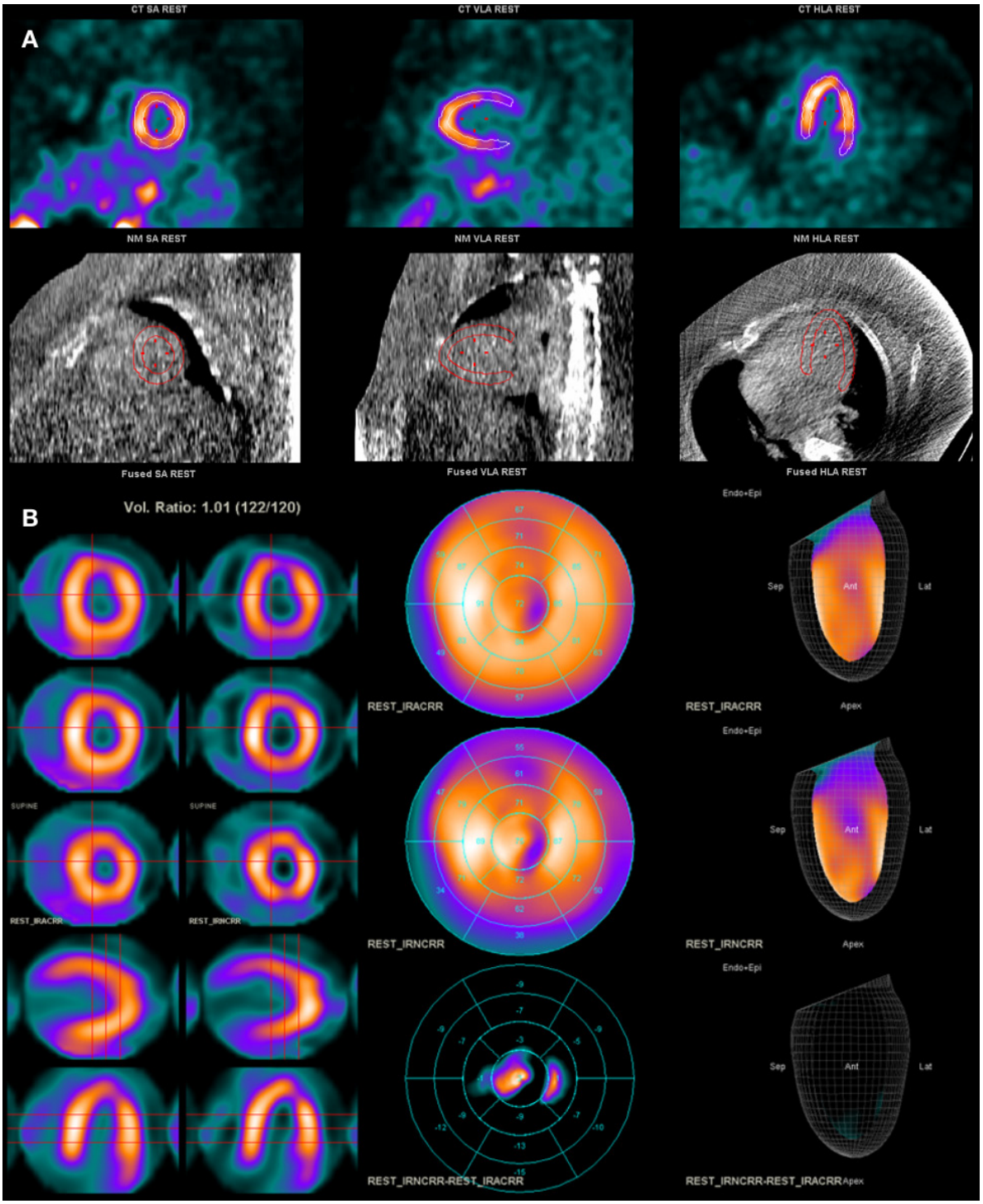

FIG. 118. (A) Myocardial perfusion SPECT/CT study showing good registration between the emission and CT for attenuation scan and (B) the resulting AC (IRACRR) and NAC (IRNCRR) reconstructed images and polar maps from this registration.

Case C

In Fig. 118, the same patient study as Case B is shown with good registration between emission and CT for AC scans. Comparing the two data (good and bad registration), the difference in counts in the polar plots with and without AC shows that misregistration in the apex leads to a relatively small change in the accuracy of the AC because of the small difference in the attenuation of myocardium and soft tissue beyond the chest wall. However,

the lateral wall misregistration shows a bigger difference (most clearly seen in the polar plots) owing to the large difference in attenuation between soft tissue and lung.

Guidance

Misregistration of CT and SPECT has a detrimental effect on the accuracy of AC used for myocardial perfusion SPECT/CT studies. Most system manufacturers provide software to correct for any misregistration. Use of this software avoids any potential misinterpretation of clinical myocardial perfusion studies.

4.6.4.2. Respiratory motion

Background

Mismatch between transmission and emission data is relatively common in SPECT/CT imaging of the thoracic region. With a breathing cycle typically taking around 6 s, a 15–20 s SPECT projection will capture an average image over the time period. However, a CT over the same area can take just over a second, and therefore captures the respiratory cycle at a particular phase. During a typical breathing cycle, most time is spent in the end expiration phase, which means that misregistration between SPECT and CT is often avoided or is small in magnitude. However, if CT captures an inspiration phase misregistration will be seen — typically in the base of the lung or in the dome of the liver where motion is largest.

In addition to misregistration, there can also be additional artefacts when CTAC is performed. These present as an underestimation of the signal in the liver, and can also lead to an underestimation in the uptake in the inferior wall of the heart in myocardial perfusion studies.

Case

A 65 year old man with metastatic neuroendocrine cancer was sent for post-therapy scanning following a therapeutic 7.7 GBq infusion of ^{177}Lu-DOTATATE. In the SPECT/CT scan acquired 24 hours post-infusion (see Fig. 119), there is mismatch between the CT scan used for localization and AC, and the SPECT data. The likely cause of this misregistration is the acquisition of CT data in an inspiration phase. The dome of the liver from SPECT (D) extends into what is seen as lung tissue on the CT (A). As a consequence, the area of mismatch is undercorrected (B and C) because the reconstruction algorithm is correcting for lung attenuation when it should be correcting for liver tissue attenuation. Figure 119(D), which does not use AC, provides a more accurate representation of the activity distribution.

Guidance

Mismatch of SPECT and CT data in the thoracic region is difficult to avoid, given that it is difficult to acquire the CT in the same phase as the time averaged SPECT. Although some have advocated the use of breath hold end expiration CT to avoid this issue, the best results have been found when allowing free breathing. Steps to minimize misregistration include warning the patient to avoid deep breathing during the scan, and allowing the patient to rest for a short period on the bed before starting the CT scan. This final technique allows the patient to settle into a regular resting breathing cycle before the CT starts.

4.6.4.3. Bladder

Background

Mismatch between CT and SPECT can occur in the pelvic region owing to the time difference between the two acquisitions. During this time, the bladder may undergo significant filling, which will displace surrounding tissue and potentially lesions. The probability of large changes increases with time, and therefore multiple position SPECT images are more likely to show such an effect if performed with the head first (assuming that CT is performed before SPECT).

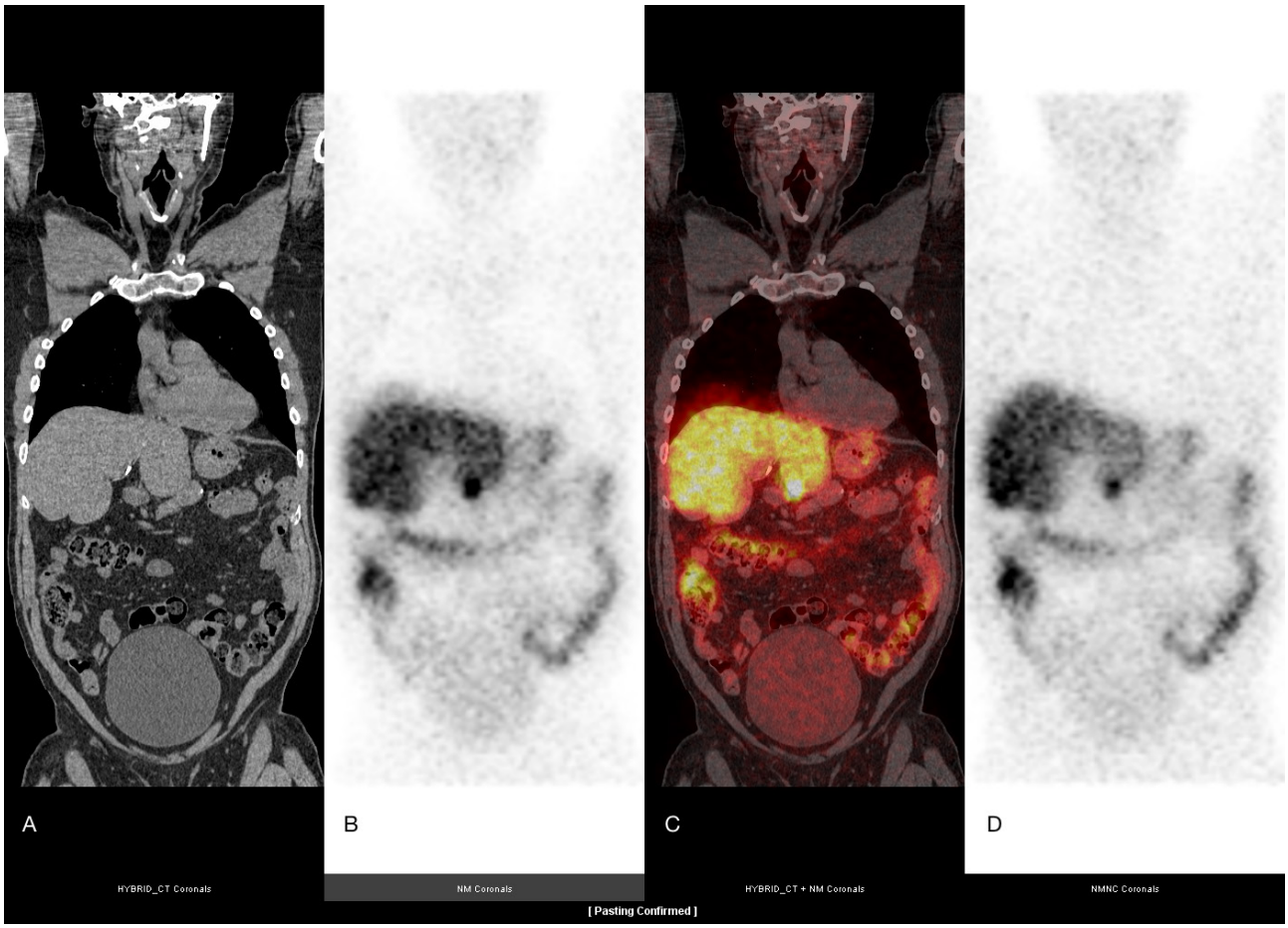

FIG. 119. ^{177}Lu-DOTATATE SPECT/CT study showing (A) the CT used for localization and AC; (B) AC SPECT; (C) fused CT and AC SPECT; and (D) uncorrected SPECT data.

Case

A 73 year old man underwent a whole body planar bone scintigraphy with ^{99m}Tc followed by a SPECT/CT extending over three camera FOV, each lasting 8 min. The SPECT scan was started from the head position. The time difference between the CT and the SPECT of the bladder (midpoint time) was approximately 25 min. Figure 120 shows a considerable change in bladder size between the two modalities. In this case, there were no lesions in the vicinity of the bladder, and the displacement is therefore without clinical significance. If a lesion is displaced, it is important to remember that its anatomical correlate on the CT is not correctly placed.

Guidance

Looking for lesions in the pelvis, it is important to notice potential differences in bladder filling that may displace lesions between CT and SPECT. In order to shorten the time between the scans, a composite SPECT scan should be started from the pelvis upwards (assuming that CT is performed before SPECT).

4.6.4.4. Patient motion

Background

When using CT for AC, it is important that the SPECT and CT scans be in alignment so that appropriate correction factors are applied. While misregistration can occur anywhere in the body, movement of limbs during the scan can be particularly problematic.

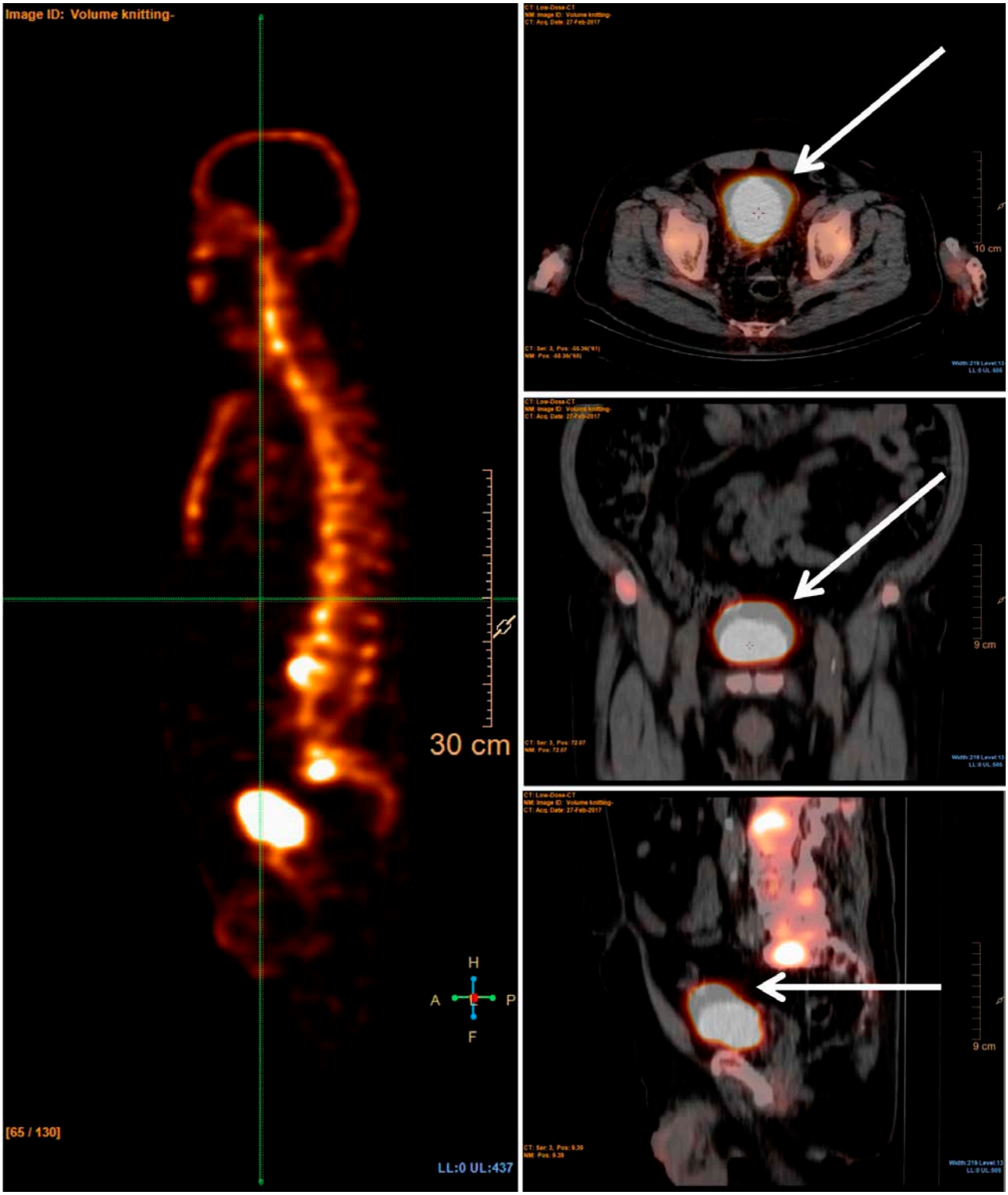

FIG. 120. The time difference between CT and SPECT may cause the bladder to present with different degree of filling (arrows). This may potentially displace lesions, causing a mismatch.

Case

Figure 121 shows a bone SPECT/CT study of the pelvis with motion of the pelvic area. In addition, movement of the right hand (left side) can be seen in the emission data but not the CT data. There is also CT truncation of the left hand (right side) and right pelvis.

In Fig. 122(A), a transaxial slice of SPECT data and profile through the hand are shown, with the count profile from NAC reconstructed data (blue) and the ratio of CTAC to NAC counts in red. The ratio of counts in the right hand (left side) shows an AC/NAC ratio close to 1.0, which confirms that counts have not been corrected for attenuation. In the left hand (right side), there has been a very small correction for attenuation with the hand partially in the CT FOV. There are also several large spikes seen in the AC/NAC profile, which is indicative of motion or misregistration of the emission data and CT used for AC.

In Fig. 122(B), a similar profile through the anterior aspect of the pelvis is dominated by patient motion leading to misregistration between the emission and CT for AC data. This can be seen by the red peaks at either side of the body. The misregistration of the most anterior aspects of the pelvic bones with the corresponding areas on the CT have led to an under correction of counts in this area, which can be identified by the similar correction of pixels in soft tissue areas neighbouring the bone.

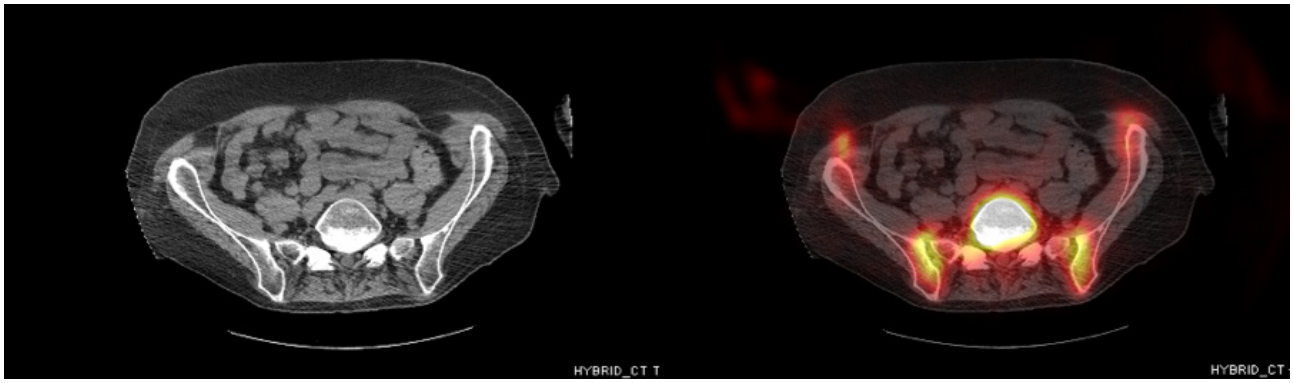

FIG. 121. CT and fused bone SPECT/CT image of the pelvis area showing motion of the pelvis and hand, and truncation of the opposite hand and slight truncation of the right pelvis (left side).

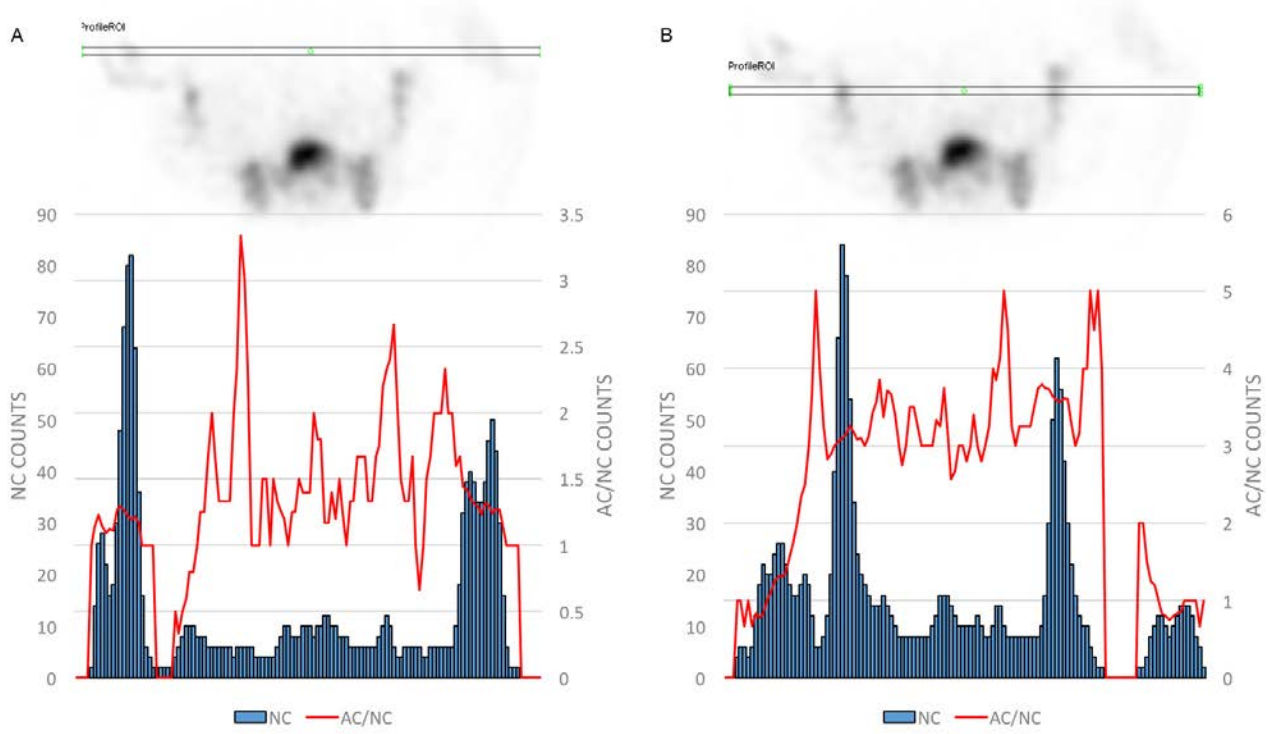

FIG. 122. Bone SPECT profiles showing the NAC counts (blue) and the ratio of CTAC to NAC counts (red) (A) through the hands and (B) through the pelvis.

Guidance

Misregistration of CT and SPECT clearly has an effect on CTAC of counts. Good patient instructions and strapping and light immobilization can help to avoid these problems in many instances.

4.7. QUANTITATIVE ISSUES

The addition of CTAC to SPECT imaging along with a host of other corrections, such as scatter, dead time and efficiency for various radionuclides and collimators, has introduced for the first time a reliable approach to generate quantitative SPECT data. Today, several commercial SPECT/CT systems have optional quantitative modules that allow the user to quantify SPECT images in terms of standardized uptake value (SUV) similar to what is used in PET imaging. The accuracy of quantification, however, depends on several factors, such as the reconstruction algorithm parameters (number of iterations and subsets), the accuracy of data corrections (i.e. attenuation and scatter), the presence of contrast or metal, and patient motion (voluntary or involuntary) that leads to mismatch between CT and SPECT data.

4.7.1. Iterations and subsets

Background

SPECT iterative reconstruction creates a tomographic image by making many attempts (iterations) at matching an estimated image to the measured projections updating estimates typically using MLEM. One method of accelerating this process is to use OSEM, in which each update to the image is based only on angularly spaced subset of the projections rather than comparing all projections. The product of subsets and iterations in OSEM can be considered to be equivalent to the number of full expectation maximization realizations.

This process provides at each iteration an improved estimate of the image, and is typically stopped when an acceptable image has been formed. Quantitatively, the uptake in this image may not fully have reached convergence. Furthermore, convergence for different areas in the image may be reached after different numbers of iterations.

Case

A 79 year old man was referred for a ^{123}I-ioflupane study to assess whether he had idiopathic Parkinson's disease or essential tremor. Following the injection of 178 MBq of ^{123}I-ioflupane, the patient returned for a SPECT/CT scan 3.5 hours later. Figure 123 shows a transaxial slice through the basal ganglia following 1, 2, 5, 10, 15 and 20 iterations of 10 subsets effectively equivalent to 10, 20, 50, 100, 150 and 200 full MLEM iterations. It can be clearly seen how the image develops visually following multiple iterations. Figure 124(A) shows quantitatively how the uptake in the left striatum changes with iteration number as a percentage of the value measured using FBP — a method that does not have convergence issues. Not until five iterations does convergence occur in this region. However, in the background reference region, which is used to define the commonly used specific binding ratio (SBR), convergence has already occurred after two iterations.

On closer inspection, the values of uptake in the background region using iterative reconstruction are actually higher than that defined by FBP. This is a known problem with MLEM and OSEM called the non-negativity constraint bias and occurs in areas of low uptake. During the MLEM and OSEM reconstruction process estimates are not allowed to be negative, which if uptake is close to zero has the consequence of pushing the distribution on which the estimate is made upwards producing an overly high final value.

Guidance

When performing quantitative SPECT, it is essential that sufficient iterations and subsets be used to ensure convergence of uptake values. In areas of low uptake, the non-negativity constraint of MLEM and OSEM algorithms can lead to an overestimation of the true value.

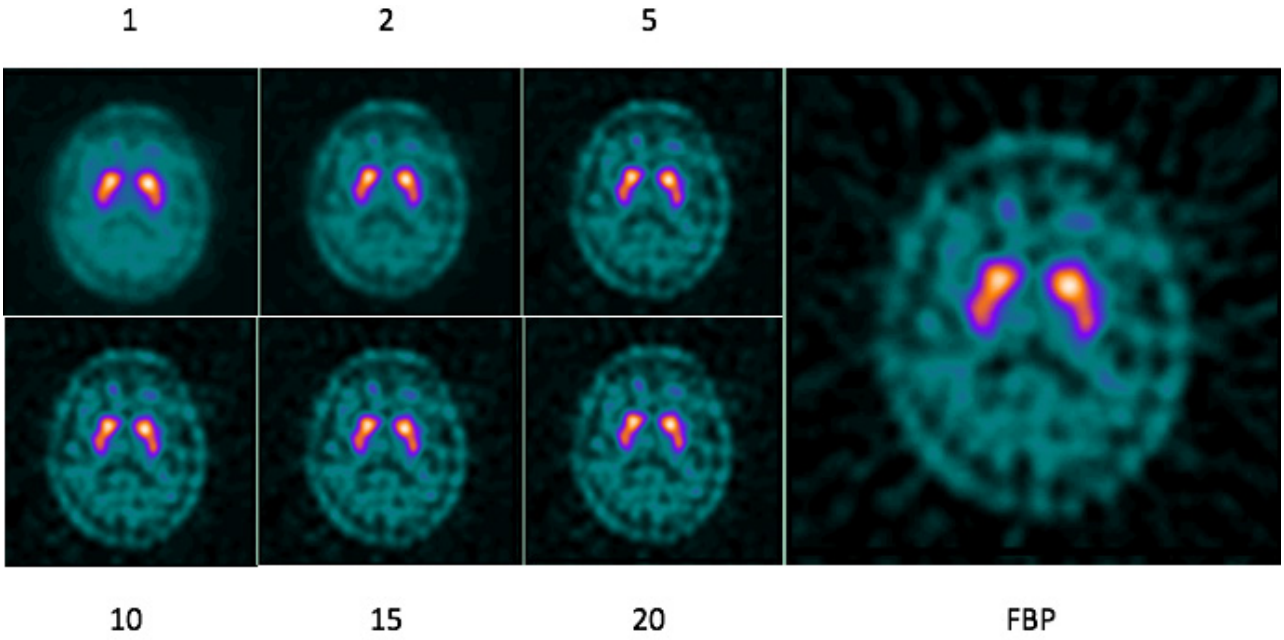

FIG. 123. ^{123}I-ioflupane image of the basal ganglia reconstructed using 1, 2, 5, 10, 15 and 20 iterations of 10 subsets and the FBP image.

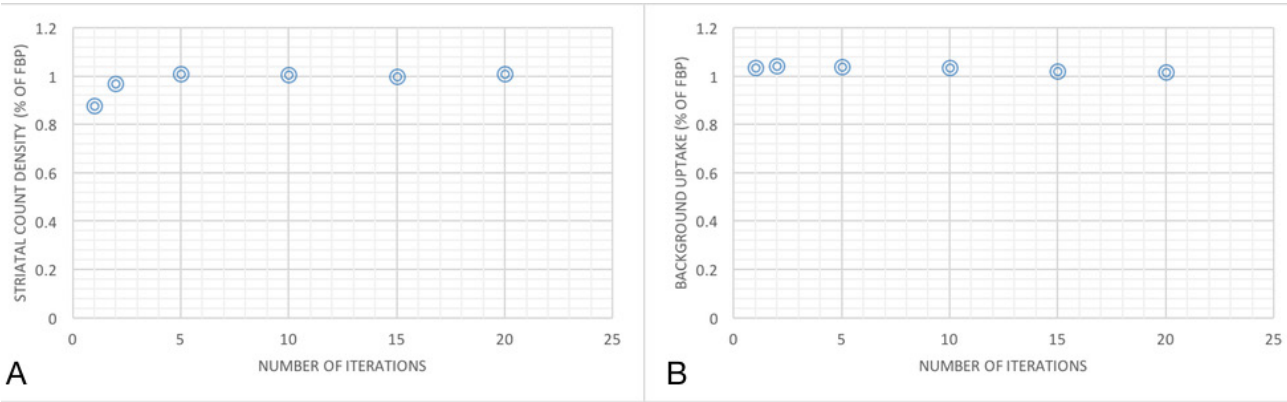

FIG. 124. (A) Striatal uptake and (B) background uptake represented as a fraction of the uptake calculated using FBP.

4.7.2. Corrections

Background

Unlike in PET, where many corrections are applied by default, in SPECT, corrections for physical effects might not be applied, owing to either complexity or unavailability of required data or software licences. However, when performing quantification, all corrections should be applied to achieve more accurate values of uptake. Modern systems have quantification modules that apply all these corrections automatically.

Case

As in Section 4.7.1, a 79 year old man was referred for a ^{123}I-ioflupane study to assess whether he had idiopathic Parkinson's disease or essential tremor. Following the injection of 178 MBq of ^{123}I-ioflupane the patient

returned for a SPECT/CT scan 3.5 hours later. Figure 125 shows a transaxial slice through the basal ganglia following OSEM reconstruction with 10 iterations and 10 subsets using:

(a) No corrections;
(b) Correction for scatter using a triple energy window scatter correction;
(c) Correction for attenuation;
(d) Correction for attenuation and scatter using a triple energy window scatter correction;
(e) Correction for attenuation, scatter and resolution losses.

Figure 126 shows the caudate count density and caudate specific binding ratio to an occipital lobe reference region following each correction:

$$\text{SBR} = \frac{\text{striata count density} - \text{reference count density}}{\text{reference count density}}$$

What is clear from both A and B is that the scatter correction makes a significant difference to the contrast between the striata and the background. Although the counts in the striata are reduced using this triple energy window method, the counts in the background are also reduced, leading to an increased caudate specific binding ratio. This benefit arises because of removal of the down scatter and septal penetration of higher energy emissions from ^{123}I. A similar measurement with ^{99m}Tc would not have shown as much of a benefit, but many other radionuclides used in nuclear medicine have several gamma emissions and therefore do significantly benefit from

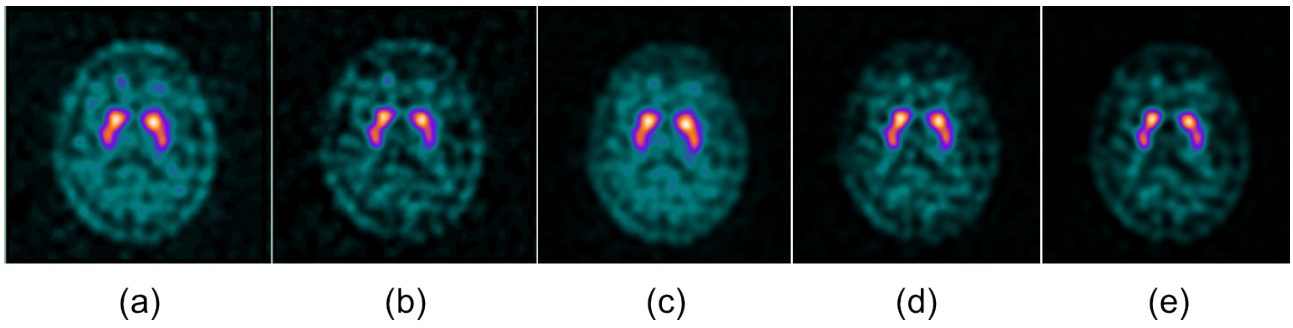

FIG. 125. Transaxial slice through the basal ganglia when reconstructed (a) without corrections, (b) with a correction for scatter, (c) with AC, (d) with correction for attenuation and scatter and (e) with correction for attenuation, scatter and resolution losses.

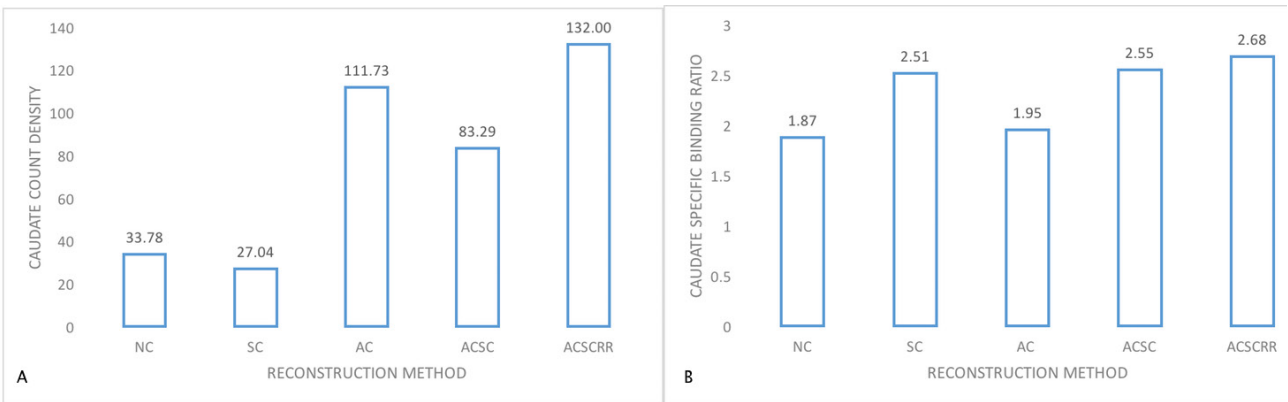

FIG. 126. Charts showing caudate count density and caudate specific binding ratio (to an occipital lobe reference region) with different reconstruction strategies.

this correction. AC makes an additional increase to counts and uptake ratios (dependent on the position of the reference region). Owing to the size of the organ, resolution modelling makes a large difference to the caudate count density and also increases specific binding ratios.

Guidance

The values derived from quantitative SPECT will depend on the corrections applied. To yield the most accurate values, corrections for all physical effects should generally be used, although in some instances this might lead to greater uncertainty in the measure. Where absolute quantification is required, a sensitivity calibration is necessary to relate count densities in the image to activities per unit volume.

4.7.3. Iodine contrast in ^{99m}Tc- and ^{111}In-SPECT

Background

When iodine contrast is applied in a patient, the number of projection counts slightly decreases owing to the excess attenuation of the iodine. This effect depends on the gamma energy and is larger for ^{99m}Tc than for ^{111}In (see Fig. 127). However, CTAC generally increases the quantitative values of the final reconstructed SPECT image, as explained in Section 2.3.2. Two situations of interest should be considered. A high and visible local concentration of contrast in the blood vessels at the time of CT (which is one reason for applying contrast media) may, at least in principle, lead to local SPECT artefacts by reconstruction, although the low SPECT resolution and the filtering of attenuation maps can tend to hide them. A more distributed concentration at later times (e.g. repeated CT scans) will slightly affect overall quantification. The latter situation is shown here.

Case

Phantom studies were performed to illustrate the effects (exaggerated). A 20 cm cylinder phantom (5.15 L) was filled with water and activity was added (two independent studies with 50 MBq of ^{111}In and 300 MBq of ^{99m}Tc). Measurements were performed with pure water, and with iodine contrast added (100 mL and 200 mL of ioversol, 350 mg/mL), leading to iodine concentrations in the phantom of 6.8 g/L and 13.5 g/L, respectively. The total amount of contrast agent given to a patient would normally be in the order of 100 mL (i.e. <50 g), and

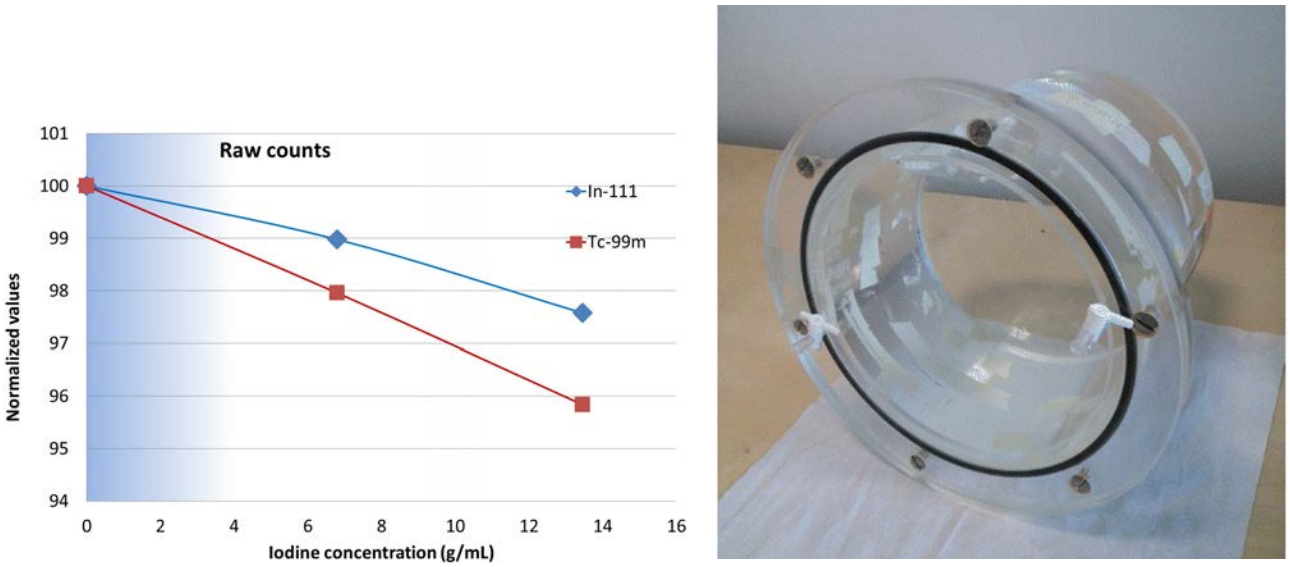

FIG. 127. Relative detected raw counts (in %) from ^{99m}Tc and ^{111}In as a function of increasing iodine concentration in a 20 cm cylinder phantom. Likely patient concentrations are in the shaded area to the left.

therefore the average concentration over extended volumes during SPECT would not exceed a few g/L (shaded area in Fig. 127). SPECT acquisitions were performed on a Philips Precedence 16.

Images were reconstructed without AC (NAC) and with attenuation maps derived from CT scans at peak voltages of 90, 120 and 140 kV. When an attenuation map for SPECT is created from the CT, the HU are typically converted using a bilinear mapping (see Section 2.3.2). The presence of CT contrast will tend to create an overestimation of the SPECT attenuation, and the size of the effect will depend on CT energy, actual SPECT energy as well as the local concentration of iodine (see Figs 128 and 129). The effect on ^{99m}Tc (140 keV) is smaller than that for ^{111}In (average of 171 keV and 245 keV). Numerical values will depend on the actual implementation that may differ between vendors.

Guidance

The quantitative effect of distributed iodine contrast during CT scans used for AC of SPECT is rather limited and does not exclude the use of contrast scans for this purpose.

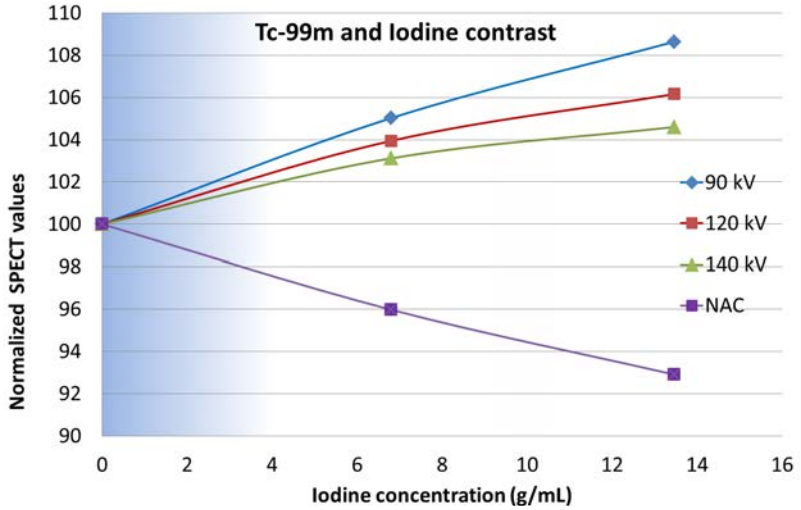

FIG. 128. Relative change of reconstructed ^{99m}Tc-SPECT values as a function of the concentration of iodine for NAC and for three different CT energies. Likely patient concentrations are in the shaded area to the left.

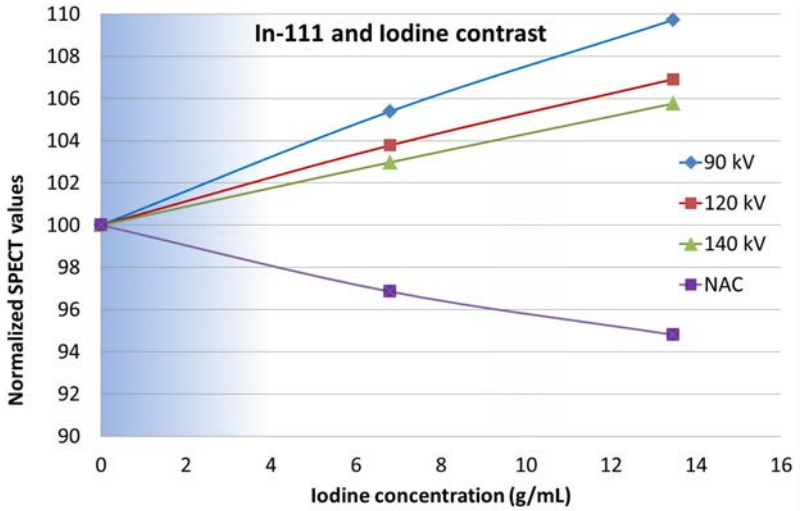

FIG. 129. Relative change of reconstructed ^{111} In-SPECT values as a function of the concentration of iodine for NAC and for three different CT energies. Likely patient concentrations are in the shaded area to the left.

4.7.4. Local effects of iodine contrast in ^{99m}Tc-SPECT

Background

Iodine contrast is applied in CT examinations with the purpose of enhancing structures like blood vessels. The timing of the CT scan relative to injection determines the distribution (e.g. arterial or venous). Within a few minutes, the contrast will be distributed in a large volume of body fluids, and therefore have a relatively low concentration. If a CT scan with applied contrast is followed by a SPECT scan, the influence of contrast on the SPECT scan itself is very limited. However, if the contrast enhanced CT scan is used to create an attenuation map for SPECT, the AC may, in principle, create artificially high activity concentrations in the area where contrast is present. The size of the effect depends on the contrast concentration, the CT energy applied and the SPECT energy (see Section 2.3.2). The problem is much smaller for SPECT than for PET due to: (i) the lower energy of SPECT (closer to CT); and (ii) the limited resolution where the CT based attenuation maps are filtered by a smooth filter to match the resolution of SPECT.

Case A

A phantom study was performed to illustrate this effect (slightly exaggerated). The phantom (see Fig. 130) is a simplified thorax with fillable heart. The lungs are made from a light material that displaces water but cannot take up activity. The lid has a number of valves that allow independent filling of internal structures. A tube was connected in an internal loop between two valves, allowing it to be filled with contrast (ioversol, 350 mg/mL) without removing it from the scanner. Figure 130 shows a three dimensional rendering of the phantom with contrast. The phantom background (6.7 L) and the 'myocardium' (0.30 L) were injected with 300 MBq and 40 MBq of ^{99m}Tc, respectively, leading to a ratio of 3:1. The experiments were performed on a Philips Precedence 16. The CT scans were performed at peak voltage 90 kV and 140 kV followed by SPECT for one hour (see Fig. 131). The internal tube 'vessel' was then injected with undiluted contrast and the scans repeated.

Images were reconstructed NAC (not shown) and with attenuation maps derived from the CT scans with and without contrast present (see Fig. 132). Only SPECT data without contrast are shown in Fig. 133, since this is the most relevant condition, simulating that the injected contrast has been distributed in the body. Only if a difference image is calculated is it clear that the contrast material induces an increase in reconstructed SPECT counts through the attenuation map (see Fig. 134).

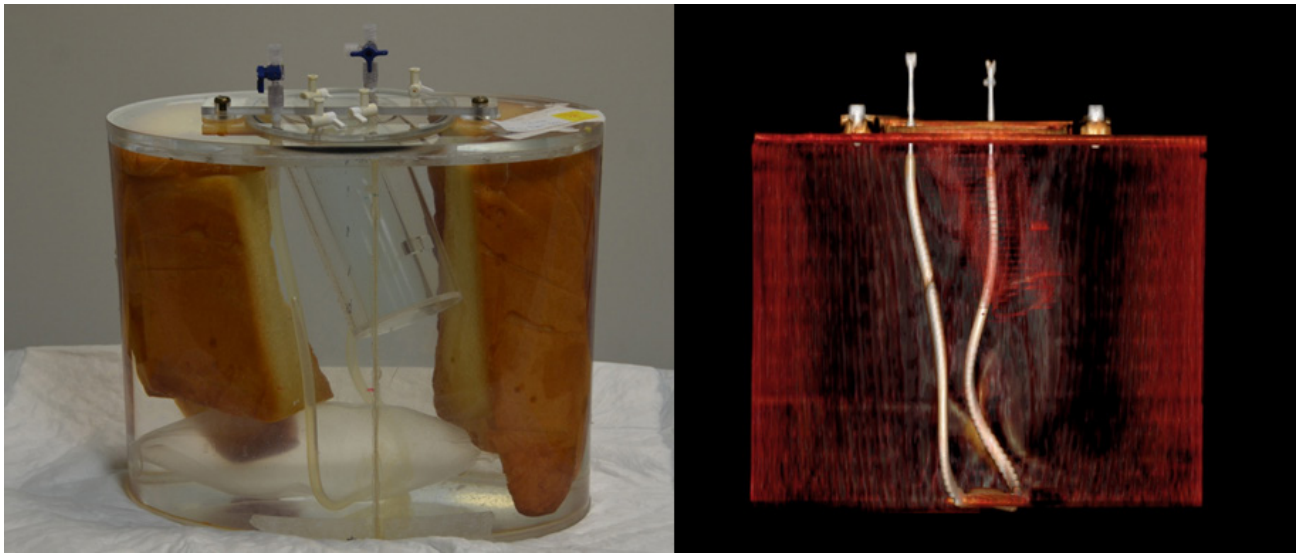

FIG. 130. Thorax phantom and a three dimensional rendering of SPECT/CT with contrast.

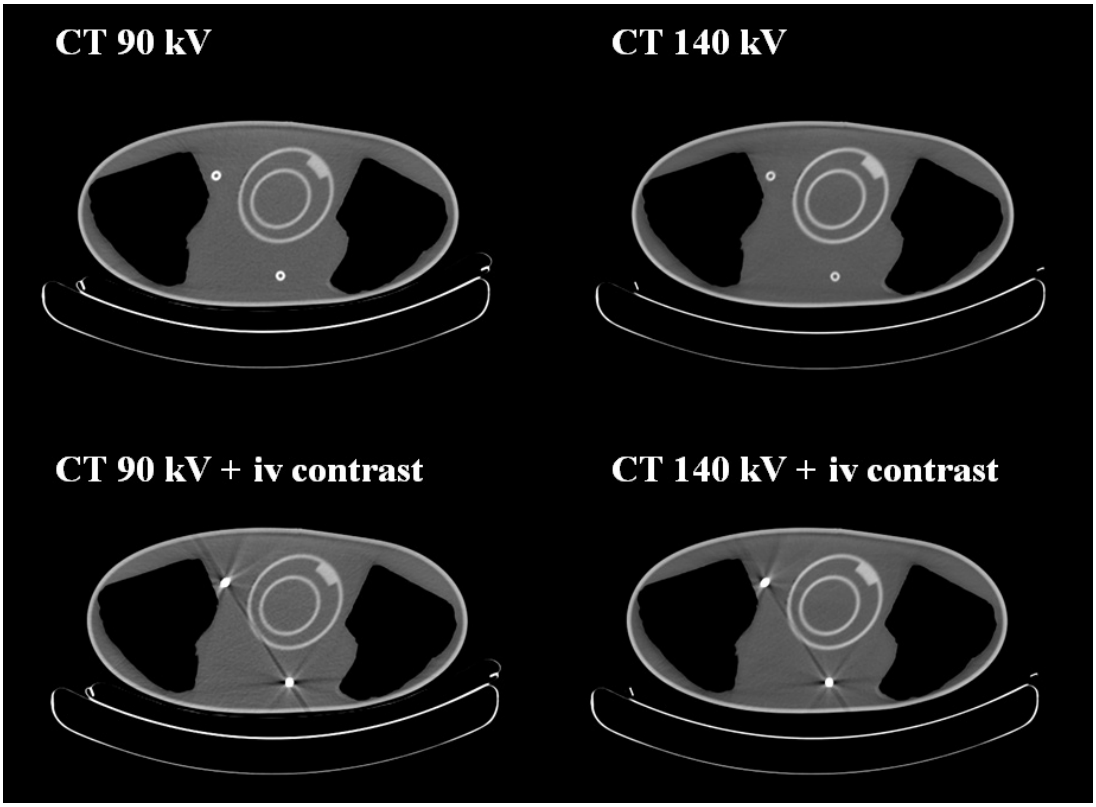

FIG. 131. Reconstructed transaxial CT scans at two energies and with and without contrast present. The contrast induces streak artefacts at tube sites, slightly worse at 90 kV than at 140 kV.

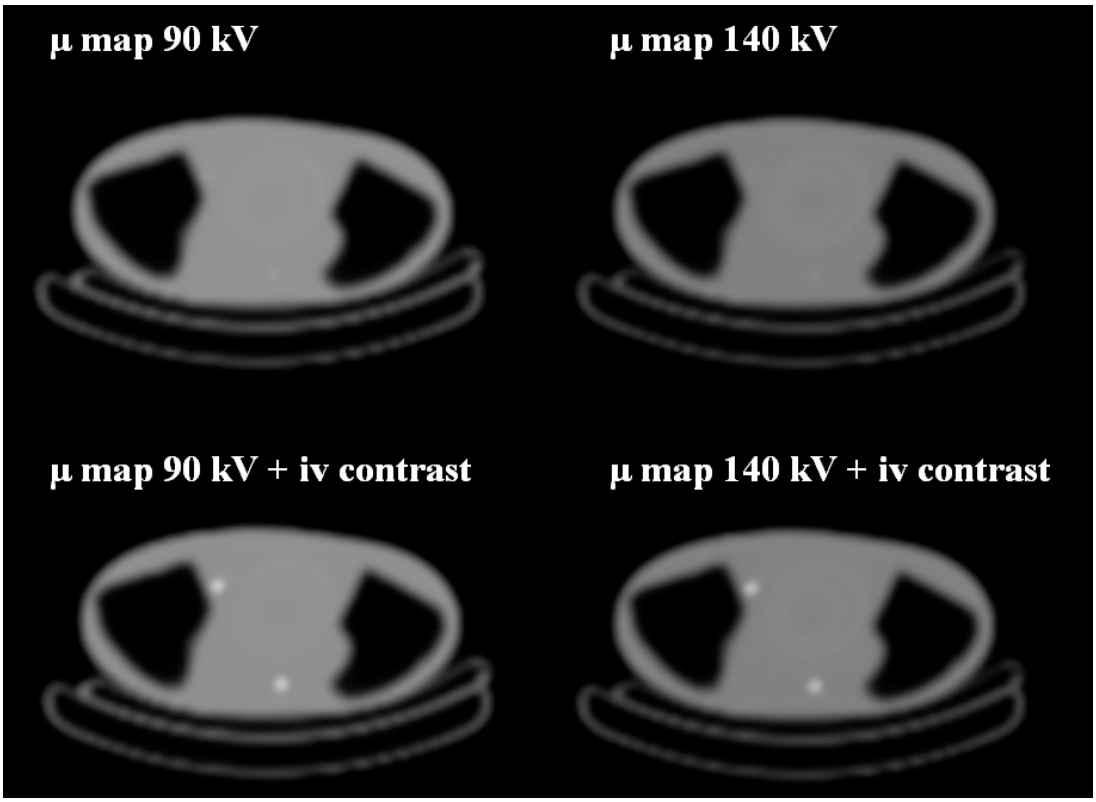

FIG. 132. The generated attenuation maps from two different CT kV values each with and without contrast. The extent of the area of increased attenuation is larger than the tube due to the applied smoothing. No streak artefacts are visible.

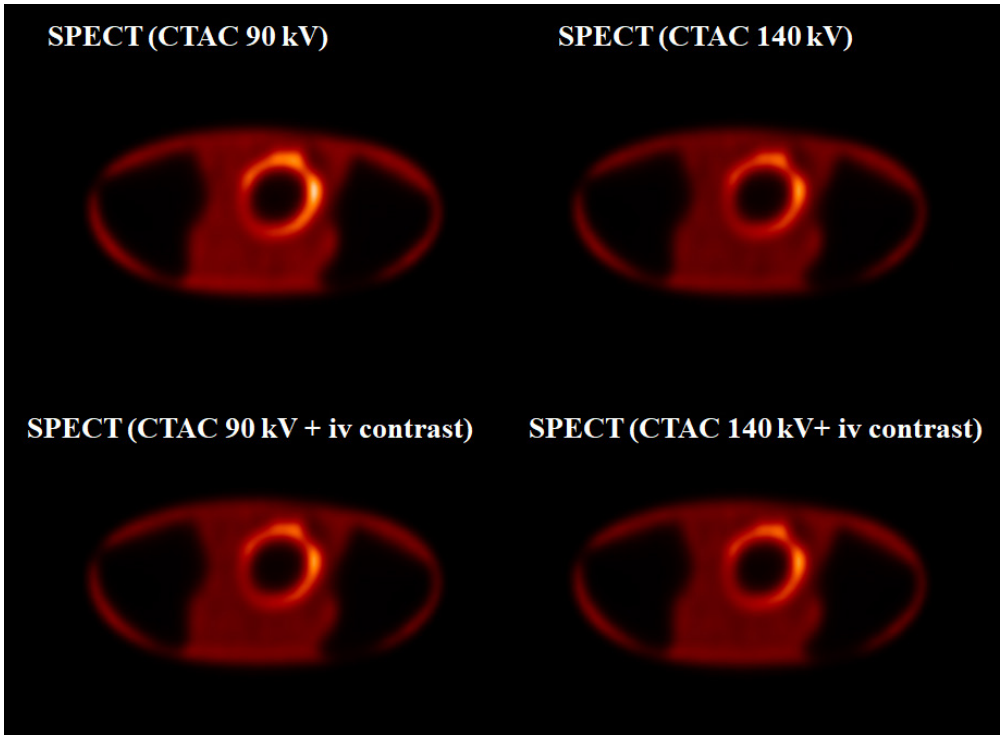

FIG. 133. Reconstructed SPECT images based on attenuation maps from two different CT kV values, with and without contrast. It is difficult to detect differences by pure visual inspection.

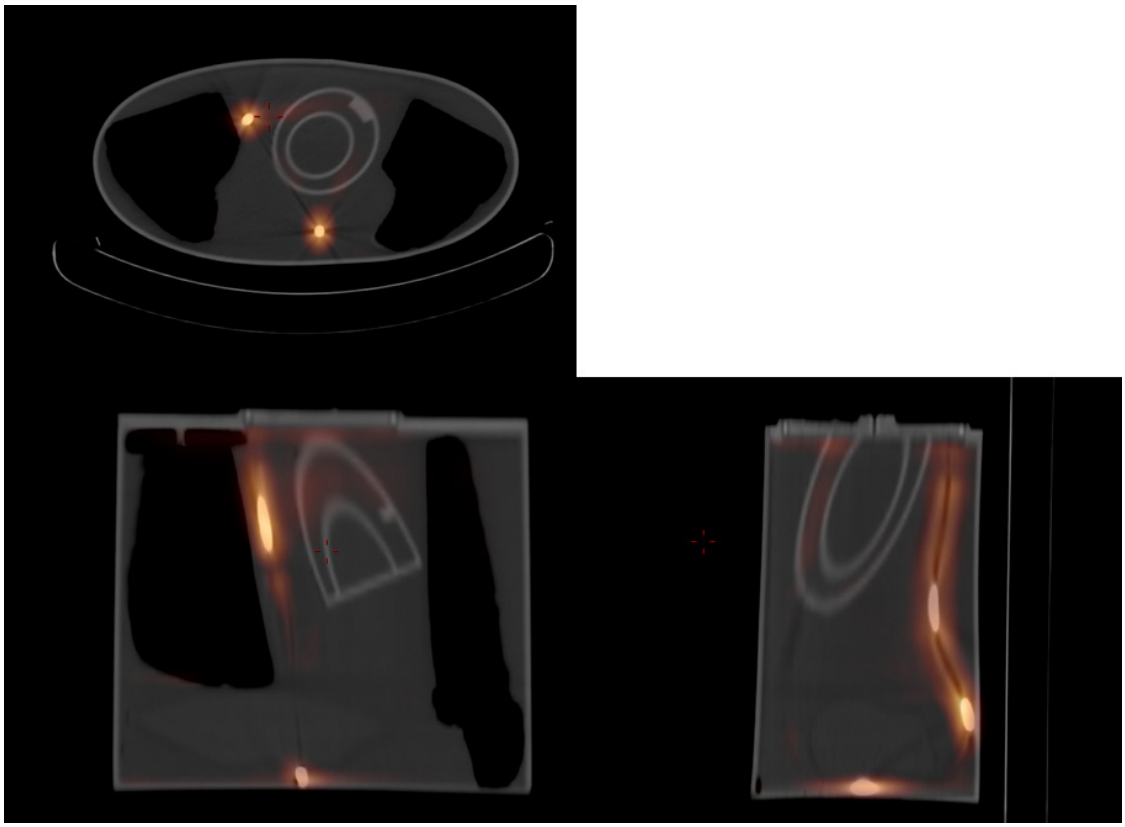

FIG. 134. Difference image between reconstructions of acquisitions performed with and without contrast. Only if a difference image is calculated is it clear that the contrast material introduces an increase in reconstructed SPECT counts through the attenuation correction. In this case about 5–10% of maximum. Images reconstructed with attenuation maps based on 140 kV CT.

Case B

A 22 year old woman had a renal arteriography with iodine contrast in the morning, followed by a SPECT/CT of the abdomen later the same day after injection with 80 MBq of ^{99m}Tc-DMSA. Owing to reduced kidney function, local, high iodine concentrations were seen in the CT images used for AC of SPECT, for example in the right kidney (see Fig. 135). A visual comparison of the SPECT images without and with CTAC does not show any significant difference (artefact) from the iodine (see Figs 136 and 137).

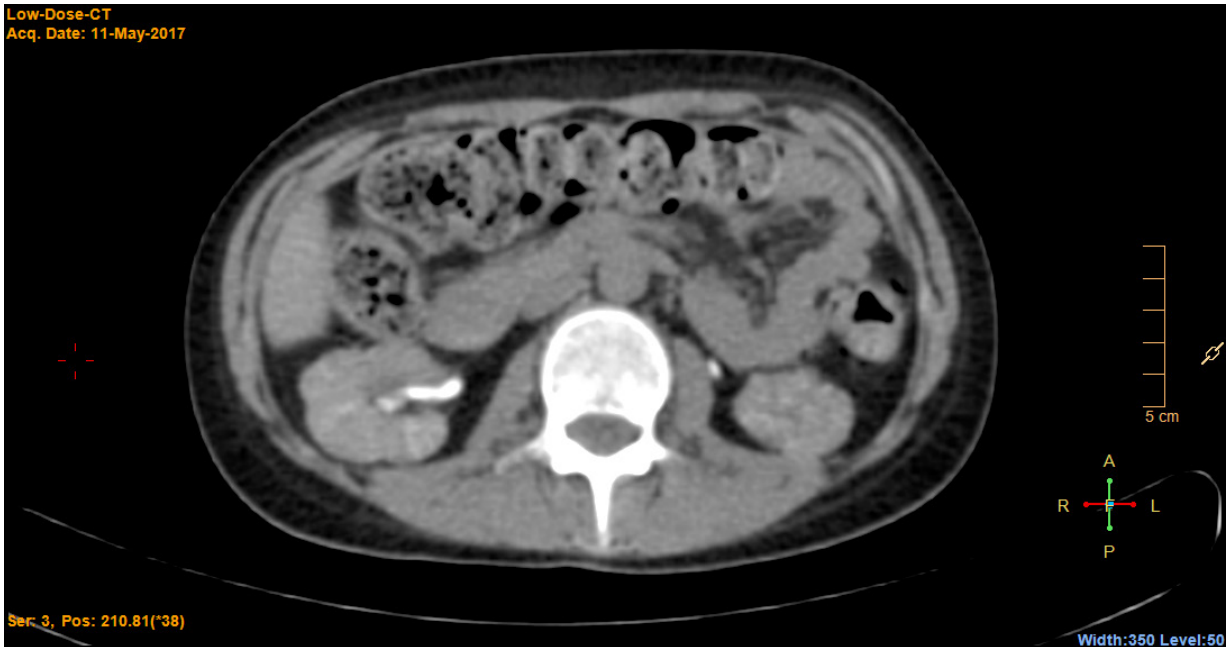

FIG. 135. Iodine contrast is present in the right kidney (maximum value on the CT scan is about 400 HU).

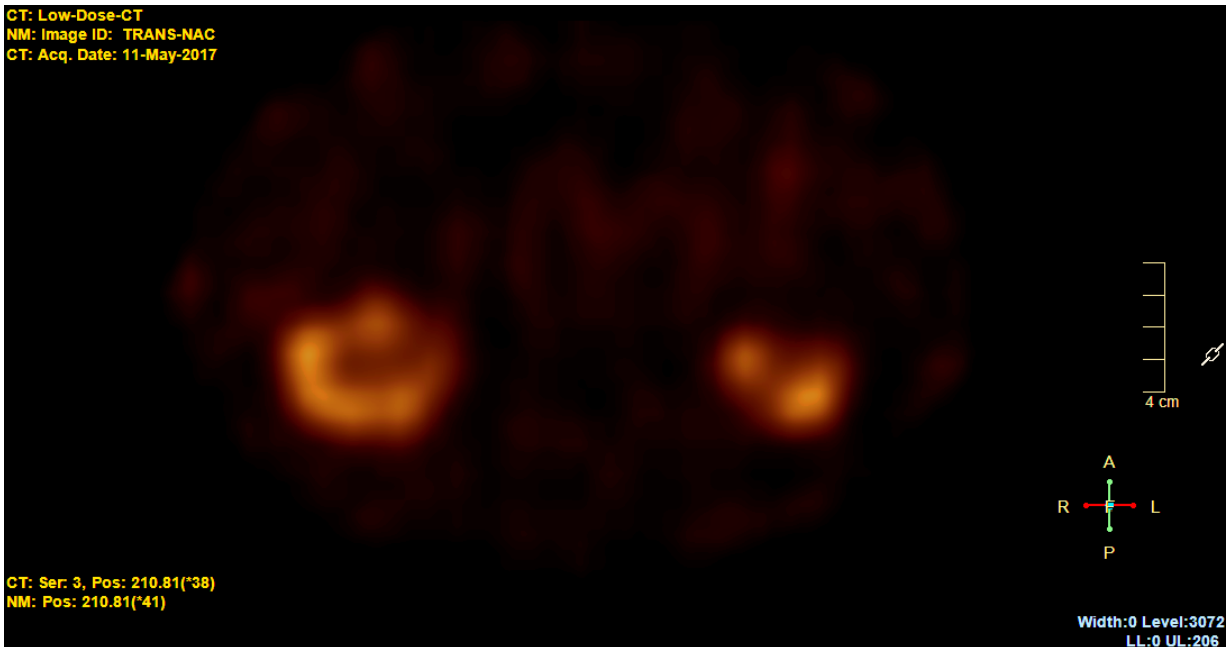

FIG. 136. SPECT image without CTAC.

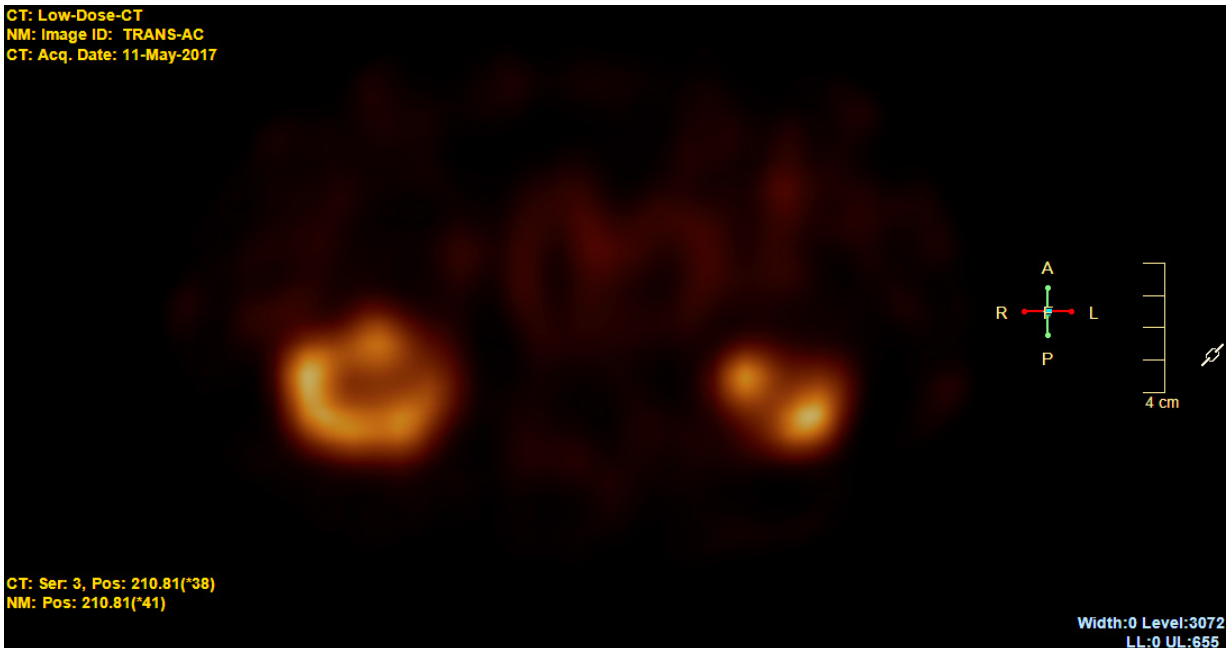

FIG. 137. SPECT image with CTAC.

Guidance

The local effect of the presence of iodine contrast during CT scans used for AC of SPECT is generally rather limited and does not exclude the use of contrast scans for this purpose. The magnitude of the effect depends on several parameters, and it will also depend on the vendor's actual implementation of the algorithm.

4.7.5. ECG gating: Arrhythmia

Background

Many myocardial SPECT studies require ECG gating to assess cardiac kinetics. If the regularity of the cardiac cycle is compromised (e.g. by atypical cardiac arrhythmias), the resulting analysis of gated data can be affected.

Case

In the myocardial perfusion study shown in Fig. 138(A), an arrhythmia has caused problems with the analysis of the cardiac study resulting in an inversion of the cardiac volume versus time curve and an inaccurate measured left ventricular ejection fraction (LVEF). In Fig. 138(B), once the arrhythmia has been resolved in the patient, and with the same injection, the data are processed correctly and the cardiac cycle is now accurately represented.

Guidance

When performing ECG gated SPECT, the ECG trace should be assessed to ensure that the cardiac cycle is regular before acquiring data for clinical interpretation.

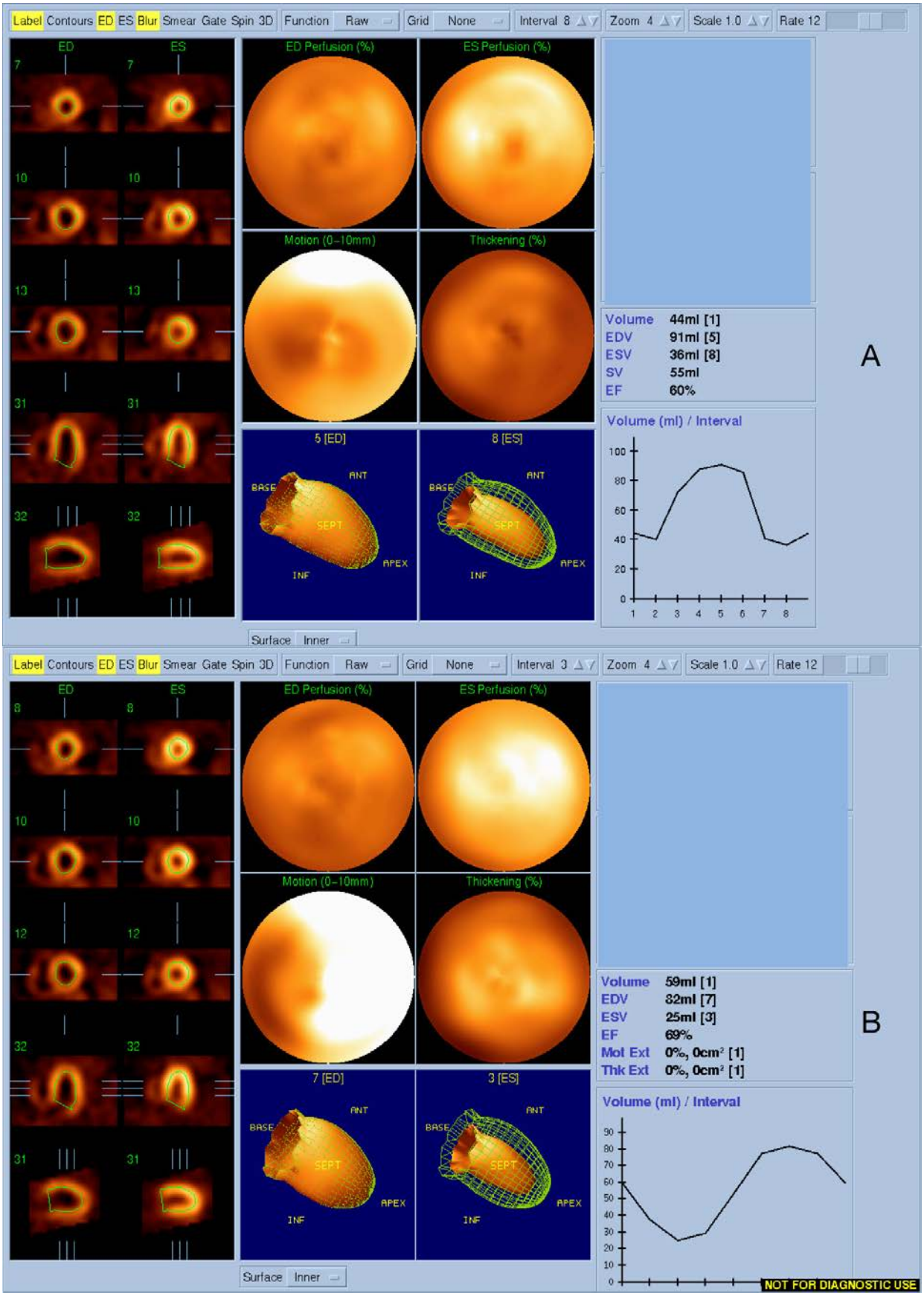

FIG. 138. Myocardial perfusion SPECT study. (A) Patient with arrhythmia demonstrating a poor representation of the myocardial cycle. (B) Once the arrhythmia has been resolved, the gated data are better represented.

REFERENCES

[1] KUHL, D.E., EDWARDS, R.Q., Image separation radioisotope scanning, Radiol. **84** (1963) 653–662.

[2] MUEHLLEHNER, G., A tomographic scintillation camera, Phys. Med. Biol. **16** (1971) 87–96.

[3] BUDINGER, T.F., GULLBERG, G.T., Three-dimensional reconstruction in nuclear medicine emission imaging, IEEE Trans. Nucl. Sci. **21** (1974) 2–20.

[4] LARSSON, S.A., Gamma camera emission tomography: Development and properties of a multi-sectional emission computed tomography system, Acta Radiol. Suppl. **363** (1980) 1–75.

[5] HASEGAWA, B.H., GINGOLD, E.L., REILLY, S.M., LIEW, S.-C., CANN, C.E., "Description of a simultaneous emission-transmission CT system", Medical Imaging IV: Image Formation (Proc. SPIE Conf. 1231, Newport Beach, CA, 1990), (SCHNEIDER, R.H., Ed.), International Society for Optics and Photonics (1990) 50–60.

[6] INTERNATIONAL ATOMIC ENERGY AGENCY, IAEA Quality Control Atlas for Scintillation Camera Systems, IAEA, Vienna (2003).

[7] INTERNATIONAL ATOMIC ENERGY AGENCY, PET/CT Atlas on Quality Control and Image Artefacts, IAEA Human Health Series No. 27, IAEA, Vienna (2014).

[8] ERLANDSSON, K., KACPERSKI, K., VAN GRAMBERG, D., HUTTON, B.F., Performance evaluation of D-SPECT: A novel SPECT system for nuclear cardiology, Phys. Med. Biol. **54** (2009) 2635–2649.

[9] BOCHER, M., et al., A fast cardiac gamma camera with dynamic SPECT capabilities: Design, system validation and future potential, Eur. J. Nucl. Med. Mol. Imaging **37** (2010) 1887–1902.

[10] DICKSON, J.C., et al., The impact of reconstruction method on the quantification of DaTSCAN images, Eur. J. Nucl. Med. Mol. Imaging **37** (2009) 23–35.

[11] JASZCZAK, R.J., LI, J., WANG, H., ZALUTSKY, M.R., COLEMAN, R.E., Pinhole collimation for ultra-high-resolution, small-field-of-view SPECT, Phys. Med. Biol. **39** 3 (1994) 425–437.

[12] MAHMOOD, S.T., ERLANDSSON, K., CULLUM, I., HUTTON, B.F., Design of a novel slit-slat collimator system for SPECT imaging of the human brain, Phys. Med. Biol. **54** (2009) 3433–3449.

[13] GOORDEN, M.C., RENTMEESTER, M.C., BEEKMAN, F.J., Theoretical analysis of full-ring multi-pinhole brain SPECT, Phys. Med. Biol. **54** (2009) 6593–6610.

[14] VIDAL, R., et al., Impact of attenuation correction by simultaneous emission/transmission tomography on visual assessment of ^{201}Tl myocardial perfusion images, J. Nucl. Med. **40** (1999) 1301–1309.

[15] HAWMAN, P.C., HAINES, E.J., The cardiofocal collimator: A variable-focus collimator for cardiac SPECT, Phys. Med. Biol. **39** (1994) 439–450.

[16] BORGES-NETO, S., et al., Clinical results of a novel wide beam reconstruction method for shortening scan time of Tc-99m cardiac SPECT perfusion studies, J. Nucl. Cardiol. **14** (2007) 555–565.

[17] GAMBHIR, S.S., et al., A novel high-sensitivity rapid-acquisition single-photon cardiac imaging camera, J. Nucl. Med. **50** (2009) 635–643.

[18] DEPUEY, E.G., BOMMIREDDIPALLI, S., CLARK, J., THOMPSON, L., SROUR, Y., Wide beam reconstruction 'quarter-time' gated myocardial perfusion SPECT functional imaging: A comparison to 'full-time' ordered subset expectation maximum, J. Nucl. Cardiol. **16** (2009) 736–752.

[19] STONE, J.M., BRESSAN, R.A., ERLANDSSON, K., ELL, P.J., PILOWSKY, L.S., Non-uniform blockade of intrastriatal D2/D3 receptors by risperidone and amisulpride, Psychopharmacol. **180** (2005) 664–669.

[20] STONE, J.M., et al., Ketamine displaces the novel NMDA receptor SPET probe [^{123}I]CNS-1261 in humans in vivo, Nucl. Med. Biol. **33** (2006) 239–243.

[21] BEN-HAIM, S., et al., Quantification of myocardial perfusion reserve using dynamic SPECT imaging in humans: A feasibility study, J. Nucl. Med. **54** (2013) 873–879.

[22] CHERRY, S.R., SORENSON, J.A., PHELPS, M.E., Physics in Nuclear Medicine, Elsevier Health Sciences, Philadelphia, PA (2012).

[23] BRUYANT, P.P., Analytic and iterative reconstruction algorithms in SPECT, J Nucl Med **43** 10 (2002) 1343–1358.

[24] SHEPP, L.A., VARDI, Y., Maximum likelihood reconstruction for emission tomography, IEEE Trans. Med. Imaging **1** (1982) 113–122.

[25] LANGE, K., CARSON, R., EM reconstruction algorithms for emission and transmission tomography, J. Comput. Assist. Tomogr. **8** (1984) 306–316.

[26] NUYTS, J., et al., Simultaneous maximum a posteriori reconstruction of attenuation and activity distributions from emission sinograms, IEEE Trans. Med. Imaging **18** (1999) 393–403.

[27] LEHOVICH, A., et al., Human-observer LROC study of lesion detection in Ga-67 SPECT images reconstructed using map with anatomical priors, IEEE Nucl. Sci. Symp. Conf. Rec. **3** (2006) 1699–1702.

[28] VIJA, H., Introduction to xSPECT* Technology: Evolving Multi-modal SPECT to Become Context-based and Quantitative, White Paper, Siemens Medical Solutions USA, Hoffman Estates, IL (2015).
[29] HUDSON, H.M., LARKIN, R.S., Accelerated image reconstruction using ordered subsets of projection data, IEEE Trans. Med. Imaging **13** (1994) 601–609.
[30] CHANG, L.T., A method for attenuation correction in radionuclide computed tomography, IEEE Trans. Nucl. Sci. **25** (1978) 638–643.
[31] SOHLBERG, A., WATABE, H., IIDA, H., Three-dimensional SPECT reconstruction with transmission-dependent scatter correction, Ann. Nucl. Med. **22** (2008) 549–556.
[32] ICHIHARA, T., OGAWA, K., MOTOMURA, N., KUBO, A., HASHIMOTO, S., Compton scatter compensation using the triple-energy window method for single- and dual-isotope SPECT, J. Nucl. Med. **34** (1993) 2216–2221.
[33] INTERNATIONAL ATOMIC ENERGY AGENCY, Nuclear Medicine Physics: A Handbook for Teachers and Students, IAEA, Vienna (2014).
[34] WILLEMINK, M.J., et al., Iterative reconstruction techniques for computed tomography — Part 1: Technical principles, Eur. Radiol. **23** (2013) 1623–1631.
[35] INTERNATIONAL ATOMIC ENERGY AGENCY, Quality Assurance Programme for Computed Tomography: Diagnostic and Therapy Applications, IAEA Human Health Series No. 19, IAEA, Vienna (2012).
[36] BEISTER, M., KOLDITZ, D., KALENDER, W.A., Iterative reconstruction methods in X-ray CT, Phys. Med. **28** (2012) 94–108.
[37] KALENDER, W.A., Computed Tomography, 2nd edn, Publicis, Erlangen (2005).
[38] BERGER, M.J., et al., XCOM: Photon Cross Sections Database, NIST Standard Reference Database 8 (XGAM), National Institute of Standards and Technology,
www.nist.gov/pml/xcom-photon-cross-sections-database
[39] HUBBELL, J.H., SELTZER, S.M., X-ray Mass Attenuation Coefficients, NIST Standard Reference Database 126, National Institute of Standards and Technology,
www.nist.gov/pml/x-ray-mass-attenuation-coefficients
[40] CHUANYONG, B., LING, S., DA SILVA, A.J., ZUO, Z., A generalized model for the conversion from CT numbers to linear attenuation coefficients, IEEE Trans. Nucl. Sci. **50** (2003) 1510–1515.
[41] INTERNATIONAL COMMISSION ON RADIATION UNITS AND MEASUREMENTS, Tissue Substitutes in Radiation Dosimetry and Measurement, ICRU Report 44, ICRU, Bethesda, MD (1989).
[42] INTERNATIONAL ATOMIC ENERGY AGENCY, Quantitative Nuclear Medicine Imaging: Concepts, Requirements and Methods, IAEA Human Health Reports No. 9, IAEA, Vienna (2014).
[43] BLANKESPOOR, S.C., et al., Development of an emission-transmission CT system combining X-ray CT and SPECT, IEEE Nucl. Sci. Symp. Conf. Rec. **4** (1994) 1758–1761.
[44] SERET, A., NGUYEN, D., BERNARD, C., Quantitative capabilities of four state-of-the-art SPECT–CT cameras, EJNMMI Res. **2** (2012) 45.
[45] INTERNATIONAL ATOMIC ENERGY AGENCY, Quality Assurance for SPECT Systems, IAEA Human Health Series No. 6, IAEA, Vienna (2009).
[46] AMERICAN ASSOCIATION OF PHYSICISTS IN MEDICINE, Acceptance Testing and Annual Physics Survey Recommendations for Gamma Camera, SPECT, and SPECT/CT Systems, AAPM Report No. 177, AAPM, Alexandria, VA (2019).
[47] NATIONAL ELECTRICAL MANUFACTURERS ASSOCIATION, Performance Measurements of Gamma Cameras, NEMA Standard NU 1-2018, Rosslyn, VA (2019).
[48] BUSEMANN SOKOLE, E., PŁACHCINSKA, A., BRITTEN, A., Acceptance testing for nuclear medicine instrumentation, Eur. J. Nucl. Med. Mol. Imaging **37** (2010) 672–681.
[49] BUSEMANN SOKOLE, E., et al., Routine quality control recommendations for nuclear medicine instrumentation, Eur. J. Nucl. Med. Mol. Imaging **37** (2010) 662–671.
[50] ALDRIDGE, M.D., et al., Clinical evaluation of reducing acquisition time on single-photon emission computed tomography image quality using proprietary resolution recovery software, Nucl. Med. Commun. **34** (2013) 1116–1123.
[51] MAWLAWI, O., et al., Truncation artifact on PET/CT: Impact on measurements of activity concentration and assessment of a correction algorithm, AJR Am. J. Roentgenol. **186** (2006) 1458–1467.

ABBREVIATIONS

AAPM	American Association of Physicists in Medicine
AC	attenuation correction
AOR	axis of rotation
CFOV	central field of view
COR	centre of rotation
CT	computed tomography
CTAC	CT based attenuation correction
CTDI	computed tomography dose index
CZT	cadmium zinc telluride
EANM	European Association of Nuclear Medicine
ECG	electrocardiogram
FBP	filtered back projection
FOV	field of view
FWHM	full width at half maximum
HDP	hydroxyethylene diphosphonate
HU	Hounsfield unit
LEHR	low energy high resolution
LEUHR	low energy ultra high resolution
LPO	left posterior oblique
MEGP	medium energy general purpose
MHR	multiple head registration
MIBI	methoxyisobutylisonitrile
MLEM	maximum likelihood expectation maximization
NAC	no attenuation correction
NEMA	National Electrical Manufacturers Association
OSEM	ordered subset expectation maximization
PET	positron emission tomography
PSF	point spread function
RAO	right anterior oblique
ROI	region of interest
SBR	specific binding ratio
SPECT	single photon emission computed tomography
UFOV	useful field of view

CONTRIBUTORS TO DRAFTING AND REVIEW

Arreola, M.	University of Florida, United States of America
Bianchi, C.	ASST Papa Giovanni XXIII, Italy
Dickson, J.C.	University College London Hospitals, United Kingdom
Fuglsang, S.	Copenhagen University Hospital, Denmark
Holm, S.	Rigshospitalet, Copenhagen University Hospital, Denmark
Izaki, M.	Instituto do Coração, Hospital das Clínicas da Faculdade de Medicina da Universidade de São Paulo, Brazil
Kappadath, C.S.	The University of Texas MD Anderson Cancer Center, United States of America
Mawlawi, O.	The University of Texas MD Anderson Cancer Center, United States of America
de Nijs, R.	Rigshospitalet, Copenhagen University Hospital, Denmark
Oliveira, M.A.	Instituto do Coração, Hospital das Clínicas da Faculdade de Medicina da Universidade de São Paulo, Brazil
Poli, G.L.	International Atomic Energy Agency
Reichkendler, M.H.	Rigshospitalet, Copenhagen University Hospital, Denmark
Robilotta, C.C.	Institute of Physics, University of São Paulo, Brazil
Søndergaard, L.R.	Copenhagen University Hospital, Denmark
Teles Garcez, A.	Instituto de Radiologia, Hospital das Clínicas da Faculdade de Medicina da Universidade de São Paulo, Brazil

Consultants Meetings

Vienna, Austria: 29–31 October 2014, 6–8 May 2015, 22–26 February 2016, 12–16 December 2016

IAEA
International Atomic Energy Agency

No. 26

ORDERING LOCALLY

IAEA priced publications may be purchased from the sources listed below or from major local booksellers.

Orders for unpriced publications should be made directly to the IAEA. The contact details are given at the end of this list.

NORTH AMERICA

Bernan / Rowman & Littlefield

15250 NBN Way, Blue Ridge Summit, PA 17214, USA
Telephone: +1 800 462 6420 • Fax: +1 800 338 4550
Email: orders@rowman.com • Web site: www.rowman.com/bernan

Renouf Publishing Co. Ltd

22-1010 Polytek Street, Ottawa, ON K1J 9J1, CANADA
Telephone: +1 613 745 2665 • Fax: +1 613 745 7660
Email: orders@renoufbooks.com • Web site: www.renoufbooks.com

REST OF WORLD

Please contact your preferred local supplier, or our lead distributor:

Eurospan Group

Gray's Inn House
127 Clerkenwell Road
London EC1R 5DB
United Kingdom

Trade orders and enquiries:

Telephone: +44 (0)176 760 4972 • Fax: +44 (0)176 760 1640
Email: eurospan@turpin-distribution.com

Individual orders:

www.eurospanbookstore.com/iaea

For further information:

Telephone: +44 (0)207 240 0856 • Fax: +44 (0)207 379 0609
Email: info@eurospangroup.com • Web site: www.eurospangroup.com

Orders for both priced and unpriced publications may be addressed directly to:

Marketing and Sales Unit
International Atomic Energy Agency
Vienna International Centre, PO Box 100, 1400 Vienna, Austria
Telephone: +43 1 2600 22529 or 22530 • Fax: +43 1 26007 22529
Email: sales.publications@iaea.org • Web site: www.iaea.org/publications

QUALITY ASSURANCE FOR PET AND PET/CT SYSTEMS
IAEA Human Health Series No. 1
STI/PUB/1393 (145 pp.; 2009)
ISBN 978–92–0–103609–4 Price: €32.00

QUALITY ASSURANCE FOR SPECT SYSTEMS
IAEA Human Health Series No. 6
STI/PUB/1394 (249 pp.; 2009)
ISBN 978–92–0–103709–1 Price: €52.00

QUALITY ASSURANCE PROGRAMME FOR COMPUTED TOMOGRAPHY: DIAGNOSTIC AND THERAPY APPLICATIONS
IAEA Human Health Series No. 19
STI/PUB/1557 (171 pp.; 2012)
ISBN 978–92–0–128910–0 Price: €48.00

PET/CT ATLAS ON QUALITY CONTROL AND IMAGE ARTEFACTS
IAEA Human Health Series No. 27
STI/PUB/1642 (101 pp.; 2014)
ISBN 978–92–0–101014–8 Price: €48.00

The complexity of a combined SPECT/CT system requires rigorous quality control procedures. However, the information provided by clinical examinations needs to be complemented with an understanding of potential problems arising from the combined imaging procedure. This publication presents an overview of quality control procedures in SPECT and SPECT/CT and describes the pitfalls and image artefacts that can occur.

IAEA HUMAN HEALTH SERIES

INTERNATIONAL ATOMIC ENERGY AGENCY
VIENNA
ISBN 978–92–0–103919–4
ISSN 2075–3772